Accurate Measurements of the Gas-Solid Difference in Stopping-Powers and Charge-State Distributions of Lead Ions in the Energy Range of (30-300) MeV/u

Accurate Measurements of the Gas-Solid Difference in Stopping-Powers and Charge-State Distributions of Lead Ions in the Energy Range of (30-300) MeV/u

（鉛イオンビームを用いた核子あたり30-300 MeV/u領域における阻止能と荷電状態分布に現れるGas-Solid Differenceの精密測定）

Doctoral Dissertation

by

Shunki ISHIKAWA

Department of Physics
Graduate School of Science
Tohoku University

2021

Abstract

When fast ions penetrate matter, they primarily lose energy due to elastic and inelastic collisions with the atoms of the stopping material. Furthermore, they change their directions and may even vary their ionic charge states depending on their velocities and element numbers. The description of the slowing-down process is characterized by the *stopping power* which is defined by the mean energy-loss value per unit path length of the penetrated matter. Experimental and theoretical studies of the stopping power for both light and heavy ions have been performed since the discovery of radioactivity.

Although the fundamental forces of the ion-atom interaction are well known, the complex many-body collisions are difficult to describe, especially for heavy ions at low to intermediate velocities where charge-changing collisions occur frequently. An example is the longstanding problem of the dependence of the stopping power on the density of the medium. Such a *gas-solid difference* (the Bohr-Lindhard density effect) in the slowing-down process is still neglected in most theories, and the number of experimental data is still scarce.

We performed an experiment with (35, 50, 70, 100, and 280) MeV/u lead (^{208}Pb) ions slowing down in five gaseous and five solid materials, at GSI in Darmstadt, Germany. The partially ionized projectiles were provided by the combined accelerators of UNILAC and SIS-18. The measurements of energy-loss and charge-state distributions were performed with the high-resolution magnetic spectrometer FRS.

We successfully measured the mean charge states and stopping powers within an accuracy of 1%. The gas-solid differences in mean charge states and stopping powers were clearly observed for all the applied gas-solid target materials. The effect systematically decreased with higher incident velocities and vanished at 280 MeV/u. The mean charge states of lead ions emergent from solids were, at the velocity range of (30-100) MeV/u, (3-5)% higher than for the gases with neighboring Z_2 numbers. The corresponding measured stopping powers in solids were (6-8)% higher than in gases at the same velocity. The present experiment confirmed the Bohr-Lindhard prediction on the density effect at the velocity range where the experimental data were scarce.

Acknowledgements

First and foremost, I would like to express my sincere gratitude to Prof. Dr. Dr. h.c. Hans Geissel and Prof. Naohito Iwasa. My Ph.D. work could not have been accomplished without their guidance and continuous support. They have taught me physics and scientific teamwork with dedication and the spirit to prepare and analyze complex experiments. Furthermore, even though it was an extremely complicated environment for this international collaboration research due to the pandemic, I acknowledge Prof. Dr. Dr. h.c. Hans Geissel's invaluable advice and support whenever I had any questions, whether online or onsite and the sincere support of Prof. Naohito Iwasa.

Very special gratitude goes out to Prof. Dr. Christoph Scheidenberger, who kindly accepted me in the collaborative research work in the FRS group of GSI. His warm encouragement and invaluable advice on the physics background motivated my research work.

I would like to express my great thanks to Dr. Helmut Weick, Dr. Sivaji Purushothaman, Dr. Emma Haettner, and Dr. Yoshiki Tanaka for sincere and invaluable advice and discussions and for taking care of me during my stay at GSI. Since the summer school at GSI in 2017, they have supported me a lot. It was a very fruitful experience to join the experimental preparation works at the FRS facility. They gave me lectures with patience and conviction; thus, I could learn so many things regarding all the aspects of this research. Our discussions undoubtedly led my analysis and hence my thesis to the successful direction. In scientific research and daily life, I was fortunate to stay at the same office of Dr. Sivaji Purushothaman and Dr. Emma Haettner, who always encouraged and supported me.

It is a great pleasure to express my gratitude to the scientific researchers at GSI. Special thanks go out to Dr. Bettina Lommel and Dr. Birgit Kindler, who sincerely helped me with the target evaluation. Their accurate and quick technical support was invaluable for finalizing the data analysis. I would also like to thank Dr. Stephane Pietri, Dr. Andrej Prochazka, Dr. Saskia Kraft-Bermuth, Dr. Florian Greiner, Dr. Soumya Bagchi, Dr. Fabio Schirru, Dr. Ronja Knöbel, Mr. Sönke Beck, Mr. Jan-Paul Hucka, Dr. Erika Kazantseva for invaluable discussions and lectures.

I am deeply grateful to the GET_INvolved program for providing me the financial support for the stay at GSI. Also, special thanks go out to Dr. Pradeep Ghosh, Ms.

Jennifer Steitz, and Ms. Sabrina Schulte for accepting my visit to GSI anytime, even in a pandemic situation.

I sincerely would like to express my gratitude to my friends from GSI. Dr. Daria Kostyleva and Mr. Maxim Saifulin always welcomed and stood by me in private and encouraged me at any time when I was struggling with my research work. All the moments we had hung out together were priceless. I would like to give a big thank you to Mr. Ivan Muzalevskii for having wonderful moments since summer school at GSI in 2017.

I would like to express my special thanks to the members of the experimental nuclear physics group at Tohoku University. Firstly, from the short-lived-nuclear-beam group: Mr. Takahiro Sakakibara, Mr. Fumitaka Endou, Mr. Keisuke Sakuma, Mr. Kosuke Ichimura, Mr. Taiga Haginouchi, Ms. Mika Egeta, and Mr. Shojiro Ishio. I would also like to thank the members from the different two groups of the laboratory. From the exotic-nuclear-physics group: Prof. Kimiko Sekiguchi, Prof. Kenjiro Miki, Prof. Atomu Watanabe, Dr. Shinnosuke Nakai, Mr. Shun Shibuya, Mr. Daisuke Sakai, Ms. Minami Inoue, Mr. Yuta Utsuki, Mr. Sho Kitayama, Ms. Yuko Saito, Mr. Yoshiki Maruta, and Mr. Koki Kameya. From the strangeness-nuclear-physics group: Prof. Hirokazu Tamura, Prof. Satoshi N. Nakamura, Prof. Koji Miwa, Prof. Masashi Kaneta, Prof. Sho Nagao, Dr. Yuichi Toyama and other members. Especially, I would like to thank Prof. Satoshi N. Nakamura for kindly writing the recommendation letter when I applied to the summer school of GSI, when I was in the first year of master. The opportunity of the participation of the summer school became the trigger of the collaboration with the FRS group of GSI, which resulted in the accomplishment of the present Ph.D. thesis. Lastly, my special thanks go to the technician Mr. Hiroo Umetsu, the secretaries Ms. Ayumi Takahashi and Ms. Yukie Sasaki.

A special gratitude goes out to Prof. Toshimi Suda from the research center for ELectron PHoton Science (ELPH) at Tohoku University. He kindly invited me to the ELPH seminar as a speaker, where I could exchange invaluable discussions with the researchers and students, concerning the present Ph.D. topic. The opportunity surely led my Ph.D thesis and preparation for the defense to the successful direction.

I would also like to express my enormous gratitude to the Graduate Program on Physics for the Universe (GP-PU) at Tohoku University for supporting my travels to GSI and other countries so many times and providing me with a series of lectures and training. My Ph.D. work could never have been accomplished without their support and education. For this, I would like to acknowledge Ms. Hiroko Lane Miwa, especially for her quick and thoughtful supports.

I am sincerely grateful to the Japan Society for the Promotion of Science (JSPS)

grant for the financial support and providing me a base for working on the research.

Finally, I sincerely would like to express my most enormous gratitude to my family for their continuous support, encouragement, and for letting me study physics at Tohoku University, where I could have wonderful experiences and meet wonderful people. The greatest thank you goes to Sophie Colson, who has always been by my side, and her strong supports has been keeping me going forward. Arigato and merci beaucoup!

Contents

Abstract iii

Acknowledgements v

List of Figures xiii

List of Tables xvii

1 Introduction 1

2 Theory of the Slowing Down of Heavy Ions in Matter 3
2.1 Basics . . . 3
2.2 Bohr Theory . . . 5
2.2.1 Rutherford Scattering . . . 5
2.2.2 Distant Collisions . . . 6
2.2.3 Close Collisions . . . 7
2.2.4 Validity of the Bohr Theory . . . 8
2.3 Bethe Theory . . . 8
2.3.1 Derivation of the Bethe Formula . . . 8
2.3.2 Mean Excitation Potential . . . 10
2.3.3 Validity of the Bethe Formula . . . 10
2.4 Corrections to the Bethe Formula . . . 11
2.4.1 Shell Correction . . . 11
2.4.2 Fermi Density Effect . . . 12
2.4.3 Barkas Effect . . . 13
2.4.4 Bloch Correction Term . . . 14
2.4.5 Mott Correction Term . . . 14
2.4.6 Lindhard-Sørensen Theory . . . 15
2.4.7 Contributions of Correction Terms . . . 17
2.5 Energy Loss of Partially Ionized Heavy Ions . . . 19
2.6 Charge-Changing Processes . . . 20
2.6.1 Electron Loss . . . 21
2.6.2 Electron Capture . . . 23
2.7 Effective Charge State of Projectiles . . . 24
2.7.1 Effective Charge and Scaling of Stopping Powers . . . 24
2.7.2 Equilibrium Mean Charge State . . . 26

3 Motivation and Goals of the Present Experiment **29**
3.1 Short History of Stopping-Power Measurements with Heavy Ions 29
3.2 The Gas-Solid Difference in Stopping Powers 31
3.3 Experimental Stopping Powers Compared with Theoretical Predictions . 37
3.4 Goals and Requirements of the Present Experiment 38

4 Present Experiment **41**
4.1 GSI Facilities 41
4.2 Primary Beams from the SIS-18 42
4.3 FRagment Separator FRS - High Resolution Magnetic Spectrometer . . . 43
4.4 Experimental Equipment 47
4.4.1 FRS 47
4.4.2 F0 Area 48
SIS-window 49
SEETRAM 49
4.4.3 F2 Area 50
Solid Target System 51
Gas Target System 52
4.4.4 F3 Area 54
Time Projection Chamber 55
Detector Electronics 59
4.5 Properties of the Atomic Collision Target 60
4.5.1 Target Materials 60
4.5.2 Solid Targets 61
4.5.3 Gaseous Targets 63
4.6 Principles of Measurements with the FRS 64
4.6.1 Incident Beam 64
4.6.2 Charge-State Distribution and Energy Loss 65

5 Data Analysis **71**
5.1 Determination of Mean Position and Integral of Each Peak 72
5.2 Charge-State Distribution and Mean Charge State 72
5.2.1 Detector Efficiency 72
5.2.2 Charge-State Assignment 73
5.2.3 Window Corrections 74
5.3 Mean Energy Loss and Stopping Power 79
5.3.1 Determination of Dispersion Coefficient 79
5.3.2 Energy Spectrum and Determination of Mean Energy Loss 81
5.3.3 Energy-loss Correction for the Gas Target Windows 82
5.3.4 Uncertainty of the Mean Energy Loss 82
5.3.5 Stopping-Power Determination 83

6 Results and Discussion **87**
6.1 Mean Charge States . . . 87
6.2 Stopping Powers . . . 92
6.3 The Gas-Solid Difference . . . 103
6.4 Direct Conclusions . . . 108

7 Summary and Outlook **111**

A Solid Target **113**

B Stopping Powers **115**

C Evolution of Charge-State Fractions **127**

D Mean Charge States **139**

E ATIMA Program **149**
E.1 Stopping Power Prediction . . . 149
E.1.1 Elastic Collisions . . . 149
E.1.2 Inelastic Collisions . . . 150
E.2 Mean Charge State Prediction . . . 152

Bibliography **155**

List of Figures

2.1 The calculated contributions to the total stopping power from elastic and inelastic collisions of uranium projectiles in carbon. 4
2.2 Correction terms to the Bethe stopping number L_{Bethe} for the collision case of lead in an aluminum target as a function of $\gamma - 1$. 18
2.3 Comparison of the Lindhard-Sørensen (LS-) theory with the experimental stopping powers. 19

3.1 Overview of previous and present stopping-power measurements of uranium ($Z_1 = 92$), bismuth ($Z_1 = 83$), and lead ($Z_1 = 82$) ions presented in the energy-Z_2 plane. 31
3.2 Illustration of the Bohr-Lindhard and Betz-Grodzins models. 32
3.3 Experimental discovery of the gas-solid difference of stopping powers for uranium ions. 33
3.4 The experimental stopping powers of oxygen, argon, krypton and xenon projectiles at 25 MeV/u demonstrating the gas-solid difference. 36
3.5 Experimental stopping-power data of krypton projectiles in carbon and nitrogen. 37
3.6 Comparison of stopping powers for uranium projectiles in argon and titanium between experimental values and theoretical calculations. . . . 38

4.1 Schematic drawing of the present GSI facilities. 42
4.2 The designed ion optics of the FRS (F0-F3) used for our experiment. . . . 46
4.3 The designed ion optics of the FRS (F2-F3) used for our experiment. . . . 47
4.4 Schematic drawing of the fragment separator FRS and the locations of the detectors. 48
4.5 Technical drawing of the experimental setups at the F0 area of the FRS. . 50
4.6 Schematic drawing of the experimental setups at the F2 area of the FRS. 51
4.7 The target ladders used for the solid targets. 52
4.8 Schematic drawing of the gas target installed at the F2 area. 53
4.9 Schematic drawing of the gas supply system. 54
4.10 Technical drawing of the experimental setups at the F3 area of the FRS. . 55
4.11 Schematic drawing of the TPC. 57
4.12 Photograph of the C-pads and integrated passive delay line. 57
4.13 Example of the TPC calibration by using the calibration grid with fiber scintillators embedded. 58

4.14 Typical spectrum of the control-sum distribution obtained from the measurements. . . . 59
4.15 Diagram of the detector electronics and the trigger circuit. . . . 60
4.16 Measurement of the target area via translucent-light pictures. . . . 62
4.17 Scan of the target edge for evaluating the influence of the deformation to the areal density. . . . 62
4.18 Mapping of the target thickness performed by the chromatic sensor device at the target laboratory of GSI. . . . 63
4.19 Principle of the measurement with the scaling method of the FRS spectrometer at the dispersive section from F2 to F3. . . . 64
4.20 Measured steering angle. . . . 67
4.21 The mapping data of the BL_{eff} as a function of the magnet current for the third dipole magnet of the FRS. . . . 69
4.22 Measured voltage and electric current from the power supply for the third dipole magnet of the FRS. . . . 69

5.1 Measured charge-state distributions of lead ions at the dispersive focal plane F3 71
5.2 Charge-state distributions measured at the incident energy of 100 MeV/u after penetrating the 60.1mg/cm^2 zirconium target for two magnetic field settings. . . . 73
5.3 The principle of the charge state verification according to the electron shell gaps. . . . 74
5.4 Three dimensional mapping of the deviation parameter Δ as a function of the f_{EL} and f_{EC} factors. . . . 77
5.5 The f_{EL} and f_{EC} factors as a function of energy which were deduced from the Monte-Carlo simulation method. . . . 77
5.6 Deduced shift parameter Δq as a function of the incident charge-state and energy for the GC-window. . . . 78
5.7 Examples of the fit results for obtaining the dispersion coefficients. . . . 81
5.8 Energy spectra of lead ions measured by the TPC at the dispersive focal plane F3. . . . 82
5.9 Plot of the mean energy loss $\langle \Delta E \rangle$ as a function of target thickness. . . . 85
5.10 Plot of the $P(x)$ as a function of target thickness. . . . 85

6.1 Measured mean charge-states of lead ions after penetrating tin ($Z_2 = 50$) and xenon ($Z_2 = 54$) targets. . . . 90
6.2 Measured mean charge-states of lead ions after traversing zirconium ($Z_2 = 40$) and krypton ($Z_2 = 36$) targets. . . . 90
6.3 Measured mean charge-states of lead ions after traversing titanium ($Z_2 = 22$) and argon ($Z_2 = 18$) targets. . . . 91
6.4 Measured mean charge-states of lead ions after traversing carbon ($Z_2 = 6$) and nitrogen ($Z_2 = 7$) targets. . . . 91

6.5 Measured mean charge-states of lead ions after traversing polypropylene and propene compound targets. . . . 92
6.6 Experimental stopping powers of lead ions in tin ($Z_2 = 50$) and xenon ($Z_2 = 54$) targets as a function of projectile energy. . . . 93
6.7 Experimental stopping powers of lead ions in zirconium ($Z_2 = 40$) and krypton ($Z_2 = 36$) targets as a function of projectile energy. . . . 94
6.8 Experimental stopping powers of lead ions in titanium ($Z_2 = 22$) and argon ($Z_2 = 18$) targets as a function of projectile energy. . . . 94
6.9 Experimental stopping powers of lead ions in carbon ($Z_2 = 6$) and nitrogen ($Z_2 = 7$) targets as a function of projectile energy. . . . 95
6.10 Experimental stopping powers of lead ions in polypropylene and propene compound targets as a function of projectile energy. . . . 95
6.11 Experimental stopping powers of lead ions for different Z_2 targets. . . . 96
6.12 The comparisons of theoretical and experimental stopping powers of lead ions in tin ($Z_2 = 50$) and xenon ($Z_2 = 54$) targets as a function of energy. . . . 99
6.13 The comparisons of theoretical and experimental stopping powers of lead ions in zirconium ($Z_2 = 40$) and krypton ($Z_2 = 36$) targets as a function of energy. . . . 100
6.14 The comparisons of theoretical and experimental stopping powers of lead ions in titanium ($Z_2 = 22$) and argon ($Z_2 = 18$) targets as a function of energy. . . . 101
6.15 The comparisons of theoretical and experimental stopping powers of lead ions in carbon ($Z_2 = 6$) and nitrogen ($Z_2 = 7$) targets as a function of energy. . . . 102
6.16 Comparisons of theoretical and experimental stopping powers of lead ions in polypropylene and propene compound targets as a function of energy. . . . 103
6.17 Measured gas-solid difference of stopping powers in tin ($Z_2 = 50$) and xenon ($Z_2 = 54$) targets at different energies. . . . 106
6.18 Measured gas-solid difference of stopping powers in zirconium ($Z_2 = 40$) and krypton ($Z_2 = 36$) targets at different energies. . . . 106
6.19 Measured gas-solid difference of stopping powers in titanium ($Z_2 = 22$) and argon ($Z_2 = 18$) targets at different energies. . . . 107
6.20 Measured gas-solid difference of stopping powers in carbon ($Z_2 = 6$) and nitrogen ($Z_2 = 7$) targets at different energies. . . . 107
6.21 Measured gas-solid difference of stopping powers in polypropylene and propene compound targets at different energies. . . . 108
6.22 Theoretical gas-solid difference in the squared mean charge state and the normalized stopping number. . . . 108
6.23 Difference in stopping number L of gaseous materials between the bare and dressed projectile ions. . . . 110

C.1 Charge-state fractions $F(q)$ of lead ions in carbon ($Z_2 = 6$) as a function of projectile energy. . . . 128
C.2 Charge-state fractions $F(q)$ of lead ions in nitrogen gas ($Z_2 = 7$) as a function of projectile energy. . . . 129
C.3 Charge-state fractions $F(q)$ of lead ions in polypropylene compound as a function of projectile energy. . . . 130
C.4 Charge-state fractions $F(q)$ of lead ions in propene gas as a function of projectile energy. . . . 131
C.5 Charge-state fractions $F(q)$ of lead ions in titanium ($Z_2 = 22$) as a function of projectile energy. . . . 132
C.6 Charge-state fractions $F(q)$ of lead ions in argon gas ($Z_2 = 18$) as a function of projectile energy. . . . 133
C.7 Charge-state fractions $F(q)$ of lead ions in zirconium ($Z_2 = 40$) as a function of projectile energy. . . . 134
C.8 Charge-state fractions $F(q)$ of lead ions in krypton gas ($Z_2 = 36$) as a function of projectile energy. . . . 135
C.9 Charge-state fractions $F(q)$ of lead ions in tin ($Z_2 = 50$) as a function of projectile energy. . . . 136
C.10 Charge-state fractions $F(q)$ of lead ions in xenon gas ($Z_2 = 54$) as a function of projectile energy. . . . 137

E.1 Experimental stopping powers for different heavy-ion projectiles in beryllium target. . . . 152
E.2 Overview of the mean charge prediction implemented in the ATIMA 1.4. 154

List of Tables

2.1 The mean excitation potentials for hydrogen and carbon in compounds. 11

4.1 The list of the incident beams provided from the SIS-18. 49
4.2 Calibration parameters for the x direction of the TPC installed at the third focal plane F3. 58
4.3 List of the Van der Waals constants. 64

5.1 List of the experimental charge state fractions $F(q)$ of lead ions after passing through the gas-target windows. 75
5.2 List of the charge-state q, position x, and the FWHM obtained from each peak of the charge-state distribution of lead ions at 100 MeV/u after penetrating through the 56.72 mg/cm^2 thick titanium target. 80

6.1 List of fit parameters obtained for the experimental mean charge formula. 89

A.1 List of solid targets. 113

B.1 Experimental stopping powers for lead ions in carbon, and related information. 116
B.2 Experimental stopping powers for lead ions in nitrogen gas, and related information. 117
B.3 Experimental stopping powers for lead ions in titanium, and related information. 118
B.4 Experimental stopping powers for lead ions in argon gas, and related information. 119
B.5 Experimental stopping powers for lead ions in zirconium, and related information. 120
B.6 Experimental stopping powers for lead ions in krypton gas, and related information. 121
B.7 Experimental stopping powers for lead ions in tin, and related information. 122
B.8 Experimental stopping powers for lead ions in xenon gas, and related information. 123
B.9 Experimental stopping powers for lead ions in polypropylene, and related information. 124
B.10 Experimental stopping powers for lead ions in propene gas, and related information. 125

D.1 Experimental mean charge-states for lead ions after traversing carbon targets, and related information. 139
D.2 Experimental mean charge-states for lead ions after traversing nitrogen gas targets, and related information. 140
D.3 Experimental mean charge-states for lead ions after traversing titanium targets, and related information. 141
D.4 Experimental mean charge-states for lead ions after traversing argon gas targets, and related information. 142
D.5 Experimental mean charge-states for lead ions after traversing zirconium targets, and related information. 143
D.6 Experimental mean charge-states for lead ions after traversing krypton gas targets, and related information. 144
D.7 Experimental mean charge-states for lead ions after traversing tin targets, and related information. 145
D.8 Experimental mean charge-states for lead ions after traversing xenon gas targets, and related information. 146
D.9 Experimental mean charge-states for lead ions after traversing polypropylene targets, and related information. 147
D.10 Experimental mean charge-states for lead ions after traversing propene gas targets, and related information. 148

Chapter 1

Introduction

When fast ions penetrate through matter, they primarily lose their energy due to elastic and inelastic collisions with the atoms of the stopping material. Furthermore, they change their directions and may even vary their ionic charge states depending on their velocities and element numbers. The atomic collisions represent a statistical process due to fluctuating impact parameters. Therefore, an incident beam of mono-energetic ions with a fixed velocity and charge-state will emerge from the penetrated matter with broadened distributions in energy, angle, and charge state. In principle, these features have been known for many decades and used in numerous scientific applications, such as tumor therapy, material modification, and particle detectors.

The description of the slowing-down process is characterized by the *stopping power*, which is defined by the mean energy-loss value per unit path length of the penetrated matter [Boh15]. Experimental and theoretical studies of the stopping power for light and heavy ions have been performed since the discovery of radioactivity. Alpha particles emitted from radioactive sources were one of the first light projectiles studied. The first realistic model on the structure of atoms was one of the striking results from these pioneering studies of the slowing-down and angular scattering of energetic ions by J.J. Thomson, E. Rutherford, and N. Bohr. Afterwards, fission fragments were the first heavy-ions studied. However, they were characterized by a large uncertainty due to broad statistical distributions of energy and mass. With the advent of powerful heavy-ion accelerators, both theoretical and experimental studies of heavy ions have been extended over well-defined larger energy and mass ranges.

Although the fundamental forces of the ion-atom interaction are well known, the complex many-body collisions are difficult to describe with the high accuracy needed for many applications. The latter statement holds especially for heavy ions at low and up to intermediate velocities, where charge-changing collisions occur frequently. An example is the longstanding problem of the dependence of the stopping power on the density of the medium. Such a gas-solid difference in the slowing-down process is still neglected in most theories, although experimentally, the effect has been observed with different experimental methods [Gei+82; Bim+89a; Bim+89b]. Heavy ions showed an up to 20% lower stopping power in gases near the Bragg peak than in solids. An essential remaining question is: "How much does the density effect continue and contribute over the velocity range until it vanishes?" Motivated by this question, we performed

accurate measurements of stopping power and charge-state distribution in a new velocity domain, where experimental data are scarce.

In the framework of the present doctoral thesis, the experiment was performed with (35, 50, 70, 100, and 280) MeV/u lead (^{208}Pb) ions, slowed down in five gaseous and five solid materials at GSI in Darmstadt, Germany. The partially ionized projectiles were provided by the combined accelerators of UNILAC and SIS-18. The charge-state and energy-loss measurements were performed with the high-resolution magnetic spectrometer FRS [Gei+92]. The present doctoral thesis presents the experiment, data analysis, and results compared with theoretical descriptions.

In Chapter 2, the theoretical descriptions of the slowing-down processes for heavy ions are presented. Chapter 3 will explain the background and goals of the present experiment. The experimental setup will be shown in Chapter 4, followed by the description of the data analysis in Chapter 5. Our experimental results of mean charge states, stopping powers, and gas-solid differences will be presented and discussed in Chapter 6. Finally, Chapter 7 is devoted to the summary and outlook.

Chapter 2

Theory of the Slowing Down of Heavy Ions in Matter

2.1 Basics

In this chapter, we will briefly describe the theoretical framework of the energy-loss and charge-changing processes of heavy ions passing through matter [Boh48; Sig14]. The energy loss of charged particles in matter is caused by the Coulomb interaction in statistical atomic collisions. Different types of collisions with varying impact parameters and collision frequencies in a given path length lead to a statistical distribution of energy loss characterized by a mean value and a certain width. The latter is called energy-loss straggling. The slowing-down process depends on the velocity, mass, charge, and properties of the target atoms. The atomic interaction represents a complicated many-body problem due to the many bound correlated electrons involved. The projectiles primarily undergo elastic and inelastic collisions with the target atoms, i.e., both electron systems may be excited, or even a charge-changing process may happen. Charge-changing collisions are essential and characteristic, especially for the slowing down of heavy ions, which complicates an accurate theoretical description even more.

In the theoretical description, the differential collisional cross-section $d\sigma/dT$ contains all the information of the physical processes, where T and σ denote the energy transferred in a single collision and its probability, respectively. With the differential cross-section, the mean energy loss is defined by

$$\langle \Delta E \rangle = N\Delta x \int T d\sigma = N\Delta x \int T \frac{d\sigma}{dT} dT, \tag{2.1}$$

where N and Δx denote the density of the target atoms and the path length in the penetrated matter, respectively. The specific energy loss of the projectile ions are characterized by the so-called *stopping power* defined by

$$\frac{dE}{dx} = \lim_{\Delta x \to 0} \frac{\langle \Delta E \rangle}{\Delta x}. \tag{2.2}$$

The most outstanding physicists such as Niels Bohr, Hans Bethe, and Jens Lindhard

have contributed and pioneered the field of the stopping powers. Of course, the physical dimension is a force[1]. Practically, the unit is usually represented by $\mathrm{MeV}/(\mathrm{mg}/\mathrm{cm}^2)$ which corresponds to the definition of the *mass* stopping power. Throughout this thesis, we will refer to this definition.

The projectiles' energy loss is caused primarily by elastic and inelastic collisions with the target atoms. The projectile interacts with the whole target atom in the screened Coulomb field in the elastic collisions. The result is an angular deflection of the projectile and a displacement of the target atom. In the inelastic collisions, the energy is transferred to the electron system of the target atoms, causing their excitation and ionization. The total stopping power is the sum of both contributions as $\frac{dE}{dx}(\text{total}) = \frac{dE}{dx}(\text{elastic}) + \frac{dE}{dx}(\text{inelastic})$. Figure 2.1 shows the calculated contributions from the elastic and inelastic collisions for the case of uranium projectiles slowing down in carbon. The stopping powers were calculated with the ATIMA program[2] [Wei98a]. In the investigated energy domain of (30-300) MeV/u of our present experiment, indicated by the green area on the graph, the inelastic collisions dominate the total stopping power.

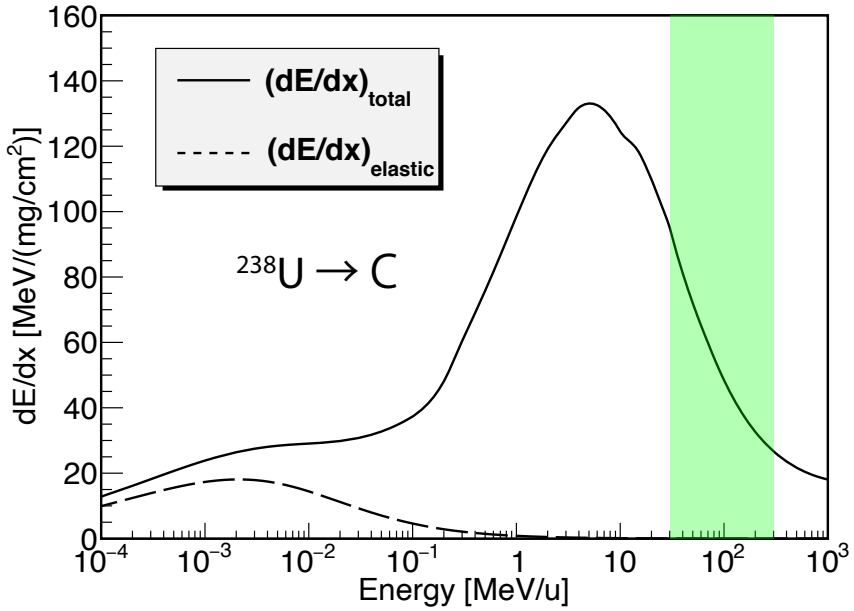

FIGURE 2.1: Calculated contributions to the total stopping power from elastic and inelastic collisions of uranium projectiles in carbon. The relevant energy range of the present experimental study is indicated by the green area. In this domain, the inelastic collisions dominate.

[1]The origin of the name *Stopping Power* is *Bremsvermögen* in German, in a sense of *Capability of Stopping*, and it was directly translated in English.

[2]See Appendix E for the description of the ATIMA program.

2.2 Bohr Theory

The present slowing-down experiment with lead projectiles in the energy domain of (30-300) MeV/u, where the corresponding velocity domain is about $\beta = 0.25\text{-}0.65$ in the unit of the speed of light in vacuum, is still in the regime of classical treatment concerning the theoretical validity. Therefore, it is relevant to review the pioneering Bohr theory, which was also the basis of the first realistic model of the atomic structure of matter [Boh13; Boh15]. For the theoretical description, first, several approximations are made for the calculations [Boh48; Ahl80]:

- The target medium is considered to be dilute.
- The velocity of the projectile is much greater than the orbital velocity of the target electrons.
- The microscopic structure of the projectile is not included.
- The charge state of the projectile does not change during the collision.

2.2.1 Rutherford Scattering

To obtain Bohr's classical framework, we first consider the Rutherford scattering. Here, the collision is considered between two free point-particles with mass and charge m_1 and q_1 for the projectile and m_2 and q_2 for the target, respectively, and with the relative velocity v. Under the pure Coulomb interaction

$$V(r) = \frac{q_1 q_2}{r} \quad , \tag{2.3}$$

the movement of the two point-particles is well known as a hyperbolic trajectory in the center of mass (c.m.) system. The deflection angle θ in the c.m. system can be deduced from a straightforward calculation as a function of the impact parameter b as

$$\tan\frac{\theta}{2} = \frac{m_1 + m_2}{m_1 m_2}\frac{1}{v^2}\frac{q_1 q_2}{b} = \frac{b_{\text{ref}}}{2b} \quad , \tag{2.4}$$

where $b_{\text{ref}} = 2(m_1 + m_2)q_1 q_2 / m_1 m_2 v^2$ is the collision diameter, which corresponds to the minimum distance in a repulsive head-on collision. The energy transfer T to the target particle is given by

$$\begin{aligned} T &= \frac{1}{2} m_2 v_2^2 \\ &= \frac{2m_1^2 m_2}{(m_1 + m_2)^2}\, v^2 \, \sin^2\frac{\theta}{2} = T_{max}\sin^2\frac{\theta}{2} \quad , \end{aligned} \tag{2.5}$$

where T_{max} represents the maximum energy transfer, corresponding to $\theta = \pi$ which is the backscattering phenomenon. With Eq.2.4 and Eq.2.5 the energy transfer is given

as a function of impact parameter as

$$T = \frac{2q_1^2 q_2^2}{m_2 v^2}\frac{1}{b^2}\frac{1}{1+\left(\frac{b_{\text{ref}}}{2b}\right)^2} = \frac{T_{max}}{1+\left(\frac{2b}{b_{\text{ref}}}\right)^2} \quad . \tag{2.6}$$

As one can see from Eqs. 2.4-2.6, if the impact parameter b is much greater than b_{ref} (when the collision occurs in *distant*) the deflection angle θ will be small, and accordingly the energy transfer will also be small. Then, the collisional differential cross section can simply be obtained from $d\sigma = d(\pi b^2)$ as

$$d\sigma = \pi\left(\frac{b_{\text{ref}}}{2}\right)^2 \frac{\cos\frac{\theta}{2}}{\sin^3\frac{\theta}{2}} d\theta = \pi\left(\frac{b_{\text{ref}}}{2}\right)^2 T_{max}\frac{dT}{T^2} \quad . \tag{2.7}$$

By inserting this differential cross section into Eq.2.1, the mean energy loss can be obtained as

$$\begin{aligned}\langle \Delta E \rangle &= N\Delta x \frac{2\pi q_1^2 q_2^2}{m_2 v^2}\int_{T_{min}}^{T_{max}} \frac{d\sigma}{dT} dT \\ &= N\Delta x \frac{2\pi q_1^2 q_2^2}{m_2 v^2} \ln\frac{T_{max}}{T_{min}} \quad ,\end{aligned} \tag{2.8}$$

or, in the form which include the impact parameter explicitly as

$$\langle \Delta E \rangle = N\Delta x \frac{2\pi q_1^2 q_2^2}{m_2 v^2}\int_{b_{min}}^{b_{max}} \frac{1}{b^2}\frac{2bdb}{1+(\frac{b_{\text{ref}}}{2b})^2} \quad . \tag{2.9}$$

Here, we shall consider the situation where the projectile particle penetrates through a monoatomic target with the atomic number Z_2, mass M_2 and N atoms in a unit volume according to Eq.2.8. There are two collision components for the target particle here, namely atoms and electrons. Therefore, the notations become

- $m_2 = M_2$, $q_2 = Z_2 e$, and $N = N$ for atoms
- $m_2 = m_e$, $q_2 = -e$, and $N = Z_2 N$ for electrons

Then, the ratio between the mean energy losses due to the target atoms and electrons would be

$$\frac{\langle \Delta E \rangle_{\text{elastic}}}{\langle \Delta E \rangle_{\text{inelastic}}} \sim Z_2 \frac{m_e}{M_2} \ll 1 \quad , \tag{2.10}$$

This calculation suggests that the energy loss due to the collision with target electrons is dominant, which is related to the comparison between the elastic and inelastic collisions mentioned in Section 2.1 before.

2.2.2 Distant Collisions

Now that we concentrate on the collision between a bare heavy-projectile ($q_1 = Z_1$) and a bound target electron. Niels Bohr, who was a student of Rutherford, extended the consideration of the *distant* collision problem by taking into account the effect of

the binding forces on the electrons. He treated the energy transfer as the excitation of harmonic oscillators with a classical harmonic oscillator frequency ω. The resulting energy transfer in the relativistic expression is given by [Ahl80]

$$T_{\text{distant}} = \frac{2Z_1^2 e^4}{m_e v^2} \frac{1}{b^2} \left[\xi^2 K_1^2(\xi) + \xi^2 K_0^2(\xi)/\gamma^2\right] \quad , \tag{2.11}$$

where $\xi = \omega b/\gamma v$ with the Lorentz factor γ, $K_0(\xi)$ and $K_1(\xi)$ are the modified Bessel functions of the zeroth and first orders, respectively. For getting the stopping power formula by integrating Eq.2.11, Bohr set a critical value for the impact parameter as b_0 to distinguish the region of the distant collisions from the *close* collisions, whose concept will be explained in the next subsection. The integration according to Eq.2.9 is performed from $b = b_0$ to $b = \infty$, resulting in

$$\left(\frac{dE}{dx}\right)_{\text{distant}} = \frac{4\pi N Z_1^2 Z_2 e^4}{m_e v^2} \left[\xi_0 K_1(\xi_0) K_0(\xi_0) - \frac{\beta^2}{2} \xi_0^2 (K_1^2(\xi_0) - K_0^2(\xi_0))\right] \quad , \tag{2.12}$$

where $\xi_0 = \xi(b_0)$, and N is the number of target atoms per unit volume [Ahl80].

2.2.3 Close Collisions

In contrast, when the impact parameter b satisfies $b < b_0$, the energy transfer is considered more significant than the binding of electrons; thus, the influence of the latter is neglected, resulting in that the collision problem being treated between two free particles under the pure Coulomb interactions as we have considered in the Rutherford scattering problem. From the Eq.2.6, the energy transfer is given as

$$T_{\text{close}} = \frac{2Z_1^2 e^4}{m_e v^2} \frac{1}{b^2} \frac{1}{1 + \left(\frac{b_{\text{ref}}}{2b}\right)^2} \quad , \tag{2.13}$$

where b_{ref} now is reduced to $2Z_1 e^2/m_e v^2 \gamma$. As was done for the distant collisions, the integration can be carried out from $b = 0$ to $b = b_0$, and lead to [Ahl80]

$$\left(\frac{dE}{dx}\right)_{\text{close}} = \frac{2\pi N Z_1^2 Z_2 e^4}{m_e v^2} \ln\left[1 + \left(\frac{2b_0}{b_{\text{ref}}}\right)^2\right] \quad . \tag{2.14}$$

Then, where can we find the critical impact parameter b_0? In the present consideration, we have assumed that the velocity of projectile is much greater than the orbital velocity of the target electrons. This leads to the collision time roughly being $\tau = 2b/\gamma v$. When compared with the oscillation period $\tau_{\text{osc.}} = 2\pi/\omega$, then, a significant momentum (energy) transfer can be expected for $\tau \ll \tau_{\text{osc.}}$; otherwise the energy transfer becomes *adiabatic*. Based on that, Bohr set a cutoff parameter as

$$a_{\text{ad}} = \frac{\gamma v}{\omega} \quad , \tag{2.15}$$

which is the so-called Bohr's adiabatic radius and beyond which the energy transfer is inefficient [Boh48]. Therefore, the critical impact parameter should be $b_0 \ll a_{\mathrm{ad}}$. Furthermore, for the collision being distant enough, it can be considered as $b_0 \gg b_{\mathrm{ref}}$. Then, in the condition of $b_{\mathrm{ref}} \ll b_0 \ll a_{\mathrm{ad}}$, the modified Bessel functions can be expanded and one can obtain Bohr's classical stopping-power formula as [Boh13; Boh48; Ahl80]

$$\left(\frac{dE}{dx}\right)_{\mathrm{Bohr}} \approx \frac{4\pi N Z_1^2 Z_2 e^4}{m_e v^2}\left[\ln\frac{1.123 m_e v^3}{Z_1 e^2 \omega} - \ln(1-\beta^2) - \frac{\beta^2}{2}\right] \quad . \tag{2.16}$$

Besides, the critical impact parameter b_0 can also be found from the crossovers between T_{distant} and T_{close} [Sig96].

2.2.4 Validity of the Bohr Theory

Bohr's classical theory, in principle, follows the picture of the Rutherford scattering. Therefore, for visualizing such classical orbital motion with a definite impact parameter, the de Broglie wave length ($\lambda\!\!\!^{-} = \hbar/m_e v$) must be smaller than the collision diameter b_{ref}. Otherwise, the quantum effect must appear. The complete picture of Rutherford and Bohr is obtained at the limit as

$$\kappa = \frac{b_{\mathrm{ref}}}{\lambda\!\!\!^{-}} = \frac{2Z_1 e^2}{\hbar v} \gg 1 \quad , \tag{2.17}$$

where κ is the so-called Bohr's kappa, which is an important measure for considering the validity of the Bohr theory [Boh48]: As κ decreases, the Bohr theory gradually lose its validity, and when $\kappa < 1$ it is not valid anymore.

2.3 Bethe Theory

2.3.1 Derivation of the Bethe Formula

After the establishment of quantum mechanics in the mid-1920s, the first quantal calculation of energy loss was performed by Hans Bethe in the manner of first-order Born approximation. In Bohr's classical theory, the impact parameter was responsible for the energy loss. However, in the Bethe theory, it is considered in terms of the momentum transfer. In 1930, the non-relativistic case was treated [Bet30], and his theory was extended to the relativistic case in 1932 [Bet32]. The potential under consideration is also the Coulomb potential; however, there is an additional interaction through the transverse vector potential, which describes the coupling of the currents between the projectile and a target electron by the virtual photon exchange. In the framework of the Dirac equation, the latter is proportional to the velocity $\vec{\beta}_t$ transverse to the momentum transfer $\vec{q}$. The differential cross-section for the inelastic collision to excite a

target atom to an energy level E_n is then expressed as [Fan63]

$$\frac{d\sigma_n}{dQ} = \frac{2\pi Z_1^2 e^4}{m_e c^2 \beta^2}\left(1+\frac{Q}{m_e c^2}\right)\left(\frac{|F_n(\vec{q})|^2}{Q^2(1+Q/(2m_e c^2))}+\frac{|\vec{\beta}_t\cdot\vec{G}_n(\vec{q})|^2}{Q^2(1+Q/(2m_e c^2))-E_n/(2m_e c^2)}\right) \quad , \tag{2.18}$$

where, Q is the energy transferred to an *unbound* electron, which is defined for convenience, and the relation to the momentum transfer ($q = |\vec{q}|$) is given by $Q(1 + Q/2m_e c^2) = q^2/2m_e$ in the relativistic regime. Therefore, when Q is small (large), the momentum transfer can also be considered small (large). The matrix elements $F_n(\vec{q})$ and $\vec{G}_n(\vec{q})$, respectively, correspond to the pure Coulomb (longitudinal) excitation and the transverse excitation as

$$\begin{aligned} F_n(\vec{q}) &= \langle n|\exp(i\vec{q}\cdot\vec{r}/\hbar)|0\rangle \\ \vec{G}_n(\vec{q}) &= \langle n|\vec{\alpha}\ \exp(i\vec{q}\cdot\vec{r}/\hbar)|0\rangle \quad , \end{aligned} \tag{2.19}$$

where the latter is proportional to the relativistic current operator $\vec{\alpha}$. In the non-relativistic limit, the differential cross section Eq.2.18 is reduced to

$$\frac{d\sigma_n}{dQ} = \frac{2\pi Z_1^2 e^4}{m_e c^2 \beta^2}\frac{|F_n(\vec{q})|^2}{Q^2} \quad . \tag{2.20}$$

For the evaluation of the matrix elements F_n and $\vec{G}_n$, different regions are distinguished according to Q [Fan63]:

- For very small Q, i.e., for the case with small scattering angles in the distant collisions, the exponential part $\exp(i\vec{q}\cdot\vec{r}/\hbar)$ in F_n and $\vec{G}_n$ can be expanded up to the first order in terms of q. This is the so-called dipole approximation.
- For very large Q, i.e., for the case with large scattering angles in the close collisions, the target electrons are considered as unbound and $E_n \approx Q$. The approximated Dirac wave functions are then used in the calculation.
- For the intermediate Q range, the transverse term is assumed to be neglected. The upper limit of this Q range is considered to be much smaller than the electron mass.

Having the approximations described above, one can perform the individual calculations according to the Q range and then obtain the famous Bethe formula (or the so-called Bethe-Bloch formula[3]) [Bet32; Fan63] as

$$\begin{aligned} -\frac{dE}{dx} &= N\sum_n E_n \int d\sigma_n \\ &= \frac{4\pi N Z_1^2 Z_2 e^4}{m_e c^2 \beta^2}\left[\ln(2m_e c^2\beta^2) - \sum_n f_n \ln(E_n) - \ln(1-\beta^2) - \beta^2\right] \quad . \end{aligned} \tag{2.21}$$

[3]The reason why it is often called the Bethe-Bloch formula would be that, Bloch helped to approximate the mean excitation potential as $I = 10Z_2$ [eV] at that early time. However, one should simply quote as the Bethe formula when different notation of the mean excitation potential is used.

The summation in the square bracket is over the excitation energies E_n and the dipole oscillator strength f_n of each atomic shell level but is usually replaced by the mean excitation potentials I. Furthermore, since the factors in front of the square bracket are simply the requirements from the first-order Born approximation, the contents in the square bracket become interesting. They are in total dimensionless and called the *stopping number* L. Consequently, the stopping power can be expressed as

$$-\frac{dE}{dx} = \frac{4\pi N Z_1^2 Z_2 e^4}{m_e c^2 \beta^2} \cdot L_{\text{Bethe}} \quad , \tag{2.22}$$

where,

$$L_{\text{Bethe}} = \ln \frac{2m_e c^2 \beta^2}{I} - \ln(1-\beta^2) - \beta^2 \tag{2.23}$$

and,

$$\ln I = \sum_n f_n \ln(E_n) \quad . \tag{2.24}$$

2.3.2 Mean Excitation Potential

The mean excitation potential I in Eq.2.23 is one of the main characteristics of the Bethe formula, which results from the calculation in the range of small-Q approximation. The calculation of the oscillator strengths f_n is needed for each atomic level, however, it is complicated as the number of electrons increases. Therefore, the mean excitation potential I is usually determined experimentally from the measurement of stopping-powers such as protons, and there is a semi-empirical formula depending on target atomic number Z_2 as [Leo94]

$$\begin{aligned} \frac{I}{Z_2} &= 12 + \frac{7}{Z_2} \quad [\text{eV}] \quad \text{for} \quad Z_2 < 13 \\ \frac{I}{Z_2} &= 9.76 + 58.8 Z_2^{-1.19} \quad [\text{eV}] \quad \text{for} \quad Z_2 \geq 13 \ . \end{aligned} \tag{2.25}$$

In the relativistic region, the mean excitation potential I is very small compared to $2m_e c^2 \beta^2$. Plus, since it appears only in the logarithmic term in the stopping number L, the uncertainty in I is not critical for the stopping power calculation. However, it is still advantageous to refer to the tabulated values in the NIST website [NISb]. Besides, Bragg's additivity rule can be adopted for the calculation of stopping powers for compounds of, e.g., carbon and hydrogen. In this case, it may be recommended to take the optimized values depending on the material state of the compounds. For example, Bär *et al.* [Bär+18] reported the values for several elements in compounds, and their values for hydrogen and carbon are listed in Tab.2.1 together with the values from the NIST table.

2.3.3 Validity of the Bethe Formula

One should notice that the stopping number L_{Bethe} does not depend on the projectile's atomic number Z_1, which is resulted from the first-order Born approximation. In

TABLE 2.1: The mean excitation potentials for hydrogen and carbon in compounds. The second column corresponds to the values from NIST table [NISb]. The third and fourth columns are the recommended values from Bär *et al.* [Bär+18] for different material states of compounds.

Element	NIST (eV)	Solid (Bär) (eV)	Gas (Bär) (eV)
H	19.2	22.07 ± 1.32	21.54 ± 0.74
C	78.0	79.91 ± 3.61	66.75 ± 1.08

turn, the stopping number may be extended for the higher orders in terms of Z_1 for considering corrections to the Bethe formula. In addition, the quantum perturbation treatment is allowed only in the adiabatic condition as

$$\kappa = \frac{2Z_1\alpha}{\beta} \ll 1 \quad , \tag{2.26}$$

where κ is the Bohr's kappa as we have introduced in Eq.2.17, and α is the fine structure constant. Therefore, if κ is larger than unity, it is the range of validity of Bohr's classical treatment for the stopping power calculation. Furthermore, the adiabatic condition is often violated for the heavy ions. For example, in our experimental energy domain from 30 to 300 MeV/u, the adiabatic parameter is 1.83-4.83 for the lead projectiles. Therefore, the present slowing-down experiment with lead projectiles may be within the classical treatment, as mentioned in Section 2.2. However, as described in the following sections, the Bethe formula has been the basis of the theoretical developments for the description of stopping powers. The theoretical improvements were performed either (1) by considering the higher orders in the Born approximation or (2) by using the exact solutions for, e.g., the wave functions.

2.4 Corrections to the Bethe Formula

This section will explain the theoretical developments for the stopping power calculation based on the Bethe formula. The correction terms to Bethe's stopping number L_{Bethe} will be represented by ΔL. Then, the Lindhard and Sørensen (LS-) theory [LS96], which includes such correction terms, will be compared to the experimental stopping-power data of bare heavy projectiles.

2.4.1 Shell Correction

In the derivation of the Bethe formula, an assumption was used that the projectile velocity was much greater than the orbital velocities of target electrons. This condition

simplifies the calculation, especially at the intermediate Q range, where the contributions from the electrons in all atomic shell levels result in

$$\sum_n E_n |F_n(\vec{q})|^2 = Q \tag{2.27}$$

with the help of the Thomas-Reiche-Kuhn sum rule [Bet30; Fan63]. This equation implies that the target electrons receive the energy transfer Q equally no matter their shell level is and as if they were unbound at rest [Fan63]. However, when the projectile velocity becomes comparable with or lower than the orbital velocity of the target electron, i.e., if the excitation energy for the inner shells of the atom increases compared to the energy transferred, the energy loss for each individual atomic shell level must be examined. The derivation of the stopping number L in Eq.2.21 must then be extended and Eq.2.23 must be modified by a correction term as

$$\Delta L_{\text{Shell}} = L - L_{\text{Bethe}} = -\frac{C}{Z_2} \tag{2.28}$$

with

$$C = C_K(v) + C_L(v) + \cdots \quad .$$

The correction factors C_i for each individual atomic shell ($i = K, L, M$) depend on the projectile velocity and disappear at the high-velocity domain. The individual contributions from the K- and L-shells are considered, e.g., in Refs. [LB37; Wal52; Wal55; Kha67]. Overall, they lead to a reduction of the stopping power since not all of the target electrons contribute to the slowing-down of projectiles. Lastly, a useful empirical formula can be found in Ref. [BB64] as

$$\begin{aligned} C(I,\eta) = &\left(0.422377\eta^{-2} + 0.0304043\eta^{-4} - 0.00038106\eta^{-6}\right) \times 10^{-6} I^2 \\ &+ \left(3.850190\eta^{-2} - 0.1667989\eta^{-4} + 0.00157955\eta^{-6}\right) \times 10^{-9} I^3 \quad , \end{aligned} \tag{2.29}$$

which is valid for $\eta = \beta\gamma \geq 0.1$.

2.4.2 Fermi Density Effect

Similar to the case of the shell correction described above, another assumption in the Bethe formula would be violated easily; the collision of a projectile occurs only with a single target atom without any interference from others. This is undoubtedly an incorrect assumption for the case of dense media such as in a solid material. One must take into account the interactions with target atoms located in distance. However, with ever-increasing velocity, meaning that with ever-increasing impact parameters, the stopping power might be summed infinitely. It was Enrico Fermi in 1940 who considered the density effect in terms of the polarization of target atoms shielding the projectile charge, resulting in the reduction of the electronic stopping power with large impact parameters [Fer40]. Therefore, this effect works to reduce the Bethe stopping

power, and it becomes significant only in the relativistic regime. The common representation is $-\delta/2$, where the half would stand for that the polarization is related only with the distant collisions. It is also noteworthy to mention the work by Sternheimer *et al.* [Ste84] who evaluated the density effect for a large number of substances since 1945. The formula proposed in 1952 is given as

$$\delta(X) = \begin{cases} 4.6052X + a\,(X_1 - X)^m + C & \text{for} \quad (X_0 < X < X_1) \\ 4.6052X + C & \text{for} \quad (X > X_1) \end{cases} \tag{2.30}$$

where $X = \log_{10}(\beta\gamma)$ whose minimum limit X_0 requires the density effect δ to be zero under the value. The coefficients a and m are to be determined by the fit to the experimental data, and C is given by

$$C = -2\ln(I/h\nu_p) - 1 \quad , \tag{2.31}$$

where the I is the mean excitation potential, and $h\nu_p$ is the plasma energy of the electrons given by

$$h\nu_p = 28.816\sqrt{\rho\frac{Z_2}{A_2}} \tag{2.32}$$

with the density ρ, atomic number Z_2, and atomic mass A_2 of the target.

2.4.3 Barkas Effect

The stopping number of the Bethe formula (Eq.2.23) does not include any dependence on the projectile charge. The correction term, then, can naturally be considered by including Z_1 dependence, such as from the higher-order approximations, or, which can semi-empirically be expressed as the expansion of the stopping number L in terms of Z_1 as $L = L_0 + Z_1 L_1 + \cdots$. In this scheme, the next leading order should be the Z_1^3 correction term.

When examining the range of slow charged-pions at $\beta \sim 0.1$ in matter, Barkas *et al.* observed a longer range for negatively charged pions compared to positively charged ones [BDH63]. Such a difference may be explained as the displacement of the target electrons during the collision (the polarization effect). The correction term to the Bethe formula due to the projectile's charge was, then, considered as follows:

In 1972, Ashley, Brandt, and Ritchie performed a classical calculation of the energy transfer from a heavy ion projectile to a target electron in the representation of a classical harmonic oscillator to evaluate the contribution from the Z_1^3 term [ABR72]. Following their work, Hill and Merzbacher carried out a calculation by the quantum mechanics, taking into account the distorted electron distribution. They found that their results were consistent with the classical calculation [HM74]. Using the similar

method to Ref.[ABR72], Jackson and McCarthy considered the difference in the stopping power formula, and their results were obtained in the form as [JM72]

$$\Delta L_{\text{Barkas}} = L\frac{Z_1}{\sqrt{Z_2}}F(V) \tag{2.33}$$

with

$$V = \frac{\beta\gamma}{\alpha\sqrt{Z_2}} \quad . \tag{2.34}$$

The $F(V)$ is the dimensionless universal function, and the exact form is given in Ref.[JM72]. Their calculation assumed that the polarization effect only led to the change in the energy transfer in the distant collisions and was neglected for the close collisions. However, Lindhard [Lin76] suggested that it consist of both contributions from distant and close collisions equally. This meant that Eq.2.33 should become about twice as large, which was considered from the comparison to the experimental data. In addition, the differences in stopping-powers for protons and anti-protons were examined by Medenwaldt *et al.* in 1991 [Med+91], and it was found that the theoretical prediction was much smaller than those observed; therefore, it would be recommended to multiply Eq.2.33 by a factor of two.

2.4.4 Bloch Correction Term

When the velocity goes toward the classical treatment region (when κ in Eq.2.26 increases), several assumptions in the Bethe formula are again violated. Moreover, one may try to replace the Bethe formula with Bohr's classical formula for the stopping-power calculation. However, the transition is not smooth, especially at $\kappa \approx 1$, and both treatments of Bethe and Bohr are, in principle, incorrect in this region [Boh48]. It was Felix Bloch in 1933 who pointed out the problem occurring in the close collisions with a large momentum transfer, where the target electron is considered unbound. He succeeded in building a bridge between the two theories, and his theory provided the correction term ΔL_{Bloch} in the stopping number at non-relativistic regime, given as [Blo33]

$$\Delta L_{\text{Bloch}} = \psi(1) - \text{Re}\psi(1 + iZ_1\alpha/\beta) \quad , \tag{2.35}$$

where ψ is the logarithmic derivative of the complex gamma function. As a tip, one should note that even though Eq.2.21 is often called the "Bethe-Bloch" formula, this Bloch correction term is not included usually.

2.4.5 Mott Correction Term

Contrarily, at the relativistic range, in the close collisions with large momentum transfer, the scattering cross-section treated with the first-order Born approximation significantly differs from the exact calculation if the projectile has a large nuclear charge. Therefore, in the framework of the Dirac equation, the exact Mott cross-section should be treated instead, as demonstrated by Mott [Mot29; Mot32]. Ahlen [Ahl78; Ahl80]

considered the scattering of a Dirac electron by a heavy point-projectile, and the correction term to the Bethe formula was given by

$$\begin{aligned}\Delta L_{\text{Mott}} =& \frac{1}{2}\left[\kappa\beta^2\left(1.725+\left(0.52-2\sqrt{\omega_0/\omega_m}\right)\pi\cos\chi\right)\right.\\ &+\kappa^2\beta^2\left(3.246-0.451\beta^2\right)\\ &+\kappa^3\beta^3\left(1.522\beta+0.987/\beta\right)\\ &+\kappa^4\beta^4\left(4.569-0.494\beta^2-2.696/\beta^2\right)\\ &\left.+\kappa^5\beta^5\left(1.254\beta+0.222/\beta-1.170/\beta^3\right)\right] \quad ,\end{aligned} \tag{2.36}$$

where $\omega_m = 2m_e v^2\gamma^2$ and $\sqrt{\omega_0} = \sum_n f_n\sqrt{\hbar\omega_n}$. The definition of $\cos\chi$ is given in Ref. [DS56] as

$$\cos\chi = \text{Re}\left[\frac{\Gamma\left(\frac{1}{2}-i\kappa\right)\Gamma\left(1+i\kappa\right)}{\Gamma\left(\frac{1}{2}+i\kappa\right)\Gamma\left(1-i\kappa\right)}\right] \tag{2.37}$$

with the complex Gamma functions.

2.4.6 Lindhard-Sørensen Theory

Following these correction terms derived from the consideration of the close collisions, such as by Bloch and Mott, a rigorous theory on the stopping power of fully-ionized heavy ions was developed by Lindhard and Sørensen in 1996, nearly 60 years later, by treating the phase shift of partial waves with different angular momenta ℓ [LS96]. The calculation method they used was to find the deviation as

$$\Delta L_{\text{LS}} = L - \left(L_{\text{Bethe}} + \Delta L_{\text{Shell}} - \frac{\delta}{2} + \Delta L_{\text{Barkas}} + \Delta L_{\text{scr.}}\right) \quad . \tag{2.38}$$

The last correction term $\Delta L_{\text{scr.}}$ in the righthand side of the equation corresponds to the screening effect due to the captured electrons by the projectiles, which we will mention in the following section; and it is omitted here since we are considering the bare projectiles. Furthermore, the ΔL_{LS} coincides with the Bloch correction term at the non-relativistic range and the Mott correction term at the relativistic range in consideration of a point charge projectile. Below, the summary of Ref.[LS96] is given.

Recall that we are interested in the scattering of an unbound target electron by a projectile nucleus with a relative velocity v. When the deflection angle in the c.m. system is θ, the stopping-power is simply expressed as

$$-\left(\frac{dE}{dx}\right)_{\text{close}} = NZ_2\frac{T_{max}}{2}\int d\sigma(1-\cos\theta) \quad , \tag{2.39}$$

where $T_{max} = 2m_e v^2\gamma^2$ is the maximum energy transferred. The integration part results in the summation of the partial waves with angular momenta ℓ (see, e.g.,

Ref.[Sch68; LL77] for the detailed calculation of the scattering theory) as

$$\int d\sigma(1-\cos\theta) = 4\pi\lambda\!\!\!^{-2} \sum_{\ell=0}(\ell+1)[\frac{\ell+2}{2\ell+3}\sin^2(\delta_{-\ell-1}-\delta_{-\ell-2}) + \frac{\ell}{2\ell+1}\sin^2(\delta_{\ell+1}-\delta_\ell) + \frac{1}{(2\ell+1)(2\ell+3)}\sin^2(\delta_{\ell+1}-\delta_{-\ell-1})] \quad , \tag{2.40}$$

where $\lambda\!\!\!^{-} = \hbar/(m_e v\gamma)$ is the de Broglie wave length, and we considered the phase shift δ for the total angular momenta of spin-up and spin-down electrons $j = \ell + 1/2$ and $j = \ell - 1/2$, respectively. Since it is more convenient to characterize the partial waves with a total angular momentum, a new quantum number $k = \pm(j+1/2)$ was introduced as

$$\ell = \begin{cases} k = j + 1/2 & \text{for} \quad k > 0 \\ -k - 1 = j - 1/2 & \text{for} \quad k < 0 \end{cases} \tag{2.41}$$

Then, after renumbering by k, the general stopping number L for the close collisions can be deduced by comparing Eq.2.39 and 2.40 to Eq.2.22 as

$$L_{\text{close}} = \frac{4}{\kappa^2}\sum_k |k| \left[\frac{k-1}{2k-1}\sin^2(\delta_k - \delta_{k-1}) + \frac{1}{2(4k^2-1)}\sin^2(\delta_k - \delta_{-k})\right] \quad . \tag{2.42}$$

In the relativistic case, the phase shift is given by

$$\delta_k = \zeta_k - \arg\Gamma(s_k + 1 + i\kappa/2) - \frac{1}{2}\pi s_k + \frac{1}{2}\pi l \tag{2.43}$$

where,

$$s_k = \sqrt{k^2 - (\alpha Z_1)^2}$$

and

$$e^{2i\zeta_k} = \frac{k - i\kappa/2\gamma}{s_k - i\kappa/2} \quad .$$

The argument of the complex gamma function ($\arg\Gamma$) can be determined numerically. Applying the perturbation limit from Eq.2.17 ($\kappa \ll 1$) with which the Bethe formula was derived, Eq.2.42 reduces to

$$L_{\text{close}}^{\text{pert}} = \sum_{k\geq 1}\frac{1}{k} - \frac{\beta^2}{2} \quad . \tag{2.44}$$

Therefore, the correction term for the close collisions is given by the difference between Eq.2.42 and Eq.2.44 as

$$\Delta L_{\text{LS}} = \sum_{k=-\infty, k\neq 0}^{\infty}\left[\frac{4|k|}{\kappa^2}\frac{k-1}{2k-1}\sin^2(\delta_k - \delta_{k-1}) - \frac{1}{2|k|}\right] + \frac{1}{\gamma^2}\sum_{k=1}^{\infty}\frac{k}{4k^2-1}\frac{1}{k^2 + (\kappa/2\gamma)^2} + \frac{\beta^2}{2} \quad . \tag{2.45}$$

In the same reference, this phase shift method is extended to take into account the influence of the finite nuclear size: When the heavy projectile is at highly relativistic,

meaning that when the de Broglie wave length of the electrons approaches the projectile nuclear size, the collision is affected by the nuclear charge distributions. This finite nuclear size correction was deduced from the difference as $\Delta L_{\mathrm{LS,fns}} \propto \int (1 - \cos\theta)(d\sigma_{fns} - d\sigma_{point})$. Consequently, the correction term ΔL_{LS} proposed by Lindhard and Sørensen is referred to as the correction term for the close collisions, taking over the Bloch and Mott corrections, plus the finite nuclear size correction.

2.4.7 Contributions of Correction Terms

Figure 2.2, which is taken from Ref.[Sch+98] and modified, shows the contributions from each correction term discussed above, calculated for the case of a lead projectile in an aluminum target as a function of projectile energy in terms of the Lorentz factor $\gamma - 1$. Since the inner shell correction is a tiny effect, it is invisible on the graph. At the low-velocity region, the Barkas (solid upper curve) and the Bloch (solid lower curve) correction terms become significant, where one would also consider the slowing-down process of heavy ions in the framework of classical treatment. The Mott correction term (dashed curve) becomes significant as the velocity increases, whereas the Bloch correction term decreases. The finite nuclear size correction term, derived from the theory of Lindhard and Sørensen, is here given as $\Delta L_{\mathrm{LS,fns}}$, and it becomes significant at the highly relativistic region ($\gamma >\sim 10$). The Fermi density effect (long dashed-dotted curve) is significant at the relativistic region to reduce the distant interactions. When implemented in actual stopping-power calculations, the correction term should be in the opposite sign. In the present slowing-down experiment with lead projectiles in the energy domain of (30-300) MeV/u, the corresponding domain on the graph is about $\gamma - 1 = 0.03$-0.3. As can be seen from the figure, the Barkas, inner shell, and Fermi's density corrections are already negligible.

Figure 2.3 [Gei+02] shows the calculation of the Lindhard-Sørensen (LS-) theory which includes the correction terms as $\Delta L = \Delta L_{\mathrm{Barkas}} + \Delta L_{\mathrm{Shell}} - \frac{\delta}{2} + \Delta L_{\mathrm{LS}}$, compared to the experimental stopping-power data for different bare projectiles (oxygen, krypton, and gold) in beryllium and copper targets. The x-axis corresponds to the projectile velocity β and y-axis to the stopping powers normalized by Bethe's formula Eq.2.21. The solid curves give the theoretical prediction by the LS-theory, and as one can see, there are excellent agreements with the experimental data for all projectiles. These results have manifested that the experimental stopping power of bare heavy-ions can be reproduced by the LS-theory, which stands on the long history of the theoretical developments.

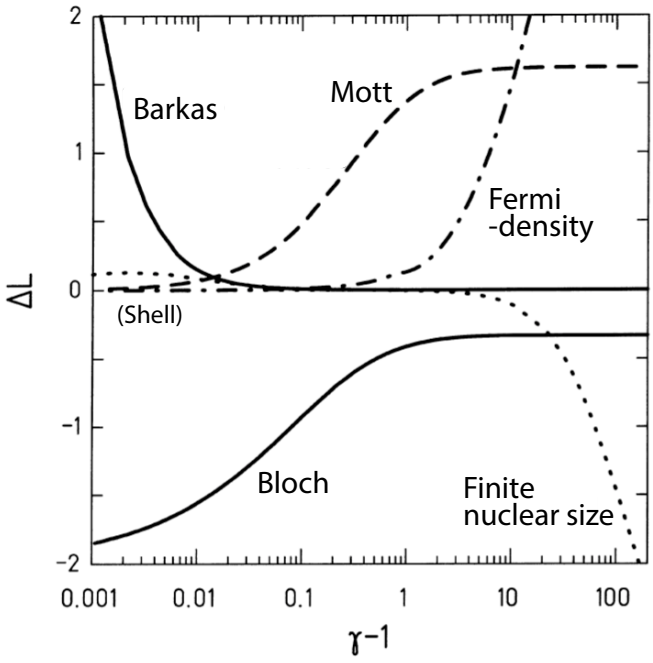

FIGURE 2.2: Correction terms to the Bethe stopping number L_{Bethe} for the slowing-down of bare lead ions in aluminum as a function of $\gamma - 1$, where γ is the relativistic Lorentz factor. This figure is taken from [Sch+98] and modified. The inner shell correction is tiny (not visible) at relativistic energies, whereas the finite nuclear size effect from the Lindhard-Sørensen theory becomes large at the highest velocities.

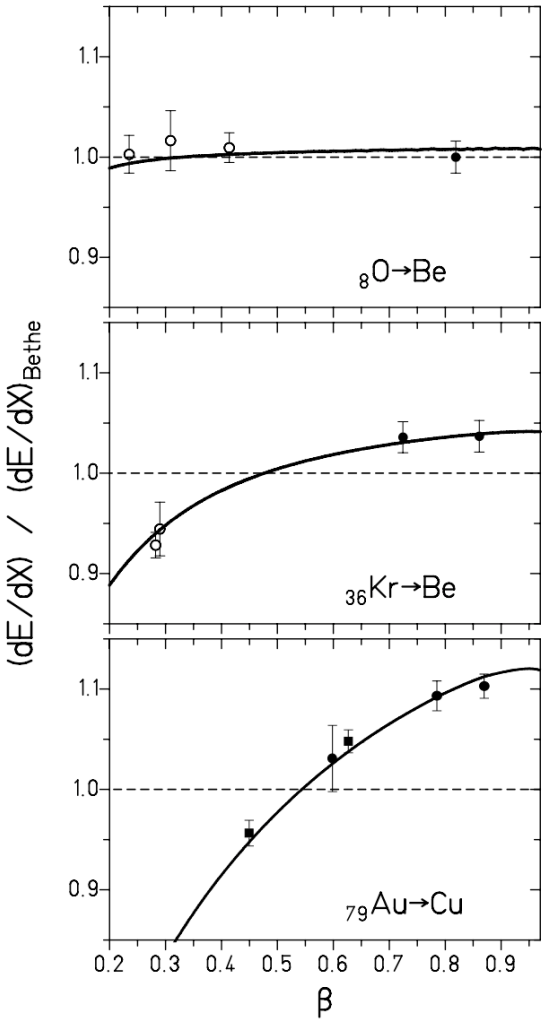

FIGURE 2.3: Comparison of the Lindhard-Sørensen (LS-) theory to the experimental stopping powers of bare oxygen, krypton, and gold projectiles in beryllium and copper targets [Gei+02].

2.5 Energy Loss of Partially Ionized Heavy Ions

So far, we have considered the slowing-down of bare heavy-ions. What would be, then, a difference in the stopping powers of the heavy projectiles if they carry electrons?

The individual energy loss of a projectile in a given ionic charge-state is characterized by the *partial* stopping-power. One may simply adopt the ionic charge into the theoretical frameworks, which we have discussed above, instead of the projectile's nuclear charge Z_1 for the calculation. However, strictly speaking, it is not a good approximation: When the collision occurs in distant, the target electron may *see* the projectile in the ionic charge-state, but when the collision occurs closer than, e.g., the ionic radius of the projectile, the effective charge may be larger than the ionic charge. Hence, a significant difference may arise in the energy loss.

Such a *screening* effect is, in general, complicated to formulate. It was first considered by Bohr [Boh48] in terms of the modification of the Coulomb potential as

$$V(r) = -\frac{Z_1 e^2}{r} \exp(-\frac{r}{a}) \quad , \tag{2.46}$$

where a is called the screening radius. Sigmund [Sig97] extended the Bohr theory in the non-relativistic regime by employing the following screened potential as

$$V(r) = -\frac{q_1 e^2}{r} - \frac{(Z_1 - q_1)\, e^2}{r} \exp\left(-\frac{r}{a_s}\right) \quad , \tag{2.47}$$

where the screening radius a_s is given by

$$a_s = \left(1 - \frac{q_1}{Z_1}\right) \cdot 0.8853 \frac{a_0}{Z_1^{1/3}} \tag{2.48}$$

with q_1 and a_0 being the ionic charge state and the Bohr radius, respectively. The choice of such potential shapes, as well as what Bohr did, made it possible to derive the collisional differential cross sections simply and analytically. The extension of the Born approximation including the screening effect was also considered by Sigmund [Sig97], but before Brandt and Kitagawa [BK82], who originally proposed the shape of the screened potential Eq.2.47, also considered with more complex screening radius. The similar results were obtained between them.

When considering of heavy ions, then, the screening effect inevitably gives an influence on the other correction terms. Schinner [SS00], together with Sigmund, considered the polarization effect, or the Barkas effect, which is responsible for the Z_1^3 correction term in the framework of the perturbation treatment. In this case, the correction term was found possible to become significant, of the order of 100%; therefore, the perturbative approach cannot be so accurate. Moreover, for the close collisions, the extension of the Lindhard-Sørensen theory would be desired. In 2001, Sørensen [Sør02] calculated the stopping power for hydrogen- and helium-like heavy ions with different potential shapes in the framework of the LS-theory. The difference in the stopping power due to the screening effect was found for hydrogen-like projectiles of the order of 1%.

2.6 Charge-Changing Processes

The understanding of the slowing-down process of heavy ions in matter requires the basic knowledge of charge-changing collisions, i.e., electron capture and loss processes simultaneously. Such phenomena of capture and loss have been known and studied since about a hundred years ago, by the pioneering works with alpha-particles of, e.g., Henderson and Rutherford in the 1920s. The study with heavy ions could be possible only after the discovery of nuclear fission in 1938. A comprehensive theoretical treatment for the charge-changing and slowing-down processes of heavy ions was first

performed by Bohr [Boh48], and following that, Bohr and Lindhard carried out the refinement of the theory for the heavy ions [BL54]. There is a common statement that the characteristics of the charge-changing processes of heavy ions are largely different from the ones of protons or alpha particles at the same velocities because the heavy ions may carry a large number of electrons along a long path length due to the continual competition between the capture and loss processes. Similar to the stopping-power description, these processes depend on the velocity and nuclear charge of the projectile and properties of the target atoms. Moreover, atomic shell configurations must be taken into account; a very, or even more, complicated many-body problem. Therefore, the theories had to rely on simple considerations and arbitrary assumptions, which ended up in the limitation of their application, e.g., only to the capture and loss of a single electron [Bet72].

The charge-state fraction $F(q, x)$ is characteristic of the charge-changing processes, which is the probability of the projectile being in a certain ionic charge-state q after passing through the target thickness x. The evolution is expressed by the differential (rate) equation [Bet72] as

$$\frac{dF(q,x)}{dx} = \sum_{q'(\neq q)} \left[\sigma(q',q)F(q',x) - \sigma(q,q')F(q,x)\right] \tag{2.49}$$

with

$$\sum_{q} F(q,x) = 1 \quad , \tag{2.50}$$

where σ is the (multiple) charge-changing cross-sections from q to q', or vice versa. Presently, there are various computer programs such as CHARGE [Sch+98], GLOBAL [Sch+98], and ETACHA [Lam+15], which can predict the charge-state evolution within matter by computing the rate equations. For instance, the GLOBAL program can take into account up to 28 electrons attached to the projectile for the calculation. However, such theoretical calculations need further improvements, and no computer programs can still provide reliable predictions for heavy ions, especially with heavy target elements, gaseous targets, and/or in the velocity range between, e.g., $\sim$ 30 and 100 MeV/u, where our experimental interest is focused on [Sch+98].

Below, we will briefly describe the important processes in our experimental energy range.

2.6.1 Electron Loss

The electron loss (EL) process is considered as the ionization of projectile heavy ions (P) by the target atoms (T), which is expressed by

$$P^{q^+} + T \rightarrow P^{(q+m)^+} + T + me^- \quad , \quad m \geq 1 \quad . \tag{2.51}$$

The total EL cross-section can be given by the summation over m numbers as

$$\sigma_{\text{total}}^{\text{EL}} = \sum_{m=1}^{N} \sigma_m^{\text{EL}}(v) \quad , \tag{2.52}$$

where N is the total number of projectile electrons, and v is the projectile velocity. The approach for calculating the cross-sections is in principle the same as in the reverse case of the ionization of the target atoms with which the stopping-power calculations were performed.

Bohr [Boh48] first considered the ionization of light ions in light media concerning the close collisions where the binding of the electrons was disregarded (free collision condition). In the calculation, it was required that the ion velocity be much greater than the Bohr velocity v_0, or more specifically, Bohr's kappa be $\kappa \ll 1$, which was contradictory to the classical picture in the calculation of stopping power. Nevertheless, the EL cross-section was obtained as

$$\sigma^{\text{EL}} = \frac{4\pi a_0^2}{Z_1^2}(Z_2^2 + Z_2)\left(\frac{v_0}{v}\right)^2 \quad , \tag{2.53}$$

where a_0 is the Bohr radius. It is in a simple form, but the scaling with $Z_2^2 + Z_2$ still gives a good approximation in general for light and heavy projectiles.

From the perspective of quantum mechanics, the electron loss is regarded as the excitation of the bound electrons of the projectile into the continuum state by the collision with the target atom. Therefore, when we consider the single ionization of the K-shell electron from the projectile based on the non-relativistic plane-wave Born approximation (PWBA), the EL cross-section can be given by [Anh+85]

$$\sigma_{1s} = 8\pi(\frac{a_0\alpha Z_2}{\beta})^2 \int_0^\infty d\epsilon \int_{q_0}^\infty \frac{dq}{q^3}|F(\vec{q})|^2 \quad . \tag{2.54}$$

where ϵ is the kinetic energy of the electron excited into the continuum state, and $q = |\vec{q}|$ is the momentum transfer. In the second integration, the lower limit $q_0 = (E_K + \epsilon)/v$ is the minimum momentum transfer needed to ionize the electron, where E_K is the binding energy. The form factor $F(\vec{q})$ contains the transfer matrix from the bound state $|1s\rangle$ to the continuum state $|\epsilon\rangle$ as

$$F(\vec{q}) = \langle\epsilon|\exp(i\vec{q}\cdot\vec{r}/\hbar)|1s\rangle \quad . \tag{2.55}$$

In the scheme of the non-relativistic PWBA, Khandelwal *et al.* [KCM69] evaluated the integral part, and the obtained cross-section is in a rather simple form as

$$\sigma_{1s} = 8\pi(\frac{a_0\alpha Z_2}{\beta Z_1})^2 f(\eta) \quad , \tag{2.56}$$

where $f(\eta)$ is a slowly varying function of $\eta = (\beta/Z_1\alpha)^2$ whose maximum can be found near $\beta = Z_1\alpha$, where the projectile velocity is equivalent to the one of the K-shell

electron. The tabulated values can be found in Ref.[KCM69]. Of course, for high-Z_1 projectiles, one should take more sophisticated considerations for the calculation, such as the Dirac wave functions for the 1s and continuum states, the distortion effects due to the strong binding of K-shell electrons, screening effects, and so on. These considerations can be found, e.g., in Ref.[Anh+85] and the references therein. Nevertheless, it is known that such calculations with PWBA overestimate the cross sections at low and intermediate velocities [Lam+15].

Not only the single EL processes, but one must note that the contribution from the multiple EL processes can be large at the low velocity region when considering the total EL cross-section. Below 10 MeV/u, multiple EL process with $m \geq 2$ may be up to 70% of the total EL cross-section [Tol+18]. The theoretical calculation is quite complicated because one must take into account many configurations; therefore, one may take the classical approximation such as suggested by Bohr [Boh48; She+10].

At the velocity region where our experiment aims, namely from 30 to 300 MeV/u, however, the single EL process is still the main contribution to the total cross-section. The asymptotic form of the total cross-section may be given as [Tol+18]

$$\sigma_{\text{total}}^{\text{EL}} \sim Z_2^2 \frac{\ln E}{q^2 E} \quad , \tag{2.57}$$

where q and E are the charge state and the energy of the projectile, respectively.

2.6.2 Electron Capture

The electron capture (EC) process is the recombination of the target electrons into the projectile ions. The single EC process is expressed by

$$P^{q^+} + T \rightarrow P^{(q-1)^+} + T^+ \quad . \tag{2.58}$$

The EC process becomes significant basically as the projectile energy goes lower. It is the competitive process to the EL process, resulting in the population of many different charge states. For the theoretical treatment of the cross-sections, one must consider a much more complicated situation than for the EL processes due to the involvement of the target atom, i.e., at least three particles exchange their momentum in this EC process. Moreover, there are difficulties such as that the particle states become different before and after the collision thus the interaction potential differs, and the orthogonality of the wave functions is not hold [Tol+18]. Therefore, we will just briefly explain the asymptotic characteristics of the capture process, and for the readers who are eager to learn, see [Eic85; Mey+85; ES07; Tol+18] and the references therein.

There are two essential types of electron capture processes. The first one is the non-radiative capture (NRC) process, in which a bound target electron is transferred to a bound state of the projectile. This is the dominant capture process in the low-velocity domain. The description of the cross-section has been long discussed in history, even with the classical mechanics taking into account the two-step collisions

by L.H. Thomas in 1927. Based on the Born approximation, Brinkman and Kramers [BK30] derived the approximated expression for the non-relativistic case by

$$\sigma_{\mathrm{NRC}} \sim \frac{q^5 Z_2^5}{E^6} \quad , \tag{2.59}$$

where q and E are the charge state and the projectile's energy, respectively. Their calculation is called the Oppenheimer-Brinkman-Kramers (OBK) approximation, and the relativistic modification was finally performed after almost 50 years in which the rapid energy dependence of E^{-6} has been modified in the relativistic calculations to be E^{-1} [MS80]. Nevertheless, even with the relativistic effect taken into account, the prediction overestimated the cross-section by more than a factor of three than the experimental data even for the low-Z_1 projectiles [Anh85]. Apart from the energy dependence, one should note that the strong dependence on the target atomic number Z_2 is the characteristic of the NRC process.

The other capture process is radiative capture (REC). This may be regarded as the reverse process of the photoelectric effect: A target electron capture is accompanied by the radiation emission. Therefore, the expression Eq.2.58 becomes

$$P^{q^+} + T \rightarrow P^{(q-1)^+} + T^+ + \hbar\omega_{\mathrm{REC}} \quad . \tag{2.60}$$

Contrary to the NRC process, the cross section weakly depends on the target atomic number as

$$\sigma_{\mathrm{REC}} \sim \frac{q^5 Z_2}{E} \tag{2.61}$$

but with the same energy dependence of E^{-1} as the relativistic calculation of the NRC process [ES07]. The REC process becomes significant as the projectile energy increases and gives the dominant contribution to the total EC cross-section at the relativistic energy domain.

As a conclusion, the total capture cross section is given by the sum of both processes as

$$\sigma_{\mathrm{total}}^{\mathrm{EC}} = \sigma_{\mathrm{NRC}} + \sigma_{\mathrm{REC}} \quad . \tag{2.62}$$

2.7 Effective Charge State of Projectiles

2.7.1 Effective Charge and Scaling of Stopping Powers

As we have explained, the population of different charge states occurs due to the competition of electron-loss and electron-capture processes. Therefore, when considering the slowing down of heavy ions, the total stopping power must be averaged over the partial stopping powers of the individual charge states. However, it may be more convenient to take a single *effective* value of the charge-state distribution instead. In the first principle, this is suggested because the exact charge-state distribution within a material cannot be directly measured and is difficult to predict theoretically.

There are two concepts for the description of the *effective* charge-state within matter. The first one is the effective charge Z_{eff} which is defined experimentally via the ratio of stopping-powers between the heavy projectile of interest and the reference particle as

$$Z_{eff}^2 = (\gamma Z_1)^2 = Z_0^2 \frac{dE/dx(v, Z_1)}{dE/dx(v, Z_0)} \quad , \tag{2.63}$$

where γ is the effective charge parameter, Z_0 and Z_1 denote the nuclear charges of the reference particle and the heavy projectile of interest, respectively. The most common reference particles would be protons and alpha particles, whose experimental stopping-power data can be found numerously, such as in [NISa; Pau21]. Furthermore, this effective charge concept follows the proportionality of Z_1^2 in stopping-powers which is resulted from the perturbation treatment. Therefore, if the projectile does not satisfy the condition Eq.2.26, the effective charge Z_{eff} is not a good parameter [Sig14].

However, using the semi-empirical formula of the effective charge reversely provides an effective prediction of stopping powers. Since the discovery of nuclear fission, this scaling law was the most helpful way to relate various heavy projectiles, energies, and target materials [Zie77a]. The first attempt of the scaling was based on Bohr's criterion [Boh48] that projectiles are ionized when the velocity is greater than the orbital velocity of the electrons. In the Thomas-Fermi model, the latter velocity is proportional to $v_0 Z_1^{2/3}$ with the Bohr velocity v_0. Therefore, the effective charge was assumed to be

$$\frac{Z_{eff}}{Z_1} \approx \frac{v}{v_0 Z_1^{2/3}} \quad . \tag{2.64}$$

The first attempt was done by Northcliffe [Nor60] who modified the Bohr's expression into the following exponential form

$$\left(\frac{Z_{eff}}{Z_1}\right)^2 = 1 - a \exp\left(-b \frac{v}{v_0 Z_1^{2/3}}\right) \quad , \tag{2.65}$$

where a and b are the fitting parameters. Similarly, Pierce and Blann [PB68] suggested the effective charge as

$$Z_{eff} = Z_1 \left[1 - \exp\left(-0.95 \frac{v}{v_0 Z_1^{2/3}}\right)\right] \tag{2.66}$$

which was obtained from the fitting to the experimental stopping-powers of heavy ions by using the ones of protons and alpha-particles as the reference. This so-called P&B formula is in a very simple form but is still helpful in many applications. However, one should note that the target dependence such as Z_2 and density ρ is completely omitted from the expression: We will come back to this point in the next chapter. Moreover, Ziegler [Zie77a] suggested the following semi-empirical formula of effective charge from the fitting to the experimental stopping-powers of heavy ions by

using the ones of protons as the reference:

$$\frac{Z_{eff}(v)}{Z_1} = 1 - \exp\left(-v_2\right)\left[1.034 - 0.1777\exp\left(-0.08114Z_1\right)\right] \quad , \tag{2.67}$$

where

$$v_2 = v_1 + 0.0378\sin\left(\frac{1}{2}v_1\pi\right) \tag{2.68}$$

with

$$v_1 = 0.886\frac{v}{v_0 Z_1^{2/3}} \quad . \tag{2.69}$$

In addition, the following semi-empirical formula based on alpha particles as the reference was obtained as [Zie85]

$$\frac{Z_{eff}}{2} = 1 - \exp\left(-\sum_{i=0}^{5} a_i \ln^i E\right) \tag{2.70}$$

where a_i are the fitting parameters and E is the projectile energy in keV/u. Note that the scaling law including the fitting to experimental stopping-powers has been the basis of the famous calculation code SRIM [Zie+10].

2.7.2 Equilibrium Mean Charge State

The other concept is the equilibrium mean charge $\bar{q}$ given by

$$\bar{q} = \sum_q qF(q,\infty) \tag{2.71}$$

where $F(q,\infty)$ are the equilibrium charge-state fractions. Of course, theoretical predictions for $F(q)$ and eventually $\bar{q}$ is possible, based on cross sections and by computing the differential equation Eq.2.49. However, it is very complicated because one needs to know as many charge-changing cross-sections as the number of electrons increases. Moreover, there is often a limitation of theory depending on velocity. Therefore, in practice, this value can be determined experimentally from the measured charge-state distributions of heavy ions *after* the target, and there are various semi-empirical formulae according to gaseous and solid target materials. For example, Betz *et al.* [Bet+66] measured the charge-state distributions of (10-70) MeV heavy projectiles (sulfur, arsenic, iodine, and uranium) after gaseous and solid targets. The semi-empirical formula was obtained from the fitting to the experimental mean charge states as

$$\frac{\bar{q}}{Z_1} = 1 - C\exp\left(-Z_1^{-\gamma}\frac{v}{v_0}\right) \quad \text{for} \quad v \geq v_0 \quad , \tag{2.72}$$

where C and γ are the fitting parameters whose values are different according to the projectile and the target material, but it was found to be $C \approx 1$ and $\gamma \approx 2/3$, respectively. The most recent work on the mean charge state may be by Schiwietz and Grande [SG01] in which the more complicated empirical formulae were obtained for

the projectiles ranging from protons to uranium after gaseous and solid targets based on the fitting to a large set of experimental data. For gaseous targets, the expression is given by

$$\bar{q}_{\text{gas}} = Z_1 \frac{376x + x^6}{1428 - 1206x^{1/2} + 690x + x^6} \quad , \tag{2.73}$$

with

$$x = \left(\frac{v}{v_0} Z_1^{-0.52} Z_2^{0.03 - 0.017 Z_1^{-0.52} v/v_0} \right)^{1.0 + 0.4/Z_1} \quad . \tag{2.74}$$

And,

$$\bar{q}_{\text{solid}} = Z_1 \frac{12x + x^4}{0.07/x + 6 + 0.3x^{1/2} + 10.37x + x^4} \quad , \tag{2.75}$$

with

$$x = \left(\frac{v}{v_0} Z_1^{-0.52} Z_2^{-0.019 Z_1^{-0.52} v/v_0} \frac{1}{1.68} \right)^{1.0 + 1.8/Z_1} \tag{2.76}$$

for solid targets.

In the framework of the present experiment, it is interesting to investigate how the influence of the projectile charge state appears in the description of stopping powers. We will describe this point in more detail in the next chapter.

Chapter 3

Motivation and Goals of the Present Experiment

This chapter will briefly describe the experimental status of stopping-power measurements with fast heavy ions. The lack of accurate experimental data and the investigation of the gas-solid difference of the charge-state population and the stopping power remain essential because the theoretical prediction is still not accurate enough for many applications.

3.1 Short History of Stopping-Power Measurements with Heavy Ions

The slowing-down measurements of heavy ions started with the discovery and study of nuclear fission in 1938. Fission fragments represent heavy ions with medium mass and charge. A large emittance characterizes them, i.e., they are emitted from the radioactive source in all directions with large energy spread and many ionic charge-states. Nevertheless, pioneering measurements have been performed by Lassen *et al.* [Las51a; Las51b] to study the energy loss and charge-state distribution of fission fragments in solid and gaseous targets. With the advent of powerful heavy-ion accelerators, the kinematic properties of the projectiles became well defined, and thus dedicated slowing-down measurements could be performed for a specific projectile isotope at fixed incident energy.

New accelerator-based slowing-down experiments started to contribute to the basic knowledge of the ion interaction with matter. It enabled the development of new applications, such as in material science. Moreover, accurate experimental stopping power values were revealed to deviate strongly from the theoretical descriptions, especially for partially ionized heavy ions. On the other hand, for light ions, such as protons and alpha particles, the situation was better because they were fully ionized over a broad energy range when they penetrated matter: The interaction could be theoretically well described with the first-order Born approximation, applying the stopping-power formula of Bethe. Below, we will briefly describe the history of experimental and theoretical developments for the study on the slowing-down processes of heavy ions.

With the advent of powerful synchrotrons, the projectiles can reach relativistic velocities ($\beta \approx 0.9$), and even the heaviest ions can penetrate the targets while being fully ionized. This valuable situation was achieved for the first time with the BEVALAC synchrotron at LBL in the 1970s, and the accurate range measurements with bare uranium ions were performed [AT83]. The results yielded the evidence that the higher-order correction terms to the Bethe theory were needed to explain the experimental data [TS78; SAT81]. Unfortunately, there was no magnetic spectrometer at LBL to extend the range measurements with direct stopping power measurements for relativistic heavy ions. The latter could be achieved about ten years later by combining the heavy-ion synchrotron SIS-18 and the in-flight separator FRS at GSI. Accurate stopping power measurements have manifested the failure of the Bethe theory for relativistic bare heavy ions [Sch+94] and initiated a new theoretical treatment by Lindhard and Sørensen (LS-theory) [LS96] in the end of the 1990s. Excellent agreements were found between the LS-theory and the experimental stopping-power data for fully ionized projectiles as shown in the previous chapter [GS98; SG98]. At lower energies down to 100 MeV/u, where only a few charge states are involved in the slowing-down process, the validity of the LS-theory was again confirmed with gold, lead, and bismuth projectiles. The experimental stopping-power data could be reproduced by the LS-theory by taking into account the partial stopping-powers of individual charge states in combination with the measured charge-state fractions [Wei+00].

Despite the successful theory at relativistic energies, further research is needed experimentally and theoretically at lower energy regions towards the maximum point of the stopping-power, the Bragg peak. The theoretical predictions are complicated due to the involvement of many ionic charge states. Moreover, there is still a lack of accurate experimental data to challenge and guide the theoretical efforts. Figure 3.1 gives an overview of the stopping-power measurements performed in the past for lead, bismuth, and uranium projectiles. Especially in the energy range from 10 to 100 MeV/u, one can see that the experimental data are scarce. Below 10 MeV/u, the theoretical predictions are also very complicated, but many experimental data exist, as illustrated in the figure. These experimental data have significantly contributed to the development of reliable theoretical and semi-empirical predictions of stopping powers and ranges, such as by using the scaling method of the effective charge (Eq.2.63) [Zie85].

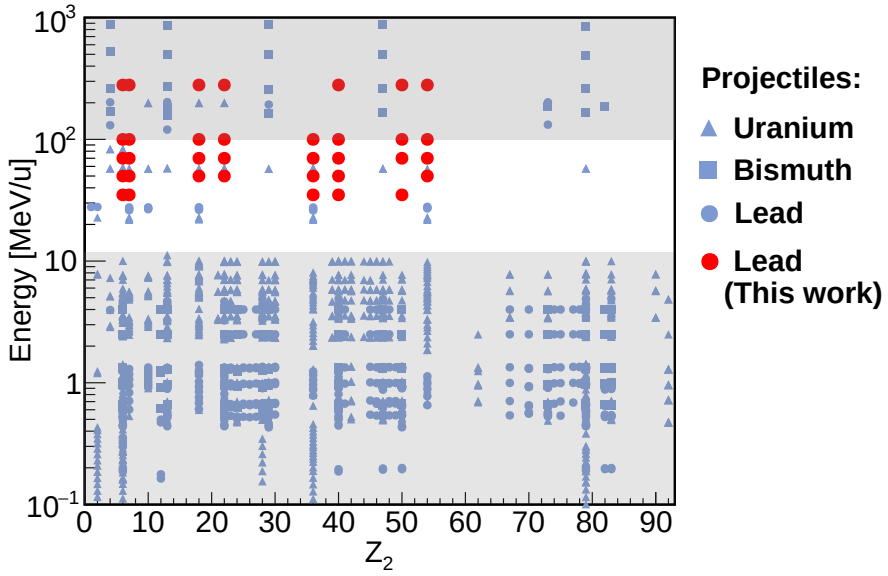

FIGURE 3.1: Overview of previous and present stopping-power measurements of uranium ($Z_1 = 92$), bismuth ($Z_1 = 83$), and lead ($Z_1 = 82$) ions presented in the energy-Z_2 plane. Z_2 is the atomic element number of the target material. The data points are referred to Ref.[Pau21].

3.2 The Gas-Solid Difference in Stopping Powers

Here, we shall return to the time when nuclear fission was discovered and explain another aspect of the study. In 1951, Lassen experimentally discovered that the mean charge state of fission fragments after penetrating through amorphous solid targets became larger compared to gaseous targets [Las51a; Las51b]. Soon after, Bohr and Lindhard [BL54] explained this observation by the concept of a higher ionization rate in solids than in gases due to the higher collision frequencies expected in the higher material density: The electrons captured, or excited, in the excited states of projectile ions are more easily stripped in solid materials due to the frequent collisions, and more likely to be captured into the bound states in gaseous materials before the next collision. Consequently, due to the difference in the effective charge state within matter, they predicted that the stopping powers, which may be proportional to the square of the projectile charge, should become larger in solids than in gases (the Bohr-Lindhard prediction).

However, it was not possible for a long time to confirm the relation between the effective charge and stopping powers without an advent of powerful heavy-ion accelerators. Such as, the so-called Z_2-oscillations in stopping powers [CP69] masked the comparison between neighboring gas and solid elements at the low-energy region up to $\sim$1 MeV/u, where measurements were accessible at that time. Moreover, Betz and Grodzins [BG70] proposed a totally different model from the one of Bohr and Lindhard, regarding the observation of the gas-solid difference in charge states: They explained the difference by the concept of the emission of Auger electrons *after* the

projectile ions left the solid materials, as illustrated in Fig.3.2 below. Therefore, there is not a big difference in the charge state between the insides of solid and gas, indicating that the stopping powers also do not differ much. However, such Auger electrons could not be measured in any experiment.

A breakthrough finally happened with the newly developed accelerator UNILAC of GSI in the 1980s. The measured stopping-power values in monoatomic targets were systematically higher by about 20% in solids than for neighboring gaseous elements in the energy range of (1.4-10) MeV/u, as shown in Fig.3.3 [Gei+82]. The discovery by Geissel *et al.* confirmed the model of Bohr and Lindhard almost after 30 years it was introduced. Following that, the gas-solid difference in stopping-powers has been confirmed by a series of experiments at the ALICE accelerator in Orsay [Bim+89a; Bim+89b] and has been extended at higher energies with the GANIL accelerators in Caen [Her+91; Bim+96; Bim+00].

Here, respecting the successful discoveries, we shall propose to name the gas-solid difference as **the Bohr-Lindhard density effect**. Then, to clarify the remaining problem related to the effect, we shall look into the details of the experimental results obtained at the GANIL accelerator.

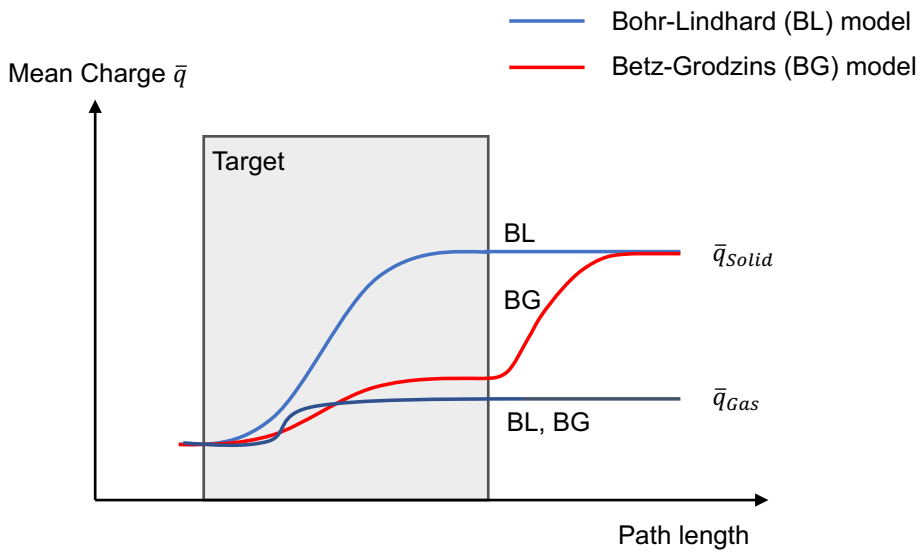

FIGURE 3.2: Illustration of the Bohr-Lindhard [BL54] (blue solid curve) and Betz-Grodzins [BG70] (red solid curve) models, explaining the observation of the gas-solid difference for charge states. Bohr-Lindard model: The difference originates from a higher ionization rate in solids due to the higher collision frequencies. Betz-Grodzins model: The difference mainly occurs due to the emission of Auger electrons after the ions emerge from the solid material.

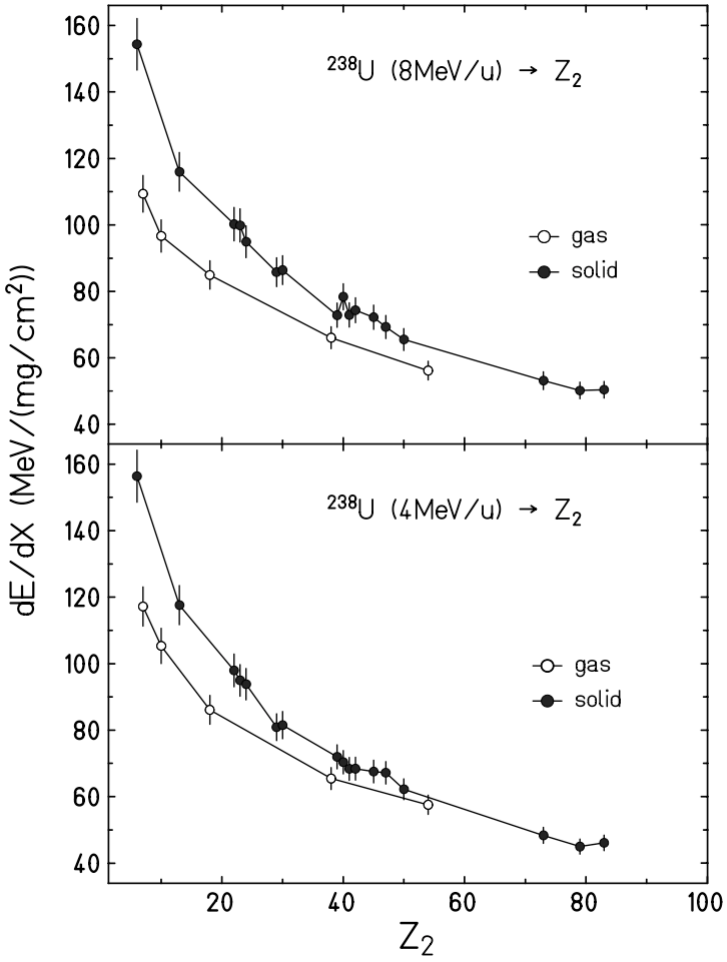

FIGURE 3.3: Experimental discovery of the gas-solid difference of stopping powers for uranium ions. The figure is taken from ref. [Gei+82].

Herault *et al.* [Her+91] measured the stopping powers in gaseous matter for the heavy projectiles of oxygen ($Z_1 = 6$) from 20 to 85 MeV/u, argon ($Z_1 = 18$) from 25 to 60 MeV/u, krypton ($Z_1 = 36$) from 20 to 40 MeV/u, and xenon ($Z_1 = 54$) from 25 to 30 MeV/u. Figure 3.4 shows their experimental stopping-powers by the full circles as a function of the target atomic number Z_2 for the incident energy of 25 MeV/u. For displaying the gas-solid difference, the stopping-power data of solid targets are shown with the open squares, which were taken from Refs.[Bim+86; Gau+87; Gau+90]. The γ_s in the graphs is the effective charge parameter in solid targets, which is defined in the scaling expression of the stopping power as

$$\frac{dE}{dx} = \left(\frac{dE}{dx}\right)_{\mathrm{He}} \cdot \gamma_s^2 \cdot \frac{Z_1^2}{Z_{\mathrm{He}}^2} \quad , \tag{3.1}$$

where the stopping-power of heavy ions in solids is scaled by γ_s^2 from the one of He^{2+} ion at the same velocity, whose stopping-power values were taken from Ref.[Zie77b]. The solid curves correspond to the calculation with the assumption of fully ionized

projectiles ($\gamma_s = 1$), and the dashed curves correspond to the fit result to the experimental stopping-power data in solids by using Eq.3.1.

First, as can be seen in the figure, the deduced effective charge parameter γ_s continuously decreases ($\gamma_s < 1$) as the projectile becomes heavier. The fully ionized assumption seems to be valid for oxygen projectiles. However, it starts deviating for heavier projectiles, e.g., $\gamma_s = 0.87$ for xenon projectiles, demonstrating that heavier projectiles still carry electrons even in solid targets at this velocity. Secondly, the gas-solid difference becomes more significant for heavier projectiles. It vanishes for oxygen projectiles, which are considered to be fully ionized, and strongly appears for partially ionized xenon projectiles at the same velocity. Thirdly, the difference becomes more significant for heavier targets, as can especially be seen for the xenon projectiles. These experimental observations indicate that the gas-solid difference in stopping powers may vanish when the projectiles are fully ionized during their interaction both in solid and gaseous targets. Such interpretation supports the Bohr-Lindhard prediction [BL54], which assumes that the gas-solid difference is caused by the different collision frequency in the stopping materials, creating different effective charge states of projectiles in gases and solids.

Then, based on the observations of the Bohr-Lindhard density effect from low to intermediate energy domain, an open question would be, how much the Bohr-Lindhard density effect will continue and contribute over the velocity range until it vanishes for heavy projectiles? This question certainly requires a large set of measurements of both charge-state distributions and stopping powers over a wide range of Z_1 and Z_2 numbers, and a wide velocity domain should be covered experimentally. However, a rough estimation for the first point of the question can be done as follows. As shown in Chapter 2, the K-shell ionization cross-section σ_{EL} in the framework of the non-relativistic PWBA calculation can be expressed according to Eq.2.56 as

$$\sigma_{\mathrm{EL}} = \sigma_0 f\left(\frac{v}{v_{\mathrm{K}}}\right) \quad ,$$

where v and v_{K} are the velocities of the projectile and its K-shell electron, respectively, and $\sigma_0 = 4\pi a_0^2 Z_2^2/Z_1^2$ with the Bohr radius a_0. Since the function $f(v/v_{\mathrm{K}})$ reaches the maximum when the projectile velocity becomes around $v = v_{\mathrm{K}} = Z_1 v_0$, projectiles are likely to get fully ionized at this velocity. Therefore, the gas-solid difference may vanish simultaneously. Figure 3.5 shows the experimental stopping-power data available in the literature for the case of krypton projectiles ($Z_1 = 36$) in nitrogen gas (red dots) and carbon (blue dots) as a function of projectile energy. The solid curves correspond to the fit by the second-order polynomials, which are displayed for the purpose to guide the eye. At the low velocity domain, the gas-solid difference is still obvious, but when the velocity increases, the two solid curves seem to converge around 30 MeV/u, indicating the vanishing of the difference. This velocity for the vanishing is indeed close to the orbital velocity of the K-shell electrons of krypton projectiles $v_{\mathrm{K}} = Z_1 v_0 \sim 33$ MeV/u, which may suggest that the projectiles be fully ionized in

both gaseous and solid targets.

Based on this simple assumption, the velocity range for the vanishing of the Bohr-Lindhard density effect for very heavy ions such as lead ($Z_1 = 82$), bismuth ($Z_1 = 83$), and uranium ($Z_1 = 92$) would be around 100-300 MeV/u. Then, the investigation requires the measurement start from the lower velocity domain to quantify the second question; how much does the gas-solid effect contribute over the velocity range until it vanishes? By combining both points of the question, the investigation should be in the velocity domain where the experimental data are scarce for the three projectiles, as shown in Fig.3.1.

In 2006, Fettouhi *et al.* measured the charge-state distributions and stopping powers of uranium projectiles at 60.2 and 200 MeV/u [Fet+06]. Their result of the mean charge states, at the interpolated velocity of 55.5 MeV/u, showed a clear gas-solid difference, and it was found to be more significant up to nearly 5% as the target atomic number Z_2 increases. By simply considering the dependence of stopping powers on the square of the projectile charge q^2, the gas-solid difference may be expected for about 10% at this velocity. However, at the similar interpolated velocity of 57.8 MeV/u, they showed that the gas-solid difference in stopping powers appeared only for the light target elements and vanished for heavier ones. Since these data are included in the velocity domain in Fig.3.1, where experimental data are scarce, further measurements are strongly required.

In addition, we would like to emphasize again that the theoretical treatment for the stopping power and charge-changing process are very complicated for the heavy ions around this velocity domain due to the involvement of many charge-states. Therefore, an experimental investigation would be desired and interesting for understanding the essential atomic interaction in gases and solids.

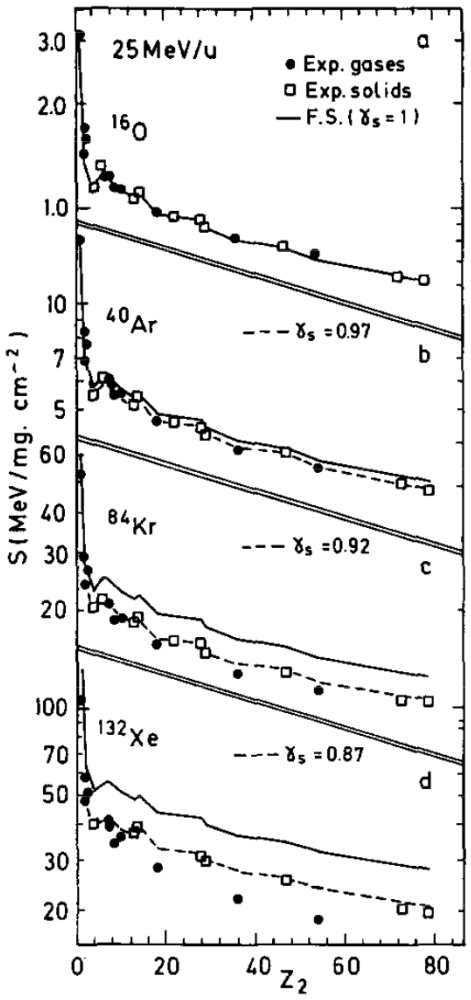

FIGURE 3.4: The experimental stopping powers of (a) oxygen, (b) argon, (c) krypton and (d) xenon projectiles at 25 MeV/u are plotted. The solid curves correspond to the scaling from alpha particles with the assumption of fully ionized heavy projectiles ($\gamma_s = 1$) and the dashed curves correspond to the fitted effective charge parameter γ_s obtained in previous experiments for solids. The figure is taken from Ref.[Her+91].

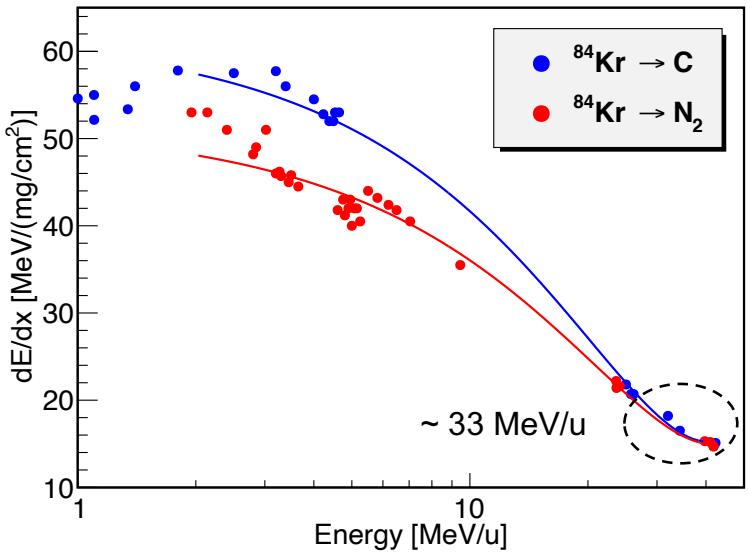

FIGURE 3.5: Experimental stopping-power data of krypton projectiles in carbon [Bim+78; Bim+80; Gau+90; GS98] and nitrogen [Her+91; Bim+89b]. The gas-solid difference seems to vanish around 30 MeV/u. The curves are drawn to guide the eye.

3.3 Experimental Stopping Powers Compared with Theoretical Predictions

Figure 3.6 shows the comparison between the experimental stopping-power values available to date [Pau21] and the calculations by several computer programs (ATIMA1.4 [Wei98a], SRIM [Zie+10], and DPASS [SS19]) for the uranium projectiles in titanium (right panel) and argon gas (left panel) targets. The recent versions of SRIM and DPASS reproduce very well the stopping-power data for the case of titanium target. A deviation can be found for the ATIMA1.4 because it adopts scaling formula of Ziegler, by using the stopping powers of protons with the old parameters from the 1990s for the calculation below 10 MeV/u (See the Appendix E for the program description). In contrast, none of the computer programs can reproduce the experimental stopping-power data for the argon gas target, as can be seen in the left panel. Furthermore, the calculations are close to the one for the titanium target, even though there is about 20% difference in the experimental stopping-power data. These facts imply that the Bohr-Lindhard density effect in stopping-powers is neglected in the present theories.

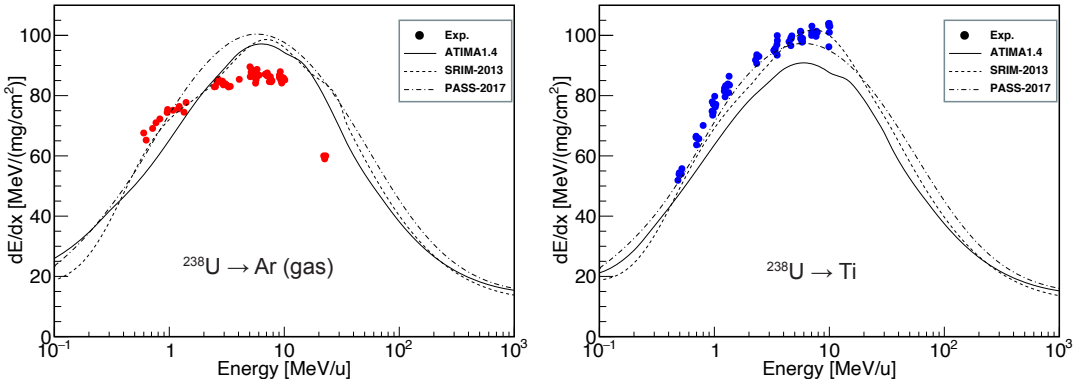

FIGURE 3.6: Measured low-energy stopping-power data of uranium projectiles in argon gas (left) and solid titanium (right) [Pau21] are compared with theoretical predictions of ATIMA1.4 (solid curve), SRIM (dashed curve), and DPASS (long dashed dotted curve).

3.4 Goals and Requirements of the Present Experiment

Based on the research backgrounds explained above, the main goals of the present slowing-down experiment are:

- Measurements of the stopping powers and charge-state distributions for partially ionized heavy-ions. Especially in the energy range of 10-100 MeV/u, where experimental data are scarce for the heaviest ions such as lead, bismuth, and uranium.
- Contributions to the knowledge of the gas-solid difference to test the present slowing-down theory.

Therefore, we have proposed an experiment of the measurements of stopping-powers and charge-state distributions of xenon, lead, and uranium projectiles in gases and solids in the energy domain from 30 to 300 MeV/u to investigate the Bohr-Lindhard density effect from the velocity domain where the effect may be obvious to the domain where it may vanish. In this thesis, we will present and discuss the experimental results obtained with the lead projectiles (^{208}Pb). The experiment was performed in 2020 at the FRS facility of GSI Helmholtz Center for Heavy Ion Research, Germany. We have prepared five gaseous and five solid materials as atomic collision targets for the investigation of the gas-solid effect. The investigated target materials and projectile energies are depicted by the red full-circles in Fig.3.1.

Our results will definitely contribute to the further developments of the slowing-down theory and the valuable computer programs such as the ATIMA code, which is developed at GSI. Furthermore, the knowledge will also be essential for many applications of atomic ion-matter interaction, such as hadron therapy, in-flight separation of exotic nuclei, and performance of heavy-ion detectors, e.g., gas-filled chambers at

the Low-Energy Branch of the future Super-FRS facility at GSI.

Finally, the required overall experimental accuracy of our planned stopping-power results should be below 2% to properly investigate the Bohr-Lindhard density effect for neighboring elements. For the achievement of the expected accuracy, the following aspects are essential:

- High-resolution energy-loss and charge-state distribution measurements.
- Well-known properties of targets.

From the next chapter, we will describe our experimental setup, methods, data analysis, and the experimental results in detail.

Chapter 4

Present Experiment

The measurements of the energy-loss and charge-state distribution of lead ions (^{208}Pb) in gases and solids were performed at the FRS facility of GSI Helmholtz Center for Heavy Ion Research in Darmstadt, Germany. This chapter will explain the accelerator facilities and the experimental setup for our experiment.

4.1 GSI Facilities

The GSI facilities are schematically shown in Fig.4.1 [GSI21]. The combination of the UNIversal Linear ACcelerator (UNILAC) and the Heavy-Ion Synchrotron (SIS-18) can provide projectile beams up to uranium with a maximum magnetic rigidity of 18 Tm, corresponding to the kinetic energy of about (1-2) GeV/u. The UNILAC accelerates ions to an energy of 11.4 MeV/u before injecting the ions into the SIS-18. In the transfer channel, the ions pass through a second stripper section. Inside the SIS-18, the energy of the circulating ions can be measured via the Schottky frequency spectrometry and multiple position measurements with an accuracy of better than 10^{-3}. When the ions are accelerated to the specific energy required in the experiment, the ion bunches are extracted, usually over a period of several seconds (slow extraction), and are transported to the different experimental areas, including the entrance of the FRagment Separator (FRS). For our experiment, the FRS facility was used as a high-resolution magnetic spectrometer.

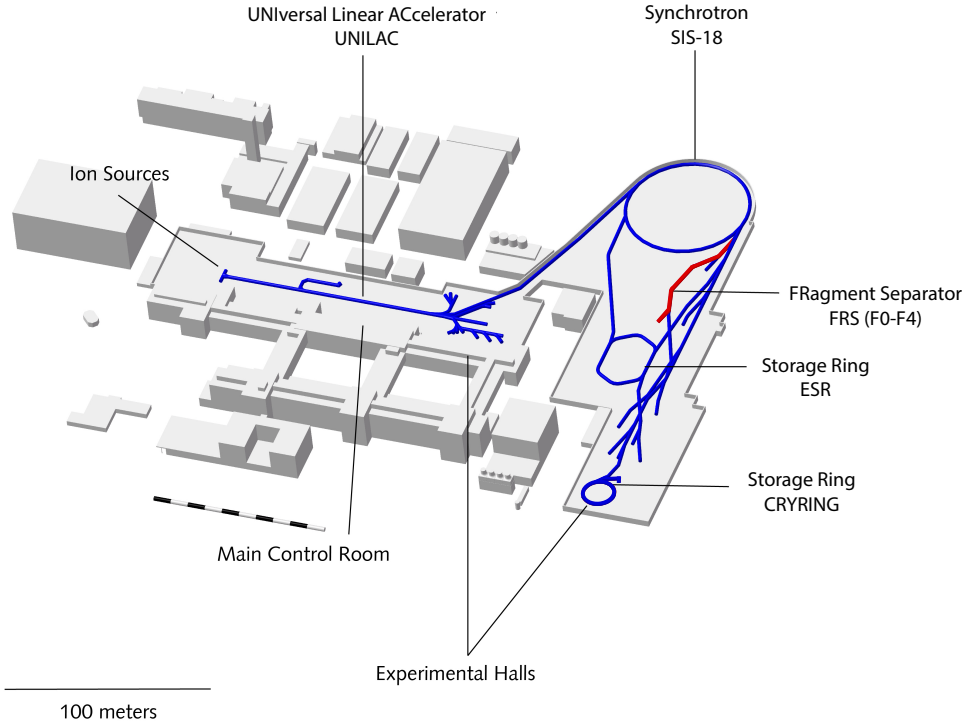

FIGURE 4.1: Schematic drawing of the present GSI facilities. This figure was taken from Ref.[GSI21] and modified. The linear accelerator UNILAC and the synchrotron SIS-18 can provide projectile beams of all elements up to uranium for experimental studies and applications over the energy range from the Coulomb barrier up to 2000 MeV/u, i.e., up to the maximum magnetic rigidity of 18 Tm. The UNILAC injects the pre-accelerated beams into the SIS-18 at 11.4 MeV/u.

4.2 Primary Beams from the SIS-18

The advantage of a synchrotron, compared to a cyclotron, is that the beam energy can be quickly changed even from one bunch to the next. For the present energy-loss and charge-state distribution measurements, the lead (^{208}Pb) ion beams with a selected charge state of 67^{+} behind the second stripper section were accelerated by the SIS-18 and extracted at five different energies, namely 35.508, 50.396, 70.342, 100.289, and 280.365 MeV/u. In addition, the slow extraction mode with 10 seconds duration was selected with a low beam intensity of the order of 10^{3}-10^{4} ions per spill. These accelerator conditions were chosen to avoid any significant radiation damage to the atomic collision targets and effects on the particle detector performance. The momentum spread and the transverse emittance of extracted beams are about 5×10^{-4} and less than 5π mm mrad, respectively.

4.3 FRagment Separator FRS - High Resolution Magnetic Spectrometer

The accelerated beams from the SIS-18 are transported via a dedicated beamline to the entrance of the fragment separator FRS [Gei+92]. The FRS consists of 4 independent dispersive stages. The whole configuration is expressed by

(F0)-QQQSDSQQ-(F1)-QQSDSQQQ-(F2)-QQQSDSQQ-(F3)-QQSDSQQQ-(F4) .

Each dispersive stage consists of a dipole magnet (D) with a deflection angle of 30 degrees horizontal and a bending radius of 11.25 m. A dipole magnet is characterized by the bending radius ρ and the homogeneous magnetic field with a flux density B, which is perpendicular to the direction of the ion trajectory. The deflection of a charged particle in the dipole field is determined by the magnetic rigidity $B\rho$. According to the Lorentz force, the magnetic rigidity is simply the ratio of the momentum p in the laboratory system and the ionic charge state q as

$$B\rho = \frac{p}{q} \quad . \tag{4.1}$$

The ion beams are focused/defocused by the quadrupole (Q) triplets or doublets in front of and behind the dipole magnet. In addition, two sextupole magnets (S) are also placed at the entrance and exit of the dipole magnet. For the present experiment, the sextupole magnets were not used. An image of the beam spot is then generated at each focal plane (F0-F4). Furthermore, experimental equipment such as position-sensitive detectors is installed at the different focal planes to determine the individual ions' position and thereby its charge state and momentum. In our experiment, at the focal plane F0, there is the thin vacuum window to populate an incident charge-state distribution. With the mechanical slits placed at F1, only one charge state is selected to impinge the atomic collision targets installed in the central focal plane F2. Then, the subsequent FRS spectrometer stages are used to analyze the momentum and charge states of the ions emergent from the targets, the position of which are measured with the time projection chamber at F3. For these measurements, the ion-optical properties of the magnetic spectrometer are essential and will be explained below.

A particle beam is represented by an ensemble in the 6-dimensional phase space of the ion-optical coordinates [Wol87], which are defined as the deviations from the coordinates of a reference particle that moves on the optical axis in z-direction. Perpendicular to the z-direction, the horizontal (x) and vertical (y) planes are defined, as well as the associated angles which are defined by the corresponding ratio of the traverse and the reference momenta, i.e., $a = p_x/p_{ref}$ and $b = p_y/p_{ref}$ for x and y directions, respectively. In addition, the relative path length ℓ and momentum deviation δ form all together with the 6-dimensional phase space.

The change of the movement of ions within the ion-optical elements can be expressed by the so-called transfer matrix, which results from the electromagnetic forces in the optical elements and eventually describes the ion trajectories. Similar to the

light optics, the projection of the coordinates from the object plane at the position z_i to the image plane with the final coordinates at the position z_f is described. In principle, the transfer matrix represents a non-linear function, but it can be approximated by the Taylor expansions. The matrix elements in the first-order approximation can already explain the main imaging properties of a magnetic spectrometer. The first-order matrix element is defined by

$$\begin{pmatrix} x \\ a \\ y \\ b \\ \ell \\ \delta \end{pmatrix}_f = \begin{pmatrix} (x,x) & (x,a) & (x,y) & (x,b) & (x,\ell) & (x,\delta) \\ (a,x) & (a,a) & (a,y) & (a,b) & (a,\ell) & (a,\delta) \\ (y,x) & (y,a) & (y,y) & (y,b) & (y,\ell) & (y,\delta) \\ (b,x) & (b,a) & (b,y) & (b,b) & (b,\ell) & (b,\delta) \\ (\ell,x) & (\ell,a) & (\ell,y) & (\ell,b) & (\ell,\ell) & (\ell,\delta) \\ (\delta,x) & (\delta,a) & (\delta,y) & (\delta,b) & (\delta,\ell) & (\delta,\delta) \end{pmatrix} \begin{pmatrix} x \\ a \\ y \\ b \\ \ell \\ \delta \end{pmatrix}_i . \tag{4.2}$$

The matrix coefficients (C_f, C_i) are defined as $\partial C_f / \partial C_i$ which describes the derivatives of variables ($C = x,\ a,\ b,\ \ell,\ \delta$) at the final ($f$) versus the initial ($i$) coordinates. Given that the deflection due to the dipole magnet occurs only horizontally, the dispersion coefficients are considered only with x and a components. For the present experiment, only the x-coordinate is important for the energy-loss measurements.

The top panel of Fig.4.2 schematically shows the dispersive stages of the fragment separator FRS which were used for our measurement. There were mainly two experimental requirements in the settings for the ion-optical mode: The first requirement was that the beam spot size at F2, where the atomic collision targets were installed, must be as small as possible. A small beam spot was especially important for the measurement with the gaseous target, where the beam had to pass through the gas target cells, which were nearly 300 mm long and with 5 mm apertures for the entrance and exit. Of course, a small beam spot also enables a high optical resolving power. The second requirement was that the dispersion is small throughout the FRS to avoid transmission losses. On the other hand, the resolution should not suffer from the low dispersion, i.e., the magnification must be low as well. For the section from F2 to F3, the dispersion was set to be only -20.0 mm/%, enabling an almost complete measurement of the charge-state distribution with a single magnetic field setting.

Based on the requirements mentioned above, the ion optics for our experiment was designed with the MIRKO [FR81] and GICOSY [Wei98b] programs. The calculated first-order transfer matrix for the section from F0 to F2, where the incident beams enter the FRS and then are focused on the atomic collision target, is given by

$$\begin{pmatrix} (x,x) & (x,a) & (x,y) & (x,b) & (x,\delta) \\ (a,x) & (a,a) & (a,y) & (a,b) & (a,\delta) \\ (y,x) & (y,a) & (y,y) & (y,b) & (y,\delta) \\ (b,x) & (b,a) & (b,y) & (b,b) & (b,\delta) \end{pmatrix}_{\mathrm{F0 \to F2}} = \begin{pmatrix} 0.56 & 0.03 & 0.0 & 0.0 & -37.3 \\ -0.22 & 1.77 & 0.0 & 0.0 & 0.0 \\ 0.0 & 0.0 & 0.75 & -0.36 & 0.0 \\ 0.0 & 0.0 & 0.03 & 1.31 & 0.0 \end{pmatrix} , \tag{4.3}$$

where, the units are in millimeter for x and y, milliradian for a and b, and % for δ. The small values of the magnification (x,x) and the (x,a) result from the requirement that the beam spot on the atomic collision target be small. Then, the beam spot on the target is dominantly affected by the δ at F0.

The transfer matrix for the section from F2 to F3, where the measurements of the energy-loss and charge-state distribution are performed, is given by

$$\left(\begin{array}{ccccc} (x,x) & (x,a) & (x,y) & (x,b) & (x,\delta) \\ (a,x) & (a,a) & (a,y) & (a,b) & (a,\delta) \\ (y,x) & (y,a) & (y,y) & (y,b) & (y,\delta) \\ (b,x) & (b,a) & (b,y) & (b,b) & (b,\delta) \end{array}\right)_{\mathrm{F2}\rightarrow\mathrm{F3}} = \left(\begin{array}{ccccc} -1.09 & 0.08 & 0.0 & 0.0 & -20.0 \\ 0.48 & -0.95 & 0.0 & 0.0 & -1.80 \\ 0.0 & 0.0 & -3.83 & -0.51 & 0.0 \\ 0.0 & 0.0 & -0.12 & -0.28 & 0.0 \end{array}\right). \tag{4.4}$$

Note that the designed ion optics give a low dispersion coefficient $(x,\delta) = -20.0$ mm/%, which is aimed to measure the charge states as many as possible in a single magnetic field setting. The resolving power R is determined by the magnification and the dispersion coefficient as

$$R = \left|\frac{(x,\delta)}{2(x,x)x_i}\right| = 917 \quad , \tag{4.5}$$

when the beam spot at F2 is considered to be $x_i = 1$ mm.

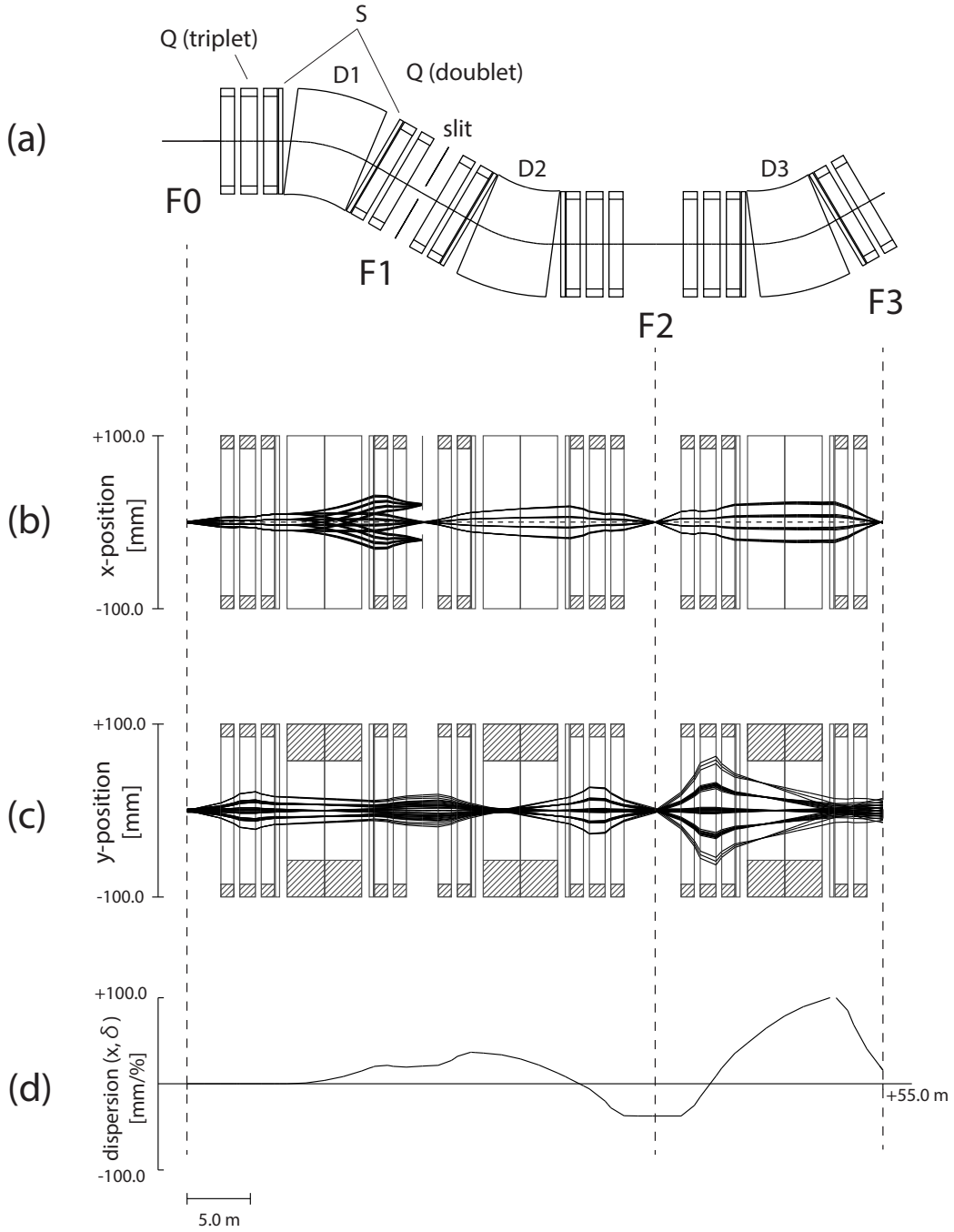

FIGURE 4.2: The designed ion-optical mode used for our experiment. Panel a): Magnetic elements of the FRS up to the focal plane F3. Panel b) and c) presents results of the calculation with the GICOSY program. The beam envelopes are calculated for the horizontal (b) and vertical direction (c). The incident beam conditions for the calculations are following: The horizontal positions and angles are distributed equally both in 6 points within the range of $-1 \leq x_{F0} \leq 1$ mm and $-3.33 \leq a_{F0} \leq 3.33$ mrad. The vertical positions and angles are distributed equally in 5 points within the range of $-2 \leq y_{F0} \leq 2$ mm and $-3.33 \leq b_{F0} \leq 3.33$ mrad. The momentum deviation is considered with 3 values of $\delta = -1, 0, 1\%$. Panel d) presents the dispersion line for +1% momentum deviation.

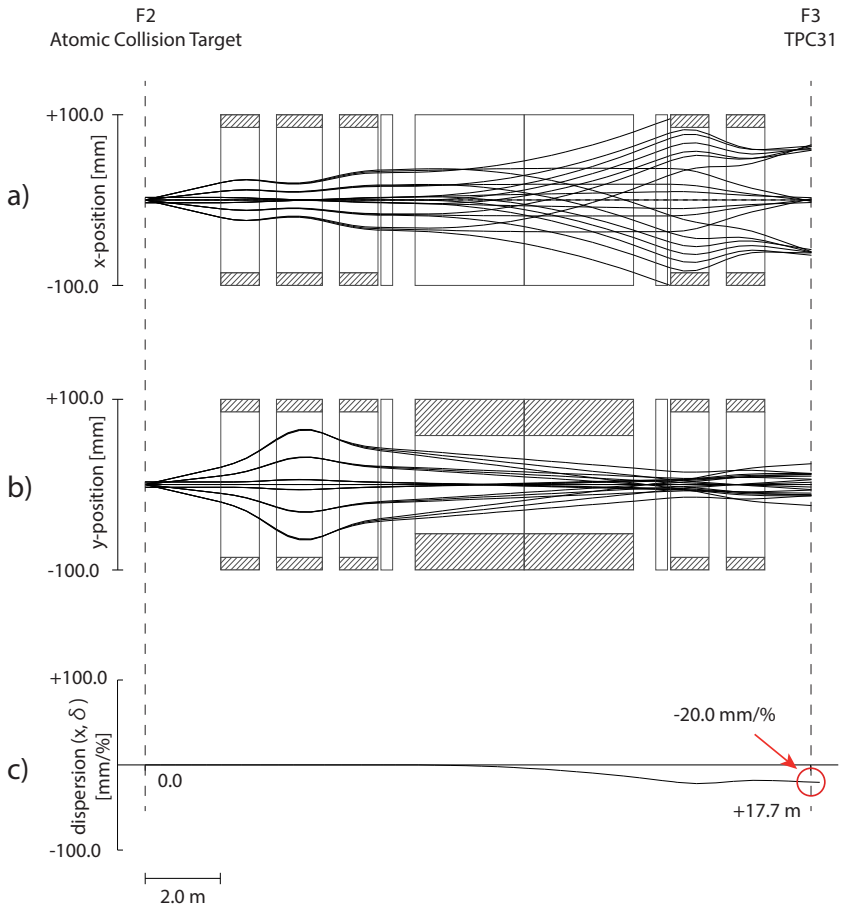

FIGURE 4.3: The designed optical mode of our experiment for the focal plane section F2-F3. In the GICOSY calculations, the following incident coordinates are selected. The horizontal (a) and vertical (b) positions are $x, y = -3, 0, +3$ mm and the corresponding angles $a, b = -10, -5, 0, +5, +10$ mrad, respectively. The momentum deviation is included with 3 values of $\delta = -3, 0, +3\%$. Panel c) presents the dispersion line for +1% momentum deviation.

4.4 Experimental Equipment

4.4.1 FRS

Figure 4.4 shows the schematic view of the experimental setup used for our experiment. The primary beams of lead ions from the SIS-18 firstly pass through the vacuum window, which separates the vacuum areas of the SIS-18 accelerator beam-line from the FRS. Furthermore, the window material inevitably creates an ionic charge-state distribution depending on the beam velocity. A thin transmission detector (SEETRAM) was mounted on the movable ladder downstream of the vacuum window. The material thickness of SEETRAM is about six times thicker than the vacuum window. Therefore, it was used as an additional stripper target for the measurements with the highest incident beam energy in our experiment. The SEETRAM was moved

out for the other energies, and only the vacuum window created the desired incident charge-state distribution. The selection of the incident charge state was performed with the first dipole magnet and the mechanical slits located at the focal plane F1. For this selection, the incident charge-state distributions were aligned by using the MWPC (MW11) position-sensitive detector placed behind the mechanical slits. After the MWPC is removed from the beam-line, the incident beam with the selected charge state was transferred to the central focal plane F2. Two time-projection chambers (TPC21 and TPC22) were installed with a plastic scintillator (SC21) in between, which were used for checking the beam profiles and position. Then, the detectors at the F2 were removed from the beam-line, and the optimized incident beam with only one charge state was finally exposed to the atomic collision target. The dispersive section after the F2 separates the trajectories of ions in different charge states according to their magnetic rigidities $B\rho$. At the focal plane F3, the energy-loss and the charge-state distributions of lead ions were measured with the time projection chamber (TPC31), the main detector used for our experiment.

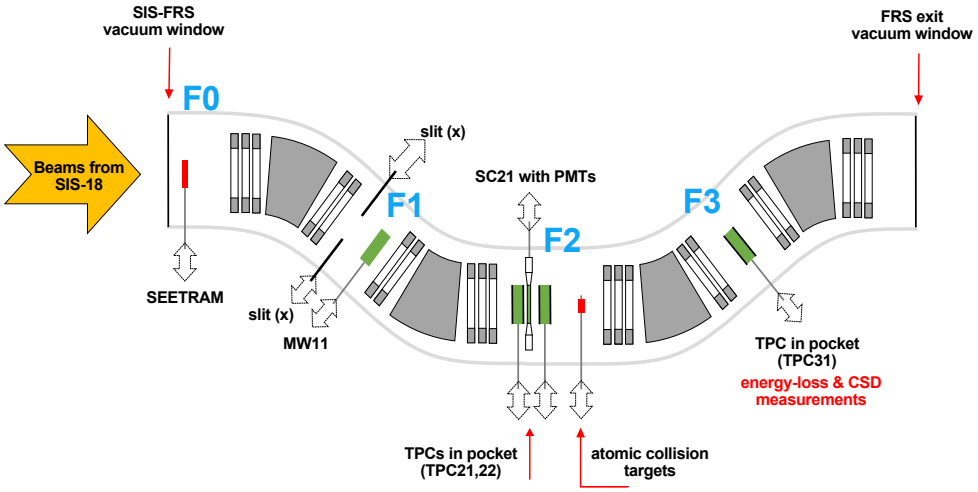

FIGURE 4.4: Schematic drawing of the experimental setup at the fragment separator FRS. The components for this slowing-down experiment are indicated at each focal plane. The atomic-collision targets were installed in the vacuum chamber at the central focal plane F2. The targets and detectors were mounted on vacuum feedthroughs and operated via remote control.

4.4.2 F0 Area

For the present experiment, there are mainly the material layers of the SIS window and the SEETRAM detector used at the F0 area, see Fig.4.4. In this thesis, the two materials are collectively called as a *stripper* target. The individual properties are explained in this subsection.

SIS-window

The primary beams from the SIS-18 are transported to the FRS, and the first object to pass through is the permanently installed SIS-window. It is a thin titanium foil that separates the SIS-18 and the FRS vacuum areas. The influence of the window has to be taken into account, i.e., the energy loss of the primary beam and the population of a charge-state distribution. The determination of the energy loss requires the thickness and material information of the window. We have measured the areal density of the SIS-window by measuring its weight and area after the experiment. The deduced areal density was 2.42 ± 0.12 mg/cm^2. From the first to third columns of Tab. 4.1 show the accelerated beam energy, the calculated energy loss values due to the SIS-window, and the corresponding incident energy used for the atomic collision experiment, respectively. The energy loss was calculated by the ATIMA program [Wei98a]. Furthermore, for convenience, we will refer to the incident energies as 35, 50, 70, 100, and 280 MeV/u throughout this thesis. The second inevitable influence due to the SIS-window is the population of a charge-state distribution, which enables the selection of the incident charge state impinging the atomic collision targets. The incident charge state was carefully chosen so that the projectiles could reach quickly to the expected equilibrium charge states in the atomic collision target. Then, the selection was performed with the mechanical slits at the focal plane F1 in combination with the check on the position spectra with the MWPC. In the last column of Tab.4.1, the selected incident charge states are also listed.

TABLE 4.1: The list of the requested beam energy from the SIS-18, the calculated energy loss at the SIS-window, and the corresponding incident energies for the atomic collision experiment. The incident charge state is also listed.
* The energy loss was calculated including the additional stripping target SEETRAM for this energy, which will be mentioned below.

Requested SIS-18 energy [MeV/u]	Energy loss [MeV/u]	Incident energy [MeV/u]	q_{in}
281.365	1.390*	279.975	81^+
100.289	0.353	99.936	79^+
70.342	0.427	69.915	77^+
50.396	0.505	49.891	$75^+, 76^+, 77^+$
35.508	0.604	34.904	$70^+, 74^+$

SEETRAM

In the standard operation of the FRS, the SEcondary-Electron TRAnsmission Monitor (SEETRAM) is used to survey and measure the beam intensity. It consists of three titanium foils of 10 μm thickness and 130 mm diameter. It is mounted perpendicular to the beam axis. When the projectiles pass through the middle foil, secondary electrons

are emitted and collected as an electric current by the outer foils, which are connected to a voltage of +80 V. The electric currents are converted into logic pulses, with which one can obtain valuable information on the subjects such as the spill structure and the extraction efficiency of the beams from the SIS-18.

In our experiment, it was used as an additional stripper target only in the measurements with the incident beam energy of 280 MeV/u, in order to populate the incident charge state of 81^+ desired for the measurements. In addition, the energy loss of the primary beams from the SIS-18 due to the SEETRAM is considered in the Tab.4.1.

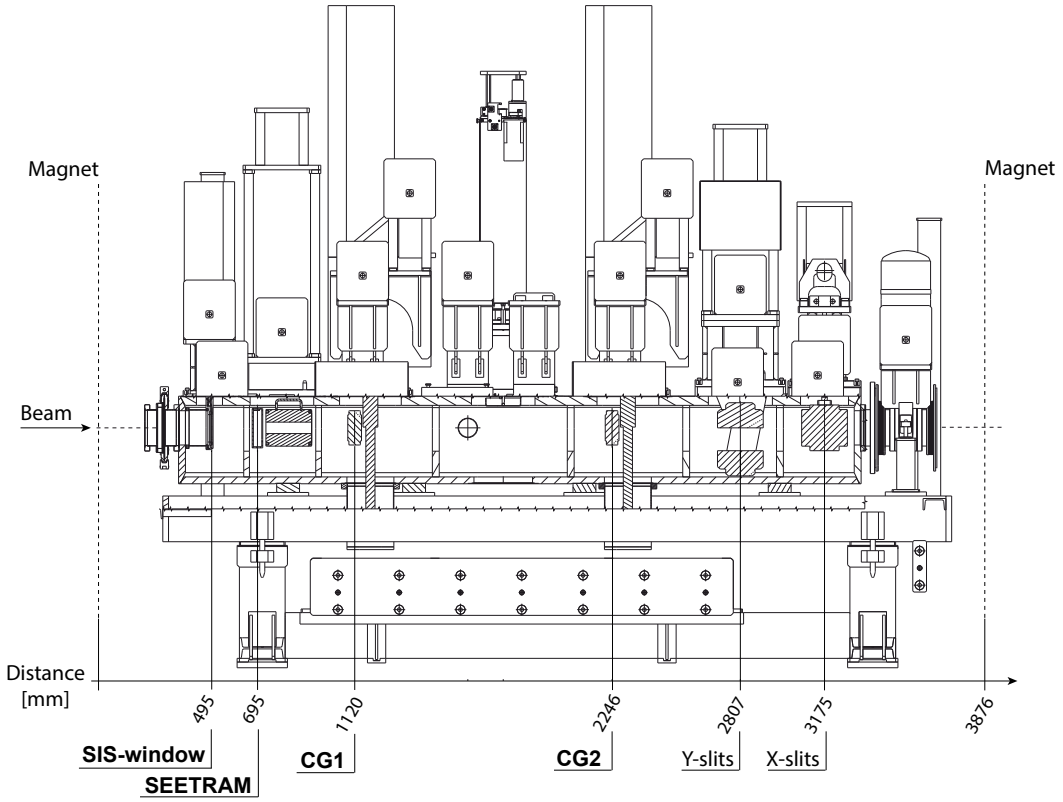

FIGURE 4.5: Technical drawing of the experimental setup at the F0 area of the FRS. During the experiment, a 5.4 μm titanium vacuum window (SIS-window) separated the ultra-high vacuum of the accelerator from high vacuum of the FRS system. The SEETRAM detector was used as an additional stripper target for the measurement with the incident beam of 280 MeV/u. The current grids (CG1 and CG2) were used to align the beam at the entrance of the FRS and removed during the measurements.

4.4.3 F2 Area

At the central focal plane F2, the atomic collision targets are installed. Five solids and five gaseous materials were prepared for the measurements of energy loss and charge-state distribution. The solid materials were carbon, polypropylene, titanium, zirconium, and tin. The gaseous materials were nitrogen, propene, argon, krypton, and xenon. In this section, only an explanation of the target systems used for our measurement will be given; and the methods for the target thickness determination will be presented in the separated section below. There are also two time projection

chambers (TPC21 and 22) and a scintillator (SC21) installed in this area for the check of the profiles and positions of incident beams. The details of the TPC will be given in the next subsection where the experimental setup at the F3 area will be presented.

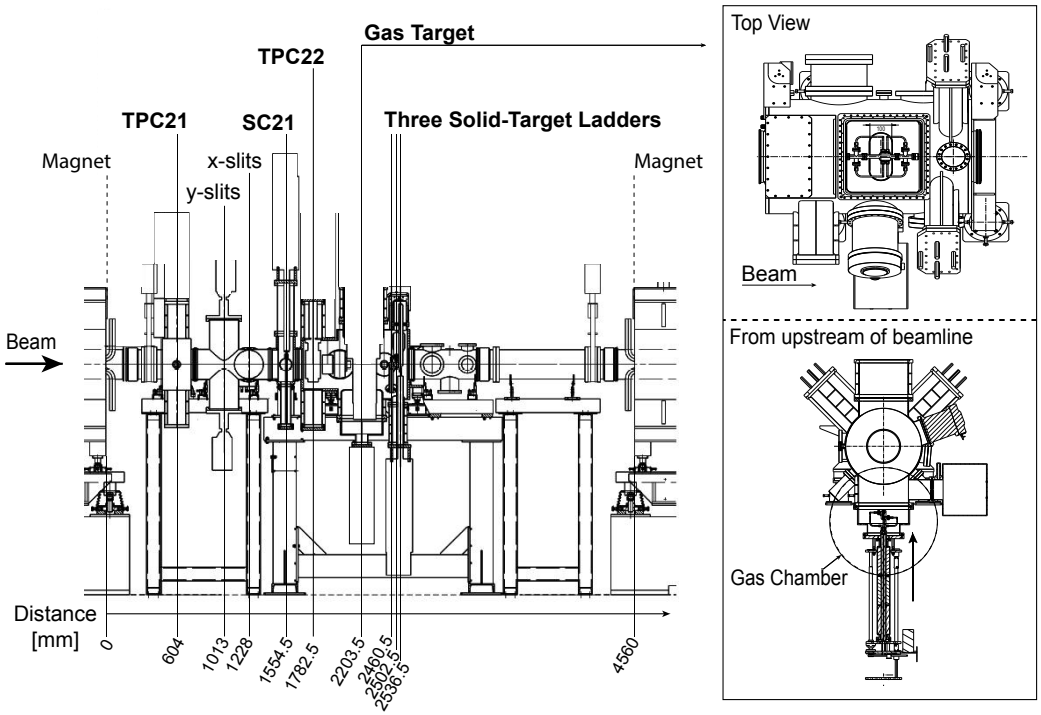

FIGURE 4.6: Experimental setup at the F2 area of the FRS. The gaseous and solid target systems are the major installations for the present slowing-down experiment. Two position-sensitive detectors, TPC21 and TPC22, were used to align the beam with respect to the target centers. The location of the installed devices are given from the yoke of the last quadrupole magnet preceding the focal plane F2. The vacuum chamber of the targets is separately shown from two directions.

Solid Target System

Each solid target was mounted with an aluminum aperture plate of 5 mm diameter on the target ladder, whose mechanical position was controlled remotely by the step motor during the measurements. There were three target-ladders, as can be seen in Fig.4.7, which shows the photograph of the system taken from the upstream of the beam-line. The spacing between the targets mounted on the first and second ladders was 42 mm, and between the second and third ladders, it was 34 mm. The mechanical alignment of the target positions on the beam-line was performed with a laser device. The laser beam is shown as the red crossing lights in the figure. During the measurements, only a single target was inserted on the beam-line for most cases. However, when a thick target was planned in the measurements, two or three targets were combined to obtain the desired thickness.

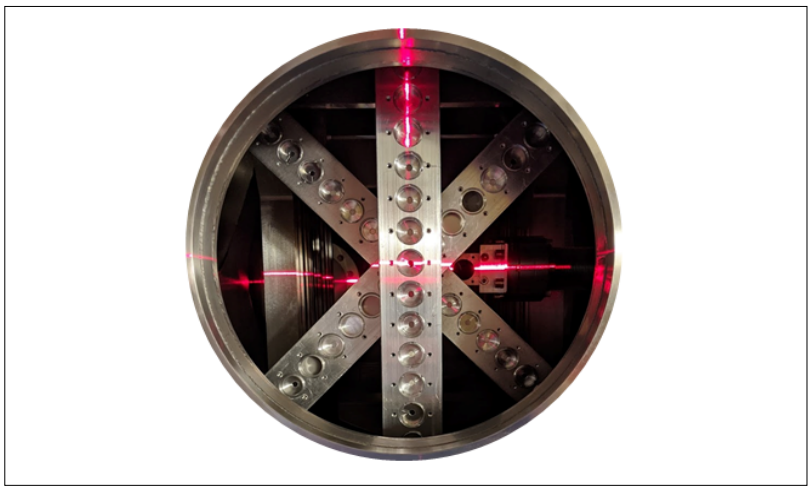

FIGURE 4.7: Three ladders used for mounting the solid targets. The photograph also shows the laser lights for mechanical alignment. The positioning was remotely performed by step motors. The aperture in front of the target foils had a diameter of 5 mm.

Gas Target System

Figure 4.8 shows the schematic drawing of the gas target cell installed at the F2 vacuum area. For the measurements, two gas target cells were prepared with different types of foils used as the entrance and exit windows. The first one was with 6 μm thick polypropylene foils (PP windows), and the other was with 1 μm thick graphenic carbon foils (GC windows). The beam entrance and exit were opened for 5 mm diameter, and the distances between the windows were 312.7 mm and 317.5 mm for the gas cells with PP windows and GC windows, respectively. The alignment was carefully performed with the laser device in the preparation of the experiment, and the positions of gas cells were controlled remotely during the measurements.

In the preparation of the experiment, pressure tests were performed to ensure the maximum pressure the gas-cell windows could withstand. It was shown that the corresponding maximum pressures were 6 bar and 1 bar over the atmospheric pressure for PP and GC windows, respectively. However, the maximum pressures were controlled under 2 bar and 1 bar in our experimental operation for the PP and GC windows, respectively. Therefore, there was no danger of getting the windows burst during the measurements. Here, the reason why we employed two gas cells are as follows: For the accurate slowing-down measurement, the gas-cell windows are desired to be as thin as possible and durable against the pressure. Therefore, the monoatomic foil of graphenic carbon was chosen, which is low Z_2. The PP windows were employed for the measurement with high incident beam energy, where higher gas pressure than

1 bar was required. In addition, the chemical composition is the same as the propene gas, which enabled to apply the same Bragg's additivity rule for a calculation.

Figure 4.9 shows the schematic drawing of the gas supply system connected to the gas chambers described above. It was controlled remotely with combined hardware and software of the National Instruments' power supply and the LabVIEW application for the following operations; opening/closing the solenoid valves (0-24 V OFF/ON), monitoring/logging the gas pressures, and regulating the inlet gas flow from the gas bottles. The pressure gauges and the flow controller were taken from the MKS company (MKS-AA02 and MKS-627F for the gauge and MKS-640B for the controller). The reported accuracy for the pressure readout is about 0.10%. The temperature measurement was separately performed with the Pt-100 thermocouple resistance. For the readout, the temperature monitor from LakeShore company (model: 218L) was used. The reported accuracy of the temperature readout is about 0.02%. The pipeline was constructed with the VCR® metal gasket face seal fittings, purchased from the Swagelok company.

In our experiment, the three vacuum pumps evacuated the gas volume after a measurement series finished and before the chambers are filled with another gas. They were the turbo pump from the Pfeiffer company, the scroll pump from the Edwards company, and the membrane pump from Leybold company. Furthermore, before a new measurement series started, the gas volume was flushed (filled and pumped) with a new gas at least for four times, so that a gas mixture could be avoided.

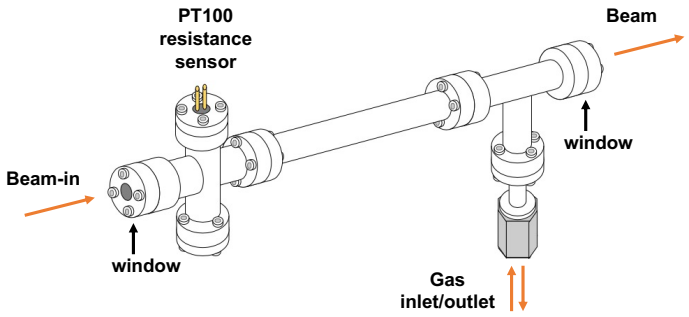

FIGURE 4.8: Schematic drawing of the gas target installed at the F2 area. The gas-filled volume was closed with two thin solid windows. Two different gas targets were prepared to cover different pressure ranges. One chamber had 6 μm thick polypropylene foils (PP windows) and the other one was sealed with 1 μm thick graphenic carbon foils (GC windows). The aperture of both windows was 5 mm diameter, and the distances between the windows were 312.7 mm and 317.5 mm for the gas chambers with PP windows and GC windows, respectively.

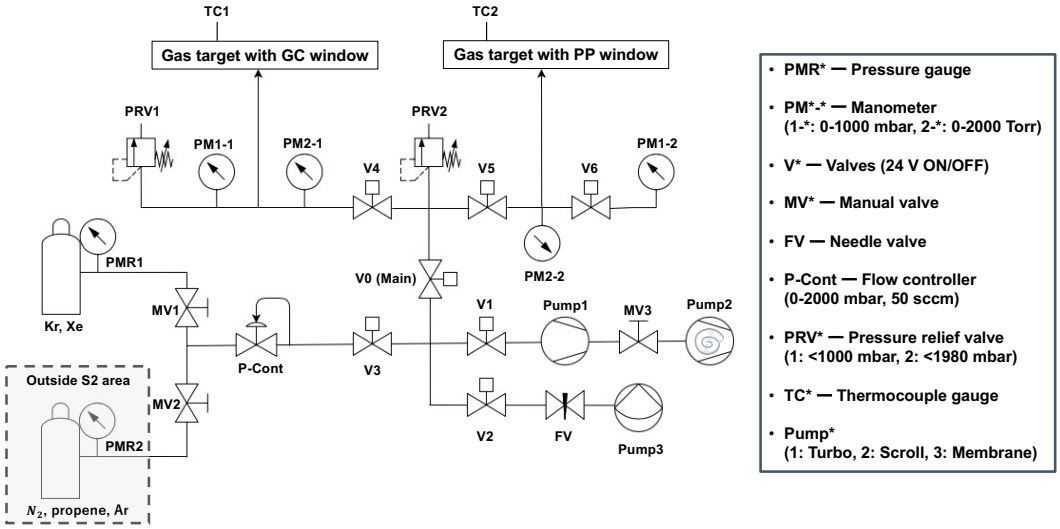

FIGURE 4.9: Operating and control system of the gas targets. The gas flow and the pressure were set, controlled, and recorded with a LabVIEW software application. During one measurement, lasting typically a few minutes, the gas parameters were kept constant and fixed. The monitoring and logging of the gas temperature was separately performed with the Pt-100 sensor connected to the LakeShore temperature monitor (model: 218L). Three vacuum pumps evacuated the gas volume after a measurement series before the chambers are filled with another gas. Before a new measurement series started, the gas volume was flushed (filled and pumped) for four times with a new gas.

4.4.4 F3 Area

At the third focal plane F3, the measurements of energy-loss and charge-state distribution were performed with a time projection chamber (TPC). Figure 4.10 shows the schematic drawing of the F3 area. In this subsection, the details of the TPC detector will be presented.

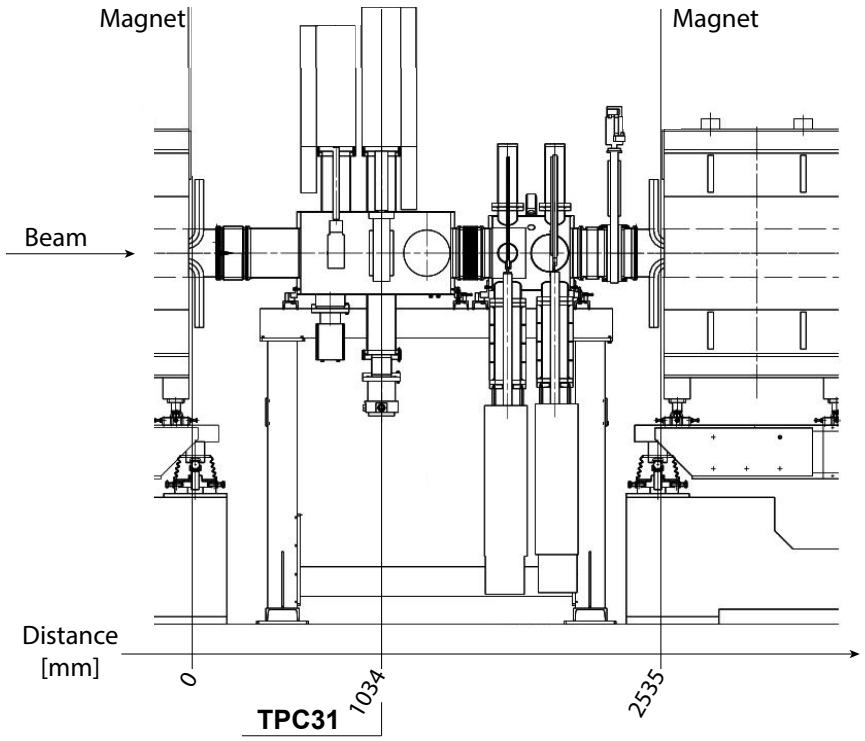

FIGURE 4.10: Technical drawing of the experimental setup at the focal plane F3 of the FRS. The TPC31 is a major component of the present experiment. From the calibrated position spectra of the TPC31, the charge-state distribution and also the energy-loss distribution have been determined.

Time Projection Chamber

The time projection chamber (TPC) [MN78; Hli+98] is a gas-filled position sensitive detector and is used to measure the particle tracks from the electron drift time and signal propagation times through delay lines. It has the vertical drift space with respect to the beam direction, with the geometry of 240 mm wide, 70 mm long, and 80 mm high. A static electric field is generated by the high voltage applied on the cathode plate and the termination of the gating grids. The linear drop of the electric potential and the resulting field homogeneity are obtained with the help of the mylar strips (each 3 mm wide and 20 μm thick with 0.5 μm aluminum coating), which are connected to the high-resistance divider. The electric field applied during the measurement was kept at 400 V/cm. The drift space is filled with the P10 gas (90% Ar and 10% CH_4) at the atmospheric pressure and the room temperature. When the charged particles pass through the drift space, ionization of gas atoms is induced. Electron clouds along the particle track drift towards the proportional region that is underneath the gating grid, where an electron avalanche occurs along the four anode wires while its position can be precisely measured via the charge induced to the cathodes, i.e., the so-called C-pads [Jan+09; Jan+11] (see the Figure 4.11 and 4.12 for the schematic drawing of the

TPC structure). A C-pad is made of the PCB with Cu traces and has the following specialized geometry; two C-shaped opening spaces, both with an opening angle of 80° and an inner diameter of 10 mm. Furthermore, each has a thickness of 2.4 mm and is placed every 0.1 mm interval. There are two independent delay lines in a TPC system which, by each, is formed with nine integrated passive delay-line-chips (Floeth Electronic GmbH), resulting in a total delay of 1350 ns. Each C-pad is connected to one of the inputs of the chips, and the induced signals are transferred to the left and right directions through the delay-line, which is horizontally perpendicular to the beam direction. Then, from the difference in the propagation times of the transferred signals, the x-position of the incident beam can be obtained as

$$x = c_0^x + c_1^x \cdot (t_l - t_r) \quad , \tag{4.6}$$

where t_l and t_r are the arrival timings of signals from the left and right side of the delay line, c_0^x and c_1^x are the constants. In addition, the electron drift time t_d can be used for the determination of the y-position of the incident beam as

$$y = c_0^y + c_1^y \cdot t_d \quad , \tag{4.7}$$

where, again, c_0^y and c_1^y are the constants. These x- and y-positions were originally recorded via timing information with TDC modules. Therefore, the conversion to the physical length, such as in millimeter, required a calibration by using the movable grid with fiber scintillators embedded as shown in Fig.4.11. Perpendicular to the beam direction, there are three gridlines horizontally and vertically. The distances between the scintillator fibers are 10 mm for the horizontal coordinate and 6 mm for the vertical coordinate. The calibration was performed with a defocused lead-ion beam. By plotting the TPC position spectra only when the grid scintillators have events, the grid pattern was observed as shown in the top panel of Fig.4.13. The single spectra in x and y were fitted with multiple Gaussian functions as shown in the bottom panels. The deduced calibration parameters for the x coordinate of the TPC installed at the third focal plane F3 are summarized in the Tab.4.2 below.

In addition, a determination of the particle positions can be done precisely and unambiguously by taking advantage of the precise delay lines of a TPC based on the following relation

$$t_{\mathrm{CS}} = t_l + t_r - 2t_d \quad . \tag{4.8}$$

t_{CS} is called the control-sum and corresponds to the total time of the delay line. A check of the t_{CS} distribution is essential to see the effects from noise and signals due to the delta electrons. Figure 4.14 shows a typical spectrum of the control-sum distribution. During the measurements, the width of t_{CS} distribution was checked to optimize the anode voltages applied to TPC. In the offline data analysis, the t_{CS} distributions were fitted with a Gaussian function as shown by the red curve in the figure, and the events within the 3σ windows were used to reconstruct the position spectra.

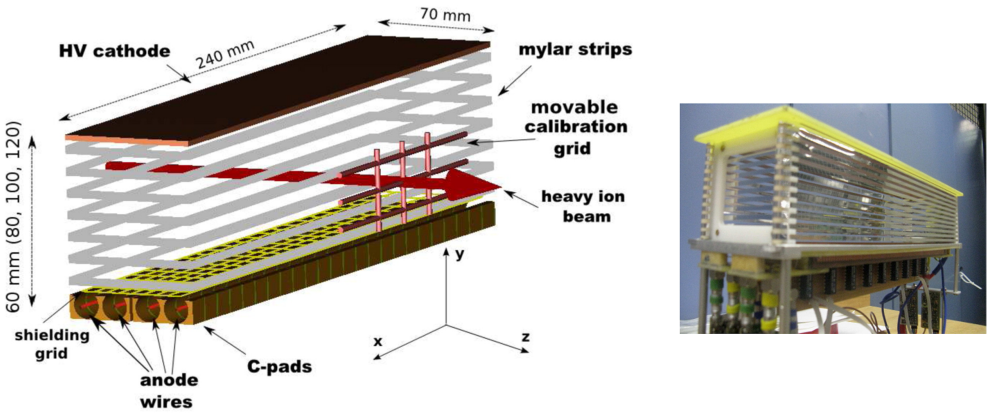

FIGURE 4.11: Setup and dimensions of an FRS Time-Projection Chamber (TPC) [Jan+11]. The drift volume, surrounded by a field cage, is filled with 90 % argon and 10% methane gas mixtures at atmospheric pressure and room temperature. When the charged particles pass through the drift space, ionization of gas atoms is caused. The electron clouds, generated along the particle track, drift towards the proportional region underneath the shielding grid. An electron avalanche is produced along the four anode wires and thus charge is induced in the cathodes, the so-called C-pads, which are connected to delay lines. The time difference between the arrival of the induced signals from the left and right sides of each delay line provides the position information in the horizontal direction, the ion-optical dispersive plane. A movable scintillation grid, coupled to a photomultiplier, was used for absolute calibration of the TPC coordinates in both directions.

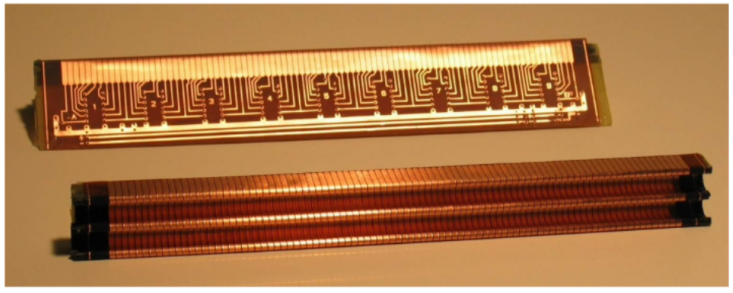

FIGURE 4.12: Photograph of the C-pads with integrated passive delay line. This figure was taken from [Jan+07]. A C-pad is made of PCB with Cu traces and has the following geometry; two C-shaped opening spaces both with an opening angle of 80° and an inner diameter of 10 mm. And each has a thickness of 2.4 mm and is placed every 0.1 mm interval. There are two independent delay-lines in a TPC system which, by each, is formed with 9 integrated passive delay-line-chips (Floeth Electronic GmbH), resulting in a total delay of 1350 ns. Each C-pad is connected to one of the inputs of the chips, and the induced signals are transferred to the left and right directions through the delay-line which is horizontally perpendicular to the beam direction.

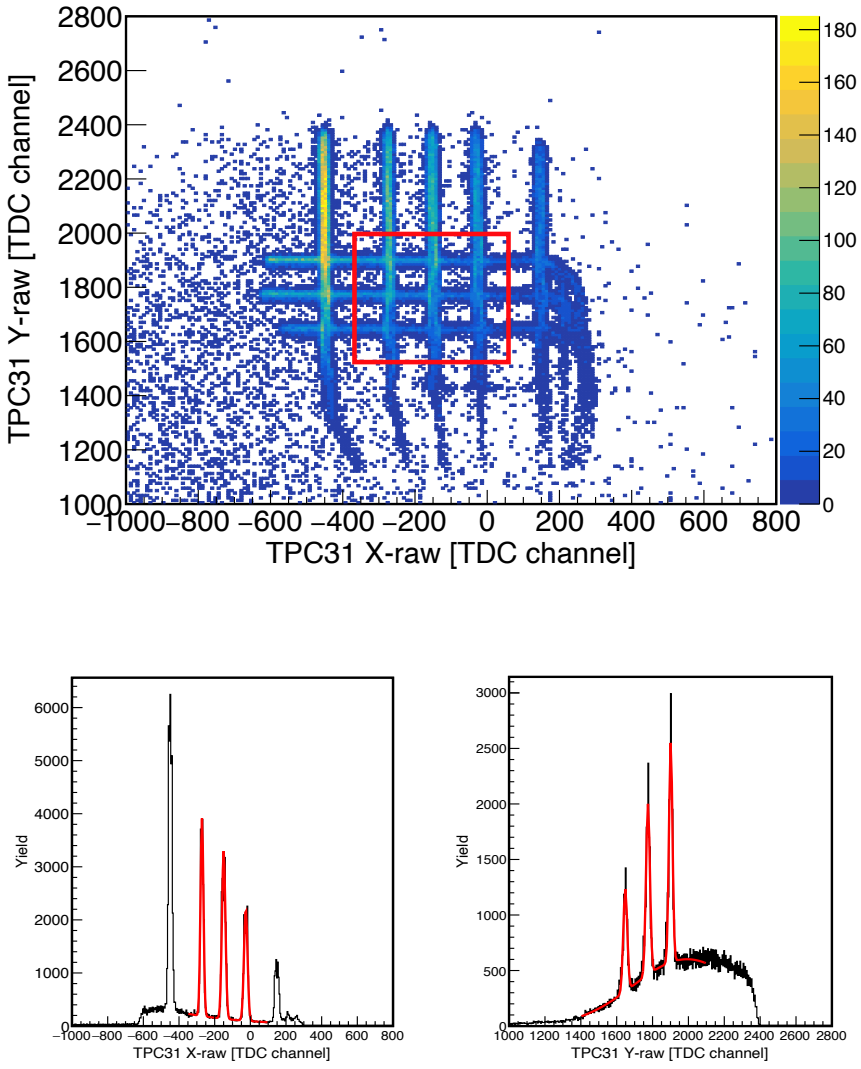

FIGURE 4.13: Example of the TPC calibration by using the calibration grid with fiber scintillators embedded. The events are plotted in coincidence when the grid scintillators are hit. In this way, the grid pattern is visible in the two-dimensional plot (upper graph). The lower panel shows the projections and the fitted peaks to determine the absolute position calibration.

TABLE 4.2: Calibration parameters for the x direction of the TPC installed at the third focal plane F3.

direction	type	factor [mm/channel]	offset [mm]
x	first delay-line	0.083	12.305
x	second delay-line	0.082	5.924

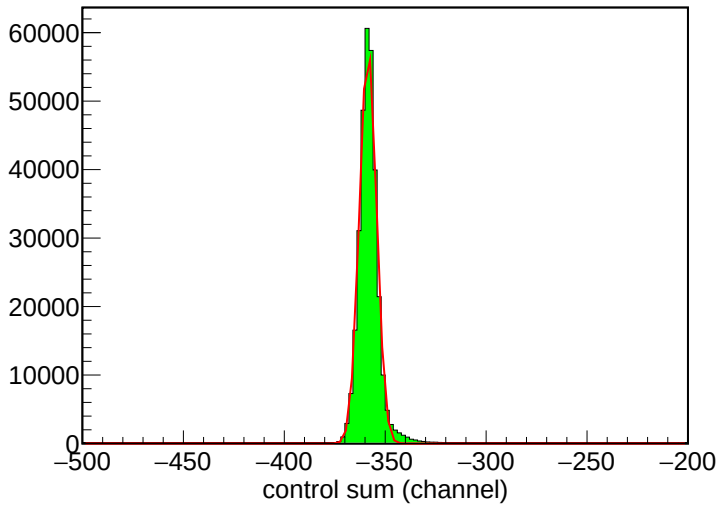

FIGURE 4.14: Typical measured spectrum of the TPC control-sum in x-direction. The events within the 3σ window, determined by the Gaussian fit, are used in the offline analysis.

Detector Electronics

The detector electronics and the trigger circuit are shown in Fig.4.15. In our measurement, the trigger circuit was prepared as the self-triggering mode. Note that we will describe only the signal transfer of the TPC which was the main detector used in our experiment.

From each of the TPC detectors, there are 8 raw signals transferred to the electronic circuit:

- 4 signals from the 4 anode wires: A11, A12, A21, A22
- 4 signals from the left and right sides of 2 delay lines: DL1, DR1, DL2, DR2

These raw signals from a TPC travel through the preamplifier located inside the detector pocket. The amplified signals, except one of the anode signals (A11), which is transferred to the trigger circuit, are optionally delayed and transferred to the main amplifier. The logic output signals from the main amplifier are transferred to the constant fraction discriminator (CFD) and are delayed by the logic delay module. The threshold level of the CFD was kept at -50 mV, which was sufficiently larger than the noise levels as it was checked with the oscilloscope during the measurements. The ECL output signals from the delay module are finally transferred to the TDC (CAEN V775) as the stop signals for the timing measurement. On the other hand, the analog output signals from the main-amplifier are delayed and transferred to the ADC (CAEN V785) for the amplitude measurement.

As explained above, one of the analog signals from a TPC is separately transferred to a CFD, and the output signal is adopted for the trigger circuit. The coincidence with the busy-end signals from the data acquisition system (DAQ) is checked, and the accepted trigger signals are transferred to the logic FAN IN/OUT module. The

divided signals are transferred to the gate generators, and then the output signals are adopted as (1) the common start signal for the TDC and (2) the gate signal for the ADC.

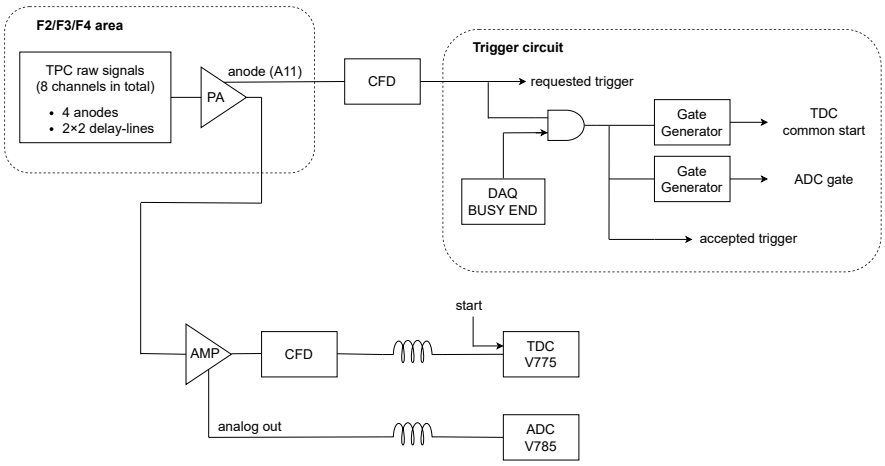

FIGURE 4.15: Diagram of the detector electronics and the trigger circuit, where PA is the preamplifier, AMP is the main amplifier, and CFD is the constant fraction discriminator.

4.5 Properties of the Atomic Collision Target

The target thickness determination plays an essential role in stopping powers measurements. This section will explain the applied methods for the determination of areal density of targets.

4.5.1 Target Materials

Five solids and five gaseous target materials were prepared for the slowing-down and charge-state distribution measurements. The solid materials are amorphous carbon ($Z_2 = 6$), titanium ($Z_2 = 22$), zirconium ($Z_2 = 40$), tin ($Z_2 = 50$), and polypropylene $(C_3H_6)_n$. These solid targets with high purity were commercially manufactured, and their material impurities were reported to be about 10^{-3} to 10^{-4}. They were all cylindrical shapes prepared by either laser-cut and lapped or rolled. The gaseous materials are nitrogen ($Z_2 = 7$), argon ($Z_2 = 18$), krypton ($Z_2 = 36$), xenon ($Z_2 = 54$), and propene C_3H_6. The gas bottles were also purchased from companies.

These solid and gaseous materials were chosen to be pairs, which have close element numbers Z_2. For example, the partner of carbon is nitrogen gas, or the one of tin is xenon gas. With these combinations, measurements of the gas-solid difference in stopping powers and charge-state distributions were aimed for a wide range of target Z_2 number. The compound materials, namely polypropylene and propene, were chosen for a direct comparison with the same chemical components but in different material states. In addition, various targets of the same material with different

thicknesses were prepared in order to meet the following experimental requirements: (1) Covering the charge-state distributions from the pre-equilibrium to equilibrium regions, and (2) Investigating the energy loss in the range from 10% to 30% of the incident energy.

4.5.2 Solid Targets

The areal density of the solid targets was determined by measuring the weight and area. The sample weight was measured by the electronic precision balance, the accuracy of which was considered to be 1 μg. The area was determined from the pixel-calculation of the sample photographs in which the sample shape emerges clearly by shining the translucent light from behind, as shown in Fig.4.16. The accuracy of the area determination was considered to be 0.50%. We have evaluated the areal density twice in this way by changing the sample size as follows: The first examination was performed before the experiment, with the original shape of 20 mm diameter disks as manufactured. The deduced values were used for the planning of the measurement. The second examination was after the experiment. Since the aperture of the solid targets was limited to 5 mm diameter during the measurement, the solid targets were cut out into 4.5 mm diameter while they were mounted with the aperture by using the laser-cutting machine. With this reduced size, we have determined the mean value of the areal density of solid targets for the data analysis. However, the influence of the deformation (bumps and dents) of the sample edge due to the laser-cutting process was estimated to be significant. Figure 4.17 shows a part of the edge of a titanium target, where one can see a bump. From the calculation of the deformed volume of the edge, the uncertainty of the deduced areal density was estimated to be less than 1.5% depending on the material.

We have performed another method to deduce the areal density as a cross check, which was by measuring the thickness and then calculating with the material density reported in the literature. The thickness measurement was performed with the chromatic sensor device (MicroProf® [Kin+20]) at the target laboratory of GSI, and the values were mapped as shown in Fig.4.18. The thickness measurement should be accurate better than 1 μm for the absolute values, and it should be better for the relative variations. However, the chromatic sensors failed to scan the thickness in some cases, as shown by the gray pixels in the right panel of Fig.4.18. This is because that the sensor edges are either too close to or too far from the surface of samples, which often happens with very thin and/or very soft materials such as tin. For such unscanned pixels, the thickness was replaced by the average value of the surrounding pixels. Then, the mean value and the standard deviation were evaluated for the 5×5 mm^2 area in the center of the sample, which is shown by the red square in Fig.4.18. This reduced area was chosen by considering (1) the possible maximum beam spot during the measurement, and (2) the manual uncertainty in the procedure when setting and centering the target on the scanner. The deduced areal densities were basically consistent within the errors, compared to the one deduced by the weight and area.

As a result, the uncertainty of the deduced areal density was, in general, determined to be 0.5-1.5%. The summary of the deduced areal densities of solid targets are given in Appendix A.

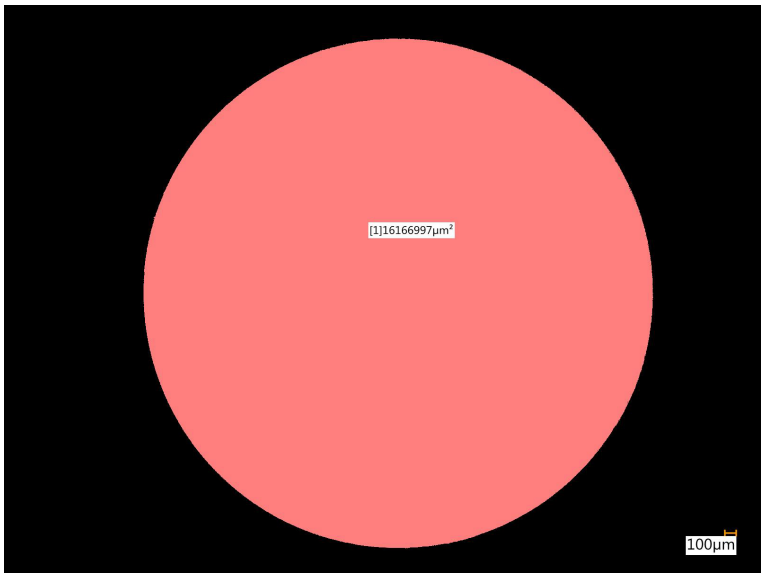

FIGURE 4.16: Measurement of the target area via translucent-light pictures. The photograph of the titanium target is shown. The automated program provided the size of the orange colored area via counting the pixels.

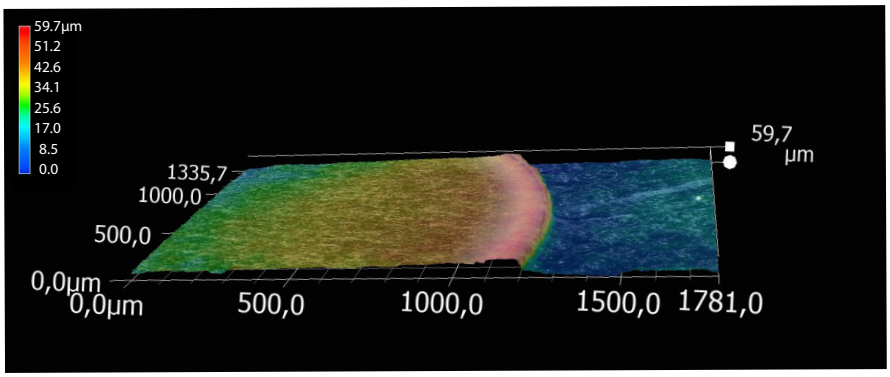

FIGURE 4.17: Scan of the target edge (titanium target) for evaluating the influence of the deformation to the areal density.

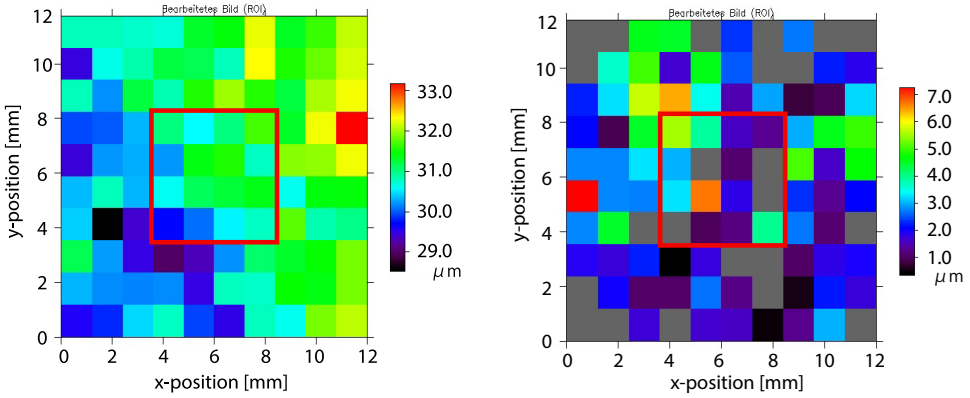

FIGURE 4.18: Mapping of the target thickness performed by a chromatic sensor device [Kin+20] at the target laboratory of GSI. Left panel: Measured thickness profile of a 30.8 μm titanium target. Right panel: Measured thickness profile of a 2.6 μm tin target.

4.5.3 Gaseous Targets

To determine the areal density of the gaseous targets, the density ρ_{gas} was first calculated with the pressure P and the temperature T, which were recorded during the measurements. The Van der Waals equation is given by

$$RT = (P + a\rho_{\text{gas}}) \left(\frac{1}{\rho_{\text{gas}}} - b \right) \quad , \tag{4.9}$$

where $R = 8.31446\ \text{J}/(\text{mol} \cdot \text{K})$ is the gas constant[1], a and b are the Van der Waals constants whose values are listed in the Table 4.3 below. Having the density, the areal density x_{gas} can be calculated by multiplying the interaction (window-to-window) length ℓ, which are 312.7 mm and 317.5 mm for the gas cells with PP and GC windows, respectively, as

$$x_{\text{gas}} = \rho_{\text{gas}} \cdot \ell \quad . \tag{4.10}$$

The deduced areal densities are summarized in Appendix B. The uncertainty in the areal density due to the pressure and temperature measurements was almost negligible. The accuracy in the readout of temperature was reported to be 0.02%, and the one of the pressure was reported to be 0.10%. The values were recorded during the measurements, and their fluctuations were less than 10^{-4} level, which were also negligible. The main contribution to the uncertainty in areal density of gases comes from the deformation of the windows due to the gas pressures. The window-bulging leads to an uncertainty in the interaction length ℓ depending on the position. The effect was evaluated by the method mentioned in the reference [Bim+89a]. The total uncertainty in the areal density was determined to be 0.25% and 0.65% for the GC-windows and PP-windows, respectively.

[1] To convert the unit to $\text{mbar} \cdot \text{cm}^3/(\text{mol} \cdot \text{K})$ which is convenient for the analysis, one just needs to multiply 10^4.

TABLE 4.3: List of the Van der Waals constants.

Material	a [bar $\cdot$ L^2/mol^2]	b [L/mol]
N_2	1.370	0.0387
C_3H_6	8.438	0.0824
Ar	1.355	0.0320
Kr	2.325	0.0396
Xe	4.192	0.0516

4.6 Principles of Measurements with the FRS

In this section, the experimental procedure is presented to provide a framework for the data analysis, which will be presented in the next chapter. An illustration of the procedure of the measurements of the energy-loss and charge-state distribution is given in Fig.4.19.

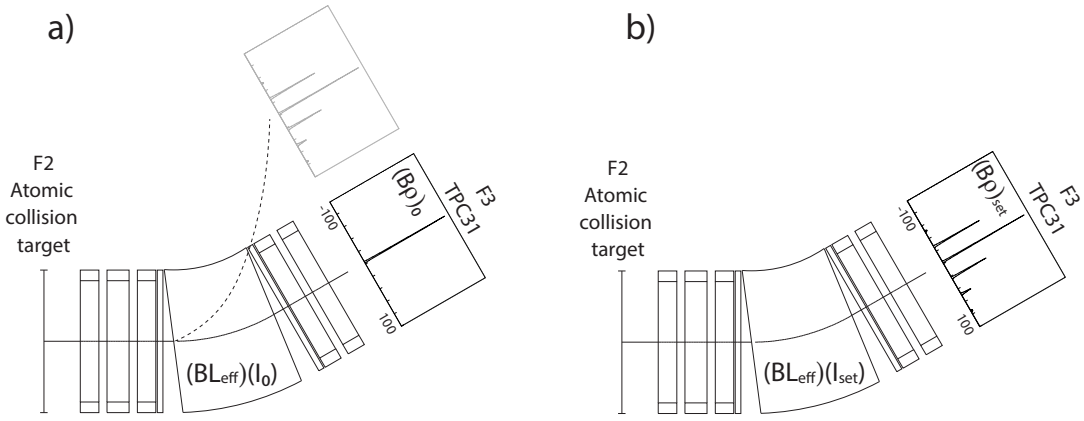

FIGURE 4.19: Principle of the magnetic rigidity ($B\rho$) measurement with scaling of the magnet fields for the complete dispersive section from F2 to F3. Left panel (a): Measurement scenario of the incident beam with the magnet field setting to $B\rho_0$. The trajectory of the expected charge-state distribution, when an atomic collision target is inserted into the beam axis, would be out of the FRS acceptance due to an energy loss of more than 2 %. Right panel (b): Measurement of the charge-state distribution after scaling the FRS to the magnetic fields of $B\rho_{\mathrm{set}}$. The scaling factor is given by the ratio of the BL_{eff} values which are a function of the magnet current I of the dipole magnet in this dispersive section.

4.6.1 Incident Beam

The measurement of incident beams takes basically three steps as

1. Determination of the incident beam energy.

2. Centering the incident beam with the magnetic rigidity $(B\rho)_0$.

3. Measurement of the position profile of the aligned beam at F2 and F3 without a target.

These steps 1-3 correspond to the left picture of Fig.4.19. As explained before, primary beams from the SIS-18 initially pass through the stripper targets at F0. Therefore, for the required beam energy in the experiment, the energy loss at the stripper targets must be considered. The momentum spread at the SIS-18 can be determined in the accuracy better than 5×10^{-4}. Having the incident energy E_0 fixed after the stripper target, one can calculate the magnetic rigidity $(B\rho)_0$ for the field setting of the FRS to transfer and center the incident beams at the following focal planes. For this, one must define the charge state to be centered from the populated charge-state distributions after the stripper target. The selection of the central charge state is performed at F1, by using the mechanical slits and an MWPC (MW11) for checking the charge state distributions. This determination of the incident charge state for the experiment can be unambiguously performed because (1) the energy loss in the stripper target is tiny and can be calculated with sufficient accuracy, and (2) a possible mistake in the identification of the incident charge state would cause a larger difference in the magnetic rigidity than the uncertainty caused by the energy loss at the stripper target. The beam profile is checked at F2 with the two TPCs, and the centering of the incident beams was performed by adding *steering angles* at each dispersive section. Finally, the incident beam is measured at F3, as shown in the left picture of Fig.4.19.

4.6.2 Charge-State Distribution and Energy Loss

The measurements of charge-state distribution and energy-loss of outgoing ions after penetrating an atomic collision target have basically four steps as

4. Insert an atomic collision target in the beam axis.

5. Scale the magnetic fields of the third dispersive stage of the FRS to center again the outgoing ions back to almost the same position as the incident beam.

6. Record the charge-state distribution with the magnetic fields according to $(B\rho)_{\mathrm{set}}$.

7. Scale the magnetic fields again to cover the complete charge-state distribution.

Since the energy loss for our entire experiment was planned to be approximately from 10% to 30% of the incident energy, the corresponding change in the magnetic rigidity was larger than the acceptance of the FRS. Therefore, the spectrum of the outgoing ions after penetrating a target could not be measured at F3 with the same magnet setting $(B\rho)_0$ as shown in the left picture of 4.19, where the dashed curve and blurred spectrum express the trajectory and the charge-state distribution of outgoing ions. Therefore, the following two procedures were taken to measure the energy loss and charge-state distribution at F3. First, the energy loss and the corresponding magnetic rigidity of a specific charge state of the emerging ions were estimated by the ATIMA program. The charge state was chosen to have a value close to the mean value of

the charge state distribution after the target, which was predicted also by the ATIMA program with the modified GLOBAL code[2]. Secondly, the field strength of the third dipole magnet was *scaled* following the estimated magnetic rigidity so that their trajectory could be brought back to the same one as the incident beam, as shown in the right picture of Fig.4.19. Below, we will explain the principle of the scaling method.

The deflection angle Φ of the particle trajectory is in principle given by the ratio between the magnetic rigidity $B\rho$ and the magnetic field $B(\ell)$ integrated along the optical axis ℓ as

$$\Phi = \frac{\int B(\ell)\, d\ell}{B\rho} \quad . \tag{4.11}$$

In practice, the line integral is replaced by the product of the effective length L_{eff} and the mean flux density B determined in the middle of the dipole magnet as

$$BL_{\text{eff}} = \int B(\ell)\, d\ell \quad , \tag{4.12}$$

and BL_{eff} is given as a function of the electric current applied to the dipole magnet. By letting the incident beams, the magnet setting of which is determined for the magnetic rigidity $(B\rho)_0$ with the magnet current I_0 applied, be as the reference and by having the deflection angle Φ including the steering angle, the magnet setting for centering the outgoing ions with expected $(B\rho)_{\text{set}}$ can be determined from the scaling relation

$$\frac{(B\rho)_{\text{set}}}{(B\rho)_0} = \frac{BL_{\text{eff}}(I_{\text{set}})}{BL_{\text{eff}}(I_0)} \quad , \tag{4.13}$$

where the scaling is performed while keeping the deflection angle at constant.

When the outgoing beam of the aimed ionic charge state is brought back to almost the same trajectory of the incident beam, at least within the scale of a few millimeters, the remaining spatial deviation Δx results exclusively from the linear portion of the dispersion of the ion-optics. Suppose that the incident beam hits the TPC on the position x_0 in the magnetic setting of $(B\rho)_0$, and the outgoing beam of a specific ionic charge state q_i hits on x_i, in the scaled setting of $(B\rho)_{\text{set}}$, the magnetic rigidity of the ions in the specific charge q_i can be obtained as

$$\frac{(B\rho)_i - (B\rho)_{\text{set}}}{(B\rho)_{\text{set}}} = \frac{\Delta x}{(x,\delta)} \quad , \tag{4.14}$$

where $\Delta x = x_i - x_0$ and (x,δ) is the first order dispersion coefficient. Furthermore, with the help of Eq.4.13 and the relation $B\rho = p/q$, the momentum of outgoing ions in a specific charge state q_i can be given by

$$p_i = p_0 \frac{BL_{\text{eff}}(I_{\text{set}})}{BL_{\text{eff}}(I_0)} \frac{q_i}{q_0} \left(1 + \frac{\Delta x}{(x,\delta)}\right) \quad . \tag{4.15}$$

[2]For the description of the ATIMA program, see Appendix E.

Accordingly, one can evaluate the mean energy loss by adopting the energy spectrum from the momentum: We will describe it in more detail in the following chapter.

Here, we mention three things regarding the scaling method explained above. The first point is the steering angle. The value is determined initially to center the incident beam, and the value is kept at constant for the succeeding measurements of the outgoing ions with a target in. However, the steering angle in principle slightly changes according to the magnet settings. Figure 4.20 shows the graph of the steering angle applied at the third dipole magnet section as a function of the magnet setting $B\rho$. The data point comes from the measurement of the oxygen beam performed in 2021. The beam energies provided by the SIS-18 were at (50, 100, 200, 370, and 465) MeV/u to cover the $B\rho$ range of the present experiment. Oxygen beam is fully ionized at these energies, plus, the magnetic rigidity can be precisely estimated including the energy loss at the stripper targets at F0. As one can see, there is almost a linear trend in the magnitude of the steering angle, which may cause an influence in the momentum calculation with Eq.4.15. However, the slight difference in the two magnet settings is negligible when the ratio of the deflection angles is taken. For example, suppose that the energy loss is 30% of the incident energy with, e.g., $(B\rho)_0 = 4.0$ Tm. In this case, the difference in the steering angle is $\delta\Phi_{steering} < 0.2$ mrad in the two magnet settings, which is totally negligible to be of the order of 10^{-4} or less compared to the total deflection angle about 30 degrees ($\sim$ 523.6 mrad). Therefore, there is no need to include a correction for the calculation in the scheme of our experiment.

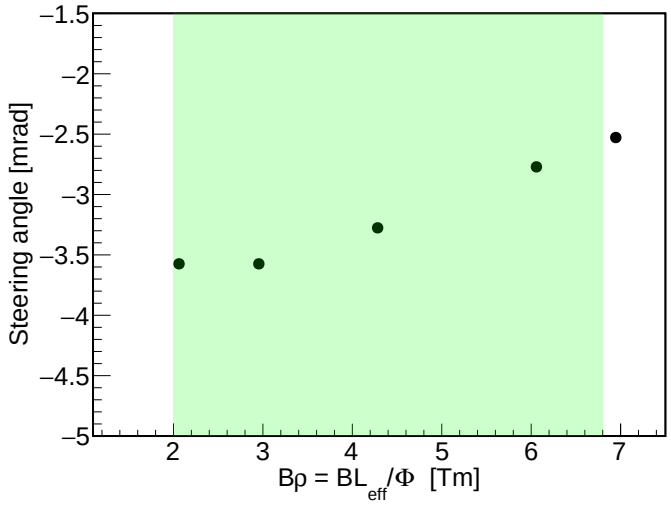

FIGURE 4.20: Measured steering angle. An important ion-optical goal during the energy-loss measurement is to have the projectile beam centered on the magnetic axis. The calculated matrix elements change for beams transported off axis. Such an alignment is performed with the dipole magnets included in the FRS lattice. In the x-direction, the nominal 30 degrees bending angle is slightly changed by steering angles which are experimentally determined for each new incident energy. An example of such determined steering angles is presented.

The second point is the determination of the BL_{eff} in the offline analysis. As it was explained, BL_{eff} is given as a function of the magnet current. In our experiment, the

electric current and additionally the corresponding voltage from the magnet power supply were recorded in text files. However, the current data were recorded every 1 minute or 3 minutes, and sometimes the automated program failed to save the values during the measurement time range. Meanwhile, the voltage values were recorded every 1 second. Therefore, to determine the BL_{eff} in the offline analysis, we had to deduce the coefficients to convert the variables among the voltage, current, and BL_{eff} values. The lower graph of Fig.4.21 shows the relation between BL_{eff} and the applied current I for the third dipole magnet of the FRS, and the colored-area corresponds to our measurement range. The red curve corresponds to the fit function of the third-order polynomials, and the parameters obtained in the fit are as follows:

$$BL_{\mathrm{eff}}(I) = a_0 + a_1 I + a_2 I^2 + a_3 I^3 \quad ,$$

where

$$\begin{aligned} a_0 &= 1.57 \times 10^{-2} \\ a_1 &= 1.11 \times 10^{-2} \\ a_2 &= 1.05 \times 10^{-6} \\ a_3 &= -1.26 \times 10^{-9} \quad . \end{aligned}$$

The upper graph of Fig.4.21 represents the plot of the residuals of BL_{eff} values compared to the fit function. In the measurement range, approximately from 80 A to 310 A, the magnitude of residual stays of the order of 10^{-4} level. Then, the lower graph of Fig.4.22 shows the relation between the voltage value and the current value, which were measured during our experiment. The voltage data plotted on the graph are the mean values of the ones recorded during the measurement in which the current values were simultaneously recorded. The red line corresponds to the first-order polynomial fitted to the data, and the parameters deduced are as follows:

$$I = b_0 + b_1 V \quad ,$$

where

$$b_0 = 0.1016 \quad \text{and} \quad b_1 = 89.8928 \quad .$$

The upper graph of Fig.4.22 shows the residuals of current data compared to the fit function. The magnitude of residual mostly stays within 10^{-4} level. As a result, in our offline analysis, the BL_{eff} values can be determined via the voltage with the accuracy less than 10^{-3} level in total.

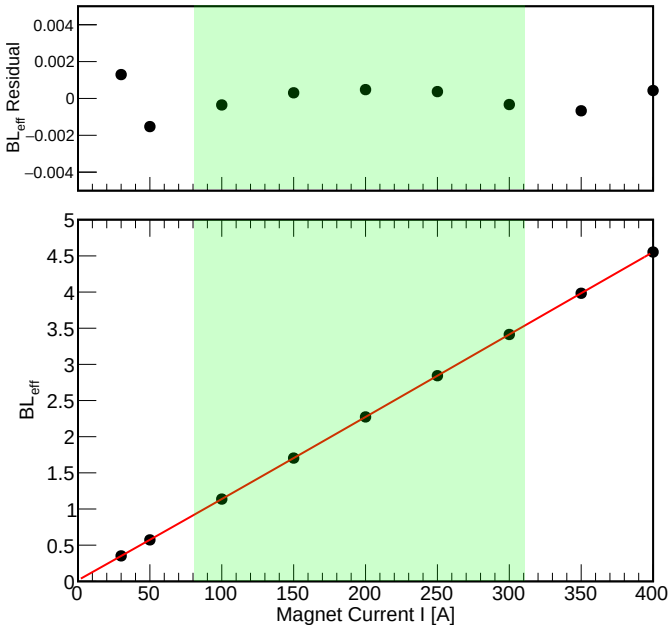

FIGURE 4.21: The mapping data of the BL_{eff} as a function of the magnet current for the third dipole magnet of the FRS. The green area covers the magnetic rigidity range of our experiment.

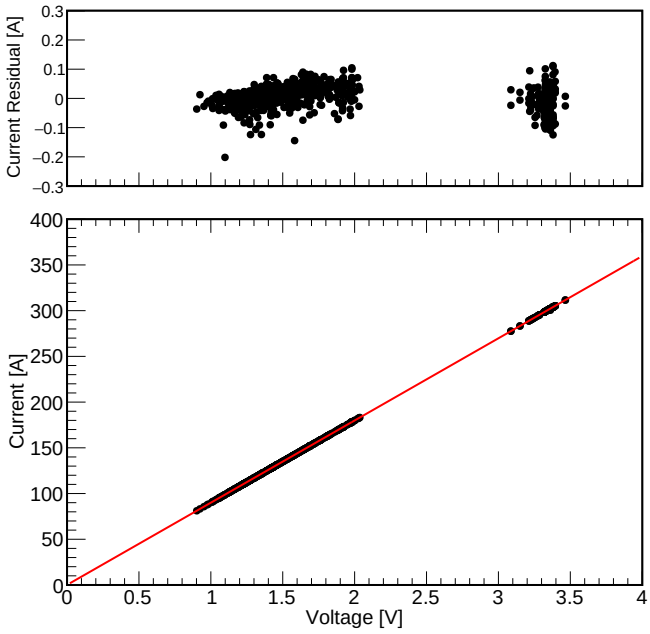

FIGURE 4.22: Measured voltage and electric current from the power supply for the third dipole magnet of the FRS. The fitted curve demonstrates the good linearity of the relation. The upper panel shows the residuals from a linear relation.

Lastly, especially in the measurement with low incident energy, there were many charge-states populated in the charge-state distribution, the spatial width of which

was wider than the detector geometry. Therefore, to measure the complete distribution, the scaling method was again adopted to shift the distribution for $\pm$(3-5)% of the dispersion, resulting in the position shift of $\pm$(60-100) mm on the TPC31. The following analysis will be explained in the next chapter. Moreover, we shall mention here that the hysteresis of the dipole magnet was treated by the ramping procedure whenever the magnet setting was changed during our measurement.

Chapter 5

Data Analysis

Based on the measurement principles described in Chapter 4, we have performed measurements of energy loss and charge-state distributions of lead ions with the TPC installed at the dispersive focal plane F3. Figure 5.1 shows examples of the charge-state distributions without (left panel) and with (right panel) an atomic collision target inserted at the F2. The different charge states of the emerging ions after an atomic collision target are dispersed in the measured position spectra due to the ion-optical properties of the magnetic spectrometer FRS. The general analysis flow on such position spectra is as follows:

1. Determination of the mean position and integral of each peak.
2. Charge-state assignment.
3. Determination of the mean charge state.
4. Determination of the dispersion coefficient.
5. Transformation of the position spectrum to the energy spectrum and determination of mean energy loss.
6. Stopping power determination.

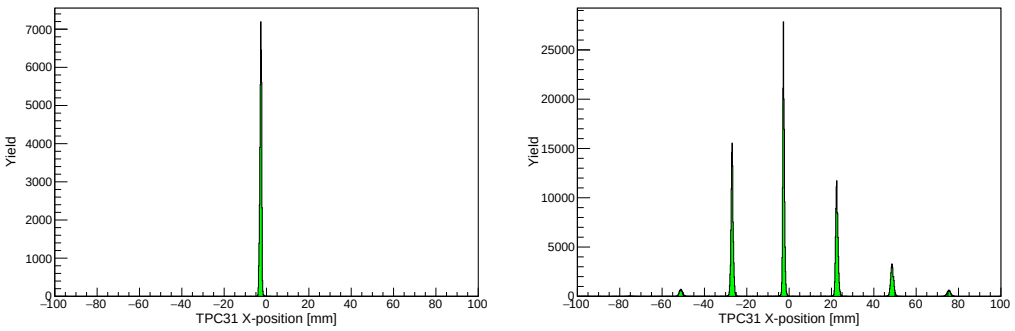

FIGURE 5.1: Measured charge-state distributions of lead ions at the dispersive focal plane F3. Left panel: Measurement of the incident beams at 100 MeV/u without an atomic collision target. Right panel: The charge-state distribution measured after penetration of the 18.64 mg/cm^2 thick titanium target.

5.1 Determination of Mean Position and Integral of Each Peak

The mean position and integral of each peak in the position spectra measured with the TPC installed at the dispersive focal plane F3 were determined by the following steps. First, the position spectra in the logarithmic scale were fitted with a function of multiple Gaussians plus an optional background function to obtain the Gaussian's mean position and width (σ) of each peak. The options for the background function were either a single Gaussian, multiple Gaussians, or an exponential function depending on the shape. However, such background functions were not needed for most of the cases, except for the data taken with the gas target with PP windows. Secondly, after subtracting the background from the position spectra, the 3σ windows were set for each peak from the peak position, and the statistical mean position and integral were evaluated within the windows. These statistical values were used for the following analysis.

5.2 Charge-State Distribution and Mean Charge State

Our first goal is to deduce the mean charge state of lead ions from the charge state distribution after penetrating atomic collision targets. The mean charge state $\bar{q}$ is defined by

$$\bar{q} = \sum_i q_i F(q_i) \quad , \tag{5.1}$$

where $F(q_i)$ are charge-state fractions which can be calculated with the integral values A_i of each peak in a charge-state distribution as

$$F(q_i) = \frac{A_i}{\sum_i A_i} \quad . \tag{5.2}$$

For this analysis, the knowledge of the detector response and efficiency are important.

5.2.1 Detector Efficiency

The detector efficiency of the TPC at the dispersive focal plane F3 was checked by shifting the charge-state distributions for $\pm 3\%$, $\pm 3.5\%$, or $\pm 4\%$ of dispersion as shown in Fig.5.2. Suppose that the central and highest peak shown in the upper panel of Fig.5.2 corresponds to the charge state q and its charge-state fraction is $F(q)$. The ratios of the charge-state fractions of neighboring charge states $F(q+1)/F(q)$ and $F(q-1)/F(q)$ were evaluated in each spectrum. It was found that the ratio became about 5% lower when the peaks of $F(q+1)$ and $F(q-1)$ were in the range of $|x| > 80$ mm in the shifted spectra compared to the central one. Therefore, the analysis on every single spectrum was limited to the range of $|x| \leq 80$ mm of the TPC, for which the variation of ratio remained less than 0.5%. To evaluate the integrals of peaks out of the range, the peaks of corresponding charge state were taken from the shifted spectra after normalizing the integrals to the central one.

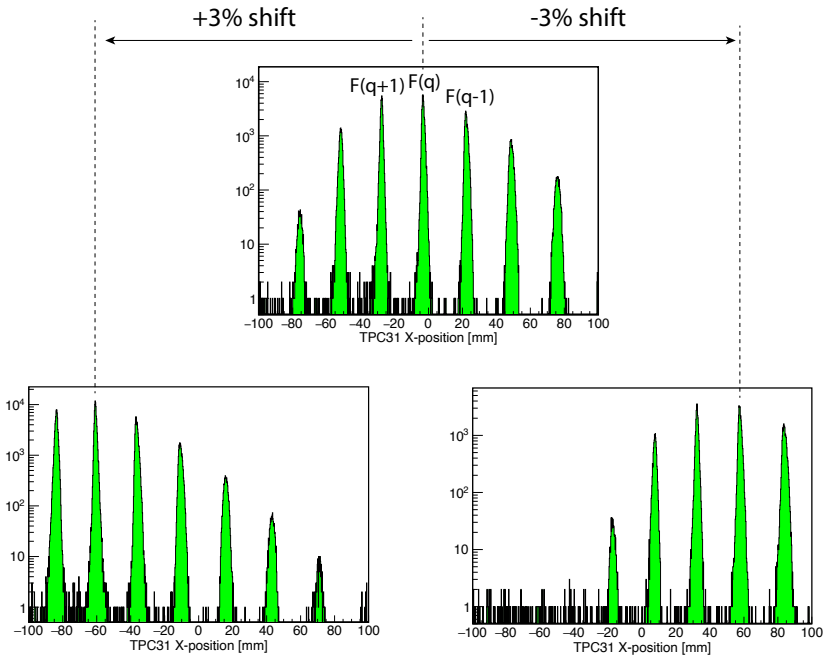

FIGURE 5.2: Charge-state distributions measured at the incident energy of 100 MeV/u after penetrating the 60.28mg/cm^2 zirconium target for two magnetic field settings. Top panel: Measured charge-state distribution when the most abundant peak was centered. Bottom left and right panels: Measured charge-state distributions where the most abundant peak was shifted by $\pm$3%.

5.2.2 Charge-State Assignment

The charge-state fractions $F(q)$ of a complete distribution were obtained from the integral values of each peak, as explained above. The next step is to assign the charge-state q to them.

The equilibrium charge-state distribution follows the Gaussian trend within each atomic shell. Therefore, a logarithmic plot of the ratio of neighboring charge-state fractions $F(q)/F(q-1)$ shows linear trends modulated by the population of the atomic shells, i.e., the binding energies determine the trends of charge-state distribution observed. The top-left panel of Fig.5.3 shows the example of the charge-state fractions $F(q)$ obtained in the measurement with the incident energy at 100 MeV/u and with the 56.72 mg/cm^2 thick titanium target, and the top-right panel shows the one with the incident energy at 50 MeV/u and with the 38.07 mg/cm^2 thick titanium target. The corresponding lower panels show the plots of the ratio $F(q)/F(q-1)$ as a function of charge-state q. Furthermore, one can see that there are differences in the linear trends after the transition from an atomic shell to the next one, namely from $q = 81^+$ in the K-shell to $q = 80^+$ in the L-shell for the left panel and from $q = 73^+$ in the L-shell to $q = 72^+$ in the M-shell for the right panel. These differences in the charge-state distributions are called the shell gaps, and this was used as an indication of charge state assignment in the present analysis.

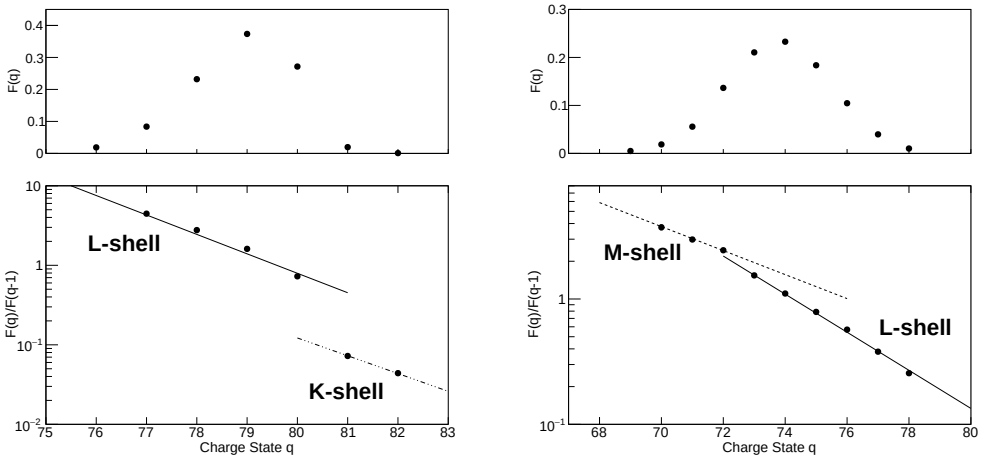

FIGURE 5.3: The principle of the charge state verification according to the electron shell gaps. Left panel: The L-K shell gap observed in the charge-state distribution measurement after the 100 MeV/u lead ions had penetrated the 57.07 mg/cm^2 titanium target. Right panel: The M-L shell gap observed in the charge-state distribution measurement after the 50 MeV/u lead ions had penetrated the 38.36 mg/cm^2 titanium target.

5.2.3 Window Corrections

Finally, with the charge-state fractions $F(q)$ and the charge state q assigned, the mean charge states $\bar{q}$ of lead ions after penetrating each atomic collision target were deduced according to Eq.5.1. For the gas target, however, the shift in the charge state due to the exit window of the gas cell must be evaluated:

In our measurement, the charge-state distributions were measured with the empty gas target cell. In addition, measurements were also performed, where a single foil of the gas target window was used as a target. In Tab.5.1, the experimental charge-state fractions of lead ions after penetrating one or two gas target windows are listed. The first and third columns correspond to the incident energy E_{in} and incident charge-state q_{in} of lead ions. In the second column, the type of gas target windows, namely polypropylene (PP) or graphenic carbon (GC), are given with the number of foils inserted, e.g., for a single GC foil, it is given as GC-1. From the fourth to the ninth column, the measured charge-state fractions are given for the emerging charge-states which are unchanged or changed by ± 1, ± 2, and $+3$ compared to the incident charge-state q_{in}. The last column, then, corresponds to the mean charge states $\bar{q}$ of the distributions. From this table of experimental results, the following characteristics can be stated: In general, the shift value in mean charge ($\Delta q = \bar{q} - q_{in}$) due to a gas target window is small. The charge-state population down to 50 MeV/u is basically dominated by the unchanged charge state $F(q_{in})$. The rest goes mainly to the singly changed charge states $F(q_{\mathrm{in}} \pm 1)$, but more significant to the $+1$ changed charge state because the electron loss process is still contributing more than the capture process at this velocity. At 35 MeV/u, when the projectiles have electrons in the outer atomic shells, such as in the M-shell, loosely bound electrons are easily stripped and the $+1$

or +2 changed charge states start contributing to the overall population. However, the shift value Δq can still be estimated less than +1 if one considers only a single window in the investigated velocity range. Therefore, to a good approximation, the charge-changing process may be described by the single charge-changing collisions for the present consideration of the effect due to the exit window of the gas target.

TABLE 5.1: List of the experimental charge state fractions $F(q)$ of lead ions after passing through the gas-target windows. GC/PP-1 means the measurement with a single window, and GC/PP-2 means the empty gas-cell with two windows.

E_{in} [MeV/u]	window type	q_{in}	$F(q_{\mathrm{in}}-2)$	$F(q_{\mathrm{in}}-1)$	$F(q_{\mathrm{in}})$	$F(q_{\mathrm{in}}+1)$	$F(q_{\mathrm{in}}+2)$	$F(q_{\mathrm{in}}+3)$	$\bar{q}$
280	GC-2	81^+	0.0000	0.0050	0.9913	0.0037	0.0000	0.0000	81.00
280	PP-2	81^+	0.0003	0.0355	0.9441	0.0201	0.0000	0.0000	80.98
100	GC-2	79^+	0.0000	0.0164	0.9319	0.0517	0.0000	0.0000	79.04
100	PP-2	79^+	0.0006	0.0405	0.8323	0.1265	0.0000	0.0000	79.08
70	GC-2	77^+	0.0023	0.0395	0.7860	0.1603	0.0119	0.0000	77.14
70	GC-1	77^+	0.0000	0.0144	0.9091	0.0739	0.0026	0.0000	77.06
70	PP-2	77^+	0.0021	0.0501	0.5889	0.3027	0.0522	0.0000	77.37
50	GC-2	77^+	0.0045	0.0879	0.7352	0.1592	0.0132	0.0000	77.09
50	PP-2	76^+	0.0120	0.0973	0.4529	0.3289	0.0945	0.0130	76.43
50	PP-2	77^+	0.0014	0.1249	0.5247	0.2818	0.0537	0.0000	77.23
35	GC-2	74^+	0.0301	0.1606	0.4803	0.2569	0.0602	0.0075	74.17
35	GC-2	70^+	0.0041	0.0286	0.1429	0.3128	0.3599	0.1519	71.45
35	GC-1	74^+	0.0079	0.1115	0.6836	0.1768	0.0197	0.0000	74.09
35	GC-1	70^+	0.0019	0.0398	0.3707	0.3651	0.1861	0.0365	70.80

Based on the statement, the numerical estimation of the shift values Δq was performed with the Monte-Carlo simulation program MOCADI [Iwa+97]. In the program, the GLOBAL code [Sch+98] is implemented for the prediction of charge-state evolutions of the projectile ions in matter. The single-electron transfer cross sections for the loss and capture processes are respectively given by

$$\sigma(n, n-1) = n_{\mathrm{K}}\sigma_{\mathrm{K}}^{\ell} + n_{\mathrm{L}}\sigma_{\mathrm{L}}^{\ell} + n_{\mathrm{M}}\sigma_{\mathrm{M}}^{\ell} \quad , \tag{5.3}$$

and

$$\sigma(n, n+1) = \frac{2-n_{\mathrm{K}}}{2}\sigma_{\mathrm{K}}^{\mathrm{c}} + \frac{8-n_{\mathrm{L}}}{8}\sigma_{\mathrm{L}}^{\mathrm{c}} + \frac{18-n_{\mathrm{M}}}{18}\sigma_{\mathrm{M}}^{\mathrm{c}} + \sigma_{\mathrm{H}}^{\mathrm{c}} \quad , \tag{5.4}$$

where n_i denotes the number of electrons occupying an atomic shell ($i = K, L, M$). The σ_i^{ℓ} and σ_i^{c} are the single electron loss and capture cross-sections of the $i = K, L, M$ atomic shells, respectively. In the present consideration, we assume a picture that the lead ions after penetrating the gaseous medium have a *single charge state of the mean charge* $\bar{q}_{\mathrm{gas}}$, which we would like to obtain in the end, and penetrate the exit window of the gas target at an emerging energy determined right after the gaseous medium. Then, the goal of the present simulation is to estimate the dependence of the shift value

Δq on the emerging energy and mean charge state just after the gaseous medium. The evaluation procedures are explained by two steps as follows:

The first step of the evaluation was to find the best factors f_{EL} and f_{EC} to be multiplied to the single electron loss and capture cross sections implemented in the GLOBAL program so that the experimental mean charge states, listed in the last column of Tab.5.1, after penetrating one or two gas target windows could be reproduced by the Monte-Carlo simulation. For this, first, the same incident charge state q_{in} was taken from the third column of the table. Then, the charge-state fractions of unchanged, $F(q_{in})$, and singly changed charge-states, $F(q_{in} \pm 1)$, predicted by the simulation were compared to the experimental values according to the following deviation parameter:

$$\Delta = \sqrt{(\Delta F(q_{in}))^2 + (\Delta F(q_{in}+1))^2 + (\Delta F(q_{in}-1))^2} \quad , \tag{5.5}$$

where $\Delta F(q)$ are the relative differences between the experimental charge-state fraction $F^{\mathrm{exp.}}(q)$ and the one predicted by the Monte-Carlo simulation $F^{\mathrm{sim.}}(q)$ as

$$\begin{aligned}
\Delta F(q_{in}) &= g(q_{in}) \times \left(\frac{F^{\mathrm{sim.}}(q_{in})}{F^{\mathrm{exp.}}(q_{in})} - 1 \right) \times 100 \quad , \\
\Delta F(q_{in}+1) &= g(q_{in}+1) \times \left(\frac{F^{\mathrm{sim.}}(q_{in}+1)}{F^{\mathrm{exp.}}(q_{in}+1)} - 1 \right) \times 100 \quad , \\
\Delta F(q_{in}-1) &= g(q_{in}-1) \times \left(\frac{F^{\mathrm{sim.}}(q_{in}-1)}{F^{\mathrm{exp.}}(q_{in}-1)} - 1 \right) \times 100 \quad ,
\end{aligned} \tag{5.6}$$

and $g(q)$ are the weights for considering the degree of the contributions from the charge state q to the experimental mean charge state as

$$g(q) = \frac{q}{\bar{q}^{exp.}} \times F^{exp.}(q) \quad . \tag{5.7}$$

For each of the fourteen cases listed in the Tab.5.1, the Monte-Carlo simulations were performed. The conditions of the simulation are following: For each combination of the incident energy E_{in} and charge-state q_{in} listed in the table, both factors, f_{EL} and f_{EC}, were changed from 0.1 to 10 at the interval of 0.1, for finding the minimum deviation Δ. The thicknesses of GC and PP windows were considered to be 1 μm and 6 μm, respectively. The composition of a PP window was considered to have H-C-H layers. Lastly, each simulation was performed with 10^5 events.

Figure 5.4 shows examples of the plot of the deviation parameter Δ as a function of the f_{EL} and f_{EC} factors. The left panel corresponds to the case of lead ions with $q_{in} = 77^+$ at $E_{in} = 50$ MeV/u penetrating two GC windows, and the right panel corresponds to the case of the same projectile penetrating two PP windows. One can see that there are locations where the deviation parameter Δ becomes at the minimum. Then, the f_{EL} and f_{EC} factors which minimize the deviation parameter Δ are determined and summarized in the Fig.5.5 for the GC window in the left panel and the PP window in the right panel as a function of incident energy. In both types of gas target windows, it was found that the f_{EC} factor (full circles) increases as the energy goes lower while the

f_{EL} factor (triangles) decreases. Moreover, the both factors were very similar between the two types of windows at each energy. Furthermore, in the case of $E_{in} = 50$ MeV/u for PP windows, there were two different incident charge states, $q_{in} = 76^+$ and 77^+, used in the measurement. Both have electrons in the L-shell, and it was found that the resulting factors were the same. Meanwhile, in the case of $E_{in} = 35$ MeV/u for GC windows, there were also two incident charge-states, $q_{in} = 70^+$ and 74^+, used in the measurement. The former has electrons up to M-shell, and the latter has electrons up to L-shell. There was a clear difference for the f_{EC} factors being $f_{EC} = 11.0$ and $f_{EC} = 7.4$, respectively, while the f_{EL} factors were close $f_{EL} = 0.6$ and $f_{EL} = 0.5$, respectively.

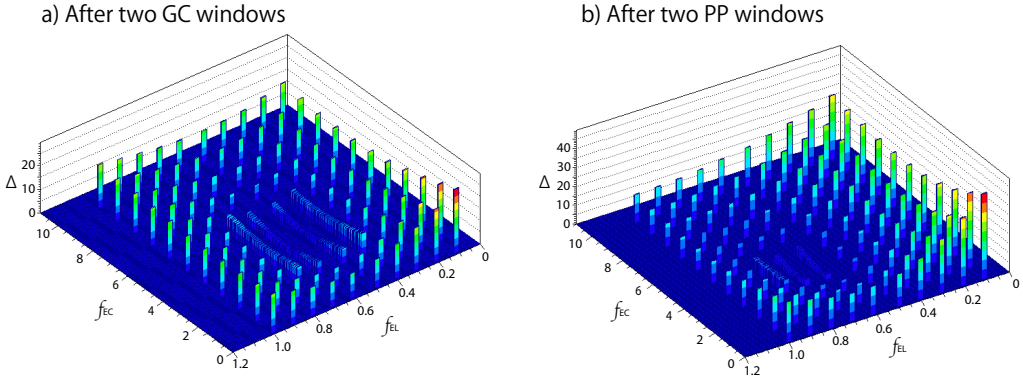

FIGURE 5.4: Three dimensional mapping of the deviation parameter Δ as a function of the f_{EL} and f_{EC} factors. The left panel corresponds to the example of $q_{in} = 77^+$ and $E_{in} = 50$ MeV/u for the penetration through two GC windows. The right panel corresponds to the same beam conditions but for the penetration through two PP windows.

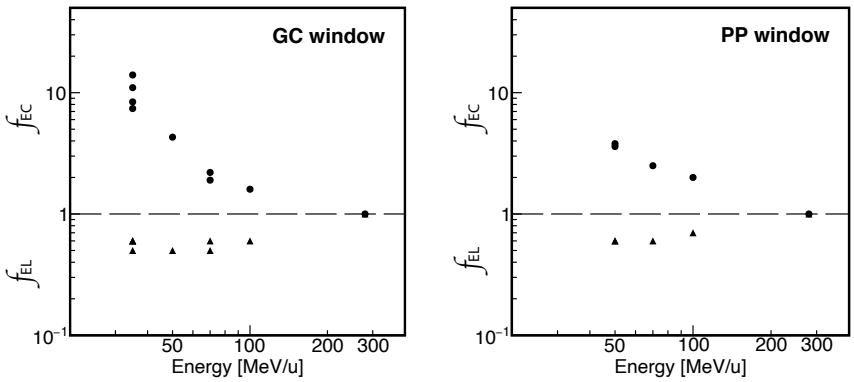

FIGURE 5.5: The f_{EL} and f_{EC} factors as a function of energy were deduced from the Monte-Carlo simulations for fourteen combinations of the incident energy and charge-state listed in Tab.5.1. The left and right panel corresponds to the GC and PP windows, respectively.

Having the factors of f_{EL} and f_{EC}, the experimental charge-state distributions after the gas target windows can be reproduced by the Monte-Carlo simulation with the MOCADI program within the scheme of the investigated energy and incident charge-state. The next step of the evaluation was, then, to calculate Δq from the simulations after only a single gas-target window at each investigated energy (35, 50, 70, 100, and 280 MeV/u), by changing the incident charge-state from $q_{in} = 65^+$ to $q_{in} = 82^+$. The left panel of Fig.5.6 shows the result of Δq after penetrating a single GC window as a function of incident charge-state q_{in} for different incident energies, and the right panel shows the plot as a function of incident energy E_{in} for different incident charge-states. Then, the values of Δq can be found as a function of E_{in} and $q_{in} + \Delta q$: The emerging energy after the gaseous material in the experiment corresponds to the E_{in} defined in the present simulation, and the measured mean charge state $\bar{q}$ after the whole gas target in the experiment corresponds to the $q_{in} + \Delta q$ defined in the present simulation. For the experimental values in between the data points of Fig.5.6 the interpolation was taken with the linear function.

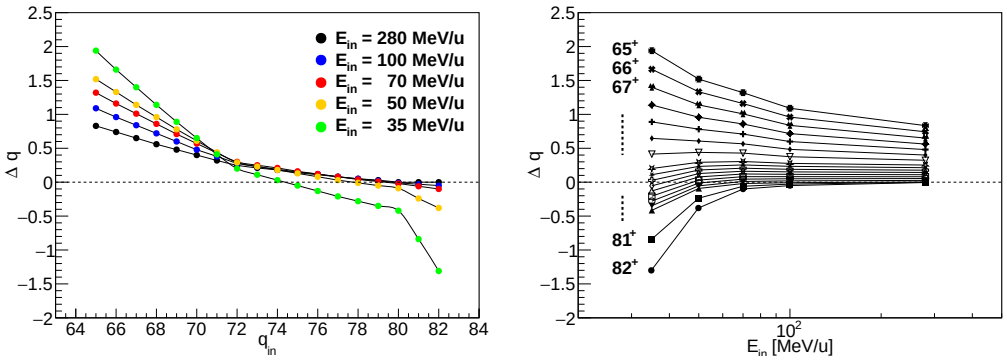

FIGURE 5.6: Determined shifts Δq as a function of the incident charge-state (left panel) and energy (right panel)for the GC-window.

The statistical uncertainty in the deduced mean charge state is small since we have accumulated a sufficiently large number of events for the peaks of charge-state distributions. We have also considered the detector efficiency as described before. However, in the evaluation of the shift value Δq of the mean charge state due to the exit window of the gas target, which was discussed in the present subsection, a consideration of the systematic uncertainty was needed. As can be seen in the right panel of Fig.5.6, when the energy becomes lower than, e.g., 35 MeV/u down to 20 MeV/u for the GC window, the trend of the shift value Δq of each charge-state was rather a guess. In the present analysis, the shift value Δq was estimated by the extrapolation of the linear trend, which corresponds to the energy range from 35 to 50 MeV/u. The uncertainty of the estimated shift at such a low energy region can be for ± 1 maximum since the charge states with electrons in the M-shell play important roles in the charge-state distributions. This systematic uncertainty was included in the experimental result of the mean charge state. As a result, our experimental mean charge states were determined within the accuracy less than about 1%. The results are summarized in

Appendix D.

5.3 Mean Energy Loss and Stopping Power

Our second goal of the present analysis is to deduce the stopping powers, defined as the mean energy loss per unit path length in matter. For the calculation of mean energy loss, the momentum p_i of the outgoing ions in charge state q_i are first deduced according to Eq.4.15:

$$p_i = p_0 \frac{(BL_{\mathrm{eff}})_{\mathrm{set}}}{(BL_{\mathrm{eff}})_0} \frac{q_i}{q_0} \left(1 + \frac{\Delta x}{(x,\delta)}\right) \quad .$$

Δx is the difference in peak positions deduced from the measurements with and without an atomic collision target. For its calculation, the mean positions, which were determined by the methodology described in Section 5.1 were used. Then, for the following mean energy loss calculation, the momentum p_i of the most centered peak on the TPC was used. The reason is as follows: Since there was no additional position-sensitive detector at the dispersive focal plane F3 in our measurement because of the geometrical limitation, the angle a of outgoing lead ions at F3 was not measured. Due to this situation, the ion optical correction for the dependence of horizontal position x on the angle a at F3 could not be performed. In Tab.5.2, the mean positions and the corresponding full-width-half-maxima (FWHM) are listed for the case of projectile lead ions at 100 MeV/u penetrating through the titanium target with thickness of 56.72 mg/cm^2. Compared to the central peak of $q = 79^+$, the FWHM becomes wider as the peaks are off from the center. The reason for this broadening may be considered due to the angle of outgoing lead ions at F3. Furthermore, the distance between peak positions of neighboring charge-states gets wider as the position x becomes positive. This may imply that the focal plane at F3 is tilted or bent, which also requires the ion-optical correction by performing the particle tracking with two position-sensitive detectors. However, the analysis on the most centered peak can be considered to have the least effect from such ion-optical properties given above. In addition, in our measurement, the centered charge-state was always chosen as closely as possible to the mean charge state of the charge-state distribution after an atomic collision target. This situation helps our purpose to obtain the mean energy loss of the mean charge state of the distribution.

5.3.1 Determination of Dispersion Coefficient

The dispersion coefficient (x,δ) was deduced using the mean positions of the peaks and corresponding charge states q as follows: In the first-order expression of the ion optics, the position x measured with the TPC installed at the dispersive focal plane F3 can be given by

$$x_{\mathrm{F3}} = (x,x)x_{\mathrm{F2}} + (x,a)a_{\mathrm{F2}} + (x,\delta)\delta \quad . \tag{5.8}$$

TABLE 5.2: List of the charge-state q, position x, and the FWHM obtained from each peak of the charge-state distribution of lead ions at 100 MeV/u after penetrating through the 57.07 mg/cm^2 thick titanium target. The distance in peak positions between the neighboring charge-states becomes wider as the position x goes positive direction. The FWHM becomes wider as the peak positions gets off-centered.

q	82^+	81^+	80^+	79^+	78^+	77^+	76^+
x [mm]	-75.41	-51.63	-27.43	-3.11	21.88	47.89	74.62
FWHM [mm]	3.04	2.42	1.76	1.38	1.73	2.24	2.75

Since the first two products on the right-hand side of the equation are the constants, the first-order dispersion coefficient (x,δ) can be obtained from the slope of the relation between x position and dispersion δ. Here, the δ is defined as the relative difference of charge state q_i compared to the one $q_{x=0}$ which is deduced from the interpolation to $x = 0$ in the x-q_i plane:

$$\delta = \frac{q_i}{q_{x=0}} - 1 \quad . \tag{5.9}$$

The left panel of Figure 5.7 shows an example of the plot of the mean positions as a function of δ. The dispersion coefficient was determined for each measurement with an atomic collision target. Generally, the values were within the range from -20.5 mm/% to -19.2 mm/%, which were almost consistent with the value of the designed ion optics: -20.0 mm/%.

If the ion optics were considered with the first-order expression plus the second-order of dispersion, the position x measured with the TPC at F3 could be rewritten as

$$x_{\mathrm{F3}} = C + (x,\delta)\delta + D\delta^2 \quad , \tag{5.10}$$

where $C = (x,x)x_{\mathrm{F2}} + (x,a)a_{\mathrm{F2}}$. The coefficient D is ideally $(x,\delta\delta)$ of the ion optics matrix if $a_{\mathrm{F3}} = 0$, but here it is conventionally defined as the universal second-order dispersion coefficient with the unit of mm/%^{2}. After subtracting the linear portion of $(x,\delta)\delta$ which was obtained from Eq.5.8, the remaining shows a parabola shape as shown in the right panel of Figure 5.7. By fitting with the second-order polynomial function, the second order dispersion coefficient D was deduced. The values were about 0.2 mm/%^{2}. The remaining parameter C was in general very small to be about -0.3 mm.

In the present analysis for the momentum determination, the difference in mean positions deduced from the measurements with and without an atomic collision target was used. The ion optical expression for the difference Δx can be given as

$$\Delta x \approx (x,\delta)\delta + D\delta^2 \quad . \tag{5.11}$$

Solving for δ will give

$$\delta = -\sqrt{\frac{\Delta x}{D} + \left(\frac{(x,\delta)}{2D}\right)^2} - \frac{(x,\delta)}{2D} \quad . \tag{5.12}$$

In the present analysis, this expression of δ was replaced with the $\Delta x/(x,\delta)$ term in Eq.4.15.

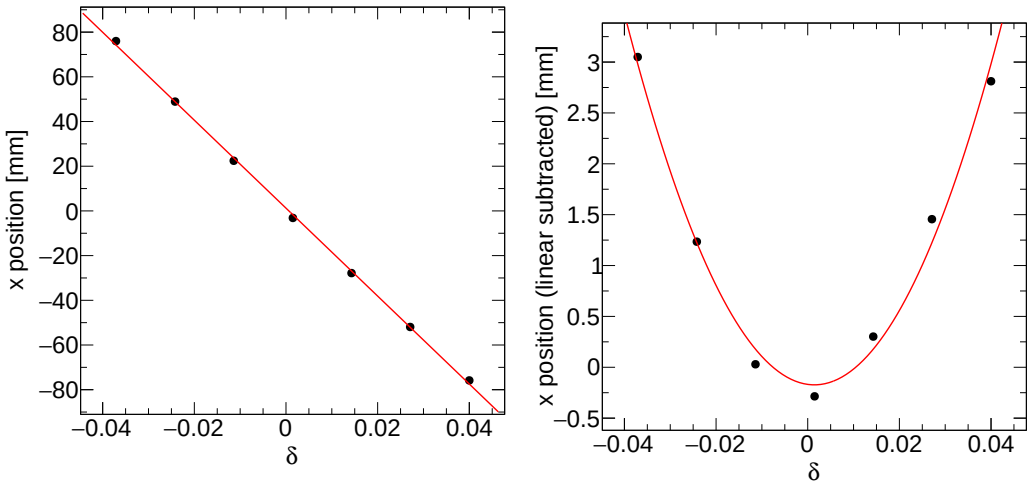

FIGURE 5.7: Determination of the dispersion coefficients at F3. The position x was fitted by a linear function of δ to get the first-order coefficient (x,δ) as shown by the red line in the left panel. The residual was fitted by the second-order polynomial function of δ to get the second order deviation D as shown by the red curve in the right panel.

5.3.2 Energy Spectrum and Determination of Mean Energy Loss

Having the dispersion coefficients, the position spectra, the background of which was subtracted, were converted to the momentum spectra by using Eq.4.15 where q_i is the centered charge state. Then, accordingly, the energy spectra were obtained by using the energy-momentum relation as

$$E_i = \sqrt{(p_i c)^2 + (m_i c^2)^2} - m_i \quad , \tag{5.13}$$

where m_i is the ionic mass of the centered charge state q_i. In this conversion process, the change in the bin width of the different histograms was taken into account. Figure 5.8 shows the energy distribution of the incident beams of lead ions at 100 MeV/u for the right peak, and the left peak shows the one after penetrating the 18.64 mg/cm^2 thick titanium target. Both peaks are truncated by the 3σ windows each in the plot. Then, the mean energies with and without an atomic collision target were determined by the statistical mean value of the peaks within the 3σ windows. For the determination of the mean energy loss $\langle \Delta E \rangle$, as we have explained, the mean energy of the centered charge-state, which was chosen as closely as possible to the mean charge state of the distribution after an atomic collision target, was taken for the following stopping-power determination.

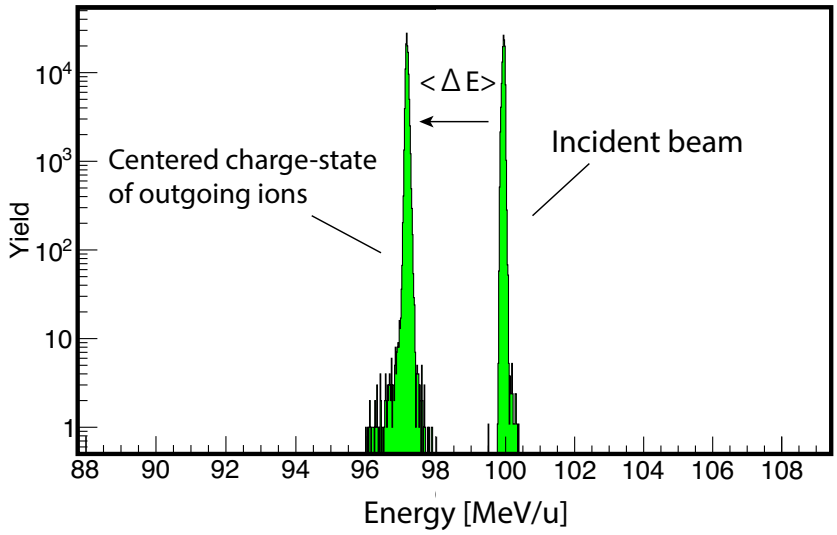

FIGURE 5.8: Energy spectra of lead ions deduced from the corresponding position spectra of the TPC31 at the dispersive focal plane F3. Right peak: Measurement of the incident beams at 100 MeV/u without an atomic collision target inserted. Left peak: The energy spectrum of the centered charge-state when the 18.64 mg/cm^2 titanium target was penetrated.

5.3.3 Energy-loss Correction for the Gas Target Windows

In the case of the gas target, the energy loss in the gas-target windows must be subtracted. In the present analysis, the mean energy loss in pure gaseous matters $\langle \Delta E \rangle_{\text{gas}}$ was deduced by subtracting the mean energy loss measured with the empty gas target cells $\langle \Delta E \rangle_{\text{window}}$ from the total mean energy loss in the gas target $\langle \Delta E \rangle$ as

$$\langle \Delta E \rangle_{\text{gas}} = \langle \Delta E \rangle - \langle \Delta E \rangle_{\text{window}} \quad . \tag{5.14}$$

Indeed, there is a slight difference between the mean energy losses in the entrance and exit windows. The effect was evaluated by the ATIMA program with the effective thickness of the windows. However, by considering that the projectile lead ions lose 30% of its incident energy in gaseous materials, it was found that such a difference became of the order of 10^{-3} or less compared to the mean energy loss in gases $\langle \Delta E \rangle_{\text{gas}}$ for both cases of the gas targets with GC and PP windows.

5.3.4 Uncertainty of the Mean Energy Loss

The statistical uncertainty in the determination of the mean energy loss is totally negligible. Below, we will mention of the systematic uncertainties associated with the determination of the mean energy loss.

Incident Momentum

The primary beam energy, provided from the SIS-18 accelerator, has an energy

spread of below 1.0×10^{-3}. Since the primary beams pass through the stripper targets at the F0 area of the FRS, the energy loss in the stripper targets are calculated by the ATIMA program. There, the uncertainties of the areal density (5%) and the stopping power calculated in the ATIMA program (2%) should be considered. The resulting uncertainty of the incident momentum p_0 was, then, determined to be (5-9) $\times 10^{-4}$ level.

The $BL_{\rm eff}$ Determination

As explained in the last section of Chapter 4, the $BL_{\rm eff}$ values are determined from the magnet current by using third-order polynomials as shown in Fig.4.21. The fluctuation in the readouts of the magnet current and voltage, i.e., the stability of the power supply during the measurements was found to be less than 10^{-5} level, which was negligible effect. The major uncertainty is in the determination of the absolute values of the magnet current and the $BL_{\rm eff}$ values by using the fitted polynomials. The maximum contribution to the systematic error was determined to be $BL_{\rm eff} \pm 0.0010$.

Reproducibility of the Magnetic Field Settings

In our measurement, we have checked the FRS reproducibility of the position spectra of the incident beams several times at the dispersive focal plane F3. The fluctuations of the measured mean positions were evaluated in the offline analysis for the data taken in the same magnet setting. It was found to be within $\pm$0.2 mm on average for all the energies. This value was included as the systematic uncertainty in the determination of mean positions of the peaks.

The resulting uncertainties in the energy loss were 1.2%, 0.6%, and 0.4% for the cases when the energy loss values were 10%, 20%, and 30% of the incident energy, respectively.

5.3.5 Stopping-Power Determination

The mean energy loss $\langle \Delta E \rangle$ was always determined with a certain target thickness x, and several measurements were performed with different thicknesses. Therefore, it can be represented as a function of the target thickness, such as shown in the lower panel of Fig.5.9. Since the stopping power is defined as

$$\frac{dE}{dx} = \lim_{\Delta x \to 0} \frac{\langle \Delta E \rangle}{\Delta x} \quad . \tag{5.15}$$

the mean energy loss depends linearly on the target thickness to a good approximation. Such a fit with a linear function, shown by the red line in the same graph, makes it easy to convert the uncertainty of the target thickness into an additional uncertainty of the energy loss. However, as shown in the upper graph where the residuals are plotted, a clear dependence on target thickness appears in the mean energy losses. This is reflected by the fact that the stopping power is energy-dependent. Therefore,

a fit function must include the non-linear term which can treat such dependence. One can try to approach by using the higher-order polynomials, but this is not an appropriate method for us because (1) the number of free parameters increases, which expands the uncertainty in the resulting stopping power, and (2) it is anyways not applicable when the number of data point is less than the one of free parameter.

However, since the energy dependence of the stopping power is well known theoretically, the best method would be to include the energy loss values predicted by a theoretical calculation as a constant contribution to the linear fit-function. In this way, one does not need to include additional free parameters, and the uncertainty in target thickness can be appropriately treated. This method can be expressed by

$$\Delta E(x) = \int_0^x \left(\frac{dE}{dx'}\right)_{\text{Theo.}} dx' + P(x) \quad , \tag{5.16}$$

where $P(x)$ is the residuals after subtracting the theoretical energy loss from the experimental one as a function of target thickness. By performing the χ^2 fit for $P(x)$ as shown in the lower panel of Fig.5.10, the experimental stopping power can be deduced by adding the dP/dx term to the theoretical stopping power:

$$\left(\frac{dE}{dx}\right)_{\text{Exp.}} = \left(\frac{dE}{dx}\right)_{\text{Theo.}} + \frac{dP}{dx} \quad . \tag{5.17}$$

Here, the same data set is taken for the analysis in Fig.5.10 as the one used in Fig.5.9, but it is clearly demonstrated that the χ^2 fit is significantly improved in this method. Then, in the present analysis, the theoretical energy loss and stopping power were calculated with the ATIMA program which adapts the Lindhard-Sørensen theory. In addition, to describe the energy dependence of the charge state in matter, the mean charge formula of Pierce and Blann from Eq.2.66

$$\bar{q} = Z_1 \left[1 - \exp\left(-0.95 \frac{v}{v_0 Z_1^{2/3}}\right)\right]$$

was implemented in the calculation, instead of the usual routine (See Appendix E for the description of the ATIMA program).

The deduced stopping powers are summarized in the Appendix B. The associated energy for the stopping power calculation was determined as the average value of the outgoing energies. In general, the stopping powers could be determined with the accuracy of (0.4-1.0)% in our experiment. The systematic uncertainty in the stopping power was found in the choice of the mean charge formula. We compared the result with the calculation in which the mean charge formula, which will be obtained in the next chapter, was used for the determination of the correction term dP/dx. The fit result of the χ^2 analysis was equivalently good. Therefore, from the difference the upper limit of the systematic error in the stopping power was determined to be 0.1%.

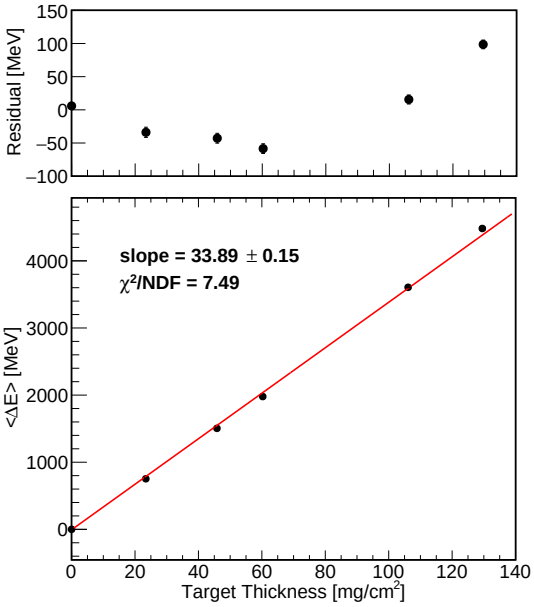

FIGURE 5.9: Lower panel: Measured mean energy loss values $\langle \Delta E \rangle$ of lead ions at 70 MeV/u after penetration of zirconium targets with different thicknesses. The red line represents a linear fit through the data. In the upper panel the residual values are plotted. It clearly demonstrates the non-linear velocity dependence of the stopping power in the measured range. The statement is also quantified by the fit results listed in the figure.

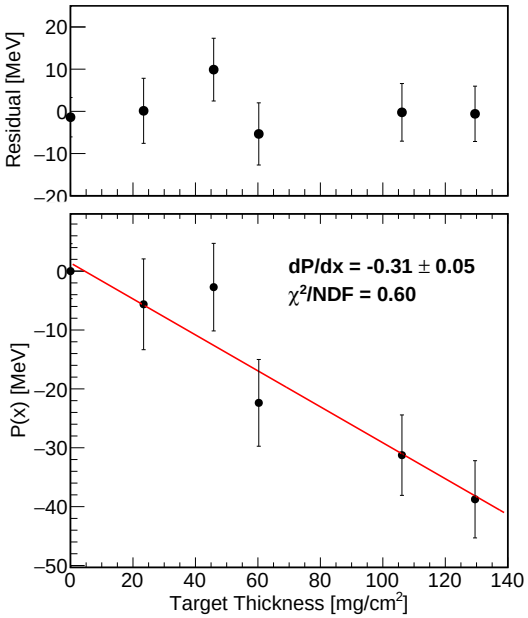

FIGURE 5.10: Lower panel: Measured deviations $P(x)$ from the theoretical stopping power values for different target thicknesses. For this example, the same projectile-target conditions are taken as presented in Fig. 5.9. The linear fit is now well suited as demonstrated with the fit results and the plotted residuals in the upper panel.

Chapter 6

Results and Discussion

6.1 Mean Charge States

The left panels of Figs.6.1 - 6.5 show our experimental results of the mean charge states of lead ions as a function of the outgoing energy. Each panel shows the comparison of the results obtained from the measurements with the gaseous and solid materials with neighboring Z_2 numbers. The results with gaseous materials are represented by the red full-circles, while the ones with solid materials are represented by the blue full-circles. As we have mentioned in Chapter 5, the statistical uncertainty is very small in general, and the error bars are under the symbol size. For the results with gaseous materials, however, the systematic uncertainty becomes significant at the low velocity domain of the present investigation, which is resulted from the estimation of the shift value Δq due to the exit window of the gas target. The solid curves correspond to the fit result to obtain the semi-empirical expression of the experimental mean charge states as a function of energy. The formula used here is as suggested in Ref.[Zie85]

$$\bar{q}(E) = Z_1 \cdot \left[1 - \exp\left(- \sum_{i=0}^{5} a_i \left(\ln(E) \right)^i \right) \right] \quad , \tag{6.1}$$

where $Z_1 = 82$, and a_i are the fit parameters, whose values were determined by the χ^2 fit and are summarized in Tab.6.1. In the ninth column of the table, the χ^2/NDF values are listed. The last column of the table corresponds to the velocity domain where the fit was performed, i.e., the valid domain of the obtained parameters.

From our experimental results, first, it was found that the gas-solid difference in the mean charge state of lead ions vanishes at the highest velocity domain ($\sim$ 280 MeV/u) in the present investigation, except for the heaviest gas-solid target pair of tin ($Z_2 = 50$) and xenon ($Z_2 = 54$). In general, at this relativistic velocity domain, the electron loss process is dominant in the charge-changing collisions; thus, the projectile ions are expected to be fully or almost fully ionized. Therefore, it is a satisfactory result to observe that the mean charge states, as well as the two fit curves, converge toward the same value (the vanishment of the gas-solid difference) at this velocity, as can be seen in the titanium ($Z_2 = 22$) and argon ($Z_2 = 18$) pair or in the carbon ($Z_2 = 6$) and nitrogen ($Z_2 = 7$) pair. Then, the contributions from the electron capture process may explain the slight difference between tin and xenon. As we have explained in Chapter

2, the cross-section of the NRC process strongly depends on the target atomic number Z_2 as [Tol+18]

$$\sigma_{\mathrm{NRC}} \propto q^5 Z_2^5 \quad , \tag{6.2}$$

and the REC also start contributing at the relativistic velocity domain through

$$\sigma_{\mathrm{REC}} \propto q^5 Z_2 \quad . \tag{6.3}$$

Since the atomic number of xenon is larger than tin, more significant contribution from electron capture, especially from the NRC process, may be expected for xenon. Therefore, slightly lower mean charge states could still be observed at this velocity.

Secondly, the mean charge states after passing through the gaseous materials become systematically lower than after passing through the solid materials at the intermediate velocity domain from 100 MeV/u down to 20 MeV/u for all the cases of the gas-solid target pairs. The deviation generally expands as the velocity decreases. The direct comparison between solid and gaseous states of the same compound material, polypropylene and propene, shows a clear deviation of the mean charge states below 100 MeV/u. This is a very positive result, which manifests the existence of the gas-solid difference in the mean charge states from our experiment. Accordingly, it strongly supports the Bohr-Lindhard model of the density effect [BL54]. Furthermore, the target pairs of zirconium ($Z_2 = 40$) and krypton ($Z_2 = 36$), or titanium ($Z_2 = 22$) and argon ($Z_2 = 18$) would support the model even more: If the collision frequency is the same in these solids and gases, the mean charge states would be smaller for solids than gases because of the strong dependence of the NRC cross-section on the Z_2 number. Another interesting characteristic is that the velocity domains where the deviations start appearing are different depending on the target pairs. For example, while the carbon-nitrogen pair seems to start deviating from about 100 MeV/u, the titanium-argon pair seems to start deviating from the higher velocity. If the Bohr-Lindhard model is correct, the same feature should be observed in the stopping power results, which we will show in the next section.

As a conclusion, the existence of the gas-solid difference in the mean charge states was confirmed in our experiment.

The right panels of the Figs.6.1-6.5 show the comparisons of the experimental mean charge states with the theory. The symbol colors are analogous to the left panels. The full circles correspond to the semi-empirical formula proposed by Pierce and Blann (P&B formula) in 1968 [PB68] as given in Eq.2.66. At the highest velocity domain in the present investigation, where the projectiles are fully or almost fully ionized, P&B formula reproduces the experimental values well. In addition, even though this formula does not depend on the target property at all, it was surprisingly found that it reproduces well (less than 5%) the experimental values for the heavy gaseous materials, such as argon, krypton, and xenon, for overall velocity domain of the present investigation. However, for nitrogen and propene, and for all the solid materials, it

always underestimates the mean charge state. The triangles correspond to the calculation by the GLOBAL program [Sch+98]. Unlike the P&B formula, it computes the rate equations based on the cross sections for charge-changing collisions. In the program, all the ions are assumed in the ground states. To deal with the density effect, an extra factor is introduced for the case of solid targets (the quasi ground state model). The calculation reproduces well the experimental mean charge states at the highest velocity domain. In addition, the deviation stays within 5% for the solid targets even at the lower velocity from 100 MeV/u down to 30 MeV/u; the latter velocity is the lower limit where the GLOBAL program is applicable. However, the deviation expands for the gaseous materials, where the calculation largely overestimates the mean charge states. This clearly demonstrates the fact that the program does not take into account properly the effect of the gas-solid difference, i.e., the effect of excited states.

TABLE 6.1: List of fit parameters obtained for the experimental mean charge formula Eq.6.1. The first and second columns show the target materials and their atomic number. From third to eighth columns are the results of fit parameters. The ninth column shows the χ^2 value divided by the degrees of freedom (NDF). The last column indicates the velocity domain, for which the experimental mean charge values were fitted, i.e., for which the fit results are applicable.

Target	Z_2	a_0	a_1	a_2	a_3	a_4	a_5	χ^2/NDF	Fitted domain
C	6	0.0019	-1.2201	0.7299	0.0965	-0.0600	0.0055	1.17	(20-300) MeV/u
N_2 (gas)	7	5.4484	0.0896	-3.1906	1.5710	-0.2654	0.0152	1.27	(20-300) MeV/u
Ar (gas)	18	0.7945	0.9601	-0.4331	0.0046	0.0294	-0.0032	0.97	(30-300) MeV/u
Ti	22	0.4288	0.1050	-0.0288	0.0800	-0.0156	0.0011	0.21	(30-300) MeV/u
Kr (gas)	36	0.7165	0.2042	-0.0100	0.0067	0.0010	0.0001	0.58	(20-300) MeV/u
Zr	40	0.9843	0.7341	-0.9115	0.4253	-0.0727	0.0045	0.03	(20-300) MeV/u
Sn	50	0.0554	-0.1093	0.2154	0.0133	-0.0082	0.0007	0.06	(30-300) MeV/u
Xe (gas)	54	0.6356	0.9582	-0.3790	-0.0044	0.0277	-0.0030	0.80	(30-300) MeV/u
$(C_3H_6)_n$		4.9731	0.3999	-3.8503	2.1142	-0.4089	0.0270	1.08	(25-300) MeV/u
C_3H_6 (gas)		1.1042	-2.0345	0.5093	0.2817	-0.0914	0.0071	1.36	(25-300) MeV/u

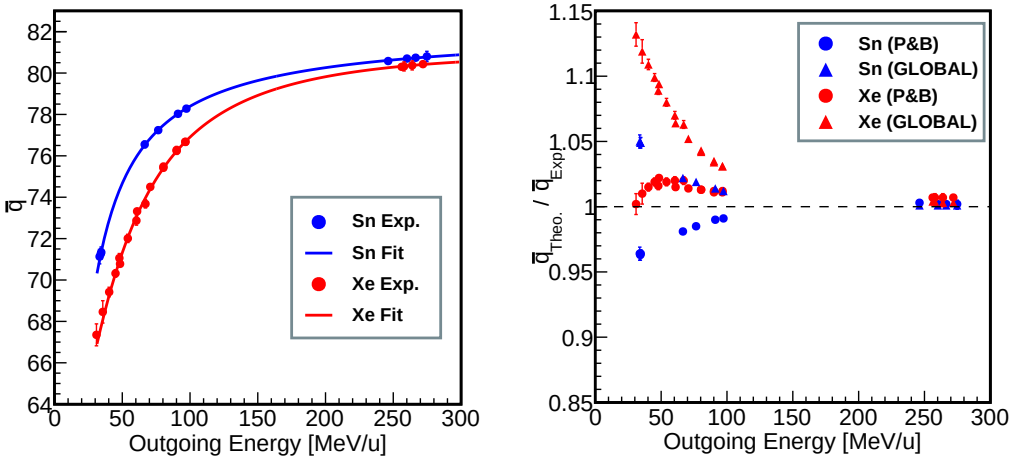

FIGURE 6.1: Measured mean charge-states of lead ions after penetrating tin ($Z_2 = 50$) and xenon ($Z_2 = 54$) targets at different incident energies. The experimental error bars are in most cases within the size of the symbols. Left panel: Measured mean charge states of lead ions after tin (blue symbols) and xenon (red symbols) targets as a function of the outgoing energy. Solid curves correspond to the fit applying the formula of Eq.6.1. Right panel: Comparison of the experimental mean charge states with the prediction of the computer program GLOBAL [Sch+98] and the semi-empirical Pierce-Blann (P&B) formula [PB68].

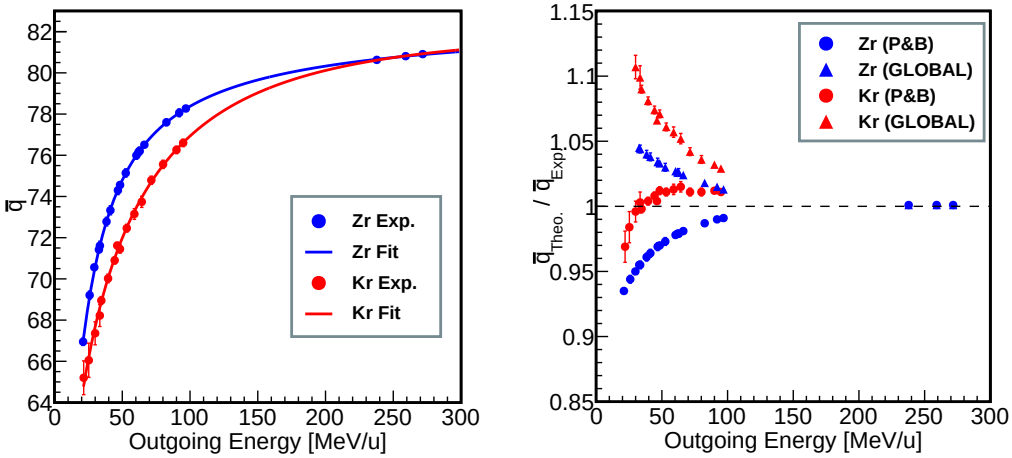

FIGURE 6.2: Measured mean charge states for lead ions in zirconium (solid) and krypton (gas) targets, otherwise the explanations are analogous as presented in Fig.6.1.

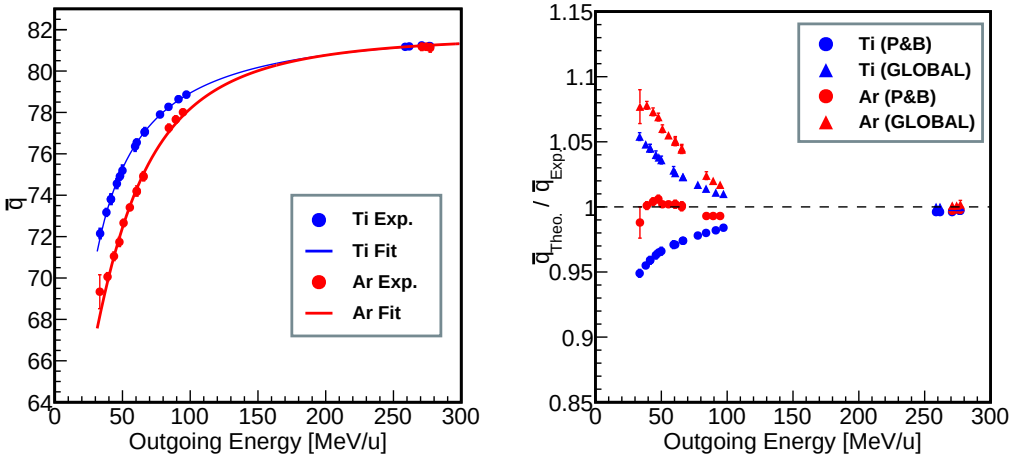

FIGURE 6.3: Measured mean charge states for lead ions in titanium (solid) and argon (gas) targets, otherwise the explanations are analogous as presented in Fig.6.1.

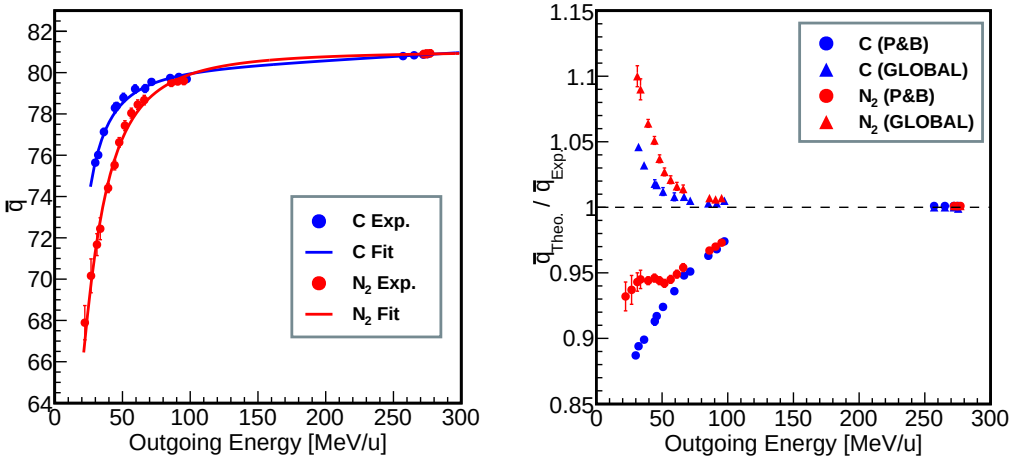

FIGURE 6.4: Measured mean charge states for lead ions in carbon (solid) and nitrogen (gas) targets, otherwise the explanations are analogous as presented in Fig.6.1.

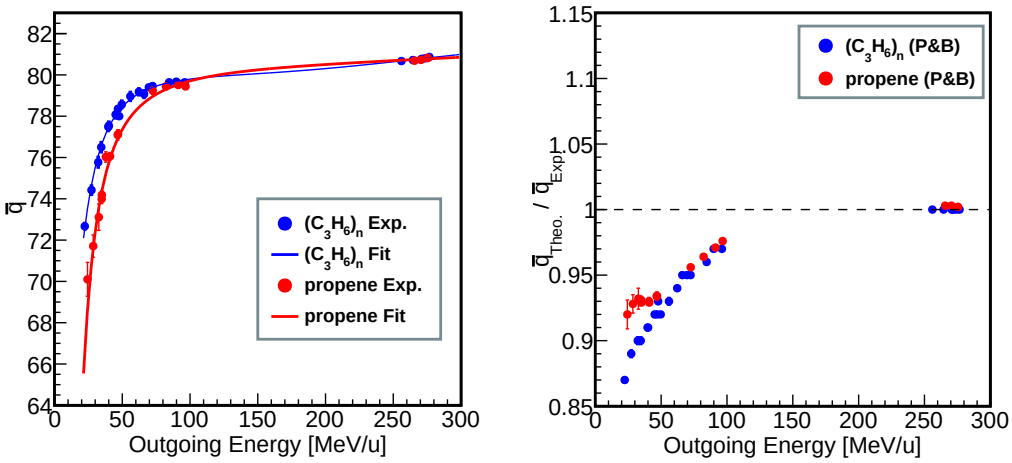

FIGURE 6.5: Measured mean charge states for lead ions in polypropylene (solid) and propene (gas) targets, otherwise the explanations are analogous as presented in Fig.6.1.

6.2 Stopping Powers

Figures 6.6-6.10 show our experimental results of stopping powers of lead ions in gases and solids with the full circle symbols as a function of energy. Similar to the graphs of the mean charge states shown before, the red color represents the gaseous materials while the blue color represents the solid materials. The error bars of the experimental data are generally under the symbol size.

First, at the highest velocity domain of the present investigation, where the projectiles are almost fully ionized, the stopping powers in gases and solids are almost the same. A slight difference was found in the tin-xenon target pair, where the stopping power in xenon gas became smaller than the one in tin, which may reflect the slight difference in the mean charge state as observed in the previous section. Then, the most important result is as follows: It has been systematically observed for all the target pairs that the stopping powers in gases are smaller than the ones in solids. Furthermore, the deviation becomes more significant as the velocity decreases. This feature can be explicitly seen in Fig.6.11, which shows the experimental stopping powers for different target Z_2 numbers at interpolated energies of 45 and 65 MeV/u. These direct comparisons of the stopping powers between neighboring solids and gases is already a good indication of the gas-solid difference. However, we will be more specific for the representation in the next section on this subject.

Besides, in the same graphs of Figs.6.6-6.10, the theoretical calculations by the ATIMA program [Wei98a], which takes into account the Lindhard-Sørensen (LS-) theory [LS96], are also shown. The dashed curves correspond to the calculation, in which the projectile's atomic number Z_1 is used for the charge-state description in matter. The solid curves, then, correspond to the calculation, in which the mean charge-state formula Eq.6.1 with the parameters obtained in the previous section is used instead.

The latter calculation is limited in the velocity domain in between the masked area because of the applicable limits of the mean charge formula. Also, note that the carbon-hydrogen compounds were calculated by adopting Bragg's additivity rule. As one can see, the calculation by the ATIMA program with the projectile's nuclear charge deviates completely from the experimental stopping powers in the domain, at least lower than 100 MeV/u, where many charge states start populating. Moreover, the predictions for gases and solids almost coincide. In contrast, when the realistic charge state Eq.6.1 is implemented in the calculation, the experimental stopping powers are reproduced very well. These calculations manifest the importance of describing the effective charge state of projectiles inside matter.

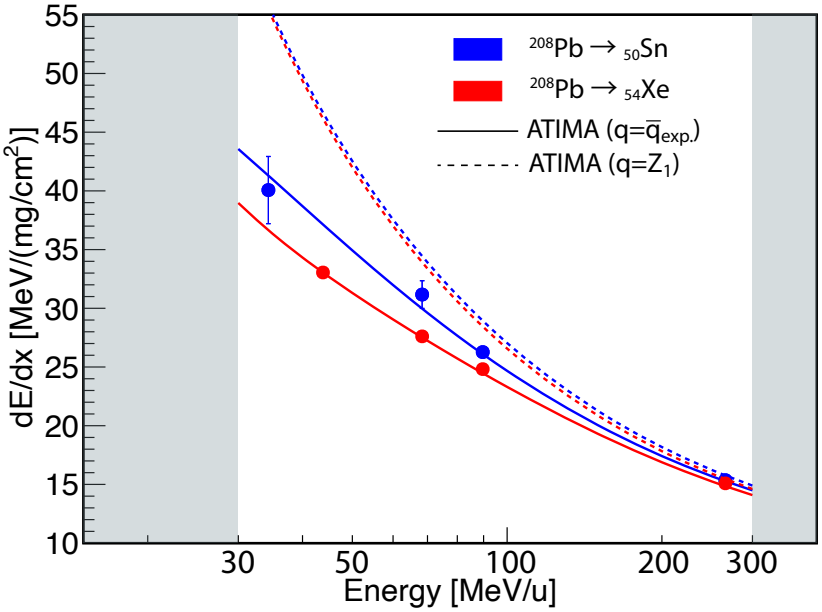

FIGURE 6.6: Experimental stopping powers of lead ions in tin ($Z_2 = 50$) and xenon ($Z_2 = 54$) targets as a function of projectile energy. The experimental error bars are within the size of the symbols, except for one tin value. The results for the solid target is presented by blue symbols and lines and the corresponding results for the gas target by red color. Solid curves correspond to the stopping powers calculated by the ATIMA program, which takes into account the Lindhard-Sørensen theory, combined with our experimental mean charge states $q = \bar{q}_{\mathrm{exp.}}$ from the previous section. The dashed curves correspond to the stopping powers calculated by the same theory but with the assumption of bare projectiles $q = Z_1$.

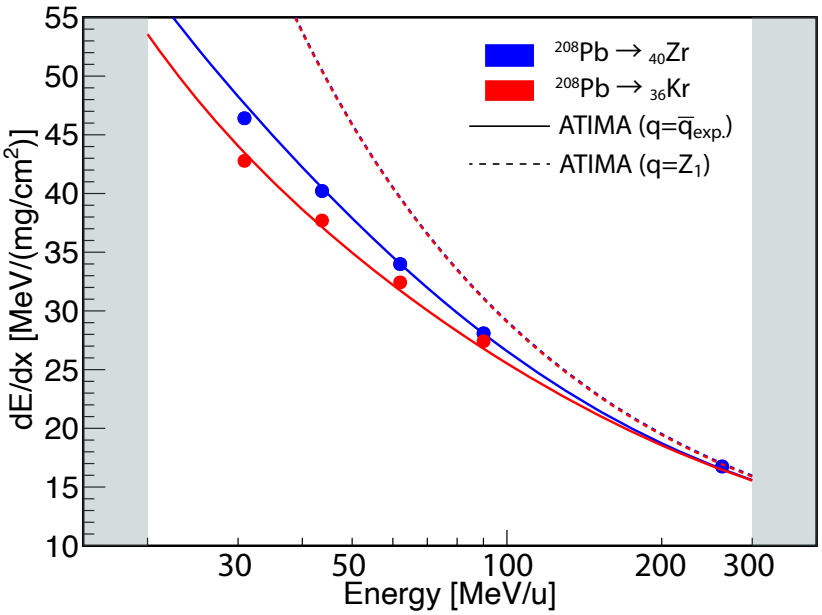

FIGURE 6.7: Measured stopping power values of lead ions in zirconium ($Z_2 = 40$) and krypton ($Z_2 = 36$) targets compared with theoretical predictions. The experimental error bars are within the size of the symbols. The explanations given in the caption of Fig.6.6 are valid.

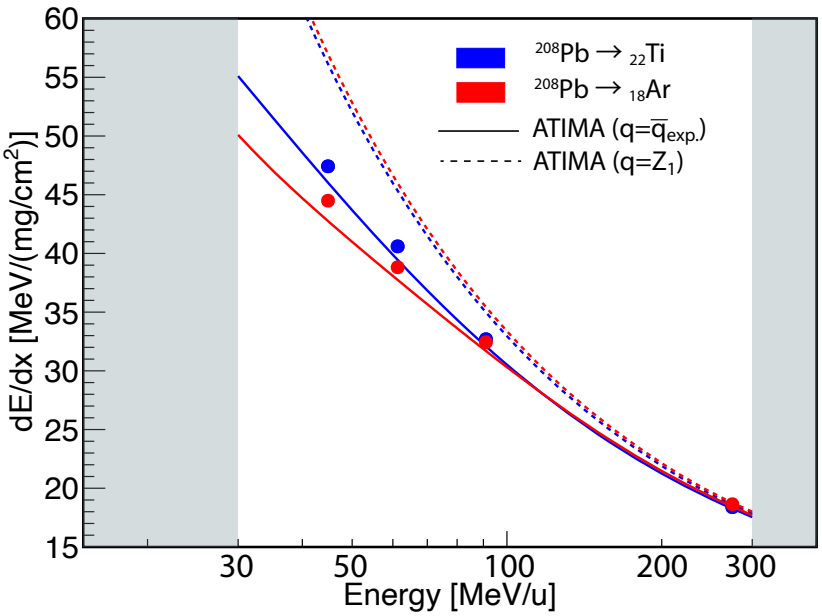

FIGURE 6.8: Measured stopping power values of lead ions in titanium ($Z_2 = 22$) and argon ($Z_2 = 18$) targets compared with theoretical predictions. The experimental error bars are within the size of the symbols. The explanations given in the caption of Fig.6.6 are valid.

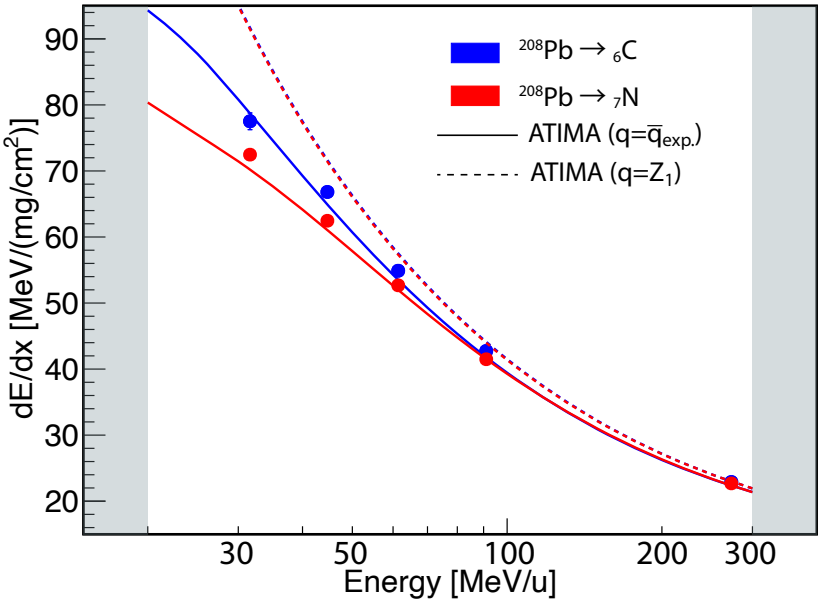

FIGURE 6.9: Measured stopping power values of lead ions in carbon ($Z_2 = 6$) and nitrogen ($Z_2 = 7$) targets compared with theoretical predictions. The experimental error bars are within the size of the symbols. The explanations given in the caption of Fig.6.6 are valid.

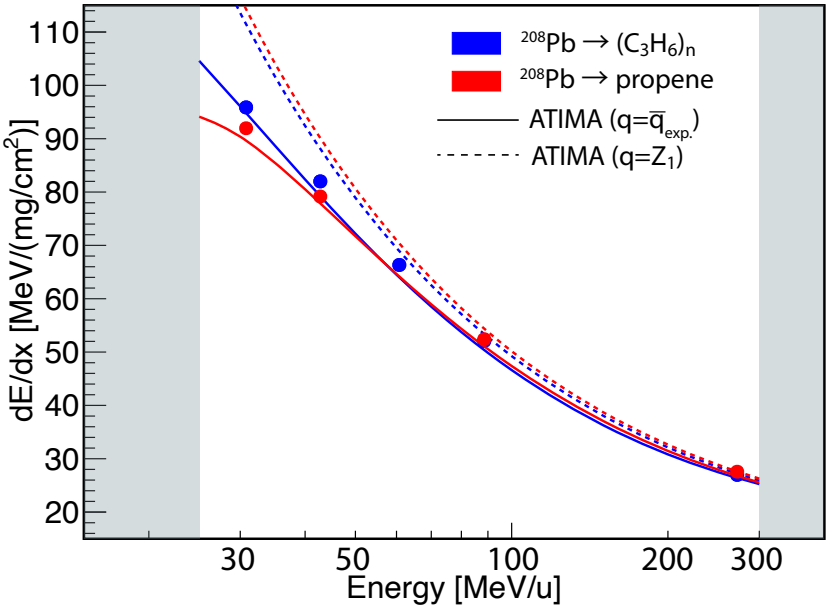

FIGURE 6.10: Measured stopping power values of lead ions in polypropylene and propene targets compared with theoretical predictions. The experimental error bars are within the size of the symbols. The explanations given in the caption of Fig.6.6 are valid. The calculation were performed by applying Bragg's additivity rule.

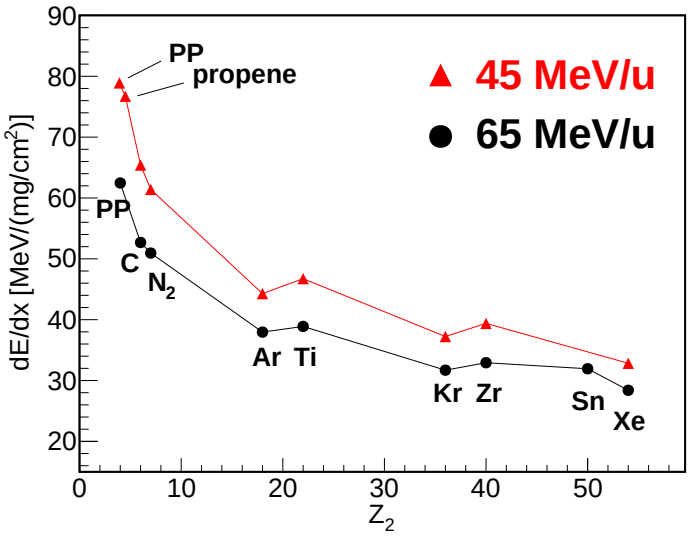

FIGURE 6.11: Experimental stopping powers of lead ions for different Z_2 targets. The target Z_2 numbers for the polypropylene and propene are approximated to be 4 and 4.5. One can see that the difference in stopping powers between solid and gas becomes more significant as the energy decreases.

Figures 6.12 - 6.16 show the comparisons of our experimental stopping powers either with the theoretical calculations or with the famous computer programs, as a function of the projectile energy. The left and right panels correspond to the comparisons of the stopping powers in solid and gaseous materials, respectively. The comparison is given by

$$\text{Ratio} := \left(\frac{\left(\frac{dE}{dx}\right)_{\text{theo.}}}{\left(\frac{dE}{dx}\right)_{\text{exp.}}} - 1 \right) \times 100 \quad [\%] \quad . \tag{6.4}$$

The theoretical calculations for the top two panels are performed by the SRIM [Zie+10] (triangle) and the DPASS [SS19] (cross mark) programs. In the third panels, the calculation by the ATIMA program (version 1.4) [Wei98a] is shown with the open circle symbols. The ATIMA program adopts the LS-theory [LS96] for the prediction of stopping powers, and it includes the routine, which provides the predictions of the projectile mean charge states in matter by the GLOBAL program [Sch+98] with some corrections (see Appendix E for the description of the ATIMA program). Meanwhile, in the same panels, the full circle symbols correspond to the calculation by the ATIMA program, but the charge state prediction is fully replaced by the mean charge-state formula Eq.6.1 with the parameters obtained in the previous section instead. In the fourth panel for the solid materials, the comparison with the Hubert tabulation [HBG90] is shown with the square symbols. The error bars on the ratio are generally invisible because they are under the symbol size.

We first consider the results for the solid targets. In general, the computer programs can reproduce the stopping powers in solid nicely, especially in carbon within

the accuracy of 10% for overall velocity domain of the present investigation. Large deviations ($\sim$ 20%) are found with the predictions by the DPASS program for the heavier solid targets. This is probably because that the present calculation by DPASS adopts the equilibrium charge state, which is calculated with the simple Thomas-Fermi-type formula [SS19]

$$\bar{q} = Z_1 \left(1 - \exp\left(-\frac{v}{v_0 Z^{2/3}}\right)\right) \quad . \tag{6.5}$$

In the formula, the target dependence is neglected, and the mean charge state is usually overestimated. An investigation of the DPASS program calculation by adopting a more realistic effective charge state would be recommended. A surprising result was found in the comparisons with the Hubert table, where the deviations are less than 10% for all the solid targets. The calculation uses the stopping powers of alpha particles in the scaling formula Eq.2.63 with the effective charge concept, and the stopping powers of heavy ions were tabulated according to the deduced parametrization in 1990 [HBG90]. In principle, the stopping numbers L of alpha particles and heavy ions differ significantly; while the former may be described well by the Bethe formula, the latter requires non-linear correction terms which depend on both projectile and target properties, as we have explained in Chapter 2. Thus, it is not easy to have a general form of stopping power only with the effective charge parametrization. However, the good predictions may have become possible due to the (almost) vanishment of the correction terms in the velocity domain of the present investigation according to Fig. 2.2. In the case of the stopping of lead ions in aluminum, the significant correction terms in the range of $0.03 \leq \gamma - 1 \leq 0.3$, which corresponds to our experiment, would be only the Mott and Bloch correction terms, the sum of which would show a smooth curve. Especially since both correction terms depend mostly only on the projectile property, it would be a preferable situation for the parametrization of stopping powers as Hubert *et al.* performed. Similarly, the SRIM program developed by Ziegler, which also takes the parametrization method by scaling the proton's stopping powers to the numerous experimental stopping powers of heavy ions, shows fine agreements to the experimental data. Then, the best agreements are found in the comparison with the ATIMA program. The ATIMA 1.4 adopts the routine for predicting the projectile's mean charge state based on the GLOBAL program with some corrections. Since the calculation results from the routine shows a great agreement with our experimental mean charge state for solids, where the maximum deviation was found to be about 2% for carbon in the present velocity domain, the resulting stopping-power prediction also showed great agreements to the experimental values. Meanwhile, when adopting the mean charge formula Eq.6.1 in the ATIMA program, the agreements are somewhat improved.

Next, we consider the results for the gaseous materials. In general, all the computer programs (SRIM, DPASS, and ATIMA) deviate largely from the experimental values. Especially, the calculations by DPASS, which adopts the Thomas-Fermi type formula Eq.6.5 for describing the equilibrium charge state, overestimate the stopping powers about 20% on average. Also, even though there are coincidence points for the SRIM

calculation with the experimental data, it should not be regarded as the reproducibility of the program. However, it is more likely just a crossing point between two curves with largely different slopes. The ATIMA 1.4 program also overestimates the stopping powers. This is due to, in the first place, the GLOBAL program does not take into account the gas-solid difference for the predictions of mean charge state, as one can see in Figs. 6.1-6.4, where it always overestimates the mean charge state at the low velocity region. Furthermore, since the correction terms to the GLOBAL program were determined from the fit to the experimental mean charge states of heavy ions after solid targets, the routine, which is implemented in ATIMA 1.4, does not provide a good estimation for gas. Then, the importance of the prediction of mean charge states inside matter becomes more explicit in the comparison with the ATIMA program when it adopts the mean charge formula obtained from our experiment. The slight deviation is stable for overall velocity domain ($\sim$ 2% in average for all the gaseous target). Therefore, theoretical developments for the charge-changing processes in matter are required to achieve better accuracy in the predictions of stopping power.

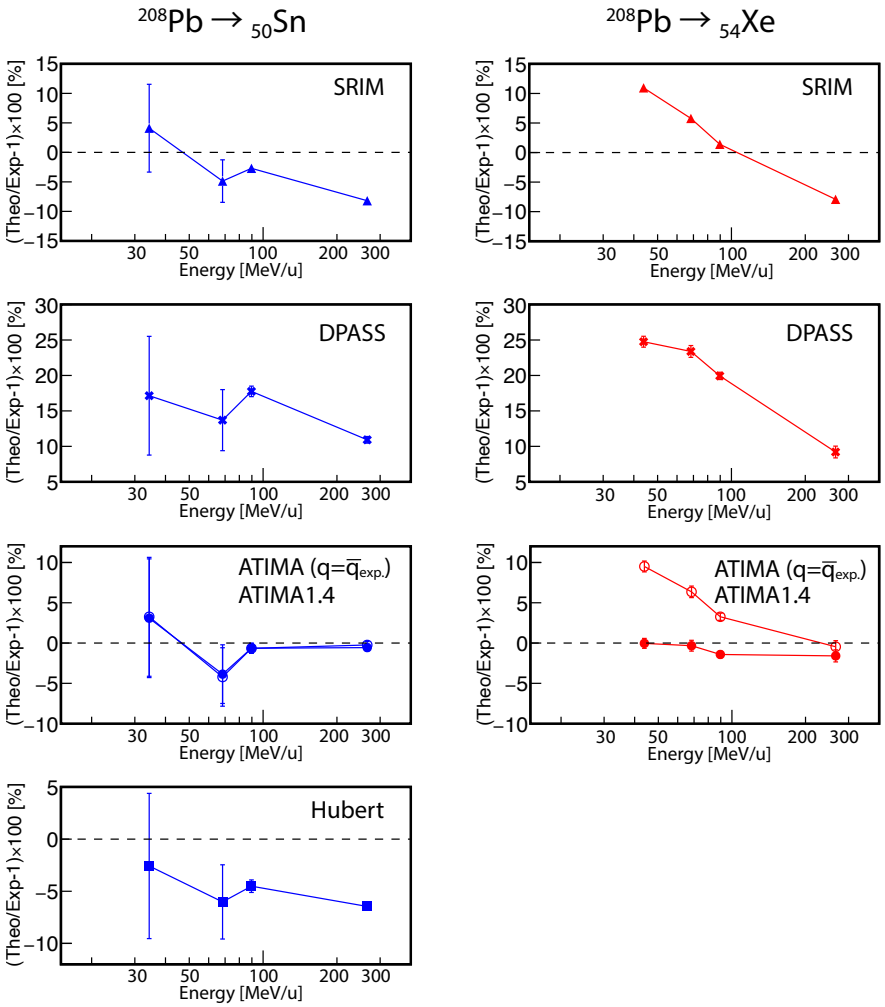

FIGURE 6.12: Comparison of theoretical and experimental stopping power values of lead ions in tin (solid) and xenon (gas) targets at different energies. The results for the solid target is indicated by the blue color in the left panels, and results for the gas target by red color in the right panels. The top three panels present the comparison with SRIM [Zie+10] (triangle), DPASS [SS19] (cross mark), and ATIMA 1.4 [Wei98a] (open circle). For solid targets, the comparison with the Hubert tabulation (filled square) is shown in the fourth panel. The Hubert tables do not include gases. In addition in the third panel, the comparison with the calculation by the ATIMA program, in which our measured mean charge states implemented instead, is shown by the full circle symbol. Note that, partially the symbols in the ATIMA comparison overlap.

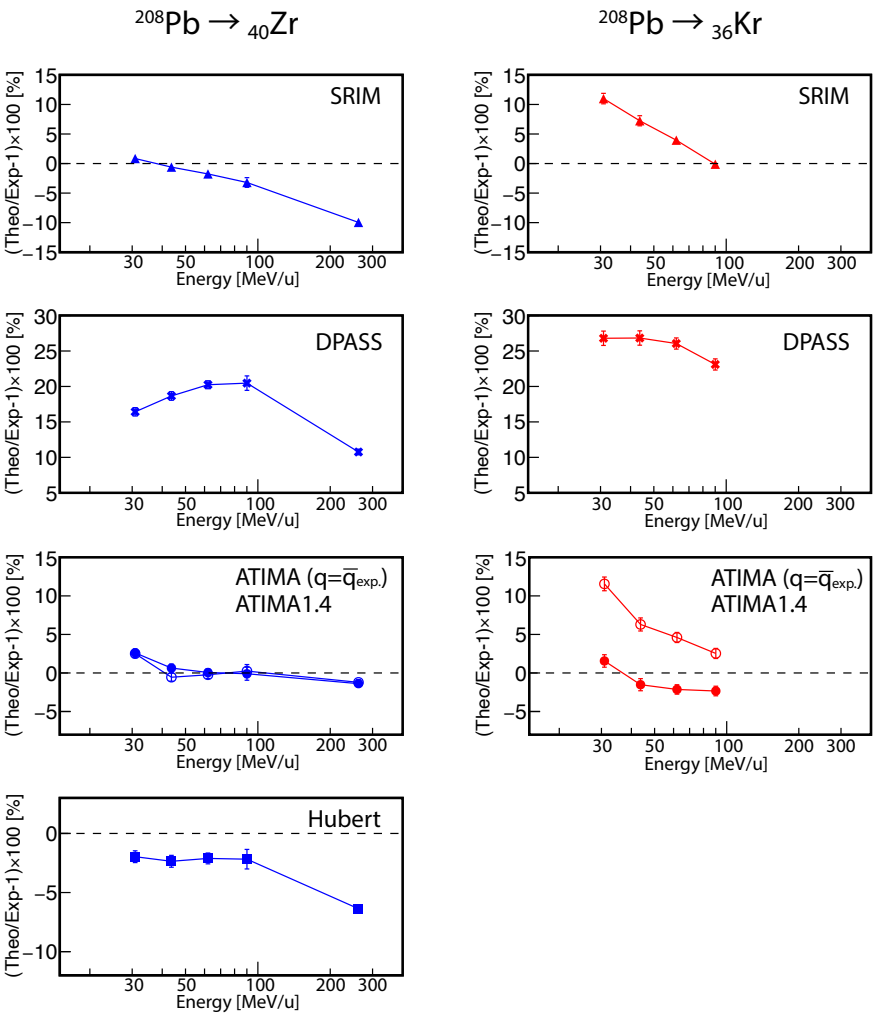

FIGURE 6.13: Comparison of theoretical and experimental stopping power values of lead ions in zirconium (solid) and krypton (gas) targets at different energies. The explanations of Fig.6.12 are applicable.

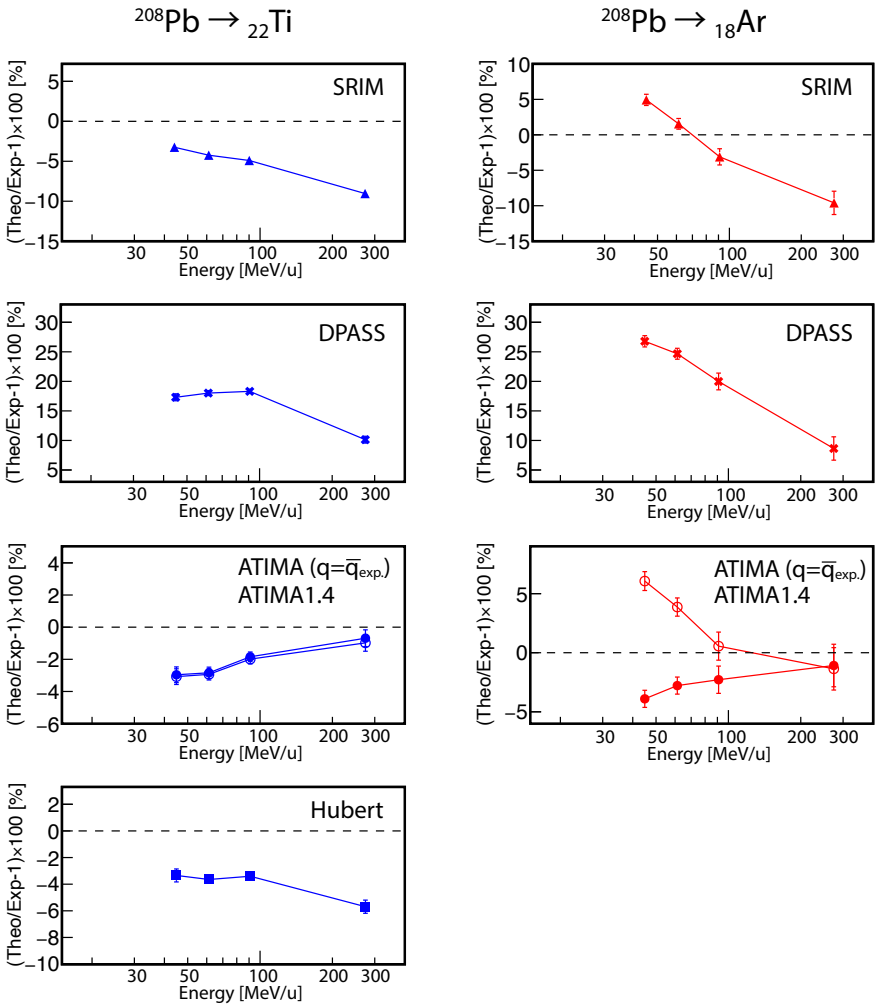

FIGURE 6.14: Comparisons of theoretical and experimental stopping power values of lead ions in in titanium ($Z_2 = 22$) and argon ($Z_2 = 18$) targets at different energies.The explanations of Fig.6.12 are applicable.

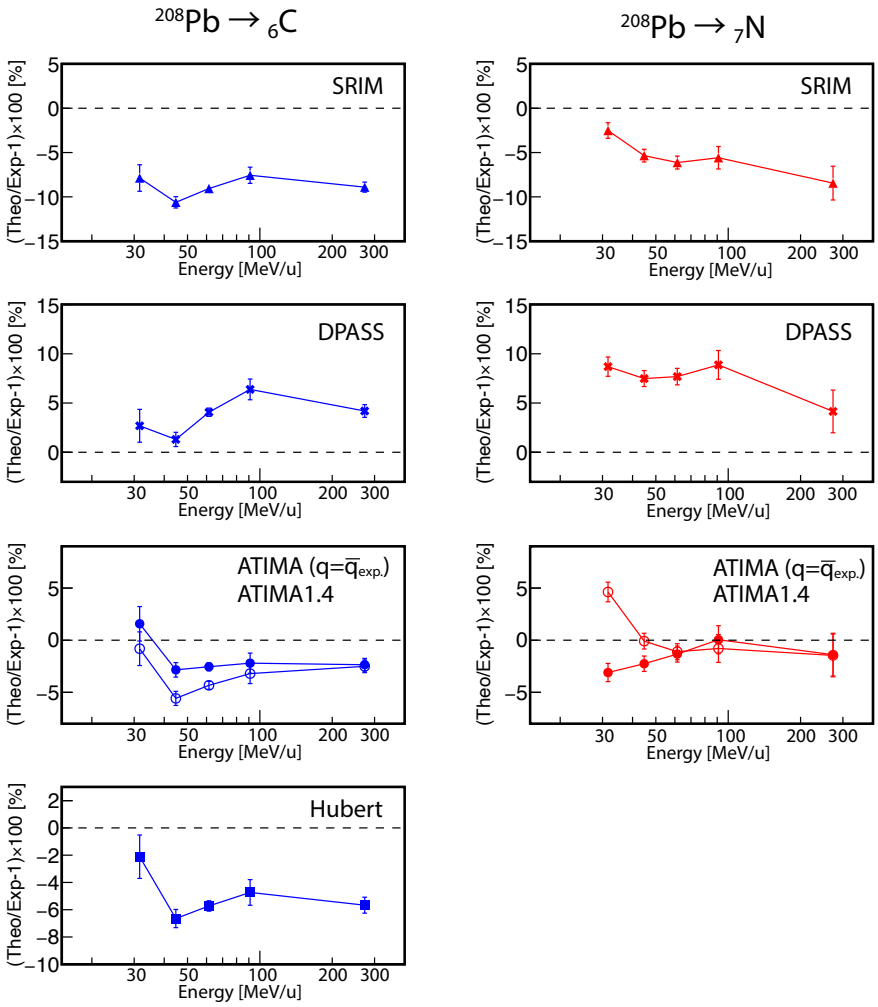

FIGURE 6.15: Comparisons of theoretical and experimental stopping power values of lead ions in carbon (solid) and nitrogen (gas) targets at different energies.The explanations of Fig.6.12 are applicable.

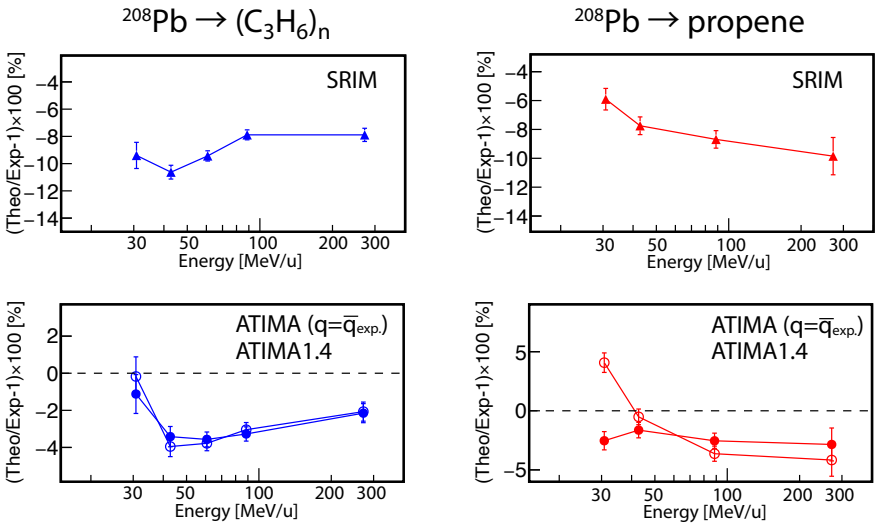

FIGURE 6.16: Comparison of theoretical and experimental stopping power values of lead ions in polypropylene (solid) and propene (gas) at different energies. However, the top two panels correspond to the comparison with the SRIM code (triangle) and the ATIMA code (open circle), respectively. Same as Fig.6.12, in the second panels the comparison was also performed with the calculation by the ATIMA program with the mean charge formula which was obtained from this work.

6.3 The Gas-Solid Difference

This section will present the gas-solid difference in the stopping-powers for the last discussion of our experimental results. The concept of this difference originates from the prediction by Bohr and Lindhard in 1954, stating that the difference in the collision frequency in gases and solids should result in the difference in the effective charge state in matter and accordingly in the difference in the stopping powers [BL54].

For the quantification of the gas-solid difference between different target materials with neighboring Z_2 numbers, it is recommended to normalize the properties of target materials, such as the mass, charge, and mean excitation potentials, given in the theoretical description of the stopping powers. Therefore, the experimental stopping powers were normalized by the stopping powers calculated by the ATIMA program, which adopts the projectile's nuclear charge charge Z_1 for the charge-state description as

$$\left(\frac{dE}{dx}\right)_{\text{norm.}} = \frac{\left(\frac{dE}{dx}\right)_{\text{Exp.}}}{\left(\frac{dE}{dx}\right)_{\text{ATIMA}(q=Z_1)}} \quad , \tag{6.6}$$

and the gas-solid difference is then defined by the relative difference as

$$\text{Gas} - \text{Solid Difference} := \left(\frac{\left(\frac{dE}{dx}\right)^{\text{solid}}_{\text{norm.}}}{\left(\frac{dE}{dx}\right)^{\text{gas}}_{\text{norm.}}} - 1 \right) \times 100 \quad \% \tag{6.7}$$

Figures 6.17-6.21 show the deduced gas-solid difference in the normalized stopping powers as a function of energy. One can clearly see that the difference systematically increases as the velocity decreases in all the gas-solid target pairs. At the highest velocity (280 MeV/u), then, the difference vanishes. These observations are consistent with the results of the experimental mean charge state. Therefore, the Bohr-Lindhard prediction on the density effect is confirmed with our experiment. Especially, the direct comparison between solid and gaseous states of the same compound material, polypropylene and propene, shows analogous trend as the one of the mean charge states; the gas-solid difference in stopping power appears below 100 MeV/u, where the gas-solid difference in mean charge state started appearing, as shown before.

In conclusion, we have confirmed the existence of the Bohr-Lindhard density effect in stopping powers. In addition, we emphasize here that we have extended the velocity domain where the experimental data of stopping powers were scarce, for a wide variety of Z_2 numbers.

Then, the interpretation of the magnitude of the gas-solid difference depending on Z_2 numbers can be considered as follows: Based on the comparisons of mean charge state and stopping powers, as shown so far, the best representation of stopping power can be given by

$$\frac{dE}{dx} = C \frac{Z_2}{A_2} \frac{\bar{q}^2}{\beta^2} \cdot L(\bar{q}) \quad , \tag{6.8}$$

where C is a constant, Z_2 and A_2 are the atomic and mass numbers of target material, $\bar{q}$ is the mean charge state of the projectile, and L is the stopping number with the mean charge implemented in. In this representation, the contributions to the gas-solid difference in stopping powers are clearly either from the square of the mean charge state $\bar{q}^2$ or the stopping number L. To demonstrate which is the major contribution, we employ the theoretical calculations for each component. The mean charge state formula Eq.6.1 with the parameters obtained from our experiment is used for the evaluation of the gas-solid difference in $\bar{q}^2$, and the calculation with the ATIMA program is used for the evaluation of the one in stopping number L. For the details of the calculation of the stopping number L in the ATIMA program, see Appendix E. The solid curves in the left panel of Fig.6.22 show the theoretical gas-solid difference for the $\bar{q}^2$ component. The full-circle symbols just indicate the points of energy at which the experimental gas-solid difference in stopping powers was deduced, corresponding to Figs.6.17-6.21. The solid curves are truncated by the limit of the validity of the mean charge state formula. Then, the right panel of Fig.6.22 shows the gas-solid difference

in the normalized stopping numbers defined as

$$L_{\text{norm.}} = \frac{L\left(\bar{q}_{exp.}\right)}{L\left(Z_1\right)} \quad , \tag{6.9}$$

where the denominator is the stopping number calculated by the ATIMA program with $\bar{q} \rightarrow Z_1$. The truncation of solid curves is analogous to the left panel. As one can see, the $\bar{q}^2$ component is the major factor to the gas-solid difference in stopping powers. The difference in $\bar{q}^2$ becomes more significant for the carbon-nitrogen pair than other heavy target pairs at the lowest velocity domain, while the situation is opposite at the higher velocities. This would be an explanation to the observed gas-solid difference in stopping powers for carbon-nitrogen pair is more significant than, e.g., for zirconium-krypton pair at the lowest velocity domain. More detailed interpretations are very complicated because it requires precise knowledge of the individual charge-changing processes for different materials. However, the following assumptions may be stated here: The magnitude of the gas-solid difference can be affected strongly by the electron capture processes. For example, since xenon has a larger Z_2 number than tin, more electron capture can occur from the perspective of, e.g., the NRC process whose cross-section is strongly dependent on the target atomic number via Z_2^5. Thus, the lower effective charge is expected in xenon. As a result, the gas-solid difference in stopping powers may be enhanced for this target pair, as one can see in Fig.6.17. This is a similar case for the carbon-nitrogen pair. Meanwhile, since krypton has a smaller Z_2 number than zirconium, the contribution of electron capture can be less. As a result, the gas-solid difference in mean charge states, and correspondingly in stopping powers may be reduced for this target pair, as one can see in Fig.6.18, where the magnitude of the difference is not so different from the lighter gas-solid target pair, e.g., of carbon and nitrogen. Therefore, theoretical developments in the description of charge-changing processes are desired to quantify the origin of the gas-solid difference in the charge state to the stopping power predictions.

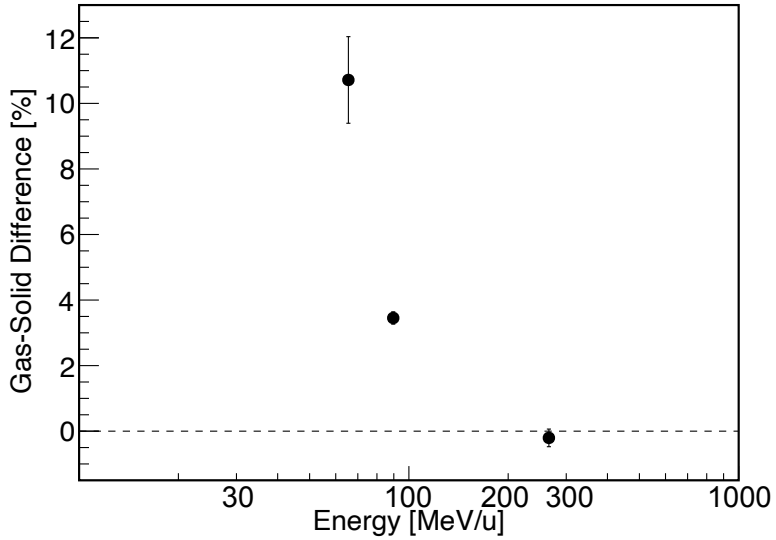

FIGURE 6.17: Measured gas-solid difference of stopping powers in tin ($Z_2 = 50$) and xenon ($Z_2 = 54$) targets at different energies.

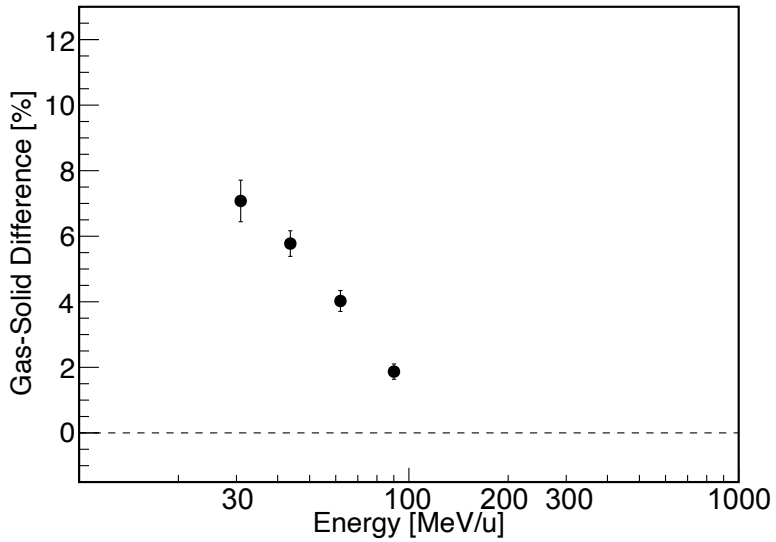

FIGURE 6.18: Measured gas-solid difference of stopping powers in zirconium ($Z_2 = 40$) and krypton ($Z_2 = 36$) targets at different energies.

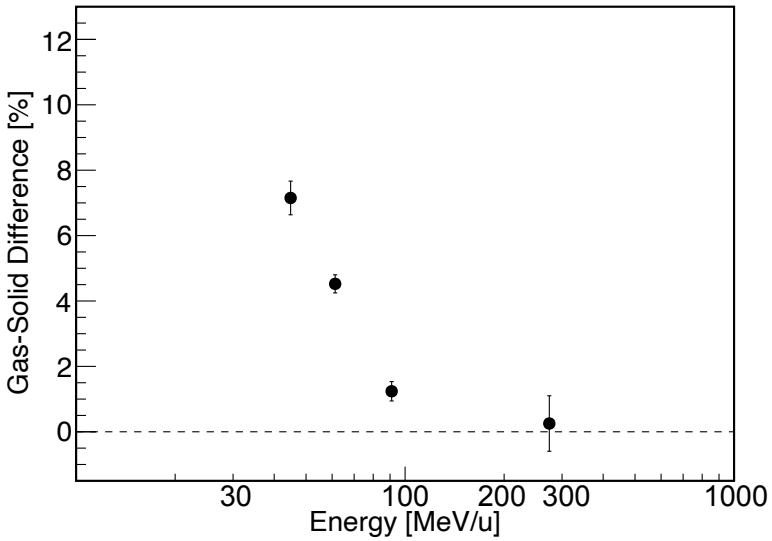

FIGURE 6.19: Measured gas-solid difference of stopping powers in titanium ($Z_2 = 22$) and argon ($Z_2 = 18$) targets at different energies.

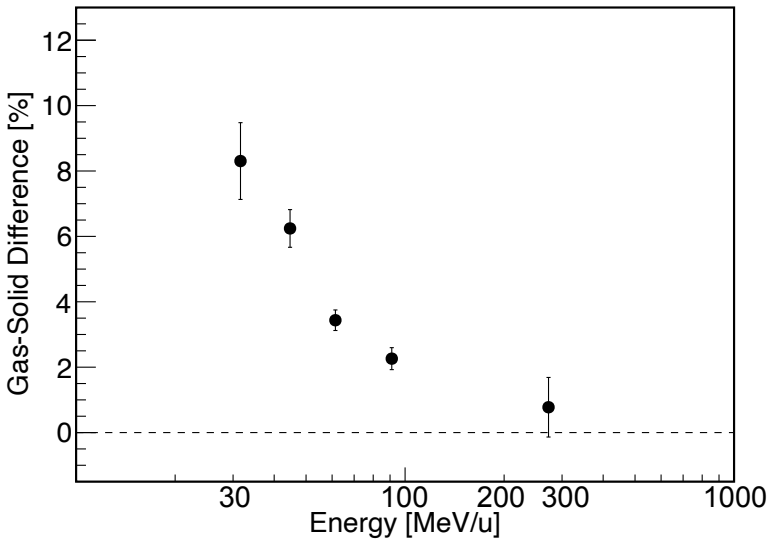

FIGURE 6.20: Measured gas-solid difference of stopping powers in carbon ($Z_2 = 6$) and nitrogen ($Z_2 = 7$) targets at different energies.

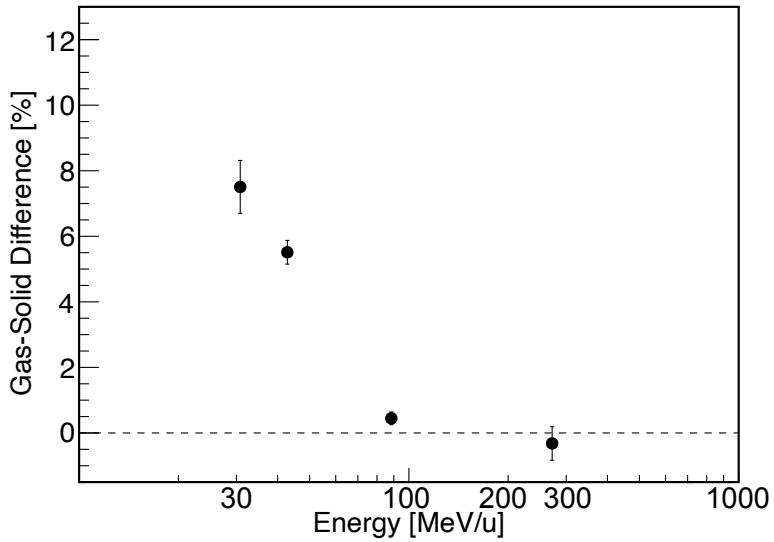

FIGURE 6.21: Measured gas-solid difference of stopping powers in polypropylene and propene compound targets at different energies.

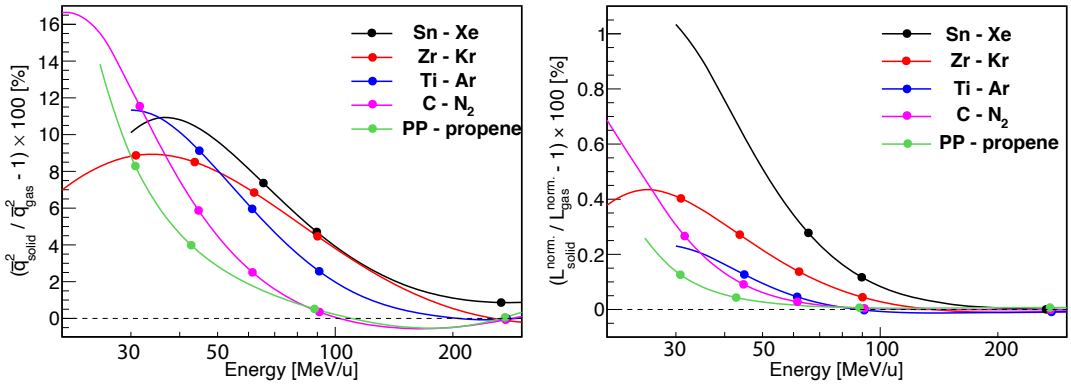

FIGURE 6.22: The gas-solid difference of the squared mean charge states (left panel) and the normalized stopping numbers $L^{\text{norm.}} = L(\bar{q}_{\text{exp.}})/L(Z_1)$ (right panel). The solid curves correspond to the theoretical calculations, and they are truncated by the limit of the validity of the formula Eq.6.1. The full-circle symbols indicate the energy data from which the experimental gas-solid difference of stopping powers was deduced, corresponding to Figs.6.17-6.21. Left: Each calculation of $\bar{q}$ was performed by the formula Eq.6.1 with obtained parameters. Right: Each stopping number was calculated by the ATIMA program with adopting either the mean charge state formula Eq.6.1 with obtained parameters, or projectile's nuclear charge Z_1. One can see that the charge-state difference is the major factor to the Bohr-Lindhard density effect of heavy ion stopping powers.

6.4 Direct Conclusions

With our experimental results, we have manifested that the ionic charge state inside matter is essential for the understanding of stopping powers of heavy ions in matter. The knowledge of charge-changing cross sections for heavy projectiles in the ground

and excited states is needed to understand the atomic ion-matter interaction, which is a longstanding problem since the discovery of nuclear fission, almost 90 years ago. The theories of multi-body charge-changing and energy dissipation processes have not been accurately solved up to now. Therefore, semi-empirical scaling methods are used to support applications of heavy ions penetrating matter. Our accurate results of the charge-state fractions, mean charge states, and stopping powers can be used as a benchmark for new theoretical developments.

In addition, since accurate *ab-initio* calculations are not on the horizon, I would propose, as an intermediate solution, to deduce a universal function of the mean charge states for different projectile and target combinations, such as for a development of fast and user-friendly programs for stopping power prediction. In the present thesis, we have demonstrated that even a simple form of mean charge state, e.g., Eq.6.1 can provide a significant improvement of the stopping power predictions. For deriving a better parametrization, the experimental data must be extended, especially for gaseous materials. Considering the situation of scarce experimental data as shown in Figure 3.1, the proposed measurements of the present research with other heavy projectiles, such as xenon and uranium, should be conducted.

Concerning the stopping number L, our results can provide a guide to the theoretical developments in the following way: Our experimental stopping powers could be reproduced nicely by the ATIMA program when it employed the mean charge state formula Eq.6.1 with the obtained experimental parameters. Therefore, the individual normalized stopping number $L^{\mathrm{norm.}}$, given in Eq.6.9, can be a good reference for considering the difference in stopping numbers between the bare and dressed projectiles. Such a difference may include, e.g., the polarization effect due to the screening of the projectiles. The left and right panels of Fig.6.23 show the deviation of the stopping number for solid and gaseous materials, respectively. The truncation of the solid curves is analogous to Fig.6.22. The deviation systematically becomes more significant for larger Z_2 target materials and for lower energies. Furthermore, the difference is slightly more significant for gaseous materials than for the neighboring solid materials. The overall deviation may stay within only -6% in stopping numbers in the velocity domain of the present investigation, thus the theoretical developments will be very sensitive.

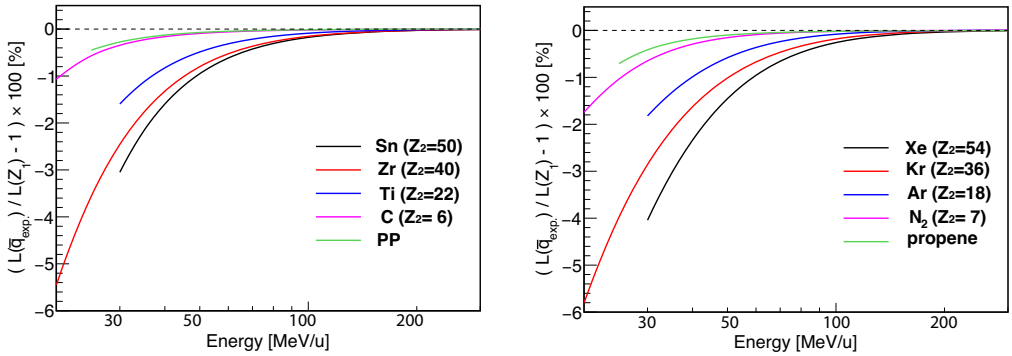

FIGURE 6.23: Difference in stopping number L of solid (left panel) and gaseous (right panel) materials between the bare and dressed projectile ions. The calculation was performed with the ATIMA program. One can see that the difference becomes more significant as the Z_2 increases and as the energy decreases. Furthermore, the difference is slightly more significant for gases than the neighboring solid materials.

Chapter 7

Summary and Outlook

We performed accurate measurements of charge-state distributions and stopping powers of ^{208}Pb ions in gases and solids at (35, 50, 70, 100, and 280) MeV/u incident energies. Five different gaseous (nitrogen, argon, krypton, xenon, and propene) target materials and five different solid (carbon, titanium, zirconium, tin, and polypropylene) target materials of different thicknesses were used in this experiment. The heavy-ion synchrotron SIS-18 provided the incident lead projectiles at different energies with a relative energy spread of less than 5×10^{-4}. The beam intensity was reduced to a few thousand particles provided in pulses of 10 seconds duration. With these low-intensity beams, any significant radiation damage to the targets and effects on the particle detector performance could thus be avoided. For the measurements of energy loss and charge-state distributions, the FRS was used as a high-resolution magnetic spectrometer. The atomic collision targets were placed at the central focal plane F2, and the emerging ions were detected at the third dispersive focal plane F3 with a time projection chamber.

We succeeded in measuring the energy loss and charge-state distributions at almost 800 field settings of the FRS. The measured stopping powers and mean charge states could be determined with an accuracy of less than 1% for most of the cases. The selected energy range provided partially ionized and almost bare projectiles to cover the appearance and disappearance of the gas-solid difference in the emerging charge-state distributions and stopping power values. Furthermore, this energy range has extended the existing experimental data in a new region where the stopping-power data for the heaviest ions were scarce. The key results of this experiment are:

- The gas-solid difference in mean charge states and stopping powers according to the Bohr-Lindhard model was clearly observed with the present experiment in the velocity range of (30-100) MeV/u. The effect systematically decreased with higher incident velocities and vanished at 280 MeV/u. The mean charge states of lead ions emergent from solids were, at the low energies, (3-5)% higher than for the gases with neighboring Z_2 numbers. The corresponding measured stopping powers in solids were (6-8)% higher than in gases at the same velocity.
- The higher stopping power values in solids can be fully attributed to the corresponding measured higher mean charge states of the projectiles.

- The Bohr-Lindhard prediction on the density effect was experimentally confirmed for all the measured gas-solid target materials contrary to a previous uranium measurement [Fet+06], where a small difference was only observed for low Z_2 targets and the difference disappeared at higher-Z_2 materials.
- The comparisons with recent theoretical predictions have revealed significant deviations, especially for the gaseous targets. The best agreement was found with the ATIMA program, which adapts the Lindhard-Sørensen theory [LS96], combined with the measured mean charge states. It was demonstrated that the gas-solid difference has to be included in the theoretical descriptions and computer codes.
- The present experimental results have demonstrated clearly the key role of the ionic charge states during the collisions. The present results will have a significant contribution to the basic understanding of the atomic interaction of energetic ions in matter.
- With the present experimental results, the accuracy of the slowing-down theory in computer codes, e.g., the ATIMA program can be significantly improved, which will be beneficial for many accelerator based experiments and applications.

In the future, the following aspects are desired for improvements:

♣ Measurements with other heavy ions, such as uranium ($Z_1 = 92$). This will provide, in the first place, an extension of the experimental data in the broader domain of velocity and Z_1-Z_2 combination, for the basic understanding of the atomic interaction of heavy ions in matter. Simultaneously, the gas-solid difference will be investigated more. Especially, an uranium measurement will revise the conclusions and results from Ref.[Fet+06].

♣ Improved theoretical developments for both charge-changing processes and stopping power predictions can be done with our present new and accurate data. The effect due to the screened projectiles must be included into theories as well.

Appendix A

Solid Target

This appendix shows the weight w, area A, and areal density x deduced for the individual solid targets. For the details of the determination, see Section 4.5.2. When a thick target was needed in the measurements, two or three targets were stacked to obtain the desired thickness.

TABLE A.1: List of solid targets.

Material	Weight w (mg)	Area A (cm^2)	Areal density x (mg/cm^2)
C	1.273 ± 0.001	0.157 ± 0.001	8.10 ± 0.04
C	2.131 ± 0.001	0.158 ± 0.001	13.47 ± 0.07
C	3.605 ± 0.001	0.158 ± 0.001	22.89 ± 0.11
C	4.628 ± 0.001	0.159 ± 0.001	29.12 ± 0.15
C	6.693 ± 0.001	0.159 ± 0.001	42.18 ± 0.21
C	11.312 ± 0.011	0.156 ± 0.001	72.42 ± 0.36
C	21.742 ± 0.001	0.162 ± 0.001	134.10 ± 0.67
$(C_3H_6)_n$	12.352 ± 0.042	2.001 ± 0.010	6.18 ± 0.03
$(C_3H_6)_n$	19.363 ± 0.052	2.001 ± 0.010	9.68 ± 0.04
$(C_3H_6)_n$	26.543 ± 0.060	1.980 ± 0.010	13.36 ± 0.05
$(C_3H_6)_n$	52.057 ± 0.042	1.957 ± 0.010	25.99 ± 0.12
$(C_3H_6)_n$	127.631 ± 0.052	1.991 ± 0.010	64.06 ± 0.19
$(C_3H_6)_n$	238.066 ± 0.067	1.990 ± 0.010	119.51 ± 0.31
$(C_3H_6)_n$	33.660 ± 0.030	2.012 ± 0.010	16.73 ± 0.08
$(C_3H_6)_n$	92.021 ± 0.030	2.004 ± 0.010	45.92 ± 0.23
$(C_3H_6)_n$	7.950 ± 0.030	3.029 ± 0.015	2.62 ± 0.02
Ti	37.891 ± 0.001	0.159 ± 0.001	238.76 ± 1.19
Ti	1.304 ± 0.001	0.156 ± 0.001	8.36 ± 0.04

TABLE A.1: List of solid targets.

Ti	2.207 ± 0.001	0.162 ± 0.001	13.65 ± 0.07
Ti	2.957 ± 0.001	0.159 ± 0.001	18.64 ± 0.09
Ti	6.060 ± 0.001	0.159 ± 0.001	38.07 ± 0.19
Ti	16.301 ± 0.001	0.159 ± 0.001	102.34 ± 0.51
Ti	16.308 ± 0.001	0.159 ± 0.001	102.82 ± 0.51
Zr	1.610 ± 0.001	0.159 ± 0.001	10.14 ± 0.05
Zr	2.693 ± 0.001	0.158 ± 0.001	17.00 ± 0.09
Zr	3.713 ± 0.001	0.159 ± 0.001	23.40 ± 0.12
Zr	7.281 ± 0.001	0.159 ± 0.001	45.84 ± 0.23
Zr	9.557 ± 0.001	0.159 ± 0.001	60.28 ± 0.30
Zr	36.810 ± 0.001	0.142 ± 0.001	259.12 ± 1.30
Zr	41.670 ± 0.001	0.159 ± 0.001	261.85 ± 1.31
Sn	42.783 ± 0.001	0.158 ± 0.001	270.80 ± 1.35
Sn	0.335 ± 0.001	0.157 ± 0.001	2.14 ± 0.01
Sn	0.584 ± 0.001	0.152 ± 0.001	3.84 ± 0.02
Sn	3.151 ± 0.001	0.158 ± 0.001	19.93 ± 0.10
Sn	3.591 ± 0.001	0.157 ± 0.001	22.83 ± 0.11
Sn	11.384 ± 0.001	0.158 ± 0.001	71.88 ± 0.36
Sn	7.195 ± 0.001	0.158 ± 0.001	45.41 ± 0.23
Sn	29.205 ± 0.001	0.158 ± 0.001	184.54 ± 0.92

Appendix B

Stopping Powers

This appendix presents additional information related to the stopping-power measurements for lead ions in matter. The columns are, by starting on the left-hand side, the incident energy (E_0), the selected incident charge-state (q_0), the target thickness (x), the mean energy loss ($\langle \Delta E \rangle$), the ion-optically centered charge-state at F3 (q_{scaled}), the mean energy (E_{M}) corresponding to the listed stopping-power value dE/dx. The associated correction term dP/dx was deduced with the mean charge formula of Pierce and Blann, as explained in Chapter 5. For gaseous targets, the mean energy loss after correction of the gas-target windows is given by $\langle \Delta E \rangle_{\text{gas}}$.

TABLE B.1: Experimental stopping powers for lead ions in carbon, and related information.

$^{208}\mathrm{Pb} \rightarrow {}_{6}\mathrm{C}$							
E_0 (MeV/u)	q_0	x (mg cm^{-2})	$\langle \Delta E \rangle$ (MeV/u)	q_{scaled}	E_{M} (MeV/u)	dP/dx (MeV/mg cm^{-2})	dE/dx (MeV/mg cm^{-2})
279.98	81^+	42.18 ± 0.28	4.56 ± 0.09	81^+	272.94 ± 0.09	0.49 ± 0.14	22.90 ± 0.14
279.98	81^+	72.42 ± 0.41	7.94 ± 0.09	81^+			
279.98	81^+	134.10 ± 0.70	14.73 ± 0.09	81^+			
279.98	81^+	206.52 ± 0.81	22.88 ± 0.09	81^+			
99.94	79^+	13.47 ± 0.20	2.51 ± 0.13	80^+	91.07 ± 0.13	3.64 ± 0.42	42.74 ± 0.42
99.94	79^+	42.18 ± 0.28	8.33 ± 0.13	79^+			
99.94	79^+	72.42 ± 0.41	14.72 ± 0.12	79^+			
99.94	79^+	134.10 ± 0.70	28.51 ± 0.11	79^+			
69.91	77^+	13.47 ± 0.20	3.20 ± 0.11	79^+	61.40 ± 0.11	7.57 ± 0.22	54.89 ± 0.22
69.91	77^+	42.18 ± 0.28	10.57 ± 0.10	78^+			
69.91	77^+	72.42 ± 0.41	19.21 ± 0.09	78^+			
69.91	77^+	95.31 ± 0.47	25.47 ± 0.09	77^+			
49.89	77^+	13.47 ± 0.20	3.99 ± 0.09	77^+	44.71 ± 0.09	12.43 ± 0.48	66.82 ± 0.48
49.89	77^+	42.18 ± 0.28	13.59 ± 0.08	76^+			
34.90	74^+	8.10 ± 0.20	2.83 ± 0.07	75^+	31.62 ± 0.07	15.40 ± 1.26	77.52 ± 1.26
34.90	74^+	13.47 ± 0.20	4.99 ± 0.07	75^+			

TABLE B.2: Experimental stopping powers for lead ions in nitrogen gas, and related information.

$^{208}Pb \rightarrow {}_{7}N$							
E_0 (MeV/u)	q_0	x (mg cm^{-2})	$\langle \Delta E \rangle_{gas}$ (MeV/u)	q_{scaled}	E_M (MeV/u)	dP/dx (MeV/mg cm^{-2})	dE/dx (MeV/mg cm^{-2})
279.98	81^+	25.75 ± 0.16	2.78 ± 0.13	81^+	272.94 ± 0.13	0.28 ± 0.47	22.69 ± 0.47
279.98	81^+	51.43 ± 0.33	5.57 ± 0.13	81^+			
279.98	81^+	70.01 ± 0.45	7.60 ± 0.13	81^+			
99.94	79^+	23.68 ± 0.06	4.55 ± 0.18	79^+	91.07 ± 0.18	2.52 ± 0.56	41.49 ± 0.56
99.94	79^+	46.18 ± 0.30	8.99 ± 0.18	79^+			
99.94	79^+	69.14 ± 0.44	13.65 ± 0.18	78^+			
69.91	77^+	15.89 ± 0.04	3.72 ± 0.15	77^+	61.40 ± 0.15	5.54 ± 0.41	52.68 ± 0.41
69.91	77^+	35.36 ± 0.08	8.53 ± 0.15	77^+			
69.91	77^+	52.52 ± 0.34	13.06 ± 0.15	77^+			
69.91	77^+	70.12 ± 0.45	17.80 ± 0.14	75^+			
49.89	77^+	5.87 ± 0.01	1.68 ± 0.13	76^+	44.71 ± 0.13	8.29 ± 0.47	62.46 ± 0.47
49.89	77^+	19.31 ± 0.05	5.58 ± 0.13	75^+			
49.89	77^+	35.03 ± 0.08	10.38 ± 0.13	74^+			
49.89	77^+	51.93 ± 0.33	15.95 ± 0.12	72^+			
34.90	74^+	10.56 ± 0.03	3.55 ± 0.10	72^+	31.62 ± 0.10	10.56 ± 0.65	72.47 ± 0.65
34.90	74^+	22.95 ± 0.06	7.94 ± 0.10	70^+			
34.90	74^+	35.01 ± 0.08	12.51 ± 0.10	69^+			

TABLE B.3: Experimental stopping powers for lead ions in titanium, and related information.

$^{208}\mathrm{Pb} \rightarrow {}_{22}\mathrm{Ti}$							
E_0 (MeV/u)	q_0	x (mg cm^{-2})	$\langle \Delta E \rangle$ (MeV/u)	q_{scaled}	E_{M} (MeV/u)	dP/dx (MeV/mg cm^{-2})	dE/dx (MeV/mg cm^{-2})
279.98	81^+	32.29 ± 0.29	2.90 ± 0.09	81^+	274.40 ± 0.09	0.25 ± 0.10	18.39 ± 0.10
279.98	81^+	38.07 ± 0.27	3.41 ± 0.09	81^+			
279.98	81^+	102.82 ± 0.55	9.14 ± 0.09	81^+			
279.98	81^+	205.15 ± 0.77	18.34 ± 0.09	81^+			
279.98	81^+	238.76 ± 1.21	21.31 ± 0.09	81^+			
99.94	79^+	18.64 ± 0.21	2.76 ± 0.13	79^+	91.03 ± 0.13	1.72 ± 0.10	32.69 ± 0.10
99.94	79^+	56.72 ± 0.34	8.58 ± 0.13	79^+			
99.94	79^+	102.82 ± 0.55	15.97 ± 0.12	78^+			
99.94	79^+	140.89 ± 0.61	22.22 ± 0.11	78^+			
99.94	79^+	205.15 ± 0.77	33.63 ± 0.11	77^+			
99.94	79^+	238.76 ± 1.21	39.42 ± 0.10	76^+			
69.91	77^+	18.64 ± 0.21	3.40 ± 0.11	77^+	61.30 ± 0.10	3.41 ± 0.15	40.60 ± 0.15
69.91	77^+	56.72 ± 0.34	10.60 ± 0.10	76^+			
69.91	77^+	102.34 ± 0.55	19.93 ± 0.09	75^+			
69.91	77^+	140.89 ± 0.61	28.39 ± 0.08	74^+			
49.89	75^+	8.36 ± 0.20	1.80 ± 0.09	75^+	44.88 ± 0.09	5.01 ± 0.24	47.42 ± 0.24
49.89	75^+	18.64 ± 0.21	4.02 ± 0.09	75^+			
49.89	75^+	38.07 ± 0.27	8.46 ± 0.08	74^+			
49.89	75^+	51.73 ± 0.33	11.75 ± 0.08	73^+			
49.89	75^+	70.37 ± 0.39	16.38 ± 0.07	72^+			

TABLE B.4: Experimental stopping powers for lead ions in argon gas, and related information.

$^{208}\mathrm{Pb} \rightarrow {}_{18}\mathrm{Ar}$							
E_0 (MeV/u)	q_0	x (mg cm^{-2})	$\langle \Delta E \rangle$ (MeV/u)	q_{scaled}	E_{M} (MeV/u)	dP/dx (MeV/mg cm^{-2})	dE/dx (MeV/mg cm^{-2})
279.98	81^+	31.83 ± 0.08	2.82 ± 0.13	81^+	274.40 ± 0.13	0.32 ± 0.34	18.64 ± 0.34
279.98	81^+	62.73 ± 0.40	5.60 ± 0.13	81^+			
279.98	81^+	100.00 ± 0.64	8.94 ± 0.13	81^+			
99.94	79^+	34.71 ± 0.08	5.21 ± 0.18	78^+	91.03 ± 0.18	1.06 ± 0.38	32.44 ± 0.38
99.94	79^+	67.72 ± 0.43	10.36 ± 0.18	78^+			
99.94	79^+	99.99 ± 0.64	15.51 ± 0.18	78^+			
69.91	77^+	23.73 ± 0.06	4.24 ± 0.15	76^+	61.30 ± 0.15	1.08 ± 0.29	38.82 ± 0.29
69.91	77^+	23.41 ± 0.15	4.18 ± 0.16	76^+			
69.91	77^+	50.16 ± 0.32	9.11 ± 0.16	73^+			
69.91	77^+	50.86 ± 0.12	9.21 ± 0.15	73^+			
69.91	77^+	76.73 ± 0.49	14.18 ± 0.15	75^+			
69.91	77^+	99.98 ± 0.64	18.81 ± 0.15	74^+			
49.89	75^+	9.79 ± 0.02	2.03 ± 0.13	71^+	44.88 ± 0.13	1.39 ± 0.34	44.49 ± 0.34
49.89	75^+	28.88 ± 0.07	6.05 ± 0.13	70^+			
49.89	75^+	50.47 ± 0.12	10.79 ± 0.13	69^+			
49.89	75^+	71.61 ± 0.46	15.79 ± 0.12	70^+			

TABLE B.5: Experimental stopping powers for lead ions in zirconium, and related information.

$^{208}\mathrm{Pb} \rightarrow {}_{40}\mathrm{Zr}$							
E_0 (MeV/u)	q_0	x (mg cm^{-2})	$\langle \Delta E \rangle$ (MeV/u)	q_{scaled}	E_{M} (MeV/u)	dP/dx (MeV/mg cm^{-2})	dE/dx (MeV/mg cm^{-2})
279.98	81^+	106.12 ± 0.46	8.26 ± 0.09	81+	262.17 ± 0.09	0.20 ± 0.06	16.75 ± 0.06
279.98	81^+	261.85 ± 1.32	20.83 ± 0.09	81^+			
279.98	81^+	520.98 ± 1.86	42.12 ± 0.09	81^+			
99.94	79^+	23.40 ± 0.22	3.01 ± 0.13	78^+	90.07 ± 0.13	0.62 ± 0.24	28.09 ± 0.24
99.94	79^+	60.28 ± 0.36	7.92 ± 0.13	78^+			
99.94	79^+	129.52 ± 0.51	17.36 ± 0.12	78^+			
99.94	79^+	259.12 ± 1.31	37.20 ± 0.10	76^+			
99.94	79^+	261.85 ± 1.32	38.08 ± 0.10	76^+			
69.91	77^+	23.40 ± 0.22	3.62 ± 0.11	77^+	62.00 ± 0.10	1.45 ± 0.16	33.99 ± 0.16
69.91	77^+	45.84 ± 0.30	7.24 ± 0.10	76^+			
69.91	77^+	60.28 ± 0.36	9.51 ± 0.10	76^+			
69.91	77^+	106.12 ± 0.46	17.34 ± 0.09	75^+			
69.91	77^+	129.52 ± 0.51	21.56 ± 0.09	74^+			
49.89	76^+	17.00 ± 0.21	3.12 ± 0.09	74^+	43.69 ± 0.08	2.56 ± 0.21	40.21 ± 0.21
49.89	76^+	45.84 ± 0.30	8.66 ± 0.08	73^+			
49.89	76^+	60.28 ± 0.36	11.53 ± 0.08	72^+			
49.89	76^+	83.68 ± 0.42	16.42 ± 0.07	71^+			
34.90	70^+	10.14 ± 0.20	2.15 ± 0.07	71^+	30.87 ± 0.07	3.55 ± 0.24	46.41 ± 0.24
34.90	70^+	23.40 ± 0.22	5.07 ± 0.07	71^+			
34.90	70^+	40.40 ± 0.30	9.00 ± 0.06	69^+			
34.90	70^+	60.28 ± 0.36	13.81 ± 0.06	68^+			

TABLE B.6: Experimental stopping powers for lead ions in krypton gas, and related information.

$^{208}\mathrm{Pb} \rightarrow {}_{36}\mathrm{Kr}$							
E_0 (MeV/u)	q_0	x (mg cm^{-2})	$\langle \Delta E \rangle$ (MeV/u)	q_{scaled}	E_{M} (MeV/u)	dP/dx (MeV/mg cm^{-2})	dE/dx (MeV/mg cm^{-2})
99.94	79^+	39.12 ± 0.25	4.92 ± 0.18	78^+	90.07 ± 0.18	0.02 ± 0.18	27.42 ± 0.18
99.94	79^+	77.17 ± 0.49	9.86 ± 0.18	77^+			
99.94	79^+	148.67 ± 0.95	19.62 ± 0.18	77^+			
99.94	79^+	209.24 ± 1.34	28.29 ± 0.17	76^+			
69.91	77^+	36.32 ± 0.09	5.45 ± 0.15	75^+	62.00 ± 0.15	-0.07 ± 0.20	32.43 ± 0.20
69.91	77^+	71.25 ± 0.17	10.89 ± 0.15	75^+			
69.91	77^+	105.81 ± 0.25	16.51 ± 0.15	74^+			
69.91	77^+	144.94 ± 0.35	23.36 ± 0.15	72^+			
49.89	76^+	8.52 ± 0.02	1.47 ± 0.13	73^+	43.69 ± 0.13	0.08 ± 0.30	37.70 ± 0.30
49.89	76^+	30.78 ± 0.07	5.38 ± 0.13	72^+			
49.89	76^+	57.20 ± 0.14	10.26 ± 0.13	72^+			
49.89	76^+	82.70 ± 0.20	15.23 ± 0.13	70^+			
34.90	70^+	6.85 ± 0.02	1.35 ± 0.10	69^+	30.87 ± 0.10	-0.06 ± 0.34	42.78 ± 0.34
34.90	70^+	23.70 ± 0.06	4.80 ± 0.10	68^+			
34.90	70^+	45.70 ± 0.11	9.52 ± 0.09	67^+			
34.90	70^+	60.21 ± 0.14	12.78 ± 0.09	67^+			

TABLE B.7: Experimental stopping powers for lead ions in tin, and related information.

$^{208}\mathrm{Pb} \rightarrow {}_{50}\mathrm{Sn}$							
E_0 (MeV/u)	q_0	x (mg cm^{-2})	$\langle \Delta E \rangle$ (MeV/u)	$q_{cent.}$	E_M (MeV/u)	dP/dx (MeV/mg cm^{-2})	dE/dx (MeV/mg cm^{-2})
279.98	81^+	71.88 ± 0.41	5.16 ± 0.09	81^+	265.77 ± 0.09	0.01 ± 0.06	15.36 ± 0.06
279.98	81^+	184.54 ± 0.94	13.46 ± 0.09	81^+			
279.98	81^+	270.80 ± 1.37	19.85 ± 0.09	81^+			
279.98	81^+	455.34 ± 1.66	33.75 ± 0.09	81^+			
99.94	79^+	22.83 ± 0.22	2.61 ± 0.13	78^+	89.65 ± 0.13	0.74 ± 0.17	26.27 ± 0.17
99.94	79^+	71.88 ± 0.41	8.85 ± 0.13	78^+			
99.94	79^+	184.54 ± 0.94	23.41 ± 0.12	77^+			
69.91	77^+	22.83 ± 0.22	3.42 ± 0.11	76^+	68.35 ± 0.11	2.31 ± 1.18	31.17 ± 1.18
34.90	74^+	2.14 ± 0.19	0.43 ± 0.08	71^+	34.33 ± 0.07	1.94 ± 2.86	40.07 ± 2.86
34.90	74^+	3.84 ± 0.20	0.74 ± 0.07	71^+			
34.90	74^+	5.97 ± 0.28	1.15 ± 0.07	70^+			

TABLE B.8: Experimental stopping powers for lead ions in xenon gas, and related information.

$^{208}Pb \rightarrow {}_{54}Xe$							
E_0 (MeV/u)	q_0	x (mg cm^{-2})	$\langle \Delta E \rangle$ (MeV/u)	$q_{cent.}$	E_M (MeV/u)	dP/dx (MeV/mg cm^{-2})	dE/dx (MeV/mg cm^{-2})
279.98	81^+	111.67 ± 0.71	7.96 ± 0.11	81^+	265.77 ± 0.11	0.04 ± 0.11	15.09 ± 0.11
279.98	81^+	221.76 ± 1.42	15.89 ± 0.11	81^+			
279.98	81^+	304.36 ± 1.95	21.94 ± 0.11	81^+			
279.98	81^+	327.11 ± 2.09	23.64 ± 0.11	81^+			
99.94	79^+	28.18 ± 0.18	3.20 ± 0.18	78^+	89.65 ± 0.18	-0.27 ± 0.11	24.82 ± 0.11
99.94	79^+	28.58 ± 0.07	3.24 ± 0.18	78^+			
99.94	79^+	84.29 ± 0.20	9.73 ± 0.18	77^+			
99.94	79^+	83.14 ± 0.53	9.62 ± 0.18	77^+			
99.94	79^+	162.23 ± 1.04	19.33 ± 0.18	77^+			
99.94	79^+	164.50 ± 0.39	19.54 ± 0.17	77^+			
99.94	79^+	237.13 ± 1.52	29.04 ± 0.17	76^+			
99.94	79^+	307.36 ± 1.97	38.75 ± 0.17	75^+			
69.91	77^+	20.27 ± 0.05	2.71 ± 0.15	75^+	68.35 ± 0.15	-0.81 ± 0.19	27.61 ± 0.19
69.91	77^+	68.83 ± 0.17	9.38 ± 0.15	74^+			
69.91	77^+	112.97 ± 0.27	15.73 ± 0.15	73^+			
69.91	77^+	154.12 ± 0.37	21.96 ± 0.14	73^+			
49.89	76^+	9.28 ± 0.06	1.42 ± 0.13	73^+	43.84 ± 0.13	-1.29 ± 0.20	33.05 ± 0.20
49.89	76^+	30.64 ± 0.20	4.72 ± 0.13	72^+			
49.89	76^+	59.83 ± 0.38	9.44 ± 0.13	72^+			
49.89	76^+	87.69 ± 0.56	14.16 ± 0.13	70^+			
49.89	76^+	113.93 ± 0.73	18.83 ± 0.12	68^+			

TABLE B.9: Experimental stopping powers for lead ions in polypropylene, and related information.

$^{208}Pb \rightarrow (C_3H_6)_n$							
E_0 (MeV/u)	q_0	x (mg cm^{-2})	$\langle \Delta E \rangle$ (MeV/u)	$q_{cent.}$	E_M (MeV/u)	dP/dx (MeV/mg cm^{-2})	dE/dx (MeV/mg cm^{-2})
279.98	81^+	25.99 ± 0.12	3.35 ± 0.09	81^+	271.94 ± 0.09	0.48 ± 0.14	26.98 ± 0.14
279.98	81^+	45.92 ± 0.23	5.90 ± 0.09	81^+			
279.98	81^+	64.06 ± 0.19	8.27 ± 0.09	81^+			
279.98	81^+	71.91 ± 0.26	9.30 ± 0.09	81^+			
279.98	81^+	119.51 ± 0.31	15.49 ± 0.09	81^+			
279.98	81^+	183.57 ± 0.36	23.98 ± 0.09	81^+			
99.94	79^+	16.73 ± 0.09	3.80 ± 0.13	80^+	88.54 ± 0.12	5.00 ± 0.21	52.10 ± 0.21
99.94	79^+	42.72 ± 0.15	10.08 ± 0.13	79^+			
99.94	79^+	64.06 ± 0.19	15.40 ± 0.12	79^+			
99.94	79^+	109.98 ± 0.30	27.59 ± 0.11	79^+			
99.94	79^+	119.51 ± 0.31	30.31 ± 0.11	79^+			
69.91	77^+	13.36 ± 0.03	3.85 ± 0.11	79^+	60.75 ± 0.10	9.73 ± 0.28	66.33 ± 0.28
69.91	77^+	25.99 ± 0.12	7.71 ± 0.10	79^+			
69.91	77^+	45.92 ± 0.23	13.97 ± 0.10	78^+			
69.91	77^+	64.06 ± 0.19	20.27 ± 0.09	78^+			
69.91	77^+	71.91 ± 0.26	23.10 ± 0.09	77^+			
69.91	77^+	90.05 ± 0.23	30.33 ± 0.08	76^+			
49.89	77^+	6.18 ± 0.02	2.18 ± 0.09	78^+	42.79 ± 0.09	15.95 ± 0.46	82.00 ± 0.46
49.89	77^+	13.36 ± 0.03	4.81 ± 0.09	77^+			
49.89	77^+	25.99 ± 0.12	9.81 ± 0.08	77^+			
49.89	77^+	39.35 ± 0.12	15.45 ± 0.08	76^+			
34.90	74^+	6.18 ± 0.02	2.68 ± 0.07	76^+	30.79 ± 0.07	20.94 ± 1.02	95.87 ± 1.02
34.90	74^+	16.73 ± 0.09	7.64 ± 0.07	75^+			

TABLE B.10: Experimental stopping powers for lead ions in propene gas, and related information.

^{208}Pb→propene							
E_0 (MeV/u)	q_0	x (mg cm^{-2})	$\langle \Delta E \rangle$ (MeV/u)	$q_{cent.}$	E_M (MeV/u)	dP/dx (MeV/mg cm^{-2})	dE/dx (MeV/mg cm^{-2})
279.98	81^+	35.28 ± 0.08	4.58 ± 0.13	81^+	271.94 ± 0.13	0.66 ± 0.40	27.57 ± 0.40
279.98	81^+	34.78 ± 0.22	4.55 ± 0.13	81^+			
279.98	81^+	72.08 ± 0.46	9.48 ± 0.13	81^+			
279.98	81^+	107.3 ± 0.69	14.17 ± 0.13	81^+			
99.94	79^+	13.85 ± 0.09	3.16 ± 0.18	80^+	88.54 ± 0.18	4.42 ± 0.35	52.41 ± 0.35
99.94	79^+	36.63 ± 0.23	8.59 ± 0.18	80^+			
99.94	79^+	71.22 ± 0.46	17.47 ± 0.18	79^+			
99.94	79^+	107.1 ± 0.69	27.28 ± 0.17	78^+			
49.89	77^+	8.12 ± 0.02	2.90 ± 0.14	78^+	42.79 ± 0.13	11.61 ± 0.53	79.17 ± 0.53
49.89	77^+	7.96 ± 0.05	2.87 ± 0.13	78^+			
49.89	77^+	23.87 ± 0.06	8.81 ± 0.13	77^+			
49.89	77^+	23.53 ± 0.15	8.76 ± 0.12	77^+			
49.89	77^+	38.86 ± 0.09	14.78 ± 0.13	76^+			
49.89	77^+	38.32 ± 0.25	14.66 ± 0.12	76^+			
34.90	74^+	4.95 ± 0.01	2.03 ± 0.10	72^+	30.79 ± 0.10	15.14 ± 0.73	91.96 ± 0.73
34.90	74^+	14.44 ± 0.03	6.18 ± 0.10	71^+			
34.90	74^+	23.45 ± 0.06	10.40 ± 0.10	71^+			

Appendix C

Evolution of Charge-State Fractions

This appendix presents the evolution of the charge-state fractions $F(q)$ as a function of projectile outgoing energy. The different atomic (K, L, and M) shells are separately displayed. The charge-state fractions for the gas targets include the window effect.

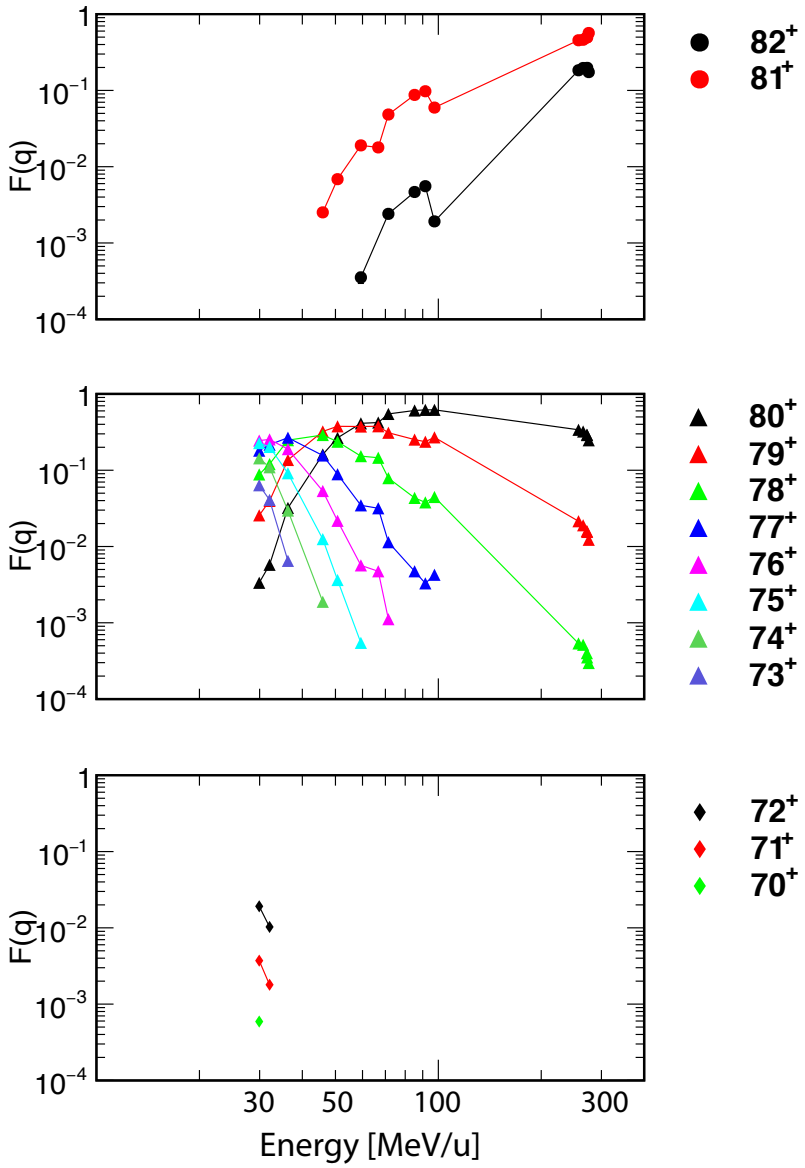

FIGURE C.1: Charge-state fractions $F(q)$ of lead ions in carbon as a function of projectile energy. The top, middle, and bottom panels are for K-, L-, and M-shell electrons, respectively.

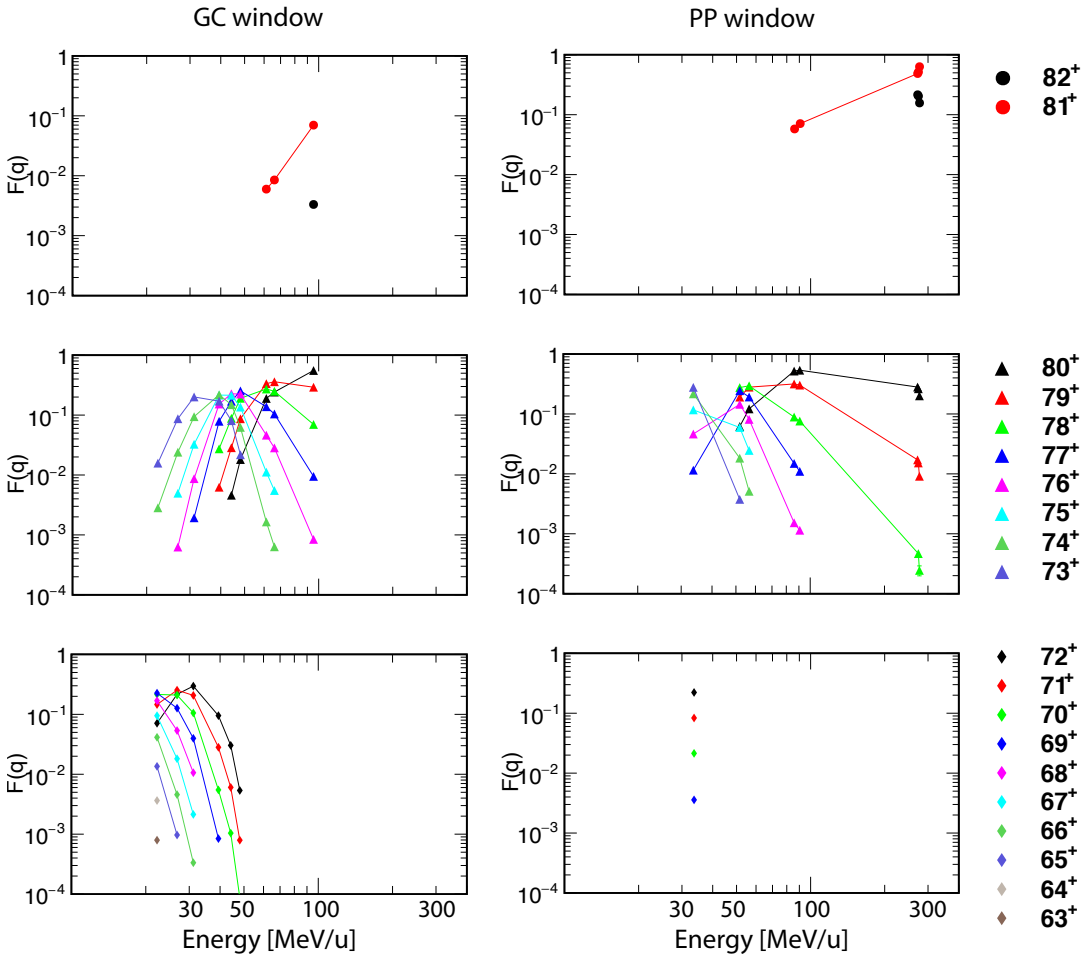

FIGURE C.2: The same figure as Fig.C.1 but for nitrogen gas plus gas target windows. The left and right panels correspond to the results obtained with the GC and PP windows, respectively.

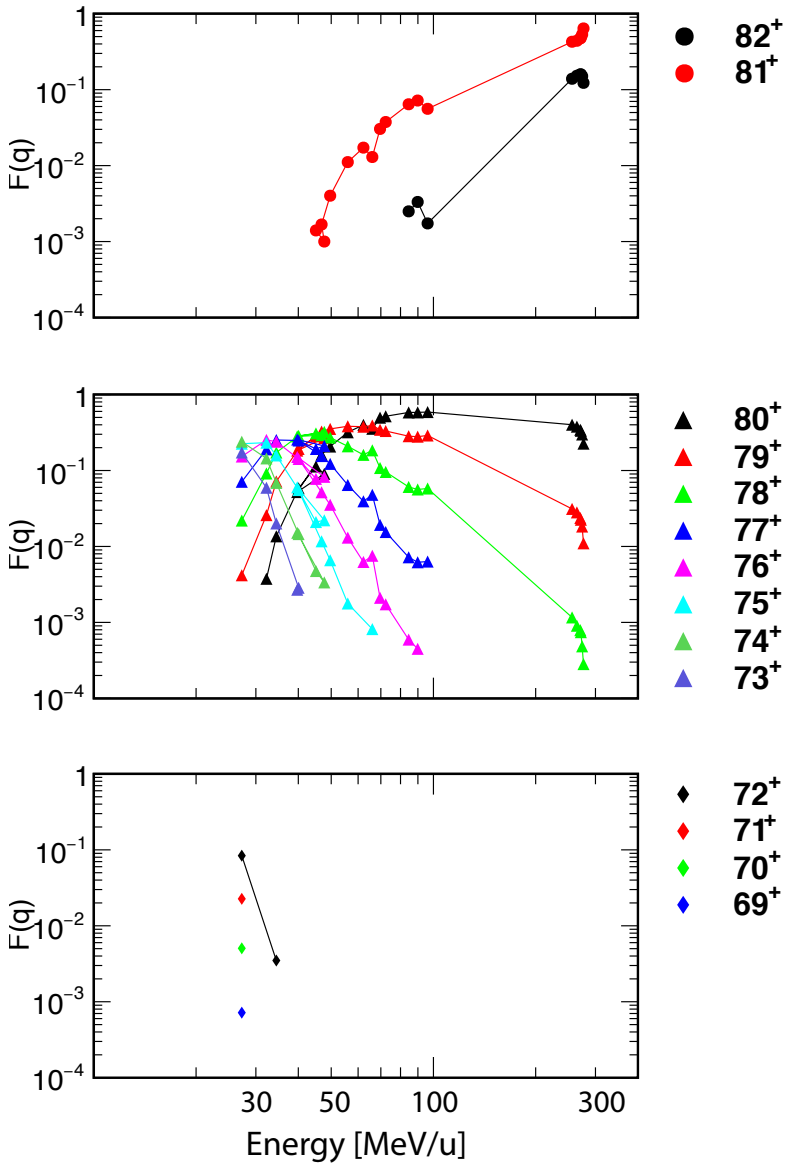

FIGURE C.3: The same figure as Fig.C.1 but for polypropylene.

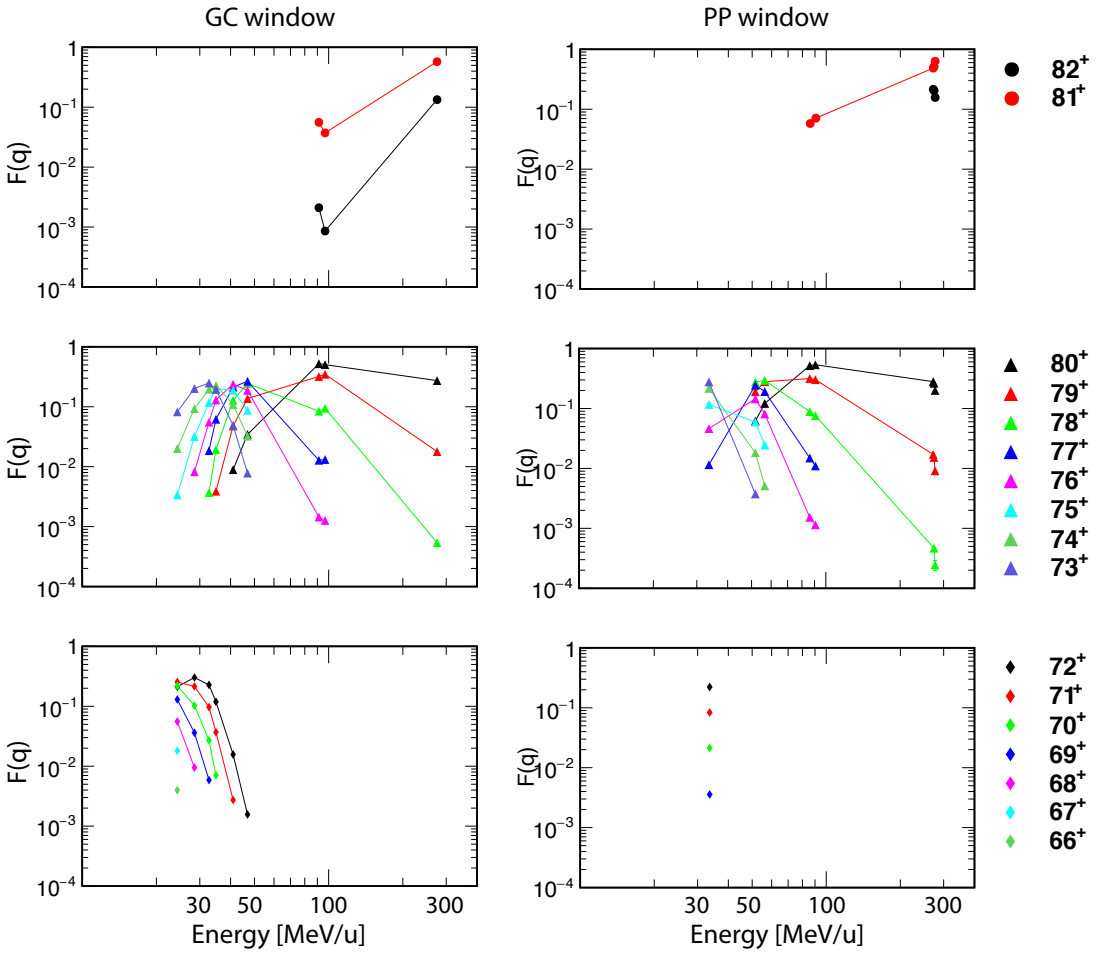

FIGURE C.4: The same figure as Fig.C.2 but for propene gas.

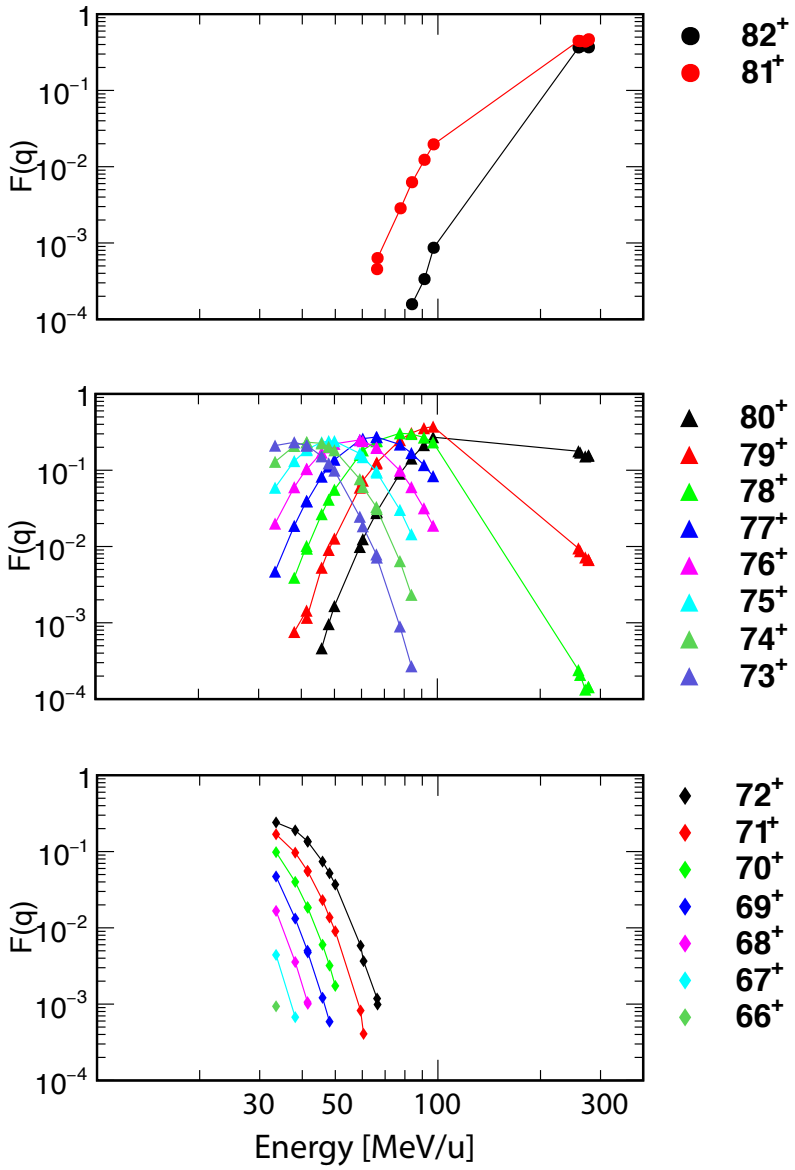

FIGURE C.5: The same figure as Fig.C.1 but for titanium.

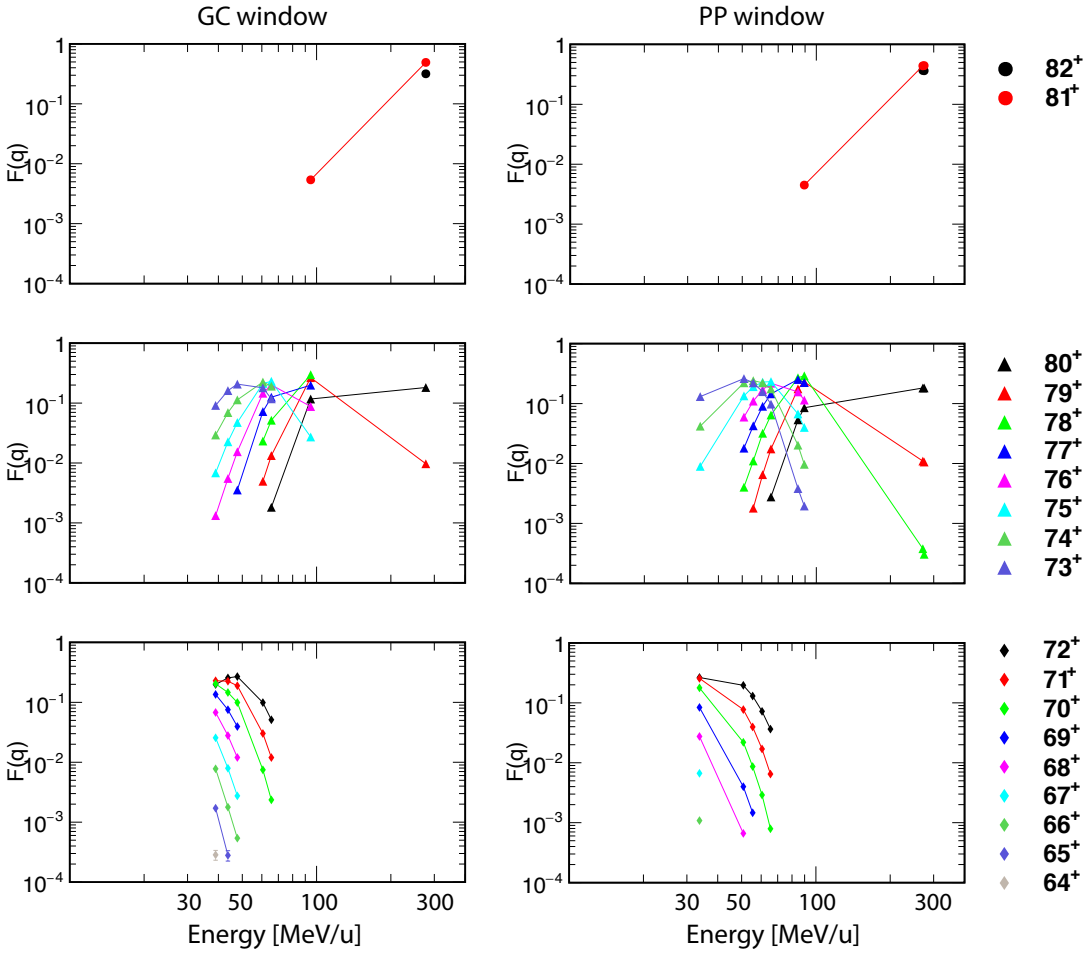

FIGURE C.6: The same figure as Fig.C.2 but for argon gas.

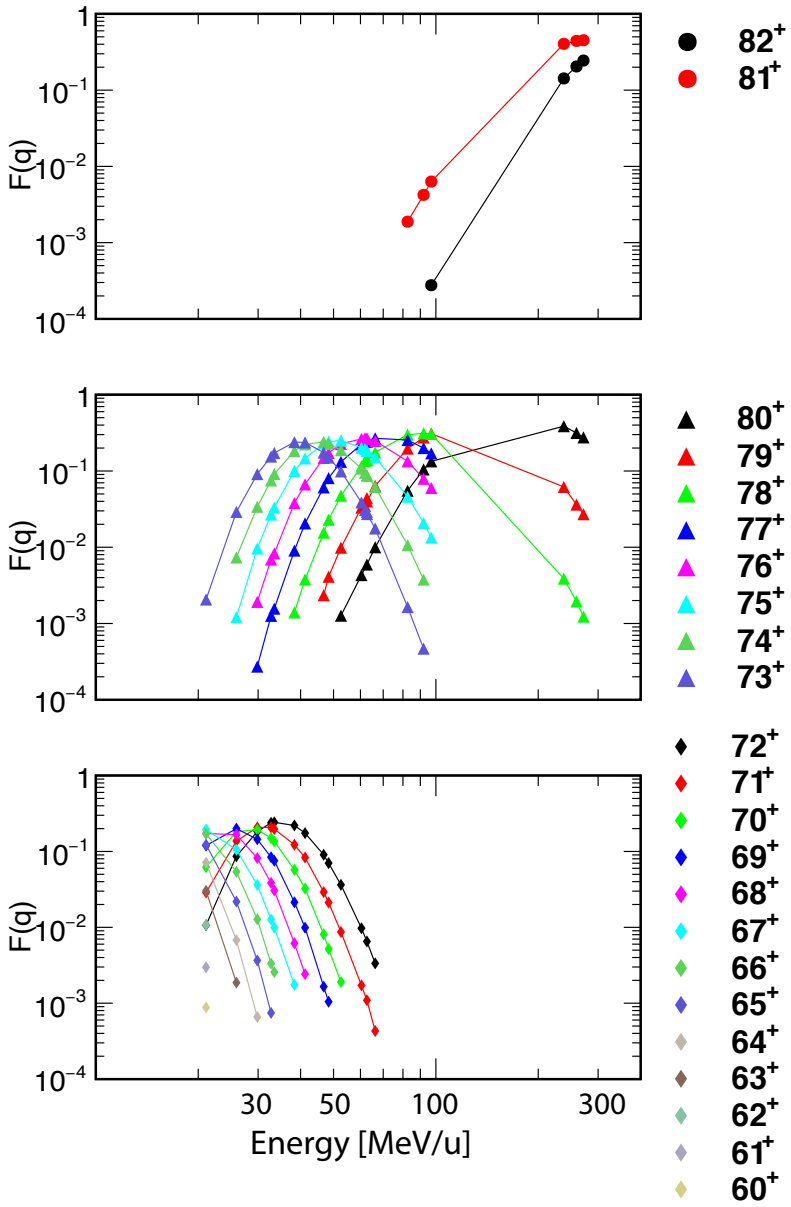

FIGURE C.7: The same figure as Fig.C.1 but for zirconium.

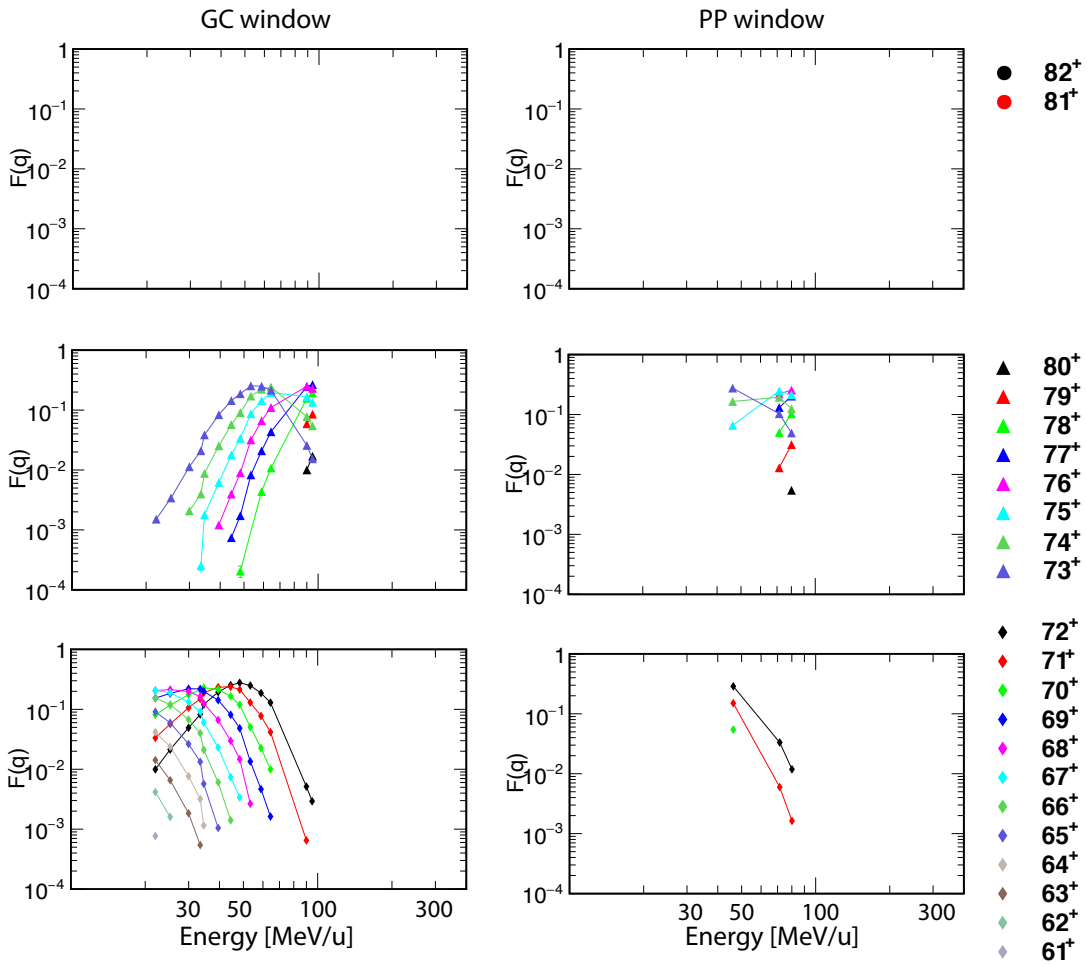

FIGURE C.8: The same figure as Fig.C.2 but for krypton gas.

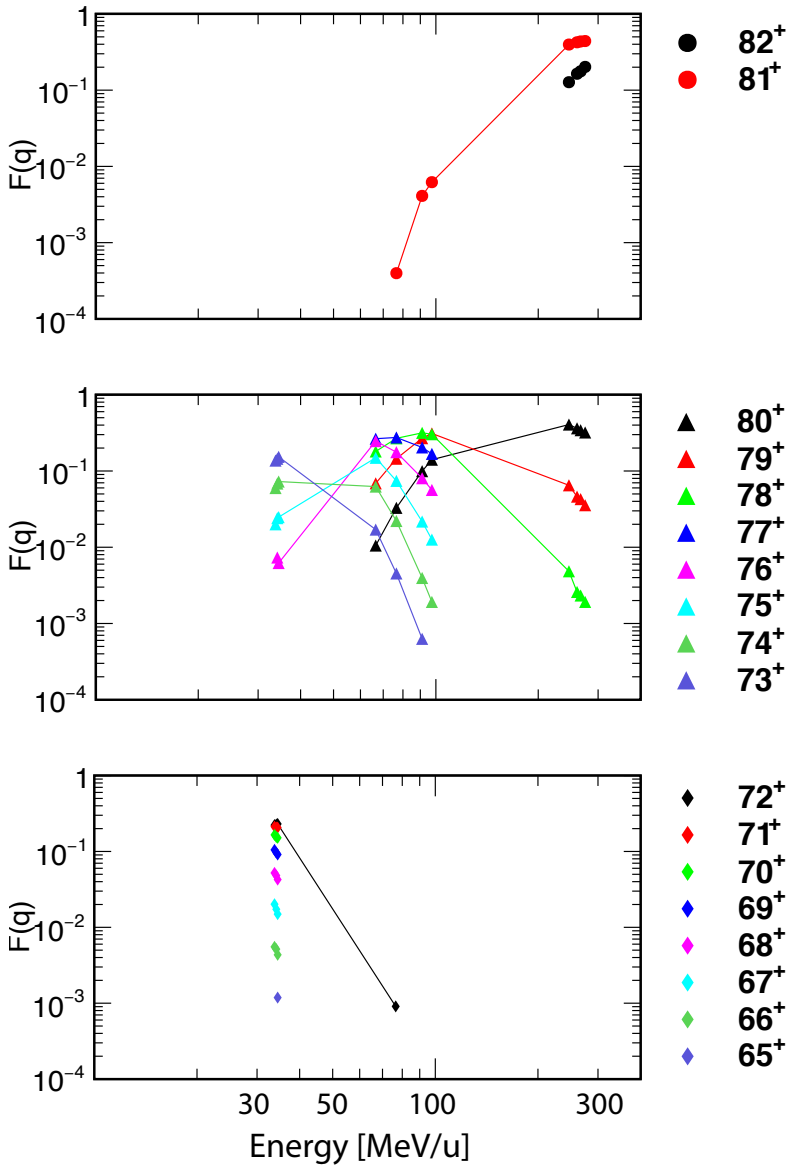

FIGURE C.9: The same figure as Fig.C.1 but for tin.

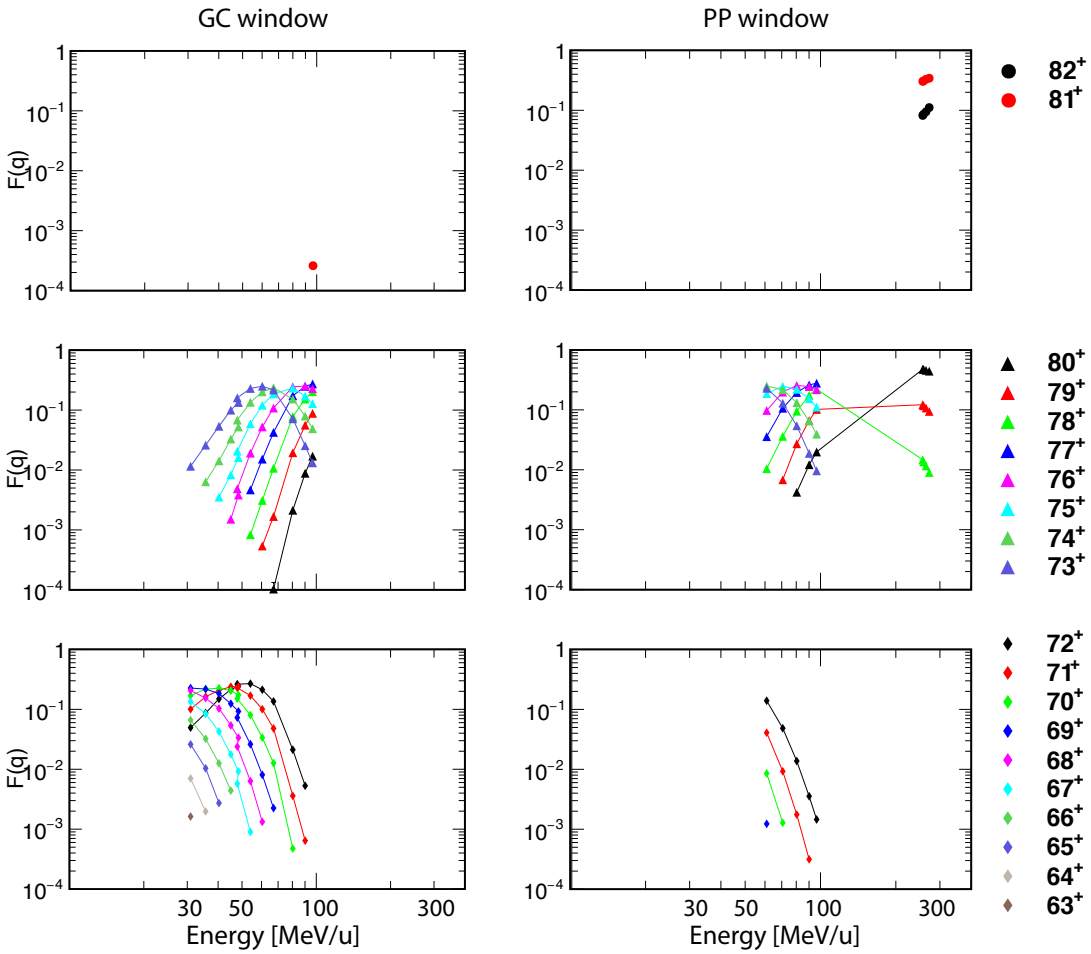

FIGURE C.10: The same figure as Fig.C.2 but for xenon gas.

Appendix D

Mean Charge States

This appendix presents the information related to the experimental mean charge states of lead ions after penetrating atomic collision targets. The columns are, from the left-hand side, the incident energy (E_0), incident charge-state (q_0), target thickness (x), energy of the centered charge state emerging from gaseous and solid targets (E_{out}), ion-optically centered charge state at F3 (q_{scaled}), standard deviation of charge-state distribution (σ_{CSD}) for solid targets, and experimental mean charge state $\bar{q}$.

TABLE D.1: Experimental mean charge-states for lead ions after traversing carbon targets, and related information.

$^{208}Pb \rightarrow {}_{6}C$						
E_0 (MeV/u)	q_0	x (mg cm^{-2})	E_{out} (MeV/u)	q_{scaled}	σ_{CSD}	$\bar{q}$
279.98	81^+	42.18 ± 0.30	275.42 ± 0.06	81^+	0.6805	80.90 ± 0.09
279.98	81^+	72.42 ± 0.52	272.04 ± 0.06	81^+	0.7345	80.87 ± 0.10
279.98	81^+	134.10 ± 0.96	265.25 ± 0.06	81^+	0.7565	80.84 ± 0.11
279.98	81^+	206.52 ± 1.09	257.09 ± 0.06	81^+	0.7575	80.80 ± 0.12
99.94	79^+	13.47 ± 0.10	97.42 ± 0.03	80^+	0.6774	79.69 ± 0.10
99.94	79^+	42.18 ± 0.30	91.61 ± 0.03	79^+	0.7015	79.79 ± 0.14
99.94	79^+	72.42 ± 0.52	85.22 ± 0.03	79^+	0.7132	79.74 ± 0.13
99.94	79^+	134.10 ± 0.96	71.43 ± 0.02	79^+	0.7735	79.55 ± 0.11
69.91	77^+	13.47 ± 0.10	66.71 ± 0.03	79^+	0.8684	79.23 ± 0.19
69.91	77^+	42.18 ± 0.30	59.34 ± 0.03	78^+	0.8939	79.21 ± 0.20
69.91	77^+	72.42 ± 0.52	50.71 ± 0.02	78^+	1.0451	78.79 ± 0.21
69.91	77^+	95.31 ± 0.54	44.44 ± 0.02	77^+	1.1698	78.29 ± 0.23
49.89	77^+	13.47 ± 0.10	45.91 ± 0.03	77^+	1.1762	78.34 ± 0.18
49.89	77^+	42.18 ± 0.30	36.30 ± 0.02	76^+	1.4106	77.13 ± 0.17
34.90	74^+	8.10 ± 0.06	32.08 ± 0.03	75^+	1.5374	76.01 ± 0.16
34.90	74^+	13.47 ± 0.10	29.92 ± 0.03	75^+	1.5759	75.64 ± 0.10

TABLE D.2: Experimental mean charge-states for lead ions after traversing nitrogen gas targets, and related information.

$^{208}Pb \rightarrow {}_{7}N$					
E_0 (MeV/u)	q_0	x (mg cm^{-2})	E_{out} (MeV/u)	q_{scaled}	$\bar{q}$
279.98	81^+	25.75 ± 0.16	277.16 ± 0.09	81^+	80.94 ± 0.17
279.98	81^+	51.43 ± 0.33	274.37 ± 0.09	81^+	80.91 ± 0.19
279.98	81^+	70.01 ± 0.45	272.34 ± 0.09	81^+	80.90 ± 0.17
99.94	79^+	23.68 ± 0.06	95.35 ± 0.05	79^+	79.60 ± 0.18
99.94	79^+	46.18 ± 0.30	90.83 ± 0.05	79^+	79.57 ± 0.14
99.94	79^+	69.14 ± 0.44	86.18 ± 0.05	78^+	79.51 ± 0.18
69.91	77^+	15.89 ± 0.04	66.14 ± 0.05	77^+	78.67 ± 0.23
69.91	77^+	35.36 ± 0.08	61.33 ± 0.05	77^+	78.45 ± 0.23
69.91	77^+	52.52 ± 0.34	56.70 ± 0.05	77^+	78.04 ± 0.24
69.91	77^+	70.12 ± 0.45	51.96 ± 0.04	75^+	77.43 ± 0.24
49.89	77^+	5.87 ± 0.01	48.15 ± 0.05	76^+	76.59 ± 0.23
49.89	77^+	19.31 ± 0.05	44.25 ± 0.05	75^+	75.52 ± 0.23
49.89	77^+	35.03 ± 0.08	39.45 ± 0.05	74^+	74.41 ± 0.22
49.89	77^+	51.93 ± 0.33	33.76 ± 0.04	72^+	72.44 ± 0.53
34.90	74^+	10.56 ± 0.03	31.26 ± 0.05	72^+	71.67 ± 0.53
34.90	74^+	22.95 ± 0.06	26.87 ± 0.05	70^+	70.16 ± 0.82
34.90	74^+	35.01 ± 0.08	22.30 ± 0.05	69^+	67.89 ± 0.83

TABLE D.3: Experimental mean charge-states for lead ions after traversing titanium targets, and related information.

$^{208}\mathrm{Pb} \rightarrow {}_{22}\mathrm{Ti}$						
E_0 (MeV/u)	q_0	x (mg cm^{-2})	E_{out} (MeV/u)	q_{scaled}	σ_{CSD}	$\bar{q}$
279.98	81^+	32.29 ± 0.54	277.08 ± 0.06	81^+	0.7167	81.20 ± 0.09
279.98	81^+	38.07 ± 0.57	276.56 ± 0.06	81^+	0.7205	81.21 ± 0.07
279.98	81^+	102.82 ± 1.54	270.84 ± 0.06	81^+	0.7275	81.24 ± 0.09
279.98	81^+	205.15 ± 2.18	261.64 ± 0.06	81^+	0.7409	81.19 ± 0.08
279.98	81^+	238.76 ± 3.58	258.66 ± 0.06	81^+	0.7450	81.17 ± 0.08
99.94	79^+	18.64 ± 0.28	97.18 ± 0.03	79^+	1.0360	78.86 ± 0.12
99.94	79^+	56.72 ± 0.64	91.35 ± 0.03	79^+	1.0768	78.64 ± 0.12
99.94	79^+	102.82 ± 1.54	83.96 ± 0.03	78^+	1.2027	78.27 ± 0.10
99.94	79^+	140.89 ± 1.64	77.71 ± 0.03	78^+	1.2786	77.90 ± 0.11
99.94	79^+	205.15 ± 2.18	66.31 ± 0.02	77^+	1.4212	77.04 ± 0.12
99.94	79^+	238.76 ± 3.58	60.51 ± 0.02	76^+	1.4719	76.55 ± 0.13
69.91	77^+	18.64 ± 0.28	66.52 ± 0.03	77^+	1.4138	77.07 ± 0.17
69.91	77^+	56.72 ± 0.64	59.32 ± 0.03	76^+	1.5000	76.36 ± 0.21
69.91	77^+	102.34 ± 1.54	49.99 ± 0.02	75^+	1.6065	75.19 ± 0.24
69.91	77^+	140.89 ± 1.64	41.52 ± 0.02	74^+	1.6696	73.81 ± 0.23
49.89	75^+	8.36 ± 0.46	48.09 ± 0.03	75^+	1.6314	74.91 ± 0.16
49.89	75^+	18.64 ± 0.28	45.87 ± 0.03	75^+	1.6442	74.56 ± 0.21
49.89	75^+	38.07 ± 0.57	41.43 ± 0.02	74^+	1.6854	73.80 ± 0.19
49.89	75^+	51.73 ± 0.73	38.14 ± 0.02	73^+	1.7120	73.17 ± 0.16
49.89	75^+	70.37 ± 0.79	33.51 ± 0.02	72^+	1.7520	72.15 ± 0.22

TABLE D.4: Experimental mean charge-states for lead ions after traversing argon gas targets, and related information.

$^{208}Pb \rightarrow {}_{18}Ar$					
E_0 (MeV/u)	q_0	x (mg cm^{-2})	E_{out} (MeV/u)	q_{scaled}	$\bar{q}$
279.98	81^+	31.83 ± 0.08	277.15 ± 0.09	81^+	81.12 ± 0.21
279.98	81^+	62.73 ± 0.40	274.33 ± 0.09	81^+	81.17 ± 0.17
279.98	81^+	100.00 ± 0.64	270.99 ± 0.09	81^+	81.17 ± 0.18
99.94	79^+	34.71 ± 0.08	94.68 ± 0.05	78^+	78.01 ± 0.15
99.94	79^+	67.72 ± 0.43	89.46 ± 0.05	78^+	77.66 ± 0.18
99.94	79^+	99.99 ± 0.64	84.32 ± 0.05	78^+	77.25 ± 0.19
69.91	77^+	23.73 ± 0.06	65.62 ± 0.05	76^+	74.89 ± 0.20
69.91	77^+	23.41 ± 0.15	65.58 ± 0.05	76^+	74.93 ± 0.21
69.91	77^+	50.16 ± 0.32	60.66 ± 0.05	73^+	74.21 ± 0.24
69.91	77^+	50.86 ± 0.12	60.65 ± 0.05	73^+	74.17 ± 0.21
69.91	77^+	76.73 ± 0.49	55.58 ± 0.05	75^+	73.41 ± 0.15
69.91	77^+	99.98 ± 0.64	50.95 ± 0.04	74^+	72.66 ± 0.18
49.89	75^+	9.79 ± 0.02	47.80 ± 0.05	71^+	72.08 ± 0.22
49.89	75^+	28.88 ± 0.07	43.78 ± 0.05	70^+	71.48 ± 0.21
49.89	75^+	50.47 ± 0.12	39.04 ± 0.05	69^+	70.67 ± 0.20
49.89	75^+	71.61 ± 0.46	33.92 ± 0.04	70^+	69.49 ± 0.82

TABLE D.5: Experimental mean charge-states for lead ions after traversing zirconium targets, and related information.

$^{208}\mathrm{Pb} \rightarrow {}_{40}\mathrm{Zr}$						
E_0 (MeV/u)	q_0	x (mg cm^{-2})	E_{out} (MeV/u)	q_{scaled}	σ_{CSD}	$\bar{q}$
279.98	81^+	106.12 ± 1.14	271.71 ± 0.06	81+	0.7950	80.91 ± 0.09
279.98	81^+	261.85 ± 5.38	259.15 ± 0.06	81^+	0.8040	80.81 ± 0.08
279.98	81^+	520.98 ± 7.52	237.86 ± 0.05	81^+	0.8170	80.63 ± 0.08
99.94	79^+	23.40 ± 0.49	96.93 ± 0.03	78^+	1.1682	78.27 ± 0.14
99.94	79^+	60.28 ± 0.90	92.02 ± 0.03	78^+	1.2263	78.06 ± 0.19
99.94	79^+	129.52 ± 1.24	82.57 ± 0.03	78^+	1.3004	77.60 ± 0.16
99.94	79^+	259.12 ± 5.25	62.74 ± 0.02	76^+	1.3847	76.21 ± 0.19
99.94	79^+	261.85 ± 5.38	61.86 ± 0.02	76^+	1.3876	76.14 ± 0.12
69.91	77^+	23.40 ± 0.49	66.29 ± 0.03	77^+	1.4378	76.51 ± 0.13
69.91	77^+	45.84 ± 0.69	62.68 ± 0.03	76^+	1.4734	76.20 ± 0.11
69.91	77^+	60.28 ± 0.90	60.40 ± 0.03	76^+	1.4935	75.99 ± 0.18
69.91	77^+	106.12 ± 1.14	52.57 ± 0.02	75^+	1.5639	75.14 ± 0.20
69.91	77^+	129.52 ± 1.24	48.36 ± 0.02	74^+	1.5949	74.56 ± 0.15
49.89	76^+	17.00 ± 0.37	46.77 ± 0.03	74^+	1.5990	74.30 ± 0.21
49.89	76^+	45.84 ± 0.69	41.23 ± 0.03	73^+	1.6561	73.33 ± 0.22
49.89	76^+	60.28 ± 0.90	38.36 ± 0.02	72^+	1.6855	72.78 ± 0.21
49.89	76^+	83.68 ± 1.03	33.48 ± 0.02	71^+	1.7626	71.61 ± 0.22
34.90	70^+	10.14 ± 0.70	32.75 ± 0.03	71^+	1.7751	71.42 ± 0.13
34.90	70^+	23.40 ± 0.49	29.83 ± 0.03	71^+	1.8535	70.55 ± 0.13
34.90	70^+	40.40 ± 0.61	25.90 ± 0.02	69^+	1.9541	69.21 ± 0.20
34.90	70^+	60.28 ± 0.90	21.10 ± 0.02	68^+	2.0526	66.95 ± 0.18

TABLE D.6: Experimental mean charge-states for lead ions after traversing krypton gas targets, and related information.

$^{208}Pb \rightarrow {}_{36}Kr$					
E_0 (MeV/u)	q_0	x (mg cm^{-2})	E_{out} (MeV/u)	q_{scaled}	$\bar{q}$
99.94	79^+	39.12 ± 0.25	94.98 ± 0.05	78^+	76.60 ± 0.18
99.94	79^+	77.17 ± 0.49	90.04 ± 0.05	77^+	76.26 ± 0.18
99.94	79^+	148.67 ± 0.95	80.21 ± 0.05	77^+	75.56 ± 0.20
99.94	79^+	209.24 ± 1.34	71.53 ± 0.04	76^+	74.79 ± 0.20
69.91	77^+	36.32 ± 0.09	64.41 ± 0.05	75^+	73.74 ± 0.27
69.91	77^+	71.25 ± 0.17	58.97 ± 0.05	75^+	73.15 ± 0.26
69.91	77^+	105.81 ± 0.25	53.36 ± 0.05	74^+	72.46 ± 0.19
69.91	77^+	144.94 ± 0.35	46.40 ± 0.04	72^+	71.62 ± 0.15
49.89	76^+	8.52 ± 0.02	48.36 ± 0.05	73^+	71.45 ± 0.20
49.89	76^+	30.78 ± 0.07	44.45 ± 0.05	72^+	70.90 ± 0.18
49.89	76^+	57.20 ± 0.14	39.56 ± 0.05	72^+	70.02 ± 0.21
49.89	76^+	82.70 ± 0.20	34.60 ± 0.04	70^+	68.95 ± 0.19
34.90	70^+	6.85 ± 0.02	33.48 ± 0.05	69^+	68.22 ± 0.53
34.90	70^+	23.70 ± 0.06	30.04 ± 0.05	68^+	67.36 ± 0.56
34.90	70^+	45.70 ± 0.11	25.31 ± 0.05	67^+	66.05 ± 0.83
34.90	70^+	60.21 ± 0.14	22.05 ± 0.05	67^+	65.20 ± 0.82

TABLE D.7: Experimental mean charge-states for lead ions after traversing tin targets, and related information.

$^{208}Pb \rightarrow {}_{50}Sn$						
E_0 (MeV/u)	q_0	x (mg cm^{-2})	E_{out} (MeV/u)	q_{scaled}	σ_{CSD}	$\bar{q}$
279.98	81^+	71.88 ± 3.16	274.82 ± 0.06	81^+	0.8022	80.80 ± 0.25
279.98	81^+	184.54 ± 2.77	266.52 ± 0.06	81^+	0.8030	80.74 ± 0.07
279.98	81^+	270.80 ± 4.06	260.13 ± 0.06	81^+	0.8034	80.70 ± 0.08
279.98	81^+	455.34 ± 4.92	246.23 ± 0.06	81^+	0.8108	80.58 ± 0.08
99.94	79^+	22.83 ± 2.29	97.33 ± 0.03	78^+	1.1772	78.28 ± 0.08
99.94	79^+	71.88 ± 3.16	91.08 ± 0.03	78^+	1.2261	78.03 ± 0.09
99.94	79^+	184.54 ± 2.77	76.53 ± 0.03	77^+	1.3487	77.24 ± 0.13
69.91	77^+	22.83 ± 2.29	66.49 ± 0.03	76^+	1.4230	76.55 ± 0.16
34.90	74^+	2.14 ± 1.03	34.48 ± 0.03	71^+	1.7967	71.34 ± 0.26
34.90	74^+	3.84 ± 1.95	34.17 ± 0.03	71^+	1.8165	71.27 ± 0.26
34.90	74^+	5.97 ± 2.20	33.75 ± 0.03	70^+	1.7692	71.12 ± 0.35

TABLE D.8: Experimental mean charge-states for lead ions after traversing xenon gas targets, and related information.

$^{208}Pb \rightarrow {}_{54}Xe$					
E_0 (MeV/u)	q_0	x (mg cm^{-2})	E_{out} (MeV/u)	q_{scaled}	$\bar{q}$
279.98	81^+	111.67 ± 0.71	271.97 ± 0.09	81^+	80.43 ± 0.10
279.98	81^+	221.76 ± 1.42	264.03 ± 0.09	81^+	80.37 ± 0.22
279.98	81^+	304.36 ± 1.95	257.99 ± 0.09	81^+	80.32 ± 0.22
279.98	81^+	327.11 ± 2.09	256.28 ± 0.09	81^+	80.30 ± 0.08
99.94	79^+	28.18 ± 0.18	96.62 ± 0.05	78^+	76.68 ± 0.13
99.94	79^+	28.58 ± 0.07	96.65 ± 0.05	78^+	76.67 ± 0.12
99.94	79^+	84.29 ± 0.20	90.17 ± 0.05	77^+	76.24 ± 0.17
99.94	79^+	83.14 ± 0.53	90.20 ± 0.05	77^+	76.28 ± 0.17
99.94	79^+	162.23 ± 1.04	80.49 ± 0.05	77^+	75.48 ± 0.15
99.94	79^+	164.50 ± 0.39	80.36 ± 0.05	77^+	75.42 ± 0.12
99.94	79^+	237.13 ± 1.52	70.78 ± 0.04	76^+	74.50 ± 0.15
99.94	79^+	307.36 ± 1.97	61.07 ± 0.04	75^+	73.32 ± 0.12
69.91	77^+	20.27 ± 0.05	67.15 ± 0.05	75^+	73.68 ± 0.20
69.91	77^+	68.83 ± 0.17	60.48 ± 0.05	74^+	72.87 ± 0.22
69.91	77^+	112.97 ± 0.27	54.13 ± 0.04	73^+	72.01 ± 0.20
69.91	77^+	154.12 ± 0.37	47.90 ± 0.04	73^+	71.06 ± 0.22
49.89	76^+	9.28 ± 0.06	48.41 ± 0.05	73^+	70.78 ± 0.12
49.89	76^+	30.64 ± 0.20	45.11 ± 0.05	72^+	70.29 ± 0.18
49.89	76^+	59.83 ± 0.38	40.39 ± 0.05	72^+	69.42 ± 0.23
49.89	76^+	87.69 ± 0.56	35.67 ± 0.04	70^+	68.46 ± 0.54
49.89	76^+	113.93 ± 0.73	31.00 ± 0.04	68^+	67.35 ± 0.53

TABLE D.9: Experimental mean charge-states for lead ions after traversing polypropylene targets, and related information.

$^{208}Pb \rightarrow (C_3H_6)_n$						
E_0 (MeV/u)	q_0	x (mg cm^{-2})	E_{out} (MeV/u)	q_{scaled}	σ_{CSD}	$\bar{q}$
279.98	81^+	25.99 ± 0.12	276.63 ± 0.06	81^+	0.6160	80.87 ± 0.09
279.98	81^+	45.92 ± 0.23	274.08 ± 0.06	81^+	0.7013	80.81 ± 0.10
279.98	81^+	64.06 ± 0.19	271.70 ± 0.06	81^+	0.7350	80.78 ± 0.09
279.98	81^+	71.91 ± 0.26	270.68 ± 0.06	81^+	0.7413	80.77 ± 0.10
279.98	81^+	119.51 ± 0.31	264.49 ± 0.06	81^+	0.7551	80.72 ± 0.09
279.98	81^+	183.57 ± 0.36	255.99 ± 0.06	81^+	0.7537	80.67 ± 0.09
99.94	79^+	16.73 ± 0.09	96.13 ± 0.03	80^+	0.7127	79.64 ± 0.10
99.94	79^+	42.72 ± 0.15	89.86 ± 0.03	79^+	0.7356	79.67 ± 0.11
99.94	79^+	64.06 ± 0.19	84.53 ± 0.03	79^+	0.7387	79.64 ± 0.10
99.94	79^+	109.98 ± 0.30	72.35 ± 0.02	79^+	0.7930	79.46 ± 0.11
99.94	79^+	119.51 ± 0.31	69.62 ± 0.02	79^+	0.8113	79.40 ± 0.08
69.91	77^+	13.36 ± 0.03	66.07 ± 0.03	79^+	0.9262	79.07 ± 0.18
69.91	77^+	25.99 ± 0.12	62.21 ± 0.03	79^+	0.9008	79.18 ± 0.16
69.91	77^+	45.92 ± 0.23	55.94 ± 0.03	78^+	0.9868	78.96 ± 0.21
69.91	77^+	64.06 ± 0.19	49.65 ± 0.02	78^+	1.1045	78.57 ± 0.18
69.91	77^+	71.91 ± 0.26	46.82 ± 0.02	77^+	1.1513	78.36 ± 0.09
69.91	77^+	90.05 ± 0.23	39.58 ± 0.02	76^+	1.3510	77.48 ± 0.19
49.89	77^+	6.18 ± 0.02	47.71 ± 0.03	78^+	1.1967	78.00 ± 0.10
49.89	77^+	13.36 ± 0.03	45.08 ± 0.03	77^+	1.2278	78.08 ± 0.18
49.89	77^+	25.99 ± 0.12	40.08 ± 0.02	77^+	1.3533	77.54 ± 0.19
49.89	77^+	39.35 ± 0.12	34.44 ± 0.02	76^+	1.4927	76.50 ± 0.24
34.90	74^+	6.18 ± 0.02	32.23 ± 0.03	76^+	1.4621	75.77 ± 0.25
34.90	74^+	16.73 ± 0.09	27.27 ± 0.03	75^+	1.6017	74.42 ± 0.22

TABLE D.10: Experimental mean charge-states for lead ions after traversing propene gas targets, and related information.

^{208}Pb→propene					
E_0 (MeV/u)	q_0	x (mg cm^{-2})	E_{out} (MeV/u)	q_{scaled}	$\bar{q}$
279.98	81^+	35.28 ± 0.08	275.38 ± 0.09	81^+	80.82 ± 0.15
279.98	81^+	34.78 ± 0.22	275.39 ± 0.09	81^+	80.82 ± 0.13
279.98	81^+	72.08 ± 0.46	270.46 ± 0.09	81^+	80.73 ± 0.14
279.98	81^+	107.3 ± 0.69	265.76 ± 0.09	81^+	80.69 ± 0.15
99.94	79^+	13.85 ± 0.09	96.74 ± 0.05	80^+	79.44 ± 0.12
99.94	79^+	36.63 ± 0.23	91.31 ± 0.05	80^+	79.51 ± 0.14
99.94	79^+	71.22 ± 0.46	82.36 ± 0.05	79^+	79.44 ± 0.15
99.94	79^+	107.1 ± 0.69	72.55 ± 0.04	78^+	79.24 ± 0.19
49.89	77^+	8.12 ± 0.02	46.93 ± 0.05	78^+	77.13 ± 0.22
49.89	77^+	7.96 ± 0.05	46.84 ± 0.05	78^+	77.09 ± 0.25
49.89	77^+	23.87 ± 0.06	41.02 ± 0.05	77^+	76.06 ± 0.18
49.89	77^+	23.53 ± 0.15	40.96 ± 0.05	77^+	75.92 ± 0.25
49.89	77^+	38.86 ± 0.09	35.05 ± 0.04	76^+	74.19 ± 0.20
49.89	77^+	38.32 ± 0.25	35.05 ± 0.04	76^+	73.99 ± 0.22
34.90	74^+	4.95 ± 0.01	32.78 ± 0.06	72^+	73.11 ± 0.64
34.90	74^+	14.44 ± 0.03	28.63 ± 0.05	71^+	71.71 ± 0.54
34.90	74^+	23.45 ± 0.06	24.41 ± 0.05	71^+	70.10 ± 0.82

Appendix E

ATIMA Program

The ATIMA (ATomic Interaction with MAtter) computer program [Wei98a] has been developed at GSI, Darmstadt in Germany since 1985. It provides predictions for the stopping power, energy-loss straggling, and angular scattering of any projectile ions from protons ($Z_1 = 1$) up to uranium ($Z_1 = 92$) and for target materials from hydrogen to uranium[1]. Since there has been no publication of this computer program, this appendix describes a main part of the program; specifically, how the stopping power calculation is performed.

The basic input parameters are the incident energy E, mass M_1, atomic number Z_1 of the projectile, and the mass M_2, atomic number Z_2, density ρ, mean excitation potential I of the target. The program adapts, then, mainly two routines for the calculation, namely the stopping power part and the mean charge prediction part. We will describe the individual parts briefly below:

E.1 Stopping Power Prediction

E.1.1 Elastic Collisions

The calculation of the stopping power consists of two contributions. One is the nuclear stopping power, which is attributed to the elastic collisions, as shortly described in Chapter 2. The formula implemented in ATIMA program comes from Lindhard *et al.* [LSS63; LNS68] as

$$\left(\frac{dE}{dx}\right)_n(\epsilon) = \begin{cases} \frac{\ln(1+1.1383\epsilon)}{2[\epsilon+0.01321\epsilon^{0.212226}+0.19593\epsilon^{0.5}]} & (\epsilon \leq 30) \\ \\ \frac{\ln(\epsilon)}{2\epsilon} & (\epsilon > 30) \end{cases} \tag{E.1}$$

where n denotes the nuclear stopping. The ϵ is the reduced energy defined as

$$\epsilon = \frac{32.53\ M_2 E}{Z_1 Z_2\ (M_1 + M_2)\ \left(Z_1^{0.23} + Z_2^{0.23}\right)} \tag{E.2}$$

[1]The projectile and target can optionally be chosen up to $Z_1 = 120$ and $Z_2 = 99$, respectively.

where the energy E is given in the unit of keV/u. In the present experiment, the contribution from the elastic collisions is negligible, as we have shown in Chapter 2.

E.1.2 Inelastic Collisions

The other contribution is from the electronic stopping power, which is attributed to the inelastic collisions with the target electrons. In the ATIMA program, the calculation is divided into three energy domains:

- For $E \leq 10$ MeV/u, the electronic stopping power is calculated according to the scaling formula of Ziegler [ZBL85] with the old parametrization from the 1990s as
$$\left(\frac{dE}{dx}\right)_e = \left(\frac{dE}{dx}\right)_e^{\text{Ziegler}} \quad . \tag{E.3}$$
The principles of this scaling procedure can be found in Ref.[ZBL85].

- For $10 < E \leq 30$ MeV/u, the electronic stopping power is averaged with weight between the Ziegler formula and the *ATIMA* stopping power, which will be shown below, as
$$\left(\frac{dE}{dx}\right)_e = (1.0 - F) \cdot \left(\frac{dE}{dx}\right)_e^{\text{Ziegler}} + \left(\frac{dE}{dx}\right)_e^{\text{ATIMA}} \tag{E.4}$$
where
$$F = 0.05 \cdot (E - 10.0) \tag{E.5}$$

- Above 30 MeV/u, the electronic stopping power is calculated by the original ATIMA code as
$$\left(\frac{dE}{dx}\right)_e = \left(\frac{dE}{dx}\right)_e^{\text{ATIMA}} \quad . \tag{E.6}$$

Here, we will explain the general equation of $(dE/dx)_e^{\text{ATIMA}}$ implemented in the ATIMA program. It adapts the Lindhard-Sørensen theory [LS96] as well as the correction terms considered in the reference as

$$-\left(\frac{dE}{dx}\right)_e^{\text{ATIMA}} = \frac{4\pi N_A e^4}{m_e c^2 \beta^2} \frac{Z_2}{M_2} q_1^2 \cdot \left[\left(L_{\text{Bethe}} - \frac{C}{Z_2}\right) \cdot B - \frac{\delta}{2} + \Delta L_{\text{LS}}\right] \quad , \tag{E.7}$$

where N_A is the Avogadro's number and q_1 is the mean charge state of projectiles: We will give a description on the latter parameter in the next section. The explanation of the terms in the square bracket are as follows:

First, L_{Bethe} is the term from the relativistic Bethe formula, which is based on the first-order Born approximation, given by

$$\begin{aligned} L_{\text{Bethe}} &= L_{\text{Bethe}}(\beta, I) \\ &= \ln \frac{2 m_e c^2 \beta^2}{I} - \ln(1 - \beta^2) - \beta^2 \quad . \end{aligned} \tag{E.8}$$

The input parameters are the velocity of projectiles and the mean excitation potential I, the values of which is taken from the NIST table [NISb]. The term C is the inner Shell correction derived in Ref. [BB64] as

$$\begin{aligned} C &= C(I,\eta) \\ &= \left(0.422377\eta^{-2} + 0.0304043\eta^{-4} - 0.00038106\eta^{-6}\right) \times 10^{-6} I^2 \\ &+ (3.850190\eta^{-2} - 0.1667989\eta^{-4} + 0.00157955\eta^{-6}) \times 10^{-9} I^3 \quad , \end{aligned} \tag{E.9}$$

where $\eta = \gamma\beta$. This equation is included in the calculation only when $\eta \geq 0.13$. Next, the factor B is responsible for the Barkas term, or the Z_1^3 correction due to the polarization effect. The formula is taken from Jackson and McCarthy [JM72], but a factor two is multiplied to the formula as suggested by Lindhard [Lin76]:

$$\begin{aligned} B &= B(q_1, Z_2, \eta) \\ &= 1 + 2\frac{Z_1}{\sqrt{Z_2}} F(V) \quad , \end{aligned} \tag{E.10}$$

where

$$V = \frac{\beta\gamma}{\alpha\sqrt{Z_2}} \quad . \tag{E.11}$$

The $F(V)$ is a dimensionless universal function, and the exact form is given in Ref.[JM72]. Note that this is the ONLY correction term affected by the charge state of projectile in the ATIMA program, and the explanation will be given in the next section. Therefore, the variable of the formula is explicitly given with the mean charge state q_1. Then, δ is the Fermi density effect, the formula of which is given by Sternheimer [Ste84]

$$\begin{aligned} \delta &= \delta(\beta, Z_2, M_2, I, \rho) \\ &= \begin{cases} 0 & (X < X_0,\ \delta_0 = 0) \\ \delta_0 \cdot 10^{2(X - X_0)} & (X < X_0,\ \delta_0 \neq 0) \\ 4.6052X + a\,(X_1 - X)^m + C & (X_0 \leq X \leq X_1) \\ 4.6052X + C & (X > X_1) \end{cases} \end{aligned} \tag{E.12}$$

with $X = \log_{10}(\beta\gamma)$. The coefficients δ_0, X_0, X_1, a, and m have Z_2 dependence. And, C is given by

$$C = -2\ln(I/h\nu_p) - 1 \quad , \tag{E.13}$$

where the I corresponds to the mean excitation potential. Lastly, the ΔL_{LS} is the correction term derived in the Lindhard-Sørensen theory [LS96]

$$\Delta L_{\mathrm{LS}} = \Delta L_{\mathrm{LS}}(Z_1, v) \quad . \tag{E.14}$$

This term consists of the correction terms of Bloch, Mott, and the finite nuclear size effect for the bare projectiles. The input parameters are Z_1, M_1, and velocity β.

With the described formulas and models for the stopping powers of heavy ions,

the ATIMA program can accurately predict the experimental stopping powers for bare and few-electron projectiles as shown in Fig.E.1[Wei+00; Gei+02]. This statement holds even for relatively thick energy degraders (d) because the absolute energy-loss calculation is still based on the atomic range difference ($d = R(E_{in}) - R(E_{out})$), i.e. the critical energy domain for stopping powers is excluded.

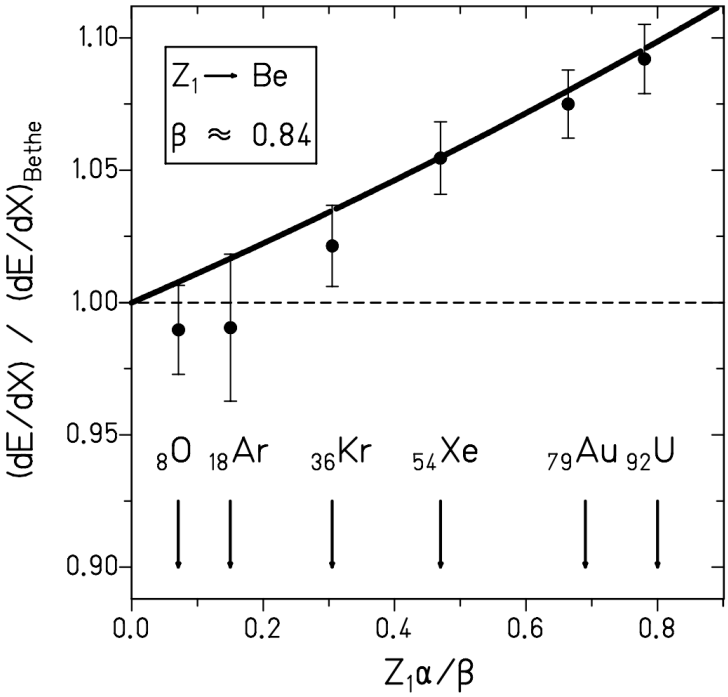

FIGURE E.1: Experimental stopping powers for different heavy-ion projectiles in beryllium target at $\beta = 0.84$. This picture was taken from Ref.[Gei+02].

E.2 Mean Charge State Prediction

The ATIMA program adopts the mean charge state of the projectiles in matters for the charge state description in the calculation of Eq.E.7. The effect enters in the q^2 term in front of the square brackets and in the term B within the stopping number. Other terms are calculated with the projectile's nuclear charge.

The latest version of the ATIMA program, which is the version 1.4, has a special routine for the prediction of mean charge state as follows: Figure E.2 (taken from [Wei98a]) shows the overview of the calculation method. The routine divides the calculation domain depending on the energy E and atomic number Z_1 ($= Z_p$ of the y-axis in the picture) of the projectile ions. First, at the high relativistic domain $E \geq 1.5$ GeV/u, the mean charge state is predicted by the fit formula to the calculation results of the CHARGE program [Sch+98] given by

$$q_{\mathrm{CHARGE}} = Z_1 \left(1.0 - \exp\left(-180\,\beta\gamma^{0.18} Z_1^{-0.82} Z_2^{0.1}\right)\right) \quad . \tag{E.15}$$

for any projectiles. For heavy projectiles with $Z_1 > 28$, at the energy domain in $70 \leq E \leq 1000$ MeV/u, the mean charge state is predicted by the subroutine of the GLOBAL program with some *corrections*. The *correction* term was determined from the comparison of the GLOBAL calculation q_{GLOBAL} with the experimental mean charge data, and the deviation was compensated by adding the semi-emperical formula of Pierce and Blann

$$q_{\mathrm{P\&B}} = Z_1 \left[1 - \exp\left(-0.95 \frac{v}{v_0 Z_1^{2/3}} \right) \right] \tag{E.16}$$

with being put some weights. Three fit parameters (c_1, c_2, c_3) were determined, and the resulting formula for the energy domain $70 \leq E \leq 1000$ MeV/u is defined by

$$q_{\mathrm{GL/c}} = \frac{c_1 \left(q_{\mathrm{GLOBAL}} - q_{\mathrm{P\&B}} \right)}{(Z_2 + 1)^{c_2}} \left(1.0 - \exp\left(-c_3 E \right) \right) + q_{\mathrm{P\&B}} \quad , \tag{E.17}$$

where $c_1 = 1.4$, $c_2 = 0.28$, and $c_3 = 0.04$, respectively. The transition from q_{CHARGE} to $q_{\mathrm{GL/c}}$ at the interval between 1000 and 1500 MeV/u, the two functions are connected simply by linear. In addition, at the lower energy interval between 30 and 70 MeV/u, the formula $q_{\mathrm{GL/c}}$ is linearly connected to the function of Winger: For the light projectiles with $Z_1 \leq 28$ at the energy domain in $30 \leq E \leq 1000$ MeV/u, the mean charge state is predicted by the fit formula obtained by Winger *et al.* [Win+92] as

$$q_{\mathrm{Winger}} = Z_1 \left(1.0 - \exp\left(a_0 + a_1 x + a_2 x^2 + a_3 x^3 + a_4 x^4 \right) \right) \tag{E.18}$$

where

$$x = \frac{\beta}{0.012 Z_1^{0.45}} \tag{E.19}$$

and

$$\begin{aligned}
a_0 &= -c_0 \\
a_1 &= -c_1 \exp\left(c_2 \ln\left(Z_1\right) - c_3 \ln^2\left(Z_1\right) + c_4 \ln^3\left(Z_1\right) - c_5 \ln\left(Z_2\right) + c_6 \ln^2\left(Z_2\right) \right) \\
a_2 &= c_7 \exp\left(c_8 \ln\left(Z_1\right) - c_9 \ln\left(Z_2\right) \right) \\
a_3 &= -c_{10} \exp\left(c_{11} \ln\left(Z_1\right) - c_{12} \ln^3\left(Z_1\right) \right) \\
a_4 &= -c_{13}
\end{aligned} \tag{E.20}$$

with $c_0 = 0.4662$, $c_1 = 0.5491$, $c_2 = 0.7028$, $c_3 = 0.1089$, $c_4 = 0.001644$, $c_5 = 0.5155$, $c_6 = 0.05633$, $c_7 = 0.005447$, $c_8 = 0.8795$, $c_9 = 1.091$, $c_{10} = 0.0008261$, $c_{11} = 2.848$, $c_{12} = 0.2442$, and $c_{13} = 0.00009293$.

Then, at the interval between 10 and 30 MeV/u, the mean charge state is calculated by the Winger formula, but since the stopping power Eq.E.7 is averaged with weight to the Ziegler formula as described in Eq.E.4, the mean charge state is accordingly modified by the transition. Finally, below 10 MeV/u, the ATIMA program fully adopts the calculation by the Ziegler formula.

With the described routines, the ATIMA program can reproduce our experimental stopping powers of solids very well. However, detailed investigation on the gas-solid difference is required to improve the program; as it was clearly shown that the ATIMA 1.4 cannot accurately reproduce the stopping powers of the gaseous materials.

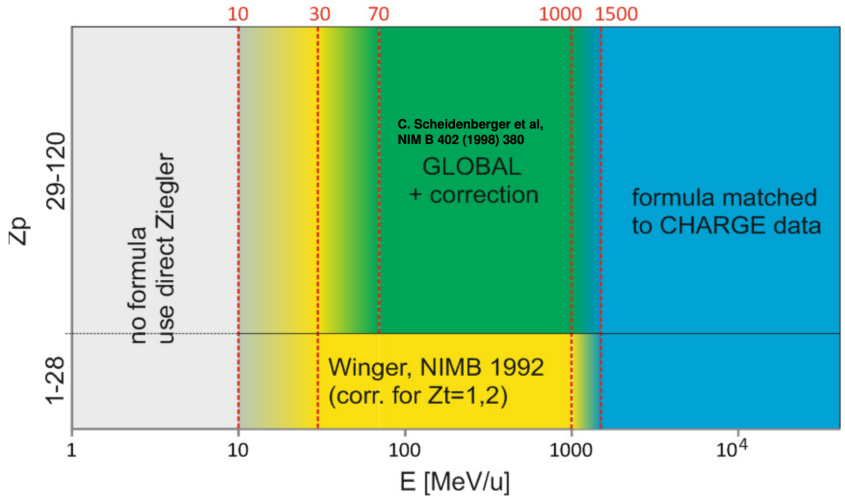

FIGURE E.2: Overview of the mean charge prediction implemented in the ATIMA 1.4. This picture was taken from Ref.[Wei98a].

Bibliography

[ABR72] J.C. Ashley, W. Brandt, and R.H. Ritchie. In: *Phys. Rev.* B5 (1972), p. 2393.

[Ahl78] S.P. Ahlen. In: *Phys. Rev. A* 17.3 (1978), p. 1236.

[Ahl80] S. Ahlen. In: *Rev. Mod. Phys.* 52 (1980), p. 121.

[Anh+85] R. Anholt et al. In: *Phys. Rev. A* 32.6 (1985), p. 3302.

[Anh85] R. Anholt. In: *Phys. Rev. A* 31.6 (1985), p. 3579.

[AT83] S. P. Ahlen and G. Tarlé. In: *Phys. Rev. Lett.* 50.15 (1983), p. 1110.

[Bär+18] E. Bär et al. In: *Phys. Med. Biol.* 63.16 (2018).

[BB64] W.H. Barkas and M.J. Berger. "Tables of Energy Losses and Ranges of Heavy Charged Particles". In: *Studies in the Penetration of Charged Particles in Matter* (1964). Ed. by National Academy of Sciences Publication 1133.

[BDH63] W.H. Barkas, N.J. Dyer, and H.H. Heckman. In: *Phys. Rev. Lett.* 11 (1963), p. 26.

[Bet+66] H.D. Betz et al. In: *Phys. Lett.* 22.5 (1966), p. 643.

[Bet30] H. Bethe. In: *Ann. d. Phys.* 5 (1930), p. 325.

[Bet32] H. Bethe. In: *Zs. f. Phys.* 76 (1932), p. 293.

[Bet72] H.D. Betz. In: *Rev. Mod. Phys.* 44.3 (1972), p. 465.

[BG70] H.D. Betz and L. Grodzins. In: *Phys. Rev. Lett.* 25.4 (1970), p. 211.

[Bim+00] R. Bimbot et al. In: *Nucl. Instr. and Meth.* B 170 (2000), p. 329.

[Bim+78] R. Bimbot et al. In: *Nucl. Instr. and Meth. Phys. Res.* 153 (1978), p. 161.

[Bim+80] R. Bimbot et al. In: *Nucl. Instr. and Meth.* 174 (1980), p. 231.

[Bim+86] R. Bimbot et al. In: *Nucl. Instr. and Meth.* B 17 (1986), p. 1.

[Bim+89a] R. Bimbot et al. In: *Nucl. Instr. and Meth. B* 44 (1989), p. 1.

[Bim+89b] R. Bimbot et al. In: *Nucl. Instr. and Meth. B* 44 (1989), p. 19.

[Bim+96] R. Bimbot et al. In: *Nucl. Instr. and Meth.* B 107 (1996), p. 9.

[BK30] H.C. Brinkman and H.A. Kramers. In: *Proc. R. Acad. Sci. Amsterdam* 33 (1930), p. 973.

[BK82] W. Brandt and M. Kitagawa. In: *Phys. Rev. B* 25.9 (1982), p. 5631.

[BL54] N. Bohr and J. Lindhard. In: *K. Dan. Vindensk. Selsk. Mat. Fys. Medd.* 26 (1954), p. 1.

[Blo33] F. Bloch. In: *Ann. d. Phys.* 16.5 (1933), p. 285.

[Boh13] N. Bohr. In: *Philos. Mag.* 25.145 (1913), p. 10.

[Boh15] N. Bohr. In: *Philos. Mag.* 30.178 (1915), p. 581.

[Boh48] N. Bohr. In: *Mat. Fys. Medd.* 18.8 (1948), p. 1.

[CP69] W.K. Chu and D. Powers. In: *Phys. Rev.* 187.2 (1969), p. 478.

[DS56] J.A. Doggett and L.V. Spencer. In: *Phys. Rev.* 103.6 (1956), p. 1597.

[Eic85] J. Eichler. In: *Phys. Rev. A* 32.1 (1985), p. 112.

[ES07] J. Eichler and T. Stöhlker. In: *Phys. Rep.* 439 (2007), p. 1.

[Fan63] U. Fano. In: *Ann. Rev. Nucl. Sci.* 13 (1963), p. 1.

[Fer40] E. Fermi. In: *Phys. Rev.* 57 (1940), p. 485.

[Fet+06] A. Fettouhi et al. In: *Nucl. Instr. and Meth. B* 245 (2006), p. 32.

[FR81] B. Franczak and C. Riedel. "an interactive computer program for ion-optical systems". In: *GSI Report* 81.2 (1981).

[Gau+87] H. Gauvin et al. In: *Nucl. Instr. and Meth.* B28 (1987), p. 191.

[Gau+90] H. Gauvin et al. In: *Nucl. Instr. and Meth.* B47 (1990), p. 339.

[Gei+02] H. Geissel et al. In: *Nucl. Instr. and Meth. B* 195 (2002), p. 3.

[Gei+82] H. Geissel et al. In: *Nucl. Instr. and Meth. B* 194 (1982), p. 21.

[Gei+92] H. Geissel et al. In: *Nucl. Instr. and Meth.* B70 (1992), p. 286.

[GS98] H. Geissel and C. Scheidenberger. In: *Nucl. Instr. and Meth.* B 136 (1998), p. 114.

[GSI21] GSI-website. 2021. URL: `https://www.gsi.de/en/researchaccelerators/accelerator_facility`.

[HBG90] F. Hubert, R. Bimbot, and H. Gauvin. In: *Atomic Data and Nuclear Data Tables* 46 (1990), p. 1.

[Her+91] J. Herault et al. In: *Nucl. Instr. and Meth.* B61 (1991), p. 156.

[Hli+98] V. Hlinka et al. In: *Nucl. Instr. and Meth. A* 419 (1998), p. 503.

[HM74] K.W. Hill and E. Merzbacher. In: *Phys. Rev.* A9 (1974), p. 156.

[Iwa+97] N. Iwasa et al. In: *Nucl. Instr. and Meth. B* 126 (1997), p. 284.

[Jan+07] R. Janik et al. In: *Acta Physica Universitaits Comenianae* XLVIII-XLIX (2007), p. 85.

[Jan+09] R. Janik et al. In: *Nucl. Instr. and Meth. A* 598 (2009), p. 681.

[Jan+11] R. Janik et al. In: *Nucl. Instr. and Meth. A* 640 (2011), p. 54.

[JM72] J.D. Jackson and R.L McCarthy. In: *Phys. Rev.* B6 (1972), p. 4131.

[KCM69] G.S. Khandelwal, B.H. Choi, and E. Merzbacher. In: *Atomic Data* 1 (1969), p. 103.

[Kha67] G.S. Khandelwal. In: *Nucl. Phys.* A116 (1967), p. 97.

[Kin+20] B. Kindler et al. In: *EPJ Web Conf.* 02002 (2020), p. 5.

[Lam+15] E. Lamour et al. In: *Phys. Rev. A* 92.042703 (2015).

[Las51a] N. O. Lassen. In: *Dan. Mat. Fys. Medd.* 26.5 (1951).

[Las51b] N. O. Lassen. In: *Dan. Mat. Fys. Medd.* 26.12 (1951).

[LB37] M.S. Livingston and H. Bethe. In: *Revs. Mod. Phys.* 9.3 (1937), p. 245.

[Leo94] William R. Leo. *Techniques for Nuclear and Particle Physics Experiments*. Springer-Verlag, 1994.

[Lin76] J. Lindhard. In: *Nucl. Instr. and Meth.* 132 (1976), p. 1.

[LL77] L.D. Landau and E.M. Lifshitz. *Quantum Mechanics*. Pergamon, Oxford, 1977.

[LNS68] J. Lindhard, V. Nielsen, and M. Scharff. In: *Mat. Fys. Medd. Dan. Vid. Selsk* 36.10 (1968).

[LS96] J. Lindhard and A.H. Sørensen. In: *Phys. Rev.* A53 (1996), p. 2443.

[LSS63] J. Lindhard, M. Scharff, and H.E. Schiott. In: *Mat. Fys. Medd. Dan. Vid. Selsk* 33.14 (1963).

[Med+91] R. Medenwaldt et al. In: *Phys. Lett.* A155 (1991), p. 155.

[Mey+85] W.E. Meyerhof et al. In: *Phys. Rev. A* 32.6 (1985), p. 3291.

[MN78] J.N. Marx and D.R. Nygren. In: *Physics Today* 31.10 (1978), p. 46.

[Mot29] N.F. Mott. In: *Proc. Roy. Soc. London* A124 (1929), p. 425.

[Mot32] N.F. Mott. In: *Proc. Roy. Soc. London* A135 (1932), p. 429.

[MS80] B.L. Moiseiwitch and S.G. Stockman. In: *J. Phys. B* 13 (1980), p. 2975.

[NISa] NIST-table. *Stopping-Power Range Tables for Electrons, Protons, and Helium Ions*. URL: `https://www.nist.gov/pml/stopping-power-range-tables-electrons-protons-and-helium-ions`.

[NISb] NIST-table. *X-Ray Mass Attenuation Coefficients*. URL: `https://physics.nist.gov/PhysRefData/XrayMassCoef/tab1.html`.

[Nor60] L.C. Northcliffe. In: *Phys. Rev.* 120 (1960), p. 1744.

[Pau21] H. Paul. *Stopping Power for Light and Heavier Ions*. June 2021. URL: `https://www-nds.iaea.org/stopping/stopping_201510/index.html`.

[PB68] T.E. Pierce and M. Blann. In: *Phys. Rev.* 173.2 (1968), p. 390.

[SAT81] M.H. Salamon, S.P. Ahlen, and G. Tarle. In: *Phys. Rev.* A23.1 (1981), p. 73.

[Sch+94] C. Scheidenberger et al. In: *Phys. Rev. Lett.* 73.1 (1994), p. 50.

[Sch+98] C. Scheidenberger et al. In: *Nucl. Instr. and Meth. B* 142 (1998), p. 441.

[Sch68] L.I. Schiff. *Quantum Mechanics*. 3rd Edition. McGraw-Hill Book Company, 1968.

[SG01] G. Schiwietz and P.L. Grande. In: *Nucl. Instr. and Meth. B* 175 (2001), p. 125.

[SG98] C. Scheidenberger and H. Geissel. In: *Nucl. Instr. and Meth.* B 135 (1998), p. 25.

[She+10] V.P. Shevelko et al. In: *J. Phys. B: At. Mol. Opt. Phys.* 43.215202–9 (2010).

[Sig14] P. Sigmund. *Particle Penetration and Radiation Effects Volume 2*. Springer Series in Solid-State Sciences. Springer, Cham, 2014.

[Sig96] P. Sigmund. In: *Phys. Rev. A* 54.4 (1996), p. 3113.

[Sig97] P. Sigmund. In: *Phys. Rev. A* 56.5 (1997), p. 3781.

[Sør02] A.H. Sørensen. In: *Nucl. Instr. and Meth. B* 195 (2002), p. 106.

[SS00] A. Schinner and P. Sigmund. In: *Nucl. Instr. and Meth. B* 164 (2000), p. 220.

[SS19] A. Schinner and P. Sigmund. In: *Nucl. Instr. and Meth. B* 460 (2019), pp. 19–26. URL: `https://www.sdu.dk/en/dpass`.

[Ste84] R.M. Sternheimer. In: *Atomic Data and Nuclear Data Tables* 30 (1984), p. 261.

[Tol+18] I. Tolstikhina et al. *Basic Atomic Interactions of Accelerated Heavy Ions in Matter*. Vol. 98. Springer Series on Atomic, Optical, and Plasma Physics, 2018.

[TS78] G. Tarlé and M. Solarz. In: *Phys. Rev. Lett.* 41.7 (1978), p. 483.

[Wal52] M.C. Walske. In: *Phys. Rev.* 88.6 (1952), p. 1283.

[Wal55] M.C. Walske. In: *Phys. Rev.* 101.3 (1955), p. 940.

[Wei+00] H. Weick et al. In: *Phys. Rev. Lett.* 85.13 (2000), p. 2725.

[Wei98a] H. Weick. ATIMA program. 1998. URL: `https://web-docs.gsi.de/~weick/atima/`.

[Wei98b] H. Weick. *GICOSY ion optical program*. 1998. URL: `https://web-docs.gsi.de/~weick/gicosy/`.

[Win+92] J. Winger et al. In: *Nucl. Instr. and Meth. B* 70 (1992), p. 380.

[Wol87] H. Wollnik. *Optics of Charged Particles*. Ed. by United States: Academic Press Inc. 1987.

[ZBL85] J.F. Ziegler, J.P. Biersack, and U. Littmark. *The Stopping and Range of Ions in Solids*. Vol. 1. New York : Pergamon Press., 1985.

[Zie+10] J.F. Ziegler et al. In: *Nucl. Instr. and Meth. B* 268 (2010), p. 1818. URL: `http://www.srim.org`.

[Zie77a] J.F. Ziegler. In: *Appl. Phys. Lett.* 31:8 (1977).

[Zie77b] J.F. Ziegler. "Helium Stopping Powers and Ranges in all Elements". In: *Pergamon, New York* (1977).

[Zie85] Biersack J.P. Ziegler J.F. *The Stopping and Range of Ions in Matter*. Springer, Boston, MA., 1985.